



HAL
open science

Numerical (1+2D)/3D tool to model the surface scattering of light in the inhibited coupling hollow fiber

Kostiantyn Vasko

► **To cite this version:**

Kostiantyn Vasko. Numerical (1+2D)/3D tool to model the surface scattering of light in the inhibited coupling hollow fiber. Optics / Photonic. Université de Limoges, 2023. English. NNT : 2023LIMO0105 . tel-04503341

HAL Id: tel-04503341

<https://theses.hal.science/tel-04503341v1>

Submitted on 13 Mar 2024

HAL is a multi-disciplinary open access archive for the deposit and dissemination of scientific research documents, whether they are published or not. The documents may come from teaching and research institutions in France or abroad, or from public or private research centers.

L'archive ouverte pluridisciplinaire **HAL**, est destinée au dépôt et à la diffusion de documents scientifiques de niveau recherche, publiés ou non, émanant des établissements d'enseignement et de recherche français ou étrangers, des laboratoires publics ou privés.

Université de Limoges

École Doctorale 653 – Sciences et Ingénierie (SI)
Faculté des Sciences et Techniques – Institut de Recherche XLIM

Thèse pour obtenir le grade de
Docteur de l'Université de Limoges
Électronique des Hautes Fréquences, Photonique et Systèmes

Présentée et soutenue par

Kostiantyn VASKO

Le 21 Decembre 2023

**OUTIL NUMÉRIQUE (1+2D)/3D POUR MODÉLISER LA DIFFUSION DE SURFACE DE LA
LUMIÈRE D'UNE FIBRE CREUSE À COUPLAGE INHIBÉ**

Thèse dirigée par Fetah BENABID et co-dirigée par Frédéric GEROME

JURY :

Président de Jury :

M. Alain REINEIX, Directeur de Recherche CNRS – XLIM-CEM & Diffraction – Université de Limoges

Rapporteurs :

M. Rodrigo Amezcua CORREA, Professeur – CREOL – University of Central Florida

M. Gilles RENVERSEZ, Professeur – Institut Fresnel – Université d'Aix-Marseille

Examineurs :

M. Luca VINCETTI, Professeur, Department of Engineering “Enzo Ferrari”, University of Modena and Reggio Emilia

M. Fetah BENABID, Directeur de Recherche CNRS, XLIM-GPPMM, Université de Limoges

M. Frédéric GEROME, Directeur de Recherche CNRS, XLIM-GPPMM, Université de Limoges



Dedicated to my family and friends scattered around all the globe.

"Still alive."

GLaDOS

“Учітєсь, читайте, І чужому научайтєсь, Й̑ свого не цурайтєсь.”

Т. Г. Шевченко

Droits d'auteurs

Cette création est mise à disposition selon le Contrat :

« Attribution-Pas d'Utilisation Commerciale-Pas de modification 3.0 France »

disponible en ligne : <http://creativecommons.org/licenses/by-nc-nd/3.0/fr/>



Table of contents

1	Introduction	16
1.1	Hollow-core photonic crystal fibers history	17
1.1.1	Photonic band gap	21
1.1.2	Inhibited coupling	23
1.2	Transmission limiting factors	27
1.3	Thesis structure	32
2	Numerical fiber analysis	35
2.1	Introduction to numerical analysis	36
2.1.1	Plane wave expansion method	37
2.1.2	Multipole method	38
2.1.3	Finite difference method	39
2.1.4	Finite element method	40
2.2	Mode solving via finite element method	41
2.2.1	Script preparation and optimisation	42
2.2.2	Results of solution	51
2.2.3	Photonic band gap	53
2.2.4	Inhibited coupling	58
2.2.5	Fourier Decomposition	60
2.3	Conclusion	63
3	Modeling of new designs of HCPCF for singlemodeness and ultra low loss	64
3.1	Introduction	65
3.2	Design rationale	65
3.3	Design #1: hybrid Kagome	67
3.3.1	Performance of ideal design	67
3.3.2	Fabrication and characterisation of the fiber	74
3.4	Design #2: snowman	77
3.4.1	Performance of ideal design	78

3.4.2	Preliminary results of fabrication	81
3.5	Design #3: hybrid PBG	82
3.5.1	Performance of ideal design	83
3.6	Conclusion	86
4	Simulation and experimental control of surface roughness in HCPCF	88
4.1	Capillary wave in hollow core photonic crystal fiber	89
4.2	Surface roughness induced scattering and microbend transmission loss in HCPCF	93
4.3	Numerical modelling confinement loss in HCPCF with surface roughness	97
4.4	Fabrication and simulation of HCPCF with shear-stress induced surface roughness reduction	107
4.4.1	Principle of the shear-stress fabrication process	107
4.4.2	Experimental demonstration	110
4.4.3	New state-of-the-art for losses in the short wavelengths of the visible and ultraviolet spectrum	114
4.5	Opto-thermal process for the fabrication of HCPCFs	119
4.5.1	Fiber drawing set-up	124
4.5.2	Fabrication and characterization of the produced fibers	124
4.6	Conclusion	132
5	Development of (2D + 1) model for confinement and scattering	134
5.1	Introduction or problem framing	135
5.2	Basic principle	136
5.3	Fiber twist and tilt induced loss	138
5.4	Scattering point	143
5.5	Surface roughness	146
5.6	Conclusion	154
6	3D beam propagation modeling and concluding prospects	156
6.1	Introduction	157
6.2	Beam Envelop Method 3D simulation	158
6.2.1	Principle and implementation	158
6.2.2	Beam propagation in HCPCF	162
6.2.3	Surface roughness perturbation	165
6.2.4	Discussion	170
6.2.5	Work Summary	171

6.2.6	Directions for future work	174
A	Appendix	176
A.1	Couple coefficients	177
A.2	Script for the λ from normalized frequency	179
A.3	Coordinates of the point which is at length of L from tangent point on tangent line to the circle	184
A.4	Mode field test functions	186
A.5	Distance function inside 3D PML	187
B	BIBLIOGRAPHY	189
	References	190
	Scientific contributions	204

Table of Figures

1.1	(a) Different cladding structures of hollow-core photonic crystal fibers of the two main families: PBG and IC fibers. Triangular (b) and Kagome (c) lattice.	18
1.2	Diagram showing potential guidance mechanisms in an optical fiber, arranged from left to right: (a) TIR, (b) PBG, and (c) IC.	20
1.3	(left) Different guiding zones of the cladding modes, apexes in yellow, struts in blue and air in red (from [1]). (right) DOPS diagram of the modes supported by the micro-structured cladding of a PBG fiber.	21
1.4	Effective indices of cladding modes calculated at high symmetry points for the structures with (a) strut thickness $t = 0.005\Lambda$ and varying apex curvature radius $r = 0.20\Lambda$ and (b) $t = 0.015\Lambda$ and $r = 0.15\Lambda$ (from [16]).	22
1.5	DOPS diagram of modes supported in the Kagome cladding type (from [1]).	24
1.6	Evolution of fibers with a hypocycloidal core contour of the Kagome lattice fiber with a quasi-circular core contour (a), Kagome with a hypocycloidal contour (b), and with a tubular lattice fiber (c). Silica nodes where light is likely to couple are shown in yellow	25
1.7	(a) CL calculated for different b parameter. Evolution of CL and m with b parameter for $\lambda = 1030$ nm (b).	26
1.8	(a) Comparison of typical spectral attenuation the silica and air Rayleigh scattering limits. (b) Minimum attenuation measured for PBG HCPCF 7 cell fibers due to SSL losses.	28
1.9	(a) In the context of solid-core fibers, bending induces the formation of additional lossy cladding modes, which can interact with the core mode. (b) Similarly, in HCPCFs, the occurrence of higher effective index lossy cladding modes exacerbates leakage.	29
1.10	Evolution of the different sources of losses for the example of an IC HCPCF with 8 tubes, a core diameter of $40 \mu\text{m}$ and silica thickness of 580 nm, $g = 2 \mu\text{m}$	31

1.11 (a) Demonstration of the downward trend in the evolution of hollow-core optical fibers losses. (b) Similar trend for solid-core fibers.	32
2.1 Simplified steps of geometry development. (a) Computational domain. (b) Air hole in (a). (c) Introduction of microstructure tubes into (b). (d) PML domain introduction into (c). (e) Meshing operation over (d).	42
2.2 Transverse cross section of a HCPCF surrounded by PML domains 1 – 8.	44
2.3 (a) Typical mesh analysis graph. (b) Time spent for each parametric step of the sweep at different platform. (c) RAM consumption tracking during solving at different platforms.	48
2.4 Geometries of conventional PBG HCPCF. 7-cell and 19-cell respectively.	54
2.5 Visualisation of single silica rod in 3D (left). Dispersion curve for LP_{01} and LP_{11} of this structure (right).	54
2.6 Visualisation of two silica rods array in 3D (left). Analytical dispersion curve for LP_{01} and LP_{11} (red and blue) and numerical simulation (with green dots) of this structure (right).	55
2.7 Visualisation of ten silica rods array in 3D (left). Analytical dispersion curve for LP_{01} and LP_{11} (red and blue) and numerical simulation (with green dots) of this structure (right).	55
2.8 Visualisation of 36 silica rods triangular lattice in 3D (left). Analytical dispersion curve of a single rod for LP_{01} and LP_{11} (red and blue) and numerical simulation (with green dots) of this structure (right).	56
2.9 Left side of this figure represent a refractive index cross-sections under letters. Right part of this figure represent the DOPS of those structures in terms of $n_{\text{eff}}(k\Lambda)$ (a) A volume with glass $n_{\text{gl}} = 1.45$, (b) a volume with doped glass $n_{\text{gl}} = 1.5$, (c) a volume with glass and defect with doped glass rod $n_{\text{gl}} = 1.45$, $n_{\text{do}} = 1.5$, (d) a volume with glass and triangular lattice made of doped glass rods $n_{\text{gl}} = 1.45$, $n_{\text{do}} = 1.5$, (e) a volume with glass and triangular lattice made of doped glass rods and with defect in the center of this lattice $n_{\text{gl}} = 1.45$, $n_{\text{do}} = 1.5$	57
2.10 Examples of geometries of IC HCPCF.	58
2.11 (a) Cross section of a 8 tubes TLF. (b) Local polar coordinated system (r, θ) centered at the center of the tube i -th. Red and orange lines highlight the outer and inner tube boundaries respectively.	60

2.12	Fundamental core mode. Left: radial $E_{co,r}$ (top) and azimuthal $E_{co,\theta}$ (bottom) electric field components along the inner (orange) and outer (red) tube boundaries. Right: modulus of the corresponding azimuthal spectra.	61
2.13	Comparison of CL spectrum of T8 TL HCPCF obtained with numerical simulation with $t = 750$ nm, $r_{ext} = 6$ μ m, $R_{co} = 13.6$ μ m, $\rho = 0.875$ and $n_{gl} = 1.45$ (black) and with Eq. 2.36 (green).	63
3.1	Demonstration of the coupling between LP_{11} -like of core to LP_{01} of tubes in T6 TLF design (left). Phase matching condition given by [83] (right).	66
3.2	Illustration of the fiber design rationale proposed for single modedness and ultra low loss based on a hybrid fiber design made of Kagome and tubular cladding lattices.	66
3.3	Cross-section profile of a hybrid Kagome HCPCF design	67
3.4	Study on the effect of adding the Kagome lattice around the tubular lattice in the HKT HCPCF design. (a) CL simulation results for fiber designs with different ξ values (see text for the definition). (b) CL values for two selected normalised frequency (F) values.	69
3.5	CL simulation results for different fiber designs. FD #1: jacketless tubular lattice; FD #2: jacketed tubular lattice; FD #3: Kagome lattice; FD #4: hybrid lattice. A comparison with solid-core fiber is added.	71
3.6	Effect on CL of having different glass thicknesses between the two cladding of HKT HCPCF.	71
3.7	Fundamental mode CL simulation results for ideal and realizable hybrid fiber designs.	72
3.8	Fundamental mode CL simulation results for the (I) tubular, (II) straight-bar tubular, (III) nested-rod tubular, (IV) conjoined tubes, (V) nested tubular, (VI) hybrid with supporting tube and (VII) ideal hybrid fiber designs.	73
3.9	HOMER vs wavelength for the different studied fiber designs.	74
3.10	(a) Cross section of the fabricated hybrid Kagome-tubular HCPCF, with an enlarged view of the supporting tube region. (b) Cutback measurement results (black curve), simulated CL and TL for the fundamental mode (red dashed and red lines, respectively), and for the two first HOMs (blue and green lines).	75
3.11	(a) S^2 measurement results for a 10 m long fiber. (b) Normalised power and near-field profiles at the fibre output at 1064 nm as a function of the input fiber offset.	76

3.12	Cross section of the snowman fiber design with the associated geometrical parameters.	78
3.13	Fundamental mode CL simulation results for snowman fiber compared to the ideal HKT HCPCF.	79
3.14	(a) Snowman fiber cross section with overlaps in red ovals and ideal design without overlap. (b) Corresponding evolution of CL for the fundamental mode for a set of overlap values ranging from 0 to 30%.	80
3.15	The fields of the fundamental mode at 579.9 nm for 0% (a) and 30% (b) overlap thickness cases are added. $E_{norm} = \sqrt{E_x \cdot E_x^* + E_y \cdot E_y^* + E_z \cdot E_z^*}$	81
3.16	HOMER vs wavelength for the snowman fiber.	81
3.17	(a) Cross section of the fabricated snowman HCPCF. (b) Cutback measurement results (black curve) and simulated CL for the fundamental mode (red dashed and red lines, respectively).	82
3.18	(a) Proposed hybrid PBG HCPCF cross section compared to (b) the classical 19-cell PBG HCPCF.	83
3.19	Key geometrical features of the hybrid PBG HCPCF.	84
3.20	(a) CL of hybrid PBG fibers with inner cladding tube thickness (t_{tubes}) of 200 nm, 500 nm and 1000 nm compared to classical 7 cell and 19 cell PBG HCPCF. (b) Fundamental core mode profiles of the five fibers at 1550 nm.	85
3.21	(a) CL for different gap size $g = 1 - 6 \mu\text{m}$. (b) Evolution of the CL at 1550 nm versus the ratio g/D_{core}	85
3.22	(a) CL for the FM (black color) and HOM (red color) for the 19-cell PBG HCPCF (dashed curves) and the hybrid IC-PBG HCPCF (solid curves). (b) spectrum of F for 7-cell (red dashed line), 19-cell (black dashed line) PBG HCPCF and hybrid IC-PBG HCPCF (black solid line).	86
4.1	(a) Schematic of the drawing of an HCPCF, (b) a sheath tube, and (c) the membrane surface associated with this tube.	90
4.2	A summary of the main published work regarding surface roughness in hollow core fibers. Measured PSD (a) and minimum loss evolution with wavelength (b) of a PBG HCPCF from [19]. Surface roughness height profile (c) and associated PSD (d) of a PBG HCPCF from [106] PSD of a PBG HCPCF compared to that of its preform (e) and auto-correlation contour (f) from [37]	95

4.3	Measured PSD and their fits using the expression of the exponential process (green curve) and the expression of a modified exponential (red curve).	98
4.4	SR. S curvilinear abscissa, θ azimuthal angle, C circumference	99
4.5	(left) A cross-section of the SR-TL HCFCF, where the vector C_p represents the shift from the reference system of a local single tube to the reference system of the fiber. (right) Visual representation of the external and internal contributions affecting the perturbation $\Delta\varepsilon$	99
4.6	Auto-correlation function and Correlation length, periodic of $2\pi r_0$	100
4.7	(a) Example of generated transverse roughness with $\sigma = 1, 5, 10$ nm and $P = 2\pi, 42$ and 60 . (b) The PSD of the given SR profiles.	103
4.8	Comparison of (a) CL, (b) optical overlap F_{00} and (c) n_{eff} of LP_{01} with different parameters of surface roughness.	104
4.9	Close-up of the CL over the 3rd and 4th transmission bands of Fig. 4.8 (a)105	
4.10	Relative difference of CL with SR according to CL without SR for different parameters of SR.	105
4.11	MBL with different parameters of surface roughness.	106
4.12	CL, SSL and MBL for SR with parameters $\sigma = 0.4$ nm and $P = 2\pi$ compare to CL of ideal design.	106
4.13	Proposed model to study the shear rate that could be achieved on the silica walls surrounding the air core of the fiber. (a) Diagram of the transition zone (or cone) between the preform and the fiber. P_1 and P_2 represent the pressure in the preform and in the fiber, while r_0 and r_f represent the radius. L is the length of the preform-fiber transition. (b) Diagram presenting the attainable values of the $\frac{\gamma_{\text{eff}}}{\gamma_0}$ ratio as a function of different pressure gradients $ \Delta P $ and the ratio of fiber radius to preform radius $\frac{r_0}{r_f}$, expression is derived using equations (4.27, 4.32). (c) Specific case for $ \Delta P $	109
4.14	(a) The diagram illustrates the pressure distribution in the fiber preform during the fabrication with shear process. The pressure applied in the fiber core is represented as P_{core} , while the pressure in the cladding tubes is depicted as P_{clad} . (b) The diagram shows the interfaces between the surfaces of the cladding tubes, the internal region of the tubes, and the fiber core.	111
4.15	Typical profiles of roughness along the axis of the fiber.	112
4.16	PSD for fibers in G#1 and G#2.	112

4.17 Measurement of the inner and outer roughness of the silica membrane surrounding the air core for 5 G#2 fibers manufactured using the shearing technique.	114
4.18 (a) Comparison of measured losses for a fiber from G#1 (here fiber VI) and G#2 (here fiber X) presenting an identical silica thickness of 600 nm. (b) Curves normalized by the air core size. (c) Study of the impact of transverse roughness on the CL (dashed line represents ideal structure i.e., without roughness and solid line with an RMS roughness of 0.15 nm).	115
4.19 Numerical calculations under Comsol to evaluate the weight of each of the loss sources namely CL, MBL, SSL, and TL (here the curvature losses are neglected) in the case of (a) standard fabrication (G#1) and (b) when the shearing technique is applied (G#2, fiber X).	117
4.20 Experimental loss curves for two record fibers with low surface roughness (a) fiber X and (b) fiber XII. An image of their cross-section is provided as an insert.	118
4.21 Plot of the performance achieved by the two fibers in comparison with the state of the art of IC HCPCFs and the fundamental Rayleigh limit of solid core silica fibers.	118
4.22 Illustration of the second process called “opto-thermal” to control the surface quality during the fiber draw.	119
4.23 Experimental configurations of the opto-thermal manufacturing device.	124
4.24 Linear characterization of fibers $F_{opto} \#1-0$ (laser OFF) and $F_{opto} \#1-1$: (a) measured loss, (b) roughness profiles, (c) Evolution of the PSD (d) in linear scale.	126
4.25 Linear characterization of the fibers $F_{opto} \#2-0$ (laser OFF) and $F_{opto} \#2-1$ (laser ON): (a) roughness profiles, (b) evolution of the PSD and (c) evolution of the PSD in linear scale.	128
4.26 Linear characterization of fibers $F_{opto} \#3-0$ (laser OFF), $F_{opto} \#3-1$ (laser 1 ON CW and laser 2 ON modulation at 2 Hz), $F_{opto} \#3-2$ (laser 1 ON CW and laser 2 ON modulation at 50 Hz), $F_{opto} \#3-3$ (laser 1 ON CW and laser 2 ON modulation at 100 Hz), and $F_{opto} \#3-4$ (laser 1 ON CW and laser 2 ON modulation at 400 Hz): (a) roughness profiles, (b) evolution of the PSD and (c) measured loss.	130

4.27 (a) Loss at minimum of different transmission band vs modulation frequency. (b) Evolution of the PSD in linear scale for the fibers $F_{\text{opto}} \#3-0$ (laser OFF), $F_{\text{opto}} \#3-1$ (laser 1 ON CW and laser 2 ON modulation at 2 Hz), $F_{\text{opto}} \#3-2$ (laser 1 ON CW and laser 2 ON modulation at 50 Hz), $F_{\text{opto}} \#3-3$ (laser 1 ON CW and laser 2 ON modulation at 100 Hz), and $F_{\text{opto}} \#3-4$ (laser 1 ON CW and laser 2 ON modulation at 400 Hz).	131
5.1 Schematics of modes coupling in the co-directional coupling configuration (a) and butt-coupling configuration (b).	136
5.2 Schematic representation of the multistage approach. (a) Decomposition of the fiber into segments. (b) Fiber tilting. (c) Fiber twisting.	139
5.3 Butt coupling coefficient C^2 of FM-FM vs angle of rotation.	140
5.4 (a) T8-TLF geometry with the key parameters (θ shown in Fig. 5.2 (c)). (b) Normalized twist induced loss evolution with the twist angle for different fiber radius.	141
5.5 Scaling laws for tilting ($\varphi = 0.01^\circ$), showing CL and core radius law effect.	142
5.6 C^2 vs F for HOMs LP_{02_x} , $LP_{11_{bx}}$, $LP_{21_{bx}}$, $LP_{12_{bx}}$ and $LP_{31_{bx}}$	142
5.7 Schematic of butt coupling between 2 designs.	143
5.8 Fraction of the lost power $1-C^2$ in linear scale (a) and in logarithmic scale (b). Orange and red lines on (a) are depicted as curves $1-C^2$ vs φ_{scat} and $1-C^2$ vs r_{scat} respectively on (c). Only fundamental mode (FM) in those simulations considered.	144
5.9 2D+1 computed transmission loss spectrum (green curves) versus the sum of CL and SSL (black curve). The red curve represents the confinement loss of a scatterer-free T8-TLF (fiber X)	145
5.10 (a) Δh profile and (b) PSD of the profile	146
5.11 (a) CL of 10 realisations of SR with $\sigma = 2$ nm and $P = 20$. (b) CL and (c) TL of 90 simulations averaged over each group of SR properties.	149
5.12 90 simulations statistics data at minimum loss wavelengths for the (a) CL and (b) TL.	150
5.13 90 simulations statistics data at minimum loss wavelengths for the fraction of lost power $1-C^2$	152
5.14 Spectra of α_{TL} and α_{2D+1} with fitted L_{ch_0} for some of the SR configurations listed in table 5.2 (a) $\sigma = 0.4$ nm, $P = 20$, (b) $\sigma = 1.0$ nm, $P = 10$, (c) $\sigma = 2.0$ nm, $P = 2\pi$	153

6.1	(a) Schematic representation of the impact on fundamental mode (FM) propagation of microdeformations in an HCPCF. (b) Appearance in 3D space of bent fiber.	158
6.2	Field approximation description.	159
6.3	Appearance of meshed in 3D HCPCF.	159
6.4	(Top) ZY -plane which show the line along which 2D cross-section of the fiber will be extruded. (Bottom) Fiber in 3D already extruded with 3 domains color-coded. Where green is input domain, yellow is bended domain and blue is straight domain after bending.	161
6.5	Plots of α for $R_{PML} = 10^{-200}$. (Left) A-A cross section is XY -plane at $Z = 0$. (Right) ZY -plane.	162
6.6	(a) Demonstration of E_{norm} in ZY -plane of ideal T8-TLF. Different components of electric field and E_{norm} at (b) $L = 0 \mu\text{m}$ and (c) $L = 100 \mu\text{m}$ at $\lambda = 581.7 \text{ nm}$	163
6.7	Mode distribution distribution and evolution with propagation. (a) coupling coefficient C^2 versus fiber length for different HCPCF modes. (b) A close-up of the fractional power in LP_{01} mode. (c) The modal power distribution at $L = 0 \mu\text{m}$ and $L = 100 \mu\text{m}$ at $\lambda = 581.7 \text{ nm}$. Note an approximation used in the equation (2.23) mentioned in the appendix A.1.	164
6.8	Losses obtained from 2D simulation and 3D Simulation (FM only).	165
6.9	Mesh of T8-TLF with a rod.	166
6.10	(a) Demonstration of E_{norm} in ZY -plane of perturbed T8-TLF. Different components of electric field and E_{norm} at (b) $L = 0 \mu\text{m}$ and (c) $L = 100 \mu\text{m}$ at $\lambda = 581.7 \text{ nm}$	167
6.11	Mode distribution distribution and evolution with propagation in perturbed T8-TLF. (a) coupling coefficient C^2 versus fiber length for different HCPCF modes. (b) A close-up of the fractional power in LP_{01} mode. (c) The modal power distribution at $L = 0 \mu\text{m}$ and $L = 100 \mu\text{m}$ at $\lambda = 581.7 \text{ nm}$. Note an approximation used in the equation (2.23) mentioned in the appendix A.1.	168
6.12	Schematic representation of 3D roughness proposed.	169
6.13	Plotted 3D roughness line with length of propagation $100 \mu\text{m}$, RMS value of roughness $\sigma = 2 \text{ nm}$, $P = 10$, number cosinusoidal components equal to 64 (for demonstration condition $\geq 100 \cdot P/(2\pi)$ is not respected) and number of elements in length equal to 800.	169

Chapter 1

Introduction

THIS introductory chapter provides a historical and current state-of-the-art overview of hollow-core photonic crystal fiber and its interest in varied applications. The chapter then delves into description of their guidance mechanisms and the different limiting factors of light transmission with impacts on their fiber design and numerical simulations along we highlight the confinement and the surface scattering losses. The chapter concludes with the description of the thesis objectives with regard to the state-of-the-art, plan and content.

Table of content

1.1	Hollow-core photonic crystal fibers history	17
1.1.1	Photonic band gap	21
1.1.2	Inhibited coupling	23
1.2	Transmission limiting factors	27
1.3	Thesis structure	32

1.1 Hollow-core photonic crystal fibers history

Hollow-core photonic crystal fibers (HCPCFs) have been a topic of significant research and development in the field of optics and photonics for more than two decades. Their unique optical properties to guide light in air at a microscale level make them suitable for a large range of applications but also leading to the emergence of a new field which could be coined “Gas photonics” [1].

The concept of photonic bandgap, introduced by John and Yablonovitch in 1987 [2]–[4], was brought to the field of optical fibers by Philip Russell with the prediction in 1991 of an out-of-plane photonic bandgap guidance. For that, he proposed the idea of photonic crystal fiber (PCF) design which consists of a periodic arrangement of air-holes surrounding a core defect through a theoretical demonstration in 1995 [5] and a first fabrication (solid-core PCF in that case) made by a specific technique named “stack and draw” process in 1996 [6].

As illustrated by Figure 1.1 (a), this resulted in a significant expansion of the PCF fiber family where we count endlessly singlemode fiber (ESM) [7], dispersion compensating fiber for telecom (DCF) [8], large mode area fiber (LMA) for laser [9], small solid-core nonlinear fiber (SC) for supercontinuum generation [10] or nano-void fiber for sensing [11] to cite a few. One notable member of this family is the HCPCFs, which stand out both in terms of their structural design and their optical guidance mechanism. Within the HCPCF category, there are two subclasses. One guided by “photonic bandgap” (PBG), and another guided by the “Inhibited Coupling” (IC) mechanism introduced by Fetah Benabid in 2002 [12], [13].

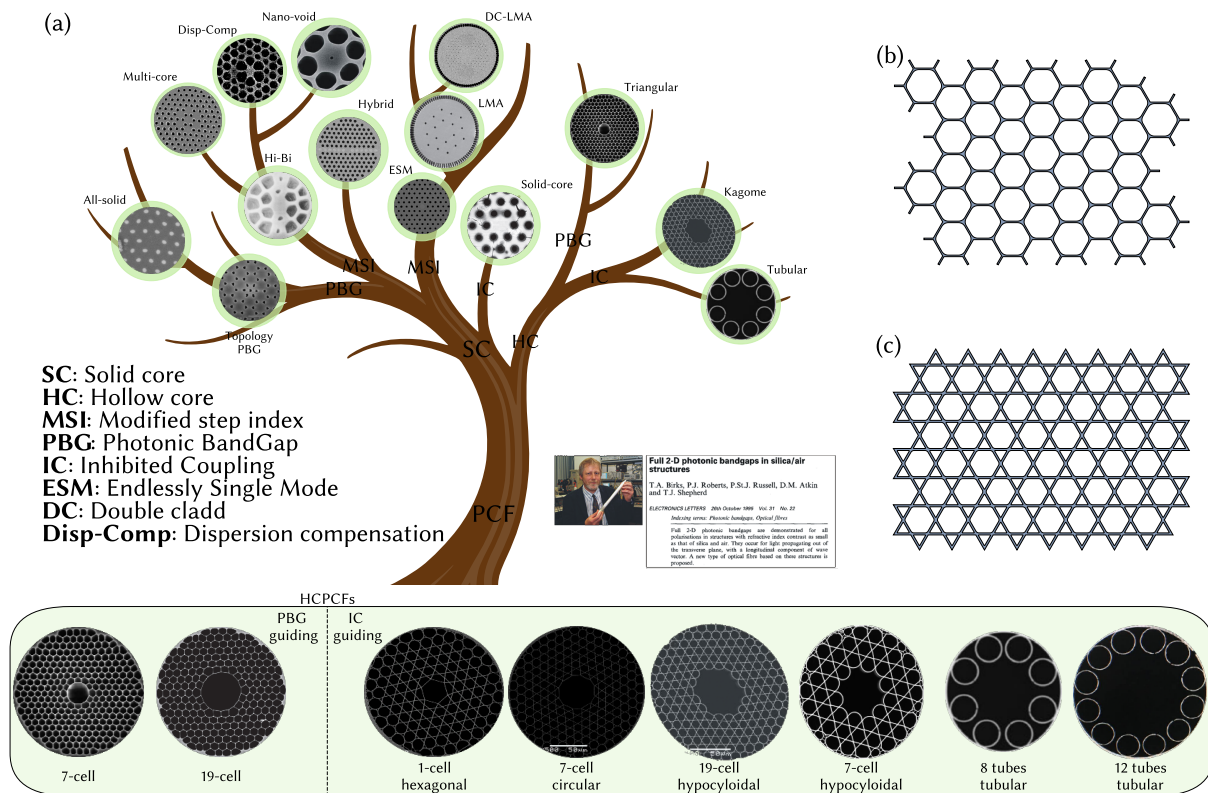


Figure 1.1: (a) Different cladding structures of hollow-core photonic crystal fibers of the two main families: PBG and IC fibers. Triangular (b) and Kagome (c) lattice.

Figure 1.1 (b),(c) shows the examples of the two original cladding studied in HCPCF with the fabricated designs in Figure 1.1 (a) completed by some of the recent structures proposed by our group based on a tubular lattice. We will therefore see in this paragraph different optical and physical properties of both members of HCPCF families, as well as their performance.

To grasp the core idea behind the way hollow-core fibers guide light in air, it's important to examine the geometric design of the cladding that surrounds the hollow-core and to analyze the modes that the cladding supports. To ensure the propagation of a mode within the fiber core with minimal propagation loss, it is necessary that the core guided mode remains uncoupled from the cladding. This requirement can be attained through either employing a cladding that doesn't support modes (i.e. a photonic bandgap guidance mechanism), or by effectively suppressing its interaction with the cladding through the suppression of coupling between the cladding modes and core guided mode of interest ($\langle \phi_{\text{clad}} | n^2 | \phi_{\text{core}} \rangle \rightarrow 0$) (i.e. Inhibited Coupling guidance mechanism).

The modal spectrum of a cladding structure is determined by several techniques (see chapter 2). This takes the form of a density of photonic states (DOPS) diagram in a frequency (or wavelength) and effective mode index, $(n_{\text{eff}} - \omega)$ space. The modes

of primary interest in guided optics are those propagating along the guide's central axis (here z). These modes are characterized by a temporal phase that conveys information about the optical wave frequency and a longitudinal spatial distribution ($e^{-i\omega t}$ and $e^{i\beta z}$ respectively). The frequency and the propagation constant β are related via the dispersion relation $\beta = n_{\text{eff}}k$ where $k = \omega c^{-1}$ and n_{eff} being the effective index. For each frequency, the resolution of the Maxwell equation is cast as an eigenfunction equation gives a set of n_{eff} each of which corresponds to a mode and the entire set forms the modal content of the cladding at that frequency. Drawing a parallel from solid-state physics, we consider a PCF as a microstructured cladding, which can be treated as a “photonic crystal”, whose symmetry is broken by a the fiber core.

In this context, figure 1.2 illustrates the modal content at a fixed frequency for three representative optical fibers. The first optical fiber is a traditional fiber that guides light through total internal reflection (TIR) and has a central core a high refractive index, n_{dg} , doped with an impurity and surrounded by a low-index cladding, n_{g} . The modal content of this fiber can be separated into two categories: cladding modes (represented by the rectangle to the left of the n_{eff} axis) and core defect modes (represented by horizontal segments to the right of the n_{eff} axis). For the TIR fiber, the cladding supports a range of modes with an effective index that satisfies the inequality $n_{\text{eff}} \leq n_{\text{g}}$. Consequently, from the perspective of solid-state physics, the region of effective indices greater than the cladding index constitutes a photonic bandgap at the fixed frequency.

The introduction of a defect with an index higher than that of the cladding means that the defect modes, whose effective indices such as $n_{\text{dg}} \leq n_{\text{eff}} \leq n_{\text{g}}$, cannot escape from the core through the cladding because there are no cladding modes to couple to. This is the principle of PBG. We observe that from this point of view the TIR mechanism is just a PBG regime achieved by introducing a defect with a refractive index higher than that of the cladding medium. The other two optical fibers are HCPCFs whose cladding is microstructured. The first noticeable difference is that the modal content of the cladding has a band structure in contrast to the TIR fiber cladding. The origin of these photonic bands can be resolved by using the equivalent of the bound states of quantum physics, which was developed by Benabid *et al.* in 2007 [1], [13], [14]. The existence of these bands implies the existence of bandgaps whose location in the effective index axis is no longer conditioned by the cladding material indices, provided the architecture is judiciously designed. As a result, PBGs with effective indices lower than that of vacuum, i.e $n_{\text{eff}} \leq 1$, can exist as illustrated in Figure 1.2 (b). More remarkable is the fact that neither the TIR index conditions nor PBG conditions in the HCPCF are necessary conditions for optical guiding. This case is illustrated in

Figure 1.2 (c) where we observe that a continuum of cladding and defect modes can coexist at the same “point” of n_{eff} axis without coupling. This is the principle of the IC mechanism which relies on the strong reduction of the scalar product between the wave functions of the cladding and core modes.

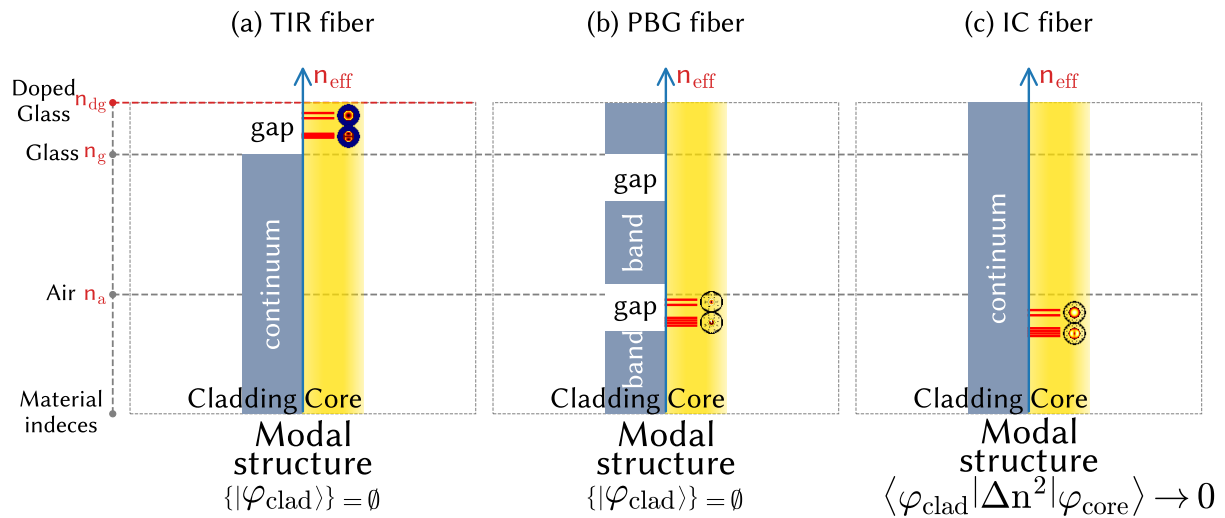


Figure 1.2: Diagram showing potential guidance mechanisms in an optical fiber, arranged from left to right: (a) TIR, (b) PBG, and (c) IC.

This is achieved through a cladding structure favoring strongly localized silica modes exhibiting a strong transverse phase mismatch. In other words, the cladding modes exhibit rapid oscillations, therefore they have very high azimuthal indices. Note that when this scalar product reaches zero, we then have a bound state in continuum (BIC) predicted by Von Neumann and Wigner in the framework of quantum physics in 1929 [15]. However, this state remained an intellectual curiosity without experimental demonstration, excluding the auto-ionization phenomenon, until these last two decades [1]. The Kagome fiber was the first photonic demonstration of this phenomenon, although the core mode is not rigorously a bound state because it always exhibit leakage, hence the term of quasi-bound state or describe guided mode in Inhibited-Coupling guiding HCPCF (IC HCPCF).

The following sections are dedicated to understanding the material and geometry parameters driving the shape of DOPS diagrams of microstructured fibers that have been previously introduced, namely the triangular cladding for PBG and the Kagome cladding, or tubular lattice for IC fibers.

1.1.1 Photonic band gap

The most common PBG HCPCF has a cladding made of triangular arrangement of air-holes (usually more than hundred) embedded in a silica glass resulting in silica web of hexagonal shape and silica rods (or apex) represented respectively by blue and yellow colors in the Figure 1.3 (left).

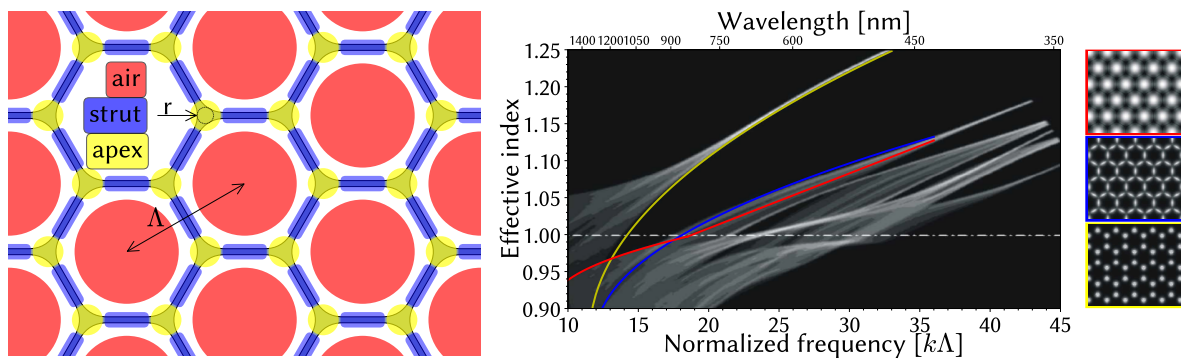


Figure 1.3: (left) Different guiding zones of the cladding modes, apexes in yellow, struts in blue and air in red (from [1]). (right) DOPS diagram of the modes supported by the micro-structured cladding of a PBG fiber.

This configuration can also be viewed as a periodic lattice made by silica rods' radius r of material index n_c with spacing Λ , which constitutes a uniform photonic crystal. Indeed, each of these guiding features can be viewed as photonic analogues of the individual constitutive atoms to form the crystal molecule. In the coming chapter 2 we will review photonic tight bonding model (P-TBM) theory to explain in more details the guiding mechanism in those PBG HCPCFs. An example of resulting DOPS diagram is plotted in Figure 1.3 (right) representing the effective mode indices of the cladding structure as a function of the normalized frequency $k\Lambda$, where k is the amplitude of the wave vector and Λ the pitch as just mentioned. We can see that three key guiding features in the HCPCF cladding appear which define the bandgap properties i.e. “strut”, “apex” and “air” modes (see the inset of Figure 1.3 (right)). As the pitch decreases, the modes separate, creating light guiding zones and forbidden zones as shown in the diagram. Using the Bloch equations to calculate the modes supported by the triangular mesh structure this behavior was modeled and verified in [14]. The PBG is then defined where no mode is supported. By creating an air defect in the center of the structure (by omitting 1 layer of capillary to define a 7 cell core, 2 layers for a 19 cell core, etc.) it became possible to confine light within the defect which corresponds to the fiber core. This core, in our case made of air with an index close to 1, allowing air guidance of light over a range of wavelengths represented by $k\Lambda = \sim 14.5 - 18$ in the graph (which corresponds to a

typical transmission band of 70 THz). This range can be adjusted by changing the size of the silica rods, the thickness of the bridges, and the distance between the rods [14]. Also a simple rule is commonly used to define the operation wavelength of the PBG which is typically found around $\Lambda = 2.5\lambda$ where λ the free-space wavelength to be guided. Finally, by optimizing the air-filling fraction (defined as the ratio between the air and the silica) to overpass 90 – 92% level, the confinement of the light can be strongly enhanced and high-order bandgap can be opened [16]. This higher-order bandgap arises due to the extremely thin struts of the silica cladding (noted t) and their fine-tuning relative to the apex size. In the example shown in Figure 1.4, a second bandgap appears by tripling t and decreasing r by 25% compared to the standard HCPCF.

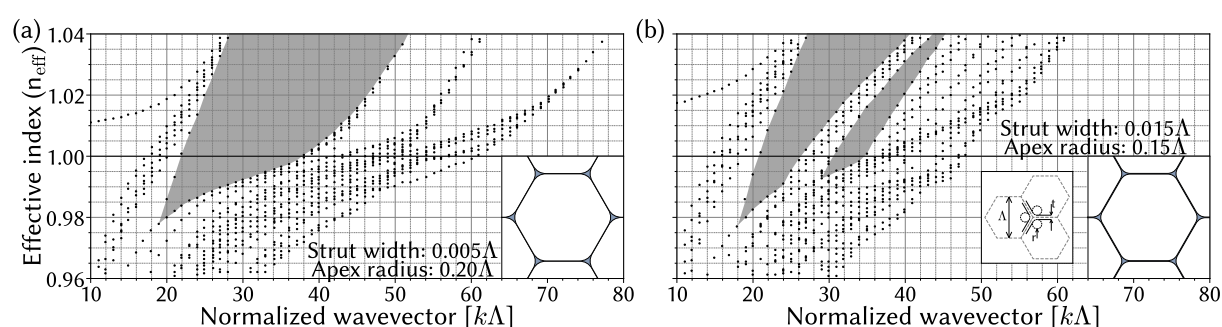


Figure 1.4: Effective indices of cladding modes calculated at high symmetry points for the structures with (a) strut thickness $t = 0.005\Lambda$ and varying apex curvature radius $r = 0.20\Lambda$ and (b) $t = 0.015\Lambda$ and $r = 0.15\Lambda$ (from [16]).

As previously mentioned, the first theoretical demonstration of this type of hollow-core fiber was reported in 1995 by Birks *et al.* [5] followed by a first experimental realization in 1999 by Cregan *et al.* [17] but with very high losses of several dB/m, values well above the expected promises. Then, by improving manufacturing techniques and refining the understanding of the rules governing the confinement of light in these structures, these losses were progressively improved (mainly at telecom wavelengths) over a few years with the work of several groups among which we can cite the Corning company in 2002 with the demonstration of 13 dB/km at 1.5 μm for a 7 cell PBG HCPCF [18] then in 2005 by the University of Bath and Blazephotonics with the record value of 1.2 dB/km at 1.62 μm for a 19 cell enlarged core fiber [19]. After this impressive demonstration, these fibers subsequently experienced very little improvement in terms of performance.

It should also be noted that this type of fiber showed limits inherent to its geometric structure. The first concerns the width of the PBG which is found relatively narrow as previously mentioned with values around 70 THz which can be problematic for several applications. In addition, it has been demonstrated the existence of modes localized at

the interface between the hollow-core and the cladding, called surface modes, which through coupling with the mode confined in the air core interfere with the performance of these fibers due to a non negligible overlap with silica bridges around 0.1 – 1%. This was found as the main limiting factor of this technology, especially for works involving high power and high energy. Another consequence of this interaction with the silica material of the core surround is the chromatic dispersion which increases to values reaching hundred ps/nm/km [20]. Finally, another major disadvantage concerns the accessible wavelengths which are mainly restricted to infrared and the top of the visible spectrum. This is explained by the fact that to shift the PBG to short wavelengths, it is necessary to reduce the pitch between the resonators of the microstructured cladding as we discussed before. Therefore, to reach the ultraviolet range, the value must be reduced to micron, which from a technological point of view is almost impossible to achieve. This problem is even more reinforced as the propagation losses are inversely proportional to $\frac{1}{\lambda^3}$ due to surface roughness which appears during the fabrication process at the silica core membrane [19]. Therefore the attenuations are found to be very high at these visible wavelengths, or even incompatible with even more exotic areas such as ultraviolet. We will return to this point later in the manuscript because it will be at the heart of the objectives of my thesis work.

1.1.2 Inhibited coupling

The second hollow-core fiber family has been introduced in 2002 [12]. Initially this class of HCPCF took the form of a Kagome lattice which consists of interweaved Star-of-David patterns and relies on a guiding mechanism conceptualized 5 years later in 2007 by the Benabid' group, adapted from quantum mechanics [13]. This fiber no longer required on cladding structuring to open a PBG but on managing the coupling between core and cladding modes. In fact, observation of the DOPS on Figure 1.5 (a) for the modes supported by the cladding allows us to see this time that the structure supports a continuum of modes at all wavelengths. We therefore find different types of modes, as for PBG, including air modes (with red dispersion profiles, closed to those of hollow-core modes when a defect is created) and which share with other modes supported by the structure the same $(n_{\text{eff}} - k\Lambda)$ couple. This is where the concept of IC guidance originated. Notice that in the literature this kind of fiber can be called anti-resonant originates from the anti-resonant reflecting optical waveguide (ARROW) introduced in [21]. This explains that IC fibers have several transmission bands which are limited by the so-called cutoff wavelengths λ_c (for which there is phase matching

between the core and cladding modes), defined as:

$$\lambda_c = \frac{2t}{j} \sqrt{n_g^2 - 1} \quad (1.1)$$

Here t is thickness of glass bridges, $j \in \mathbb{N}$ is natural numbers (1,2,3, ...) and n_g - refractive index of dielectric (for our case, silica glass). By simply playing with the thickness of the silica membrane it is then possible to adjust the bandwidths and arrange them according to the spectral ranges of interest. However, this type of anti-resonant mechanism does not explain the loss level which can be now reached mainly because the impact of the modal coupling is not considered. Indeed, for IC fiber we aim of structuring the cladding and core so that the field of the core mode ϕ_{core} and cladding modes ϕ_{cladding} have the lowest possible overlap, i.e. $\langle \phi_{\text{cladding}} | \Delta n^2 | \phi_{\text{core}} \rangle \rightarrow 0$, where Δn is the transverse index profile of the photonic structure. In other words, it is necessary to introduce a symmetry incompatibility which corresponds to two main issues :

- I) a strong phase mismatch between the transverse components of the wave vector of the core and cladding modes,
- II) and/or minimal spatial overlap between their fields.

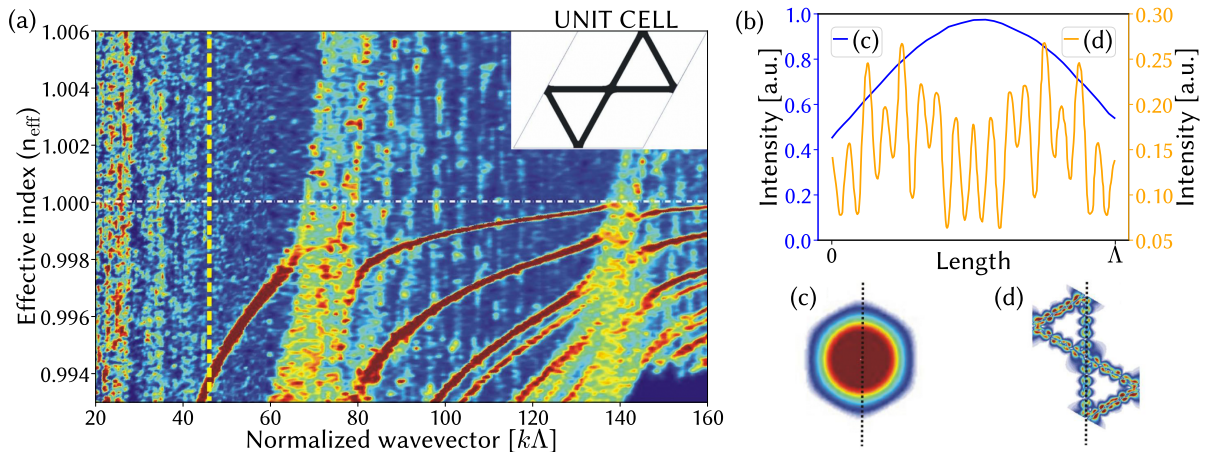


Figure 1.5: DOPS diagram of modes supported in the Kagome cladding type (from [1]).

For I) the fundamental core mode (HE_{11} or LP_{01}) having a very slow transverse phase as illustrated in Fig. 1.5 (b), it is then appropriate for the transverse phase of the cladding modes to be very fast (represented by the azimuthal number m) in order to reduce the coupled power which follows an exponential trend with this same number m . By approximating the cladding modes to those of a thin membrane of silica thickness t and length L , the number of oscillations of the transverse field of these modes can be

defined in a simplified manner by approximating the core contour to a thin membrane of thickness t and transverse length L :

$$m = n_{\text{eff}} \left(\frac{L}{\lambda} \right) \left[1 - \pi \frac{t}{L} \right] \quad (1.2)$$

From this equation, it appears that it is essential to reduce the thickness of the silica structures and increase their lengths.

For II) it mainly concerns the impact of the silica nodes inside the cladding which by their size have a low azimuthal number and therefore favor modal coupling. The trick here is to eliminate or at least move away these connecting nodes from the air-core mode as illustrated in Fig. 1.6. For this, the hollow-core of classically circular or hexagonal shape with dB/m loss level (Fig. 1.6 (a)) was modified by curving the arches of the structure delimiting the interface between the core and the cladding (Fig. 1.6 (b)). This concept introduced by our group in 2010 [22] was first named “hypocycloidal shape” to be latter coined “negative curvature” core-contour. By making such fiber core shaping, the optical overlap between core and cladding modes was strongly reduced to 0.001%, which is about 3 orders lower than PBG fiber. As a result the IC guidance is further enhanced resulting in a dramatic reduction in transmission loss which has really launched the race to the ultra low loss performances.

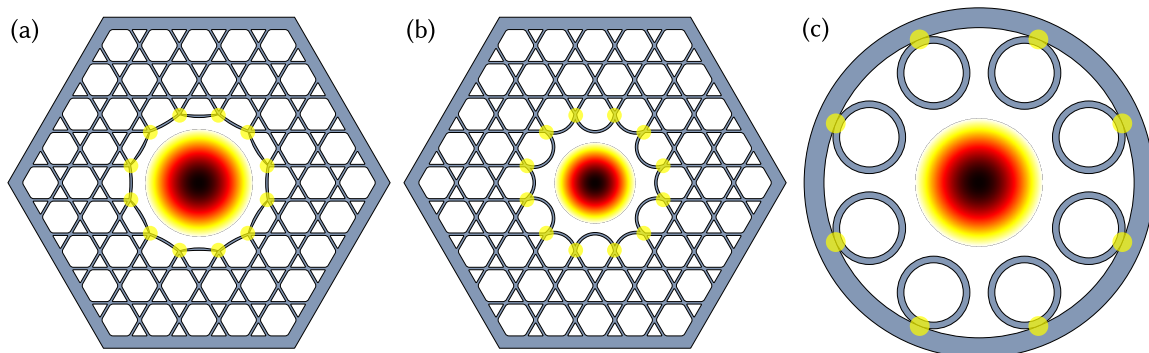


Figure 1.6: Evolution of fibers with a hypocycloidal core contour of the Kagome lattice fiber with a quasi-circular core contour (a), Kagome with a hypocycloidal contour (b), and with a tubular lattice fiber (c). Silica nodes where light is likely to couple are shown in yellow

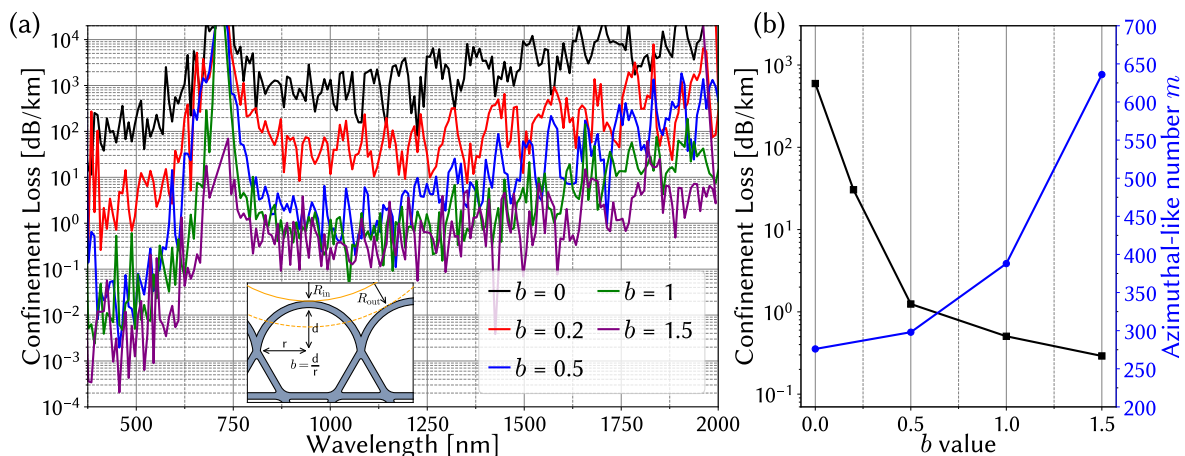


Figure 1.7: (a) CL calculated for different b parameter. Evolution of CL and m with b parameter for $\lambda = 1030$ nm (b).

Thus, the attenuation values gradually decreased from 180 dB/km at 1550 nm in 2011 [23] to a few tens of dB/km in 2013 [24] to finish below the emblematic level of 10 dB/km with the value of 8.5 dB/km at 1030 nm in 2018 [25]. In addition to this work on IC HCPCF with a Kagome lattice, a second cladding configuration was heavily studied by the community which constituted a second key step in improving the performance of these fibers. This IC fiber structure is based on a tubular cladding (Fig. 1.6 (c)) which was initiated by the work of Pryamikov *et al.* in 2011 [26]. The intrinsic advantage of this configuration is that it consists of silica tubes suspended in air necessarily implying an optimal core curvature parameter. In addition, the tubes do not touch each other, thus preventing the creation of silica nodes synonymous with strong couplings (because linked to a low azimuthal number as previously mentioned) and therefore additional losses. New records in terms of transmission could then be demonstrated as in 2017 by our group with 7.7 dB/km at 770 nm [27]. This also initiated the proposition of new designs with a more complex structure by the association of two juxtaposed tubes (configuration called “conjoined tube” [28]) or by the addition of a second tube within each tube (configuration called “nested tube” [29]) which made it possible to improve confinement to values respectively of 2 dB/km in 2018 and 0.28 dB/km in 2020 at telecom wavelengths. Finally, most recently in 2022, the fabrication of a so-called double nested fiber made it possible to reach the record value of 0.174 dB/km at 1550 nm [30], that is to say loss level comparable to the best result of standard silica SMF fibers [31], [32]. In this context, one objective of my PhD work was part of this strategy to improve performances by the fiber design. As we will see in chapter 3, I was involved in the conception of special HCPCFs called “hybrid” design mixing both cladding (Kagome and tubular) and guidance mechanism (IC and PBG) with which

I was able to demonstrate record performances.

1.2 Transmission limiting factors

The transmission of light through HCPCFs is influenced by various factors, such as absorption, scattering, dispersion, nonlinear effects, coupling, and bending losses (macro and micro). Understanding and mitigating these factors is essential for designing and implementing high-performance HCPCF systems. In this section, we review these different loss contributions with a focus on the most impacting ones with respect to my PhD works.

Absorption / Scattering

Conventional optical fiber has seen one of the greatest advances technology of the 20th century illustrated by the Nobel Prize awarded to Kao [33]. In those solid-core fibers the transmission losses is made by two fundamental contributions which are the silica material absorption and scattering losses. Absorption can be reduced by working on the impurities and defects in the fiber materials. For the second limit, it occurs as a result of variations in the refractive index of the material caused by microscopic inhomogeneities, such as fluctuations in material density or composition [34]. One of the most common causes of scattering loss is Rayleigh scattering, which is due to refractive index variations that are smaller than the wavelength of light. This type of loss can be described mathematically using an equation 1.3:

$$\alpha_{R_s}(\lambda) = 10 \log(e) \frac{8\pi^3}{3\lambda^4} n^8 p^2 k_B T_f \beta_T, \quad (1.3)$$

where n is the refractive index, p is the photoelastic coefficient, k_B is the Boltzmann constant, β_T is the isothermal compressibility of the material, and T_f is not the actual temperature of the material but the fictive temperature at which the density fluctuations are frozen. The determination methods of T_f are described by Yue *et al.* [35]. Scattering intensity is then found inversely proportional to the fourth power of the wavelength, hence the bulk Rayleigh scattering loss can be roughly estimated by:

$$\alpha_{R_s}(\lambda) = \alpha_{R_s}(\lambda_0) \left(\frac{\lambda_0}{\lambda} \right)^4 \quad (1.4)$$

Progresses of those absorption and scattering effects have been both continuous

and significant for 30 years; starting in the 70s with transmission losses of 16 dB/km up to losses of 0.15 dB/km at 1550 nm in 1987. However, this figure of losses are now marginally improved (0.142 dB/km were reported in 2018 by Tamura *et al.* [36]) because this virtual stagnation in guidance performance is due to the fundamental limit of Rayleigh scattering of silica. So, if we want to overcome this limitation it is necessary to guide light in a medium with a much lower Rayleigh scattering. In this context, the air is a preferred choice in the sense that this effect can be strongly reduced by more than 10 orders of magnitude as illustrated by the Figure 1.8 (a),

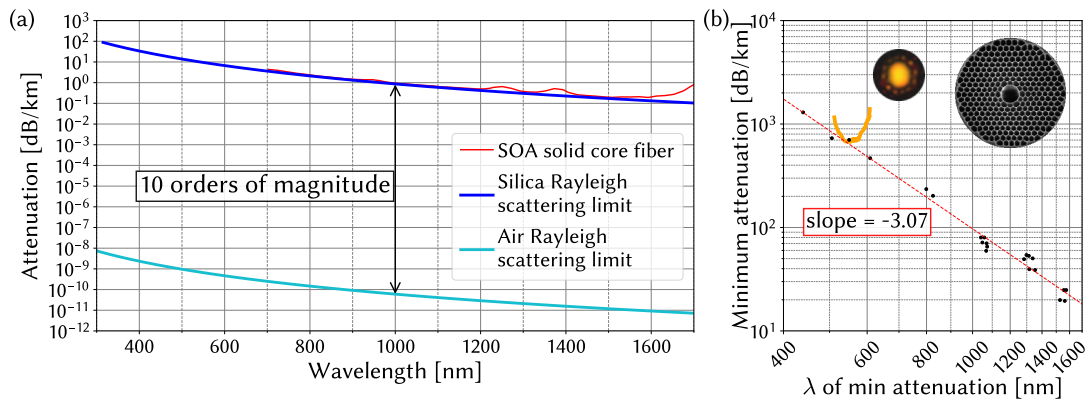


Figure 1.8: (a) Comparison of typical spectral attenuation the silica and air Rayleigh scattering limits. (b) Minimum attenuation measured for PBG HCPCF 7 cell fibers due to SSL losses.

implying that scattering losses in optical fiber should be decreased and unprecedented record transmission achieved. However during the fabrication process of those fibers, a surface scattering loss (SSL) appeared, generating by frozen-in thermal surface capillary waves (SCW) caused by the interplay between the thermal noise and the glass interface tension [37]. This effect was first observed by Roberts *et al.* in 2005 in a PBG HCPCF [19], demonstrating that this phenomenon was at the origin of the performance limitations (see Fig. 1.8 (b)). This roughness takes a stochastic form with an average peak-to-peak amplitude of $\pm 0.6 - 0.8$ nm value and can be described by a trend inversely proportional to the cube of the wavelength as [38]:

$$\alpha_{\text{SSL}} = \eta \cdot F_{\text{oo}}(\lambda) \cdot \left(\frac{\lambda_0}{\lambda} \right)^3 \quad (1.5)$$

where F_{oo} is the core mode optical overlap with the core contour, λ is the wavelength, and λ_0 is a calibrating constant. More details will be given in chapter 4. Consequently, improving the performances of HCPCF required a deep understanding and strategies on how to mitigate SSL-dominated scenarios. Today no work has been reported so

far resulting in a call for which my PhD works aim to address.

Bend loss

Bend loss (BL), also known as macrobending loss, occurs when an optical fiber is bent and is caused by the evanescent field of the guided mode extending beyond the cladding and interacting with the surrounding material. This can lead to loss of light through absorption or scattering [39].

For hollow-core fibers, PBG HCPCF are almost insensitive [18] while IC HCPCF fibers show a strong dependence [1]. To date, no analytical equation describing the BLs for IC HCPCF fibers has yet been reported in the literature although a dependence on $1/\lambda^2$ and R_{co}^3 (radius of the hollow-core) is expected by Marcatelli *et al.* from capillary waveguides [40]. A study by a Comsol type solver is therefore necessary. For this, we used through the application of conformal transformation, an analogous refractive index distribution. As a result, the bent waveguide is comparable to a straight waveguide with a sloping refractive index profile, where the index escalates from the bend's inner to outer regions. In this approach, the curved path is conformally transformed into a straight one, as shown in Figure 1.9.

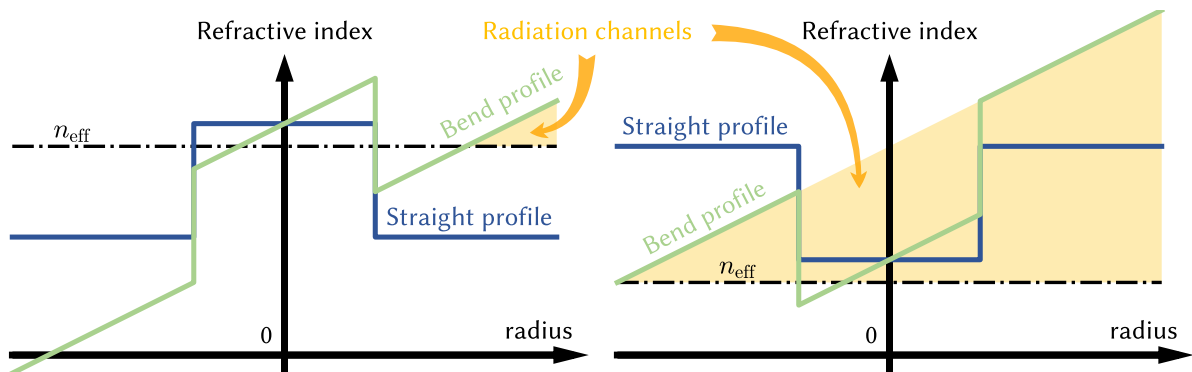


Figure 1.9: (a) In the context of solid-core fibers, bending induces the formation of additional lossy cladding modes, which can interact with the core mode. (b) Similarly, in HCPCFs, the occurrence of higher effective index lossy cladding modes exacerbates leakage.

For the simulations we can use this conformal transformation equation (1.6) for bend for implementation ($x \ll R_{\text{bend}}$):

$$n' = n_m \cdot e^{\left(\frac{x}{R_{\text{bend}}}\right)} \approx n_m \left(1 + \frac{x}{R_{\text{bend}}}\right), \quad (1.6)$$

where n_m is original refractive index of the medium, x is the coordinates of x axis across which fiber will be bended, R_{bend} is bend radius which should have the same units

as x [41]. So, the influence of the waveguide's curvature is transferred to its material properties, particularly the altered distribution of the refractive index.

Micro bend

Another source of loss has recently appeared in the literature for HCPCF named as microbending loss (MBL). In standard solid-core fibers this phenomena occurs when the fiber is subject to small, random bends along its axis. The surface roughness due to the SCW in HCPCF is typically one source for MBL. The consequence results in power coupling between modes of adjacent azimuthal mode number and also provides an avenue for additional fiber loss [42]. The MBL is usually described by the equation:

$$\text{MBL} = \beta_0^2 \cdot C(\Delta\beta_{01}) \cdot (\langle 0|\chi^2|0\rangle - |\langle 1|\chi^2|0\rangle|^2), \quad (1.7)$$

where the quantity $\langle 0|\chi^2|0\rangle$ denotes the power residing by the core fundamental mode (FM), while $|\langle 0|\chi^2|0\rangle|^2$ is the power transferred from the FM to the LP₁₁-like modes, β_0 refers to the propagation constant of the core FM, $C(\Delta\beta_{01})$ represents the power spectrum density (PSD) of the microbending stochastic process computed at $\Delta\beta_{01}$, which is the difference between the propagation constants of the core fundamental and LP₁₁-like modes [42], [43]. A recent work published in 2023 by our collaborator F. Melli *et al.* [44] made it possible to translate this effect for a tubular lattice IC HCPCF by an analytical formula scaling as:

$$\text{MBL}_{\min} = K \frac{2^{3+2p} \pi^{2+p}}{(u_{1,1}^2 - u_{0,1}^2)^p} n_{\text{eff}}^{\text{FM}^2} n_g^p C_0 \frac{R_{\text{coeff}}^{2(p+1)}}{\lambda^{2+p}}, \quad (1.8)$$

It is worth to mention that this quantity is highly depended on the fiber structure and for HCPCF this model is still under construction.

Confinement and Leakage

The last but not the least loss contribution is the phenomenon of leakage, commonly referred to as confinement loss (CL) if one ignores the loss by tunnelling due to the finite transverse dimensions of the fiber and defined in next form by Poladian *et al.* [45]:

$$\text{CL} = -20 \cdot \log_{10}(\exp(1)) \cdot k_0 \cdot \text{Im}(n_{\text{eff}}) \text{ [dB/m]}, \quad k_0 = \frac{2\pi}{\lambda} \quad (1.9)$$

This light leakage arises from the choice of opto-geometrical parameters of the fiber

design. For PBG HCPCF it is difficult to find direct links between these values and the induced attenuations implying that a numerical approach is preferred whereas for IC HCPCF several recent works have been reported in this direction. In particular, for our previous example of 8 tubes IC HCPCF, a simple formula can describe the minimum CL showing dependence again with λ and R_{co} but also on other parameters as the silica thickness t surrounding the core :

$$CL_{\min}(\lambda) = 5 \cdot 10^{-4} \frac{\lambda^{4.5}}{R_{co}^4} \left(1 - \frac{t}{r}\right)^{-12} \frac{\sqrt{n^2 - 1}}{t\sqrt{r}} e^{\frac{2\lambda}{r(n^2-1)}} \quad (1.10)$$

It is also important to note that designing such fiber is not trivial and more parameters need to be taken into account as the gap between the tubes of the cladding (or inter-tube distance) and also the number of tubes as we will see later in the first section of chapter 3.

Total loss

To conclude, the transmission of light through an HCPCF is limited by a combination of factors, which can depend on the design and guidance mechanism. Although the evolution of these losses is complex and involves multiple factors, it is interesting to plot together all these contributions to show their impact on the total loss defined as $TL = CL + BL + MBL + SSL$ for a representative IC HCPCF. Figure 1.10 shows the loss spectrum of the different mechanisms for a single ring tubular lattice IC HCPCF.

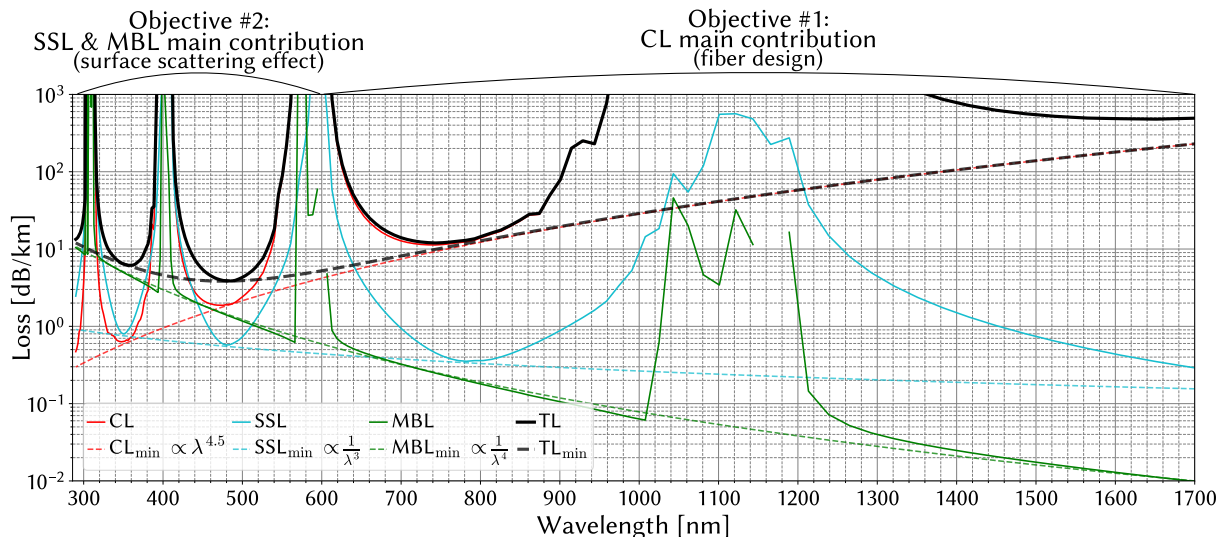


Figure 1.10: Evolution of the different sources of losses for the example of an IC HCPCF with 8 tubes, a core diameter of 40 μm and silica thickness of 580 nm, $g = 2 \mu\text{m}$.

We note that in order to improve reading, the BL are here neglected. The plot clearly indicates two transmission windows. For fibers working in the infrared, the performances are limited by CL whereas for the short wavelengths, the losses are mainly due to the SSL and MBL arising from the fiber core surface roughness. It should be noted that this crossing point between CL_{\min} and $SSL_{\min}+MBL_{\min}$ minima can be optimized and can therefore either be pushed towards shorter wavelengths such as ultraviolet (UV) by working on the dynamics of materials in order to reduce surface roughness, or shifted to longer wavelengths towards the optical telecommunications spectrum by designing new structures with stronger light confinement. Within this context, my thesis work will focus both on the design of new fibers to improve CL at the IR (Objective #1) and to investigate surface roughness in HCPCF (Objective #2).

1.3 Thesis structure

Figure 1.11 (a), shows the transmission loss evolution over the past two decades. The loss reductions in IC HCPCF seems to follow the same improvement rate of 4 dB/km as that of the solid-core telecom optical fiber in the seventies (see Figure 1.11 (b)). This illustrates the potentials of this type of fibers and its timeliness.

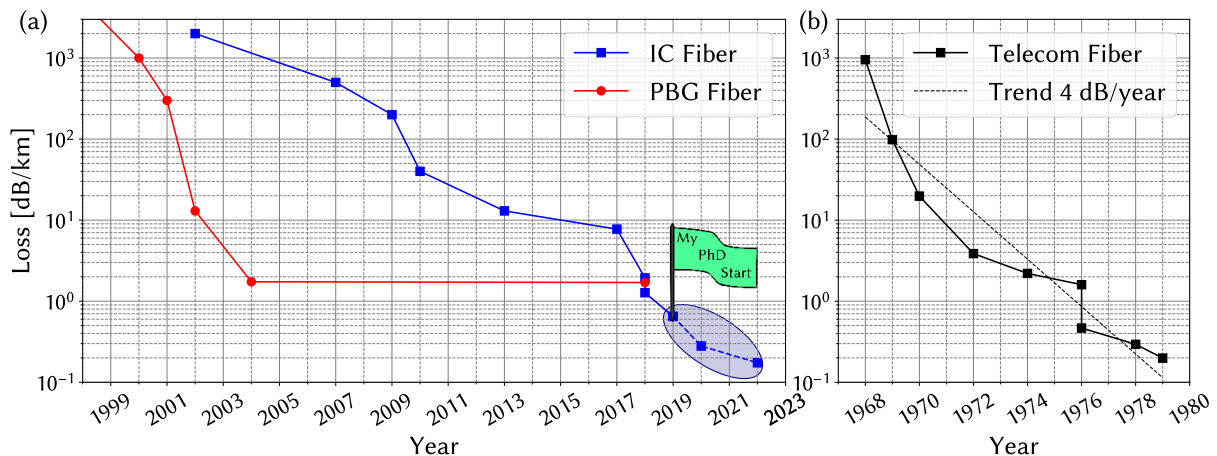


Figure 1.11: (a) Demonstration of the downward trend in the evolution of hollow-core optical fibers losses. (b) Similar trend for solid-core fibers.

In this context, the aim of this thesis is to make a meaningful contribution to the above ongoing efforts by developing advanced numerical tools tailored for optimizing HCPCF designs and mitigating various sources of loss efficiently. Specifically, the objective is to create a versatile numerical program capable of addressing specialized

designs for specific applications, spanning telecommunications [46], sensing [47], beam delivery [48] and other areas where optical fibers are widely used. Therefore, my doctoral research will primarily contribute to enhancing our fundamental comprehension of confinement loss and modal characteristics in HCPCFs, enabling the proposal of novel fiber designs. Secondly, it will assist in identifying effective strategies to minimize surface scattering loss, with the ultimate goal of achieving superior performance in the UV spectral domain. These objectives align with the broader project of the Benabid research group's GPPMM, which encompasses the establishment of an integrated framework. This framework includes the development of novel manufacturing processes, the implementation of efficient characterization setups, and the creation of a numerical platform for simulating optical propagation dynamics within HCPCFs.

The manuscript is structured in the following way:

In chapter 2 we begin by providing an overview of commonly employed numerical simulation methods in microstructured optical fibers. We then describe the Finite Element Method (FEM), a key focus of my doctoral work, which is implemented using commercial software. This chapter serves to elucidate the working principles and utilization of such simulation tools, with a more detailed exploration of Photonic Bandgap (PBG) and Inhibited Coupling (IC) guiding principles. Moreover, we introduce specific tools and strategies developed as part of this research endeavor, including Physics Interface Equations like Perfectly Matched Layers (PML), mode recognition techniques, adaptive meshing, and a novel approach for loss prediction based on azimuthal Fourier decomposition.

In chapter 3 we introduced novel HCPCF designs aimed at achieving singlemode-ness and ultra-low loss. These innovative fibers, namely the hybrid Kagome HCPCF, Snowman HCPCF, and hybrid PBG fiber, were developed by blending different cladding and guidance mechanisms. Our results showcased a substantial improvement in light confinement, up to four orders of magnitude, while maintaining singlemode guidance, surpassing the performance of conventional HCPCFs. The fabrication process has also commenced, validating the potential and feasibility of these groundbreaking fiber designs.

In chapter 4, we investigate the surface roughness in optical fiber. A review of this phenomena originated from the surface capillary waves for the specific case of our HCPCFs is made. A mathematical model of transverse roughness with controlled parameters are proposed and developed. The relationship between roughness and confinement loss is then explored. In a second time, two new experimental techniques were investigated to reduce and/or control the surface roughness in IC HCPCF, work focus on 8 tubular cladding design. The first process consists on making a counter-

directional gas and glass flows to attain a shear rate on the fiber microstructure during the fabrication process. Reduction of the roughness by a factor three has been successfully demonstrated. Fibers with record loss values in the visible and ultraviolet spectral range were reported (50 dB/km at 290 nm, 9.7 dB/km at 369 nm, 5.0 dB/km at 480 nm, 0.9 dB/km at 558 nm). These results have then been theoretically confirmed by scaling formula and published in *Nature Communications* [43]. In addition, a second technique called “opto-thermal” has begun with the idea to control the dynamics of the surface capillary waves during the fiber fabrication. A laser beam system to be applied directly within a new furnace design has been built and tested. Convincing results were observed with the presence of a non-stochastic roughness profile with a period tunable with the laser modulation frequency.

In chapter 5, we propose a novel 2D+1 approach in numerical fiber analysis based on coupled modes theory. This tool was then applied to the case of a fiber under different configurations: tilting, twisting and with scattering points along the core surround to study the effects of arbitrary surface roughness, particularly in the context of SSL. This study allowed to draw useful scaling laws and demonstrate results which successfully replicate the spectral structure of SSL.

In chapter 6, we present the transition from 2D to 3D beam propagation simulations, addressing the challenges faced, detailing the implementation of a 3D model, and showcasing preliminary findings from the new simulations. And finally we conclude by underlining all work done during my PhD and by giving some prospects.

Chapter 2

Numerical fiber analysis

THIS chapter addresses the problem of electromagnetic propagation within hetero/periodic dielectric structures and focuses on the numerical techniques employed to simulate the linear properties of HCPCFs. The chapter starts with an overview of how Maxwell's equations were formulated as an eigenvalue problem, leading to the emergence of the field of photonic crystal and photonic bandgap physics. Conversely, it covers the development of various numerical methods for studying photonic crystals. The chapter proceeds to explore the finite element method (FEM) as a valuable tool for solving modes in optical waveguides, with a specific focus on HCPCFs. It further elaborates on the interfaces created to distinguish between different modes, calculate loss using specialized perfectly matched layers (PML), and enhance computational efficiency through geometric, symmetry, and mesh optimizations. Lastly, a novel methodology based on azimuthal Fourier decomposition for analyzing loss in tubular lattice IC HCPCF is introduced.

Table of content

2.1	Introduction to numerical analysis	36
2.1.1	Plane wave expansion method	37
2.1.2	Multipole method	38
2.1.3	Finite difference method	39
2.1.4	Finite element method	40
2.2	Mode solving via finite element method	41
2.2.1	Script preparation and optimisation	42
2.2.2	Results of solution	51
2.2.3	Photonic band gap	53
2.2.4	Inhibited coupling	58
2.2.5	Fourier Decomposition	60
2.3	Conclusion	63

2.1 Introduction to numerical analysis

In numerical simulations, the primary objective is to establish a mathematical framework for gaining insights into specific areas of interest without the need for labor-intensive experimental work. This approach serves as a cost-effective and efficient alternative for identifying optimized guidance structures. But for this we want to know what we are looking at, physically. In our context, the general challenge revolves around the computational simulation of the propagation dynamics of electromagnetic waves within dielectric heterostructures and microstructures. Specific to this work, we are interested in microstructured optical fibers (MOFs).

In the domain of numerical analysis pertaining to optical waveguides, and indeed, other related phenomena, a consistent and enduring factor prevails. The initial stages of numerical simulations in electromagnetism invariably commence with the foundational Maxwell's equations. This assertion elucidates the core theory of electromagnetism, encompassing the behavior of light propagation in PCFs. The differential formulation of these equations is presented in [49], while the primary governing equation is given by [50]:

$$\begin{aligned} \nabla_{\perp}^2 \times \vec{E} + (k_0^2 n^2 - \beta^2) \cdot \vec{E} &= -\overline{(\nabla_{\perp} + i\beta\hat{z})} \cdot \left((\vec{E}_{\perp} \cdot \nabla_{\perp}) \ln n^2 \right) \\ &\parallel \\ \begin{cases} \hat{x} \left(\nabla_{\perp}^2 \times \vec{E} \right) + (k_0^2 n^2 - \beta^2) \cdot E_x = -\frac{\partial}{\partial x} \left(E_x \frac{\partial \ln n^2}{\partial x} + E_y \frac{\partial \ln n^2}{\partial y} \right) \\ \hat{y} \left(\nabla_{\perp}^2 \times \vec{E} \right) + (k_0^2 n^2 - \beta^2) \cdot E_y = -\frac{\partial}{\partial y} \left(E_x \frac{\partial \ln n^2}{\partial x} + E_y \frac{\partial \ln n^2}{\partial y} \right) \\ \hat{z} \left(\nabla_{\perp}^2 \times \vec{E} \right) + (k_0^2 n^2 - \beta^2) \cdot E_z = -i\beta \left(E_x \frac{\partial \ln n^2}{\partial x} + E_y \frac{\partial \ln n^2}{\partial y} \right) \end{cases} \end{aligned} \quad (2.1)$$

Where \vec{E} is electric field, n is displacement of refractive index, β is complex propagation constant. In our case we are assuming the two dimensional (2D) system which is uniform along propagation axis \hat{z} . Historically, it turned out that casting Maxwell's equations to the form of eigenvalue problem like eq. (2.2) was turning point for computations of optical fibers.

$$[M]\{E\} = \beta^2\{E\} \quad (2.2)$$

We will now review the different numerical method used in the literature. Since we are interested in the fibers simulations in our case we are assuming the two dimensional (2D) system which is uniform along propagation axis \hat{z} . And also area of our interest it is

to estimate loss of PCFs and for this we are utilising finite element method. But before this it is worth to mention first other numerical methods of photonics crystals analysis.

2.1.1 Plane wave expansion method

Microstructured waveguides, pivotal in photonics, demand a detailed understanding of vector Maxwell's equations. A feasible strategy for such intricate analyses is by recasting these into an eigenwave problem. The plane wave expansion method (PWEM) offers an elegant approach in this regard.

At the heart of the PWEM is the assertion that the electromagnetic fields within periodic structures can be expanded as a sum of plane waves. Symbolically, the electric field $E(\vec{r})$ in a periodic medium can be represented as:

$$E(\vec{r}) = \sum_{\vec{G}} E_{\vec{G}} e^{i(\vec{k} + \vec{G}) \cdot \vec{r}} \quad (2.3)$$

where \vec{G} represents the set of reciprocal lattice vectors and \vec{k} is the wavevector inside the Brillouin zone.

Maxwell's equations in the frequency domain, devoid of any free charges or currents, can be represented as:

$$\nabla \times \nabla \times \vec{E} - \omega^2 \mu_0 \varepsilon(\vec{r}) \vec{E} = \omega^2 \mu_0 \vec{E}_0 \quad (2.4)$$

where ω is the angular frequency, μ_0 is the permeability of free space, and $\varepsilon(\vec{r})$ is the position-dependent permittivity of the material.

Using the plane wave expansion in the above equation and incorporating the boundary conditions, a matrix eigenvalue problem arises:

$$[M] \vec{E}_{\vec{G}} = \beta^2 \vec{E}_{\vec{G}} \quad (2.5)$$

where $[M]$ is a matrix dependent on the material's permittivity and the geometry, and $\vec{E}_{\vec{G}}$ is a column vector of the plane wave coefficients.

Johnson and Joannopoulos, in their 2001 landmark paper [51], advocated for a block-iterative frequency-domain technique to bolster the PWEM. By adopting iterative solutions in the frequency domain, they achieved more rapid convergence and heightened accuracy. Their approach pivoted on the eigenvalue problem within a planewave foundation, addressing computational challenges tied to intricate photonic structures.

PWEM's intrinsic merit is in yielding the band structure of periodic media. However,

the method's precision hinges on the number of plane waves in the expansion. For intricate structures or vast frequency ranges, computational demand can surge.

In summary, the planar wave expansion method stands as an indomitable tool in the realm of photonics. It offers profound insights into the intricacies of microstructured waveguides, ensuring our grasp of photonics remains ever-evolving.

2.1.2 Multipole method

The realm of MOF demands precise and intricate modeling techniques to understand wave propagation phenomena within their unique structures. Among the techniques that have emerged, the multipole method stands out as a valuable tool. Grounded in a series of works by Kuhlmeier *et al.* [52], [53], the method offers a nuanced way to tackle the challenges posed by MOF.

The multipole method is a technique wherein the fields inside each hole of the MOF's structure are expanded using cylindrical wave functions [52]. Representatively, the electric field $E(r, \theta)$ within a hole can be expanded as:

$$E(r, \theta) = \sum_{n=-\infty}^{\infty} (A_n J_n(kr) + B_n H_n^{(1)}(kr)) e^{in\theta} \quad (2.6)$$

Here, J_n represents the Bessel function of the first kind, $H_n^{(1)}$ is the Hankel function of the first kind, and A_n and B_n are coefficients. The fundamental aspect of this method is the accurate representation of the fields within and around the holes of the MOF, incorporating the unique boundary conditions of these structures. Building upon the formulation in [53] into the computational aspects of the technique. The paper underscores the iterative methods to solve for the coefficients A_n and B_n , ensuring the boundary conditions are met for each hole in the MOF.

An interesting outcome of the multipole method is its ability to provide clear insights into both core and cladding modes of the MOF, including the nuanced behavior of modes near the light line, which are challenging to model using other techniques.

The PWEM uses a Fourier decomposition of the field across a periodic structure. PWEM inherently relies on the periodic nature of the structure, representing it in terms of Bloch modes.

While both methods aim to solve for the electromagnetic fields in MOF, their approach to the problem differs fundamentally. The multipole method emphasizes local field expansions, especially around intricate features like holes. In contrast, PWEM globally expands the field across the entire unit cell.

In terms of computational effort, the multipole method often requires fewer basis functions for convergence, especially for fibers with larger air holes. However, PWEM, due to its global perspective, can sometimes offer broader insights into the band structures of MOF.

The multipole method presents a comprehensive technique to understand the intricate wave behaviors within MOF. Its focus on local field behaviors, especially around the MOF's characteristic features, makes it an indispensable tool in the photonics modeling toolkit.

2.1.3 Finite difference method

In the rapidly evolving landscape of photonics, MOF have emerged as versatile platforms for light confinement and guidance. Their design is often complex and multi-dimensional, requiring sophisticated simulation techniques. One such technique, which has found extensive use due to its precision and tractability, is the full-vectorial finite-difference (FV-FD) method.

At the heart of this method is the vectorial formulation of Maxwell's equations. In contrast to scalar formulations that often oversimplify wave behavior in MOF, the full-vectorial approach takes into account both transverse and longitudinal electric and magnetic field components. This results in a more comprehensive representation of light propagation.

For a typical MOF, the refractive index profile ($n(x, y)^2 = \varepsilon_r$) varies across the transverse cross-section. The crux of the FV-FD method lies in discretizing this spatial variation into a mesh or grid. The resulting grid points are then used to approximate the spatial derivatives in Maxwell's equations. Using central difference approximations, the continuous differential equations are transformed into a discrete set.

Mathematically, the wave equation in terms of transverse electric field

$$(\nabla_t^2 + k_0^2 \varepsilon_r) \vec{E}_\perp + \nabla_\perp \left(\varepsilon_r^{-1} \nabla_\perp \varepsilon_r \cdot \vec{E}_\perp \right) = \beta^2 \vec{E}_\perp \quad (2.7)$$

transforms into eigenvalue problem:

$$P \begin{bmatrix} E_x \\ E_y \end{bmatrix} = \beta^2 \begin{bmatrix} E_x \\ E_y \end{bmatrix} \quad (2.8)$$

Here, \vec{E}_\perp represents the transverse electric field vector, k_0 is the free-space wave number, and ε_r denotes the waveguide dielectric constant profile and P - initial eigenvalue matrix [54]. Given the full-vectorial nature of the problem, each of the components

of the electric field vector is represented in the grid, and the resulting equations are solved concurrently.

The importance of boundary conditions underscored for MOF where the boundary may not be a simple geometric shape [54]. By employing the FV-FD method and meticulously handling boundary conditions, they managed to accurately model MOF and predict their modal behavior.

One key strength of this method, as demonstrated in the paper, is its ability to capture both the core-guided and cladding-guided modes in MOF. This distinction is crucial as it determines the confinement and propagation characteristics of light within the fiber.

Comparatively, while other methods like the plane wave expansion method might be more intuitive for periodic structures and can effectively map bandgap characteristics, FV-FD excels in analyzing the fine spatial variations in the refractive index profile, which is essential for MOF.

In conclusion, the full-vectorial finite-difference method, as detailed by Zhu and Brown [54], offers an intricate, yet computationally feasible, approach to analyzing microstructured optical fibers. By accounting for the full vectorial nature of Maxwell's equations, this method can accurately predict complex light propagation behaviors in these novel fiber structures. Overall, while the FDM is a powerful tool for modeling optical fibers, it can be computationally demanding for complex structures. It's vital to carefully balance the desired accuracy with the available computational resources to obtain meaningful results, specially when we use finite difference time domain (FDTD) method.

2.1.4 Finite element method

In the area of optical fiber analysis, accurate computational methods are quintessential to understanding and predicting the behavior of light propagation. One such computational technique that has been extensively applied is the finite element method (FEM).

The FEM breaks down the continuous domain of the fiber cross section into a set of smaller, finite elements. These elements, typically triangular or quadrilateral in shape, form a mesh over the domain, allowing for an approximate solution of the field distribution within the fiber. The method then solves the Helmholtz equation for each of these elements:

$$\nabla^2 \times \vec{E} - k_0^2 n^2(x, y) \vec{E} = \beta^2 \vec{E} \quad (2.9)$$

Here, \vec{E} is the electric field, k_0 denotes the wave number in free space, $n(x, y)$ is the spatially varying refractive index of the fiber, and β is the propagation constant.

The FEM formulation leads to a generalized eigenvalue problem, as previously mentioned.

$$[M]\vec{E} = \beta^2\vec{E} \quad (2.10)$$

One of the primary strengths of the FEM is its flexibility in dealing with irregular geometries and inhomogeneous refractive index profiles [55]. Optical fibers can have complex refractive index distributions, especially in the case of specialty fibers, and FEM's adaptability to such variations gives it an edge. Additionally, the method's precision in capturing boundary conditions, which play a crucial role in mode calculations, makes it indispensable for optical fiber analysis.

Compared to other methods:

- Plane wave expansion: While PWE is tailored more towards periodic structures and offers an intuitive approach for mapping bandgap characteristics, it might not be as versatile as FEM in modeling non-uniform refractive index profiles.
- Multipole method: This method excels in cases where a fiber's structural features are much larger than the wavelength of light. However, most of realistic fibers do exhibit structural features that are not of cylindrical. In this case FEM offers more flexibility. Also for fibers with features comparable to or smaller than the wavelength, FEM might offer more accurate results.
- Finite-difference method: FDM, which approximates derivatives using difference equations, is inherently simpler and can be faster. Yet, it can struggle with complex geometries and boundary conditions (e.g. stair-case approximation [56]), areas where FEM shines.

Emphasizing the capabilities of the FEM in mode analysis of optical fibers we chose it, namely the program COMSOL multiphysics®, as a tool for our works.

2.2 Mode solving via finite element method

This section delves into the intricacies of mode solving via FEM, shedding light on its methodologies, applications, and nuances.

2.2.1 Script preparation and optimisation

Geometry

In used software COMSOL multiphysics® we also have built-in CAD module. Before mesh optimization, it is also important to prepare a correct geometrical model. Best approach to win in efficiency is to build a geometry with as less as possible number of vertices as there are used for mesh building. The simplified steps of geometry development is shown in Figure 2.1.

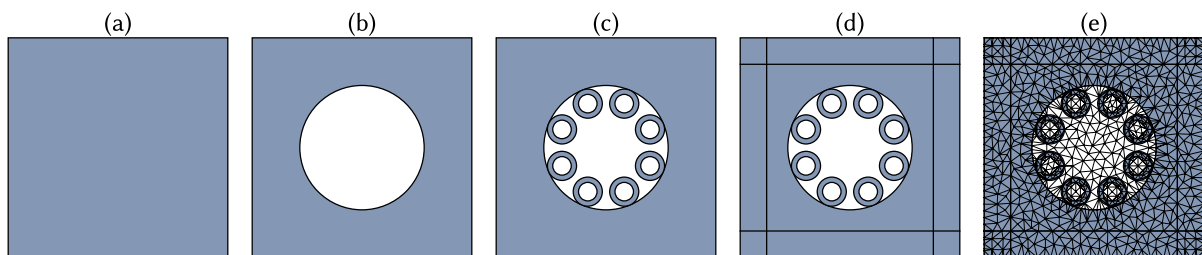


Figure 2.1: Simplified steps of geometry development. (a) Computational domain. (b) Air hole in (a). (c) Introduction of microstructure tubes into (b). (d) PML domain introduction into (c). (e) Meshing operation over (d).

Symmetry

Sometimes we can use the symmetry of a structure with special boundary conditions, like perfect electric conductor (PEC) and perfect magnetic conductor (PMC), to reduce required computational time and resources. By applying these boundary conditions to the axis of symmetry, we can simulate half or even quarter structures, which will result in 2 – 4 orders of magnitude speed increase obviously due to decreasing number of finite elements by the factor of 2 or 4 [57].

Material

Upon the completion of the geometry setup, a critical step in our simulation process, we meticulously determine the selection of domains designated for representing the refractive indices of glass and air, as thoughtfully illustrated in Figure 2.1 (d). To enhance the precision and robustness of our simulations, we refrain from employing fixed and simplified refractive index values, a common practice in various scientific works. Instead, we adopt dispersion Sellmeier equations (2.11, 2.12) [58], [59], a more comprehensive and rigorous approach that accounts for wavelength-dependent variations in refractive

indices. This ensures that our simulations accurately capture the wavelength-dependent behaviors of light propagation within the optical structures under investigation.

$$n_{\text{glass}} = \sqrt{1 + \frac{0.6961663 \cdot \lambda^2}{\lambda^2 - 0.0684043^2} + \frac{0.4079426 \cdot \lambda^2}{\lambda^2 - 0.1162414^2} + \frac{0.8974794 \cdot \lambda^2}{\lambda^2 - 9.896161^2}} \quad (2.11)$$

$$n_{\text{air}} = 1 + \frac{0.05792105}{238.0185 - \lambda^{-2}} + \frac{0.00167917}{57.362 - \lambda^{-2}} \quad (2.12)$$

Also important to note that FEM solvers usually not able to select the polarisation of solved mode but in order to force our solution to have strict linear polarisation we can add small anisotropy to refractive index matrix of air as small as 10^{-5} without significant impact on n_{eff} of the modes:

$$n_a(\lambda) = \begin{pmatrix} n_a(\lambda) & 0 & 0 \\ 0 & n_a(\lambda) - 10^{-5} & 0 \\ 0 & 0 & n_a(\lambda) \end{pmatrix} \quad (2.13)$$

Perfectly matched layers

The PML is a domain or layer (sometimes called sponge layer) that is usually added to mimic an open and nonreflecting infinite domain. It sets up a perfectly absorbing domain as an alternative to nonreflecting boundary conditions. The PML works with many types of waves, not only plane waves, excluding plasma type waves. It is also efficient at very oblique angles of incidence. In the frequency domain the PML imposes a complex-valued coordinate transformation to the selected domain that effectively makes it absorbing at a maintained wave impedance, and thus eliminating reflections at the interface. In our case it is applied to Helmholtz equation in finite element frequency domain (FEFD).

In much of the literature the PML transformation is written as a transformation of a derivative [60]–[62]:

$$\frac{d}{dx} \rightarrow \frac{d}{dx'} = \frac{1}{1 - i \frac{\sigma(x)}{\omega}} \frac{d}{dx} \quad (2.14a)$$

$$\sigma(x) = \frac{(m+1) \cdot \lambda}{4\pi \cdot n_{\text{mat}} \cdot d_{\text{PML}}} \cdot \left(\frac{\rho(x)}{d_{\text{PML}}} \right)^m \cdot \ln \left(\frac{1}{R_{\text{PML}}} \right) \quad (2.14b)$$

Typical value of $m = 2$, R_{PML} - reflectance of the PML and in its turn can be set as small as used platform can allow, in consistent with the PML principle that $R_{\text{PML}} \rightarrow 0$ for the ideal PML, d_{PML} - thickness of the PML. According to the COMSOL multiphysics® manual the physical thickness of the PML is not important in frequency domain models. Here a real stretching is applied to mathematically scale the thickness relative to the wavelength. The thickness should however be such that the mesh is more or less regular [63].

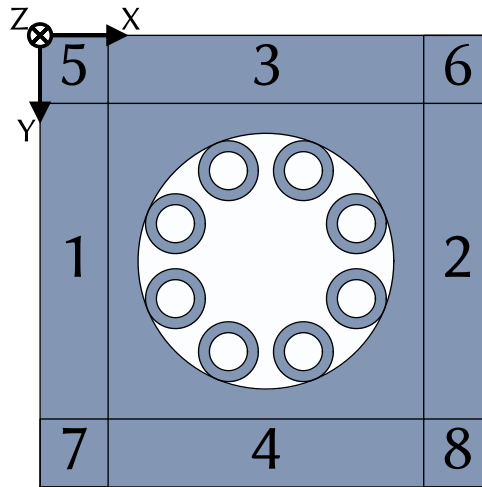


Figure 2.2: Transverse cross section of a HCPCF surrounded by PML domains 1 – 8.

And this transformation matrix can be written as:

$$[S] = \begin{bmatrix} \frac{S_y S_z}{S_x} & 0 & 0 \\ 0 & \frac{S_z S_x}{S_y} & 0 \\ 0 & 0 & \frac{S_x S_y}{S_z} \end{bmatrix} \quad (2.15)$$

Here S_x and S_y are depend on the position in the computational domain (see Fig. 2.2) but $S_z = 1$ everywhere in PML [62].

There are certain situations where PMLs yield incorrect outcomes [64] or are simply inadequate because despite principle that $R_{\text{PML}} \rightarrow 0$ - it's never actually zero. It is impossible to resolve all possible issues that may arise with PMLs. At times, it may be more appropriate to consider alternative approaches. The complication is that evanescent waves that are produced at the critical angle for Total Internal Reflection have an infinite decay length that PMLs are unable to manage. PMLs may also face challenges with backward-waves, which are defined as waves where the phase and

group velocities move in opposite directions. In contrast, forward-waves have velocities in the same direction. Assuming a harmonic plane wave enters the PML and only imaginary stretching is carried out using the (2.14) notation, a backwards-wave will cause exponential growth instead of attenuation if $\sigma > 0$. The problem can be resolved by setting $\sigma < 0$ if the medium is homogeneous and contains only backward-waves at certain frequencies. However, if the medium is inhomogeneous and has backward-waves or both forward- and backward-waves at the same frequency, the issue cannot be resolved. In such cases, alternative methods should be explored [65].

Meshing

Once the geometry is ready and materials are assigned meshing operation can be performed. Mesh optimization is a technique used to improve the accuracy and efficiency of the FEM simulation in optical fiber mode solving. Optimizing the mesh involves several strategies such as selecting the best type of elements for the mesh, refining the mesh size where needed, and using appropriate boundary conditions. Additionally, mesh optimization can also be improved by using adaptive mesh refinement, which allows for the mesh size to be changed according to the local solution requirements. Mesh optimization can also be improved by using mesh smoothing algorithms, which can help improve the accuracy of the solution without adding additional elements. Finally, mesh optimization can also be improved by using mesh coarsening techniques, which can reduce the number of elements used in the mesh, resulting in a faster and more accurate solution. Theoretically, the most accurate method for discretizing structures is to employ a wavelength-dependent technique with an optimal element size around $\lambda/50$, yet in practice this level of detail may be inefficient and require unacceptable amount of time and resources.

For each of the domains we select its own rule of meshing and modify it with variable which will be common for all the domains showed in Table (2.1). Usually we separate entire geometry into six groups:

- Small capillary glass which defined by thickness of the glass.
- Small air regions
- Large air region (core)
- Transit domain between silica jacket and capillary cladding
- Jacket
- PML domains
- sometimes can be added mesh node with remaining domains in order to avoid

fails

Table 2.1: Table with variations meshing rules for different domains groups

Domain group name	Capillary	Small air domains	Core air domain	Transit domain	Jacket	PML
Maximum mesh size equation	$\frac{t}{9} \cdot c_m$	$\frac{r}{15} \cdot c_m$	$\frac{R}{35} \cdot c_m$	$0.55 \cdot t \cdot c_m$	$0.8 \cdot t \cdot c_m$	$t \cdot c_m$

Where t - thickness of the glass capillary, r - radius of small air domain, R - radius of core air domain, c_m - variable which we varying in order to get stable and fast result. Best way to test the limits of stability before proceeding it to make sweep over range 0.5 – 5 with step of 0.1 for c_m . Demonstrated on Figure (2.3) we can see how effective index n_{eff} is approaching stable value and CL form a group of values. We assume that values in those clusters are stable enough in order to be similar (marked with black ovals) and then we take the largest possible c_m (marked with star). The simulation has been performed for different stations listed in Table (2.2). On second and third graph represented solution time vs mesh parameter and RAM consumption vs normalized RAM track event. For all 4 machines 1 node is considered. Normalized RAM track event used due to not equal distribution of events but full length of x axis represents length of simulation in time at given station.

Table 2.2: Computational stations available and used in my PhD

Name	CPU	RAM [GB]	number of nodes
Desktop	Ryzen 7 3800X	32	1
Laptop	Core i7-4910MQ	32	1
CALI [66]	2 x Xeon E5 2630 v4	128	16
	2 x Xeon E5 2650 v2	128	20
	2 x Xeon 4108	256	1
	2 x Xeon 4114	192	1
		92	3
CURTA [67]	2 x Xeon Gold SKL-6130	92	336
	4 x Xeon Gold SKL-6130	3072	4

Fiber configuration used for results presented at Figure (2.3) is presented in Table (2.3).

Table 2.3: Main geometrical parameters used for the TL TLF HCPCF simulation in Fig. 2.3.

$D_{\text{core}},$ [μm]	$g,$ [μm]	$d_{\text{tubes}},$ [μm]	$t,$ [μm]
27	3.56	11	0.6

Here t - thickness of the capillary tubes, d_{tubes} - their external diameter, g - distance between two capillaries and D_{core} - fiber core diameter.

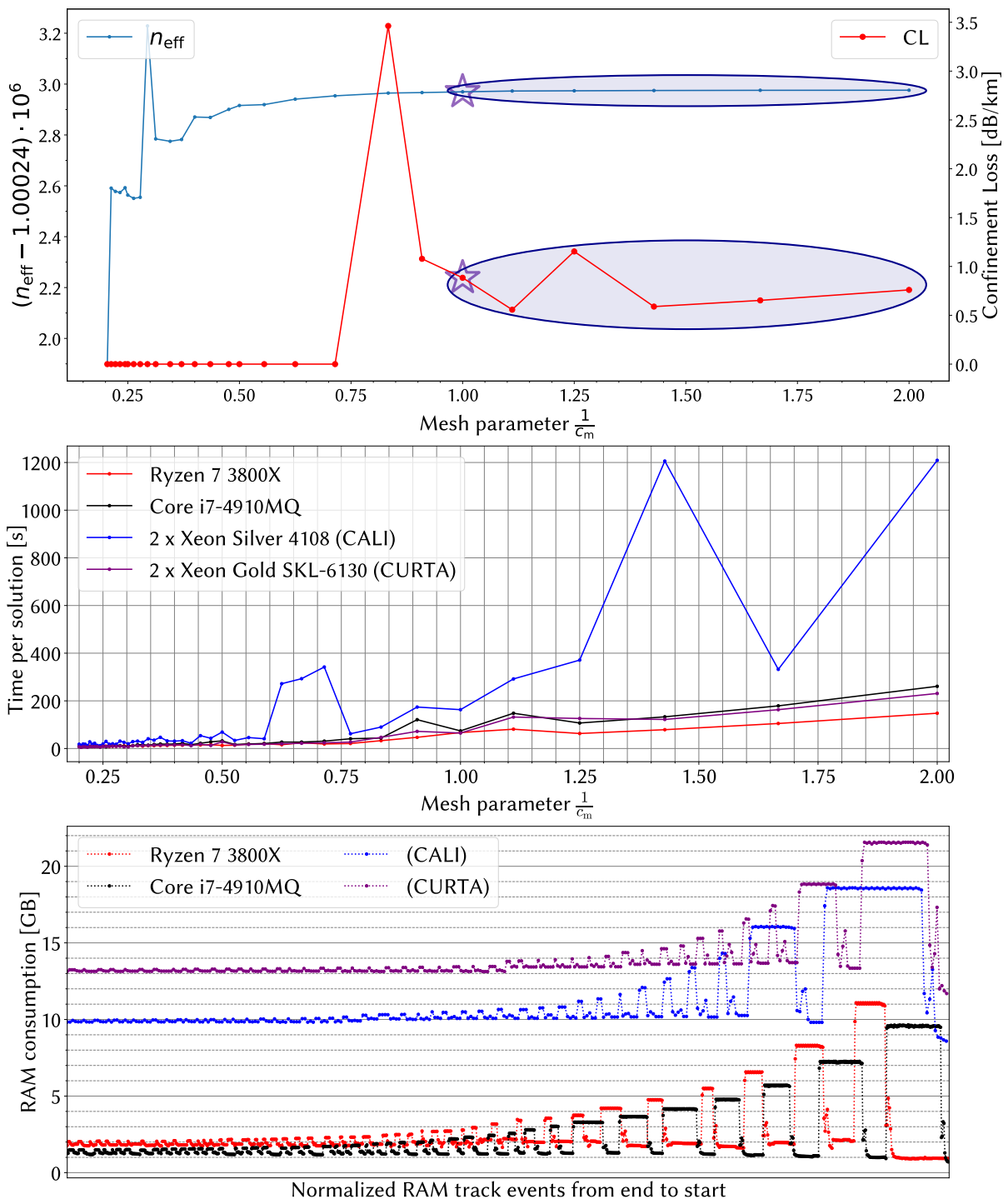


Figure 2.3: (a) Typical mesh analysis graph. (b) Time spent for each parametric step of the sweep at different platform. (c) RAM consumption tracking during solving at different platforms.

Later on for all the simulations the parameters of mesh picked to be in the sweet spot in trade-off between speed and accuracy. Also good point of taking into account accuracy decaying with decreasing of λ . In order to compensate this additionally to the

picked c_m for each next band in normalized frequency we can set it slightly smaller.

After the meshing process is completed, we can proceed to utilize the eigenvalue problem solver. This solver is applied to our governing equation (2.9), which is formulated as an eigenvalue problem (2.10). Solving this eigenvalue problem will provide us with a set of eigenvalues and eigenvectors tailored to our specific requirements.

Before embarking on the analysis of simulation results, let's first delve into the fundamental concept of the eigenvalue problem itself.

Eigenvalue problem

The general form of matrix eigenvalue problem has the form:

$$[A]\{x\} = \lambda\{x\} \quad (2.16)$$

where $[A] = ||a_{i,j}||^m$ is a square matrix, λ (in mathematical notation or γ in our case) are eigenvalues of the matrix and $\{x\}$ are eigenvectors of matrix corresponding the specific eigenvalue. Full representation as the system of scalar equations looks like:

$$\begin{aligned} a_{11}x_1 + a_{12}x_2 + \dots + a_{1m}x_m &= \lambda x_1 \\ a_{21}x_1 + a_{22}x_2 + \dots + a_{2m}x_m &= \lambda x_2 \\ &\vdots \\ a_{m1}x_1 + a_{m2}x_2 + \dots + a_{mm}x_m &= \lambda x_m \end{aligned} \quad (2.17)$$

which can be re-written in the following form:

$$\begin{aligned} (a_{11} - \lambda)x_1 + a_{12}x_2 + \dots + a_{1m}x_m &= 0 \\ a_{21}x_1 + (a_{22} - \lambda)x_2 + \dots + a_{2m}x_m &= 0 \\ &\vdots \\ a_{m1}x_1 + a_{m2}x_2 + \dots + (a_{mm} - \lambda)x_m &= 0 \end{aligned} \quad (2.18)$$

In order for the system (2.18) to have non-trivial solutions, it is necessary for the

determinant of the system to be equal to zero:

$$\begin{vmatrix} (a_{11} - \lambda) & a_{12} & \dots & a_{1m} \\ a_{21} & (a_{22} - \lambda) & \dots & a_{2m} \\ \vdots & \vdots & \ddots & \vdots \\ a_{m1} & a_{m2} & \dots & (a_{mm} - \lambda) \end{vmatrix} = 0 \quad (2.19)$$

The determinant (2.19) represents an algebraic equation of the n -th order which is called characteristic equation and its left part is known as characteristic polynomial. Thus, each eigenvalue is the root of characteristic equation. Substituting each the eigenvalue to the system (2.18) and solving it, we obtain corresponding eigenvector [68].

But for our case in eq. (2.10) we use proprietary software COMSOL multiphysics® which uses one of the most famous implementation of eigenvalue solver which is ARPACK FORTRAN routines for large-scale eigenvalue problems [69]. This code is based on a variant of the Arnoldi algorithm called the implicitly restarted Arnoldi method (IRAM).

Also important to know that any kind of eigenvalue solvers takes as an input initial guess. For the computations which we are dealing with an eigenvalue is complex effective index n_{eff} and an initial guess we call n_{eg} . We can specify for solver where it must search for an eigenvalue by those 6 simple rules:

$$\begin{array}{ll} 1) |n_{\text{eff}}| \approx |n_{\text{eg}}| & 2) \text{Re}(n_{\text{eff}}) > \text{Re}(n_{\text{eg}}) \quad 4) \text{Im}(n_{\text{eff}}) > \text{Im}(n_{\text{eg}}) \\ 3) \text{Re}(n_{\text{eff}}) < \text{Re}(n_{\text{eg}}) & 5) \text{Im}(n_{\text{eff}}) < \text{Im}(n_{\text{eg}}) \end{array} \quad 6) \begin{cases} \text{Re}(n_{\text{eg}})_{\text{max}} > \text{Re}(n_{\text{eff}}) > \text{Re}(n_{\text{eg}})_{\text{min}} \\ \text{Im}(n_{\text{eg}})_{\text{max}} > \text{Im}(n_{\text{eff}}) > \text{Im}(n_{\text{eg}})_{\text{min}} \end{cases}$$

The rule 1) is the most efficient to use in couple with Marcatili's expression for complex propagation constant [40]:

$$\gamma \approx k_0 \left(1 - \frac{1}{2} \left(\frac{u_{nm} \lambda}{2\pi a} \right)^2 \left(1 - \frac{i\nu_n \lambda}{\pi a} \right) \right) \quad (2.20)$$

$$\frac{\gamma}{k_0} \approx n_{\text{eff}}$$

where a - fiber core radius, u_{nm} - is the m -th root of the equation $J_{n-1}(u_{nm}) = 0$, $\nu_n = \frac{1}{\sqrt{n_{\text{glass}}^2 - 1}}$ for TE_{0m} modes ($n = 0$), $\frac{n_{\text{glass}}^2}{\sqrt{n_{\text{glass}}^2 - 1}}$ for TM_{0m} modes ($n = 0$) and $\frac{0.5(n_{\text{glass}}^2 + 1)}{\sqrt{n_{\text{glass}}^2 - 1}}$ for EH_{nm} modes ($n \neq 0$).

But for more broad analysis the fact that n_{eff} for FM and the most of HOM in transmission bands lies on the axis of refractive index under the n_{air} line allow as efficiently

use rule 3) as $\text{Re}(n_{\text{eff}}) < n_{\text{air}}$, where n_{air} is given by eq. (2.12).

2.2.2 Results of solution

In a single solution, the wealth of data provided by the COMSOL multiphysics® Electro-magnetic Wave Frequency Domain (EWFD) mode solver is extensive. We gain access to a comprehensive set of field components, including E_x , E_y , E_z , H_x , H_y , and H_z , as well as valuable information such as the complex effective index n_{eff} and various related entities.

This abundance of information equips us with the tools to conduct a wide range of sophisticated analyses and manipulations. With this data at our disposal, we have the capability to extract critical parameters like confinement loss (CL eq. 1.9), surface scattering Loss (SSL eq. 1.5), microbending loss (MBL eq. 1.7), and optical overlap factor F , among others. The comprehensive dataset empowers us to explore and interpret the results in depth, facilitating a deeper understanding of the optical characteristics of the guided structures under investigation.

Mode recognition

The next challenge we encounter is that the solutions provided by the eigenvalue solver are not arranged in a specific order. To address this issue, we must first identify the modes before attempting to sort them. The first thing which was used for mode recognition its overlap integral equation which was inspired with simple math equation $(a + b)^2 / (a^2 + b^2 + 2ab) = 1$:

$$O_I = \frac{\left| \int_S (E_{x_1} \cdot E_{x_2}^* + E_{y_1} \cdot E_{y_2}^*) dS \right|^2}{\int_S |E_{x_1}|^2 dS \cdot \int_S |E_{x_2}|^2 dS + \int_S |E_{y_1}|^2 dS \cdot \int_S |E_{y_2}|^2 dS + 2 \cdot \int_S |E_{x_1} \cdot E_{x_2}| dS \cdot \int_S |E_{y_1} \cdot E_{y_2}| dS} \quad (2.21)$$

Where \int_S is an integral by surface of solution S with PML excluded, E_{x,y_i} - x and y components of electric field of i -th solution, $i = 1, 2$. For better recognition quality this equation can be multiplied by analogous equation but for magnetic field in next manner $O_I = O_{I_E} \cdot O_{I_H}$.

The origin of those recognition equations are described more precisely at appendix A.1. For simple recognition equation (2.21) is enough but when we want perform more complex analysis the equation (2.22) must be used.

Another difficult task is to adapt this equation (2.22) for COMSOL multiphysics®.

For better understanding I color-coded it as

$$C^2 = \frac{|\iint_S (E_{x_1} E_{x_2}^* + E_{y_1} E_{y_2}^*) dS|^2}{(\iint_S |E_{x_1}|^2 dS + \iint_S |E_{y_1}|^2 dS)(\iint_S |E_{x_2}|^2 dS + \iint_S |E_{y_2}|^2 dS)} \quad (2.22)$$

and the code which generated by script in COMSOL multiphysics® for this equation:

```
abs(infull( withsol('sol2', ewfd.Ex, setind('lambda', 1), setval('ps_value', 0.0)) *
  conj(withsol('sol2', ewfd.Ex, setind('lambda', 4), setval('ps_value', 0.25))) +
  withsol('sol2', ewfd.Ey, setind('lambda', 1), setval('ps_value', 0.0)) *
  conj(withsol('sol2', ewfd.Ey, setind('lambda', 4), setval('ps_value', 0.25))) ) )^2 /
( (infull(abs( withsol('sol2', ewfd.Ex, setind('lambda', 1), setval('ps_value', 0.0)) ) )^2 +
  infull(abs( withsol('sol2', ewfd.Ey, setind('lambda', 1), setval('ps_value', 0.0)) ) )^2) ) *
(infull(abs( withsol('sol2', ewfd.Ex, setind('lambda', 4), setval('ps_value', 0.25)) ) )^2 +
  infull(abs( withsol('sol2', ewfd.Ey, setind('lambda', 4), setval('ps_value', 0.25)) ) )^2) )
```

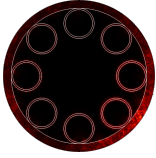
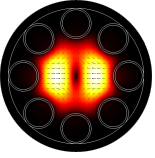
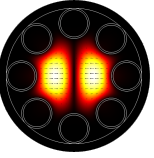
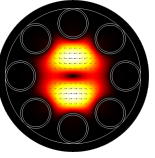
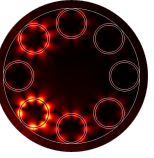
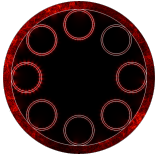
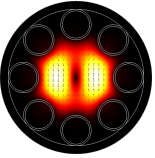
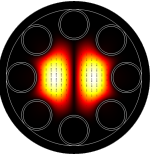

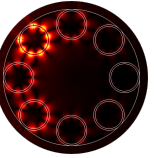
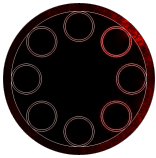
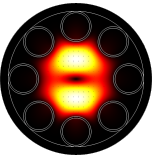
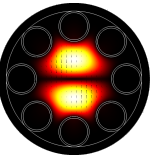
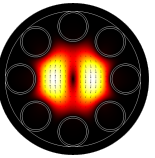
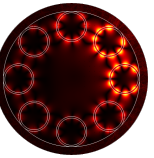
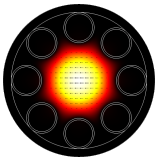
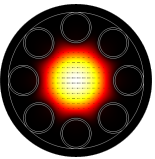
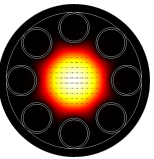
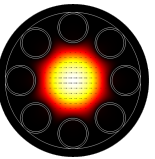
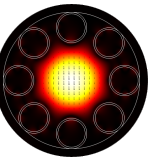
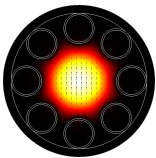
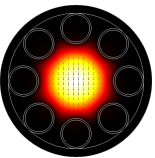
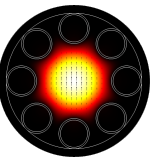
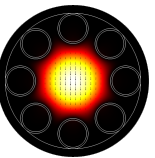
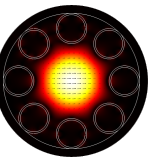
where *sol2* - name of the solution, *infull* - user defined name of integration operator, *ps_value* - user defined variable name which changing (angle of rotation in this case), *lambda* - reserved variable name for an eigenvalue. Others subcommands described in the manual [70]. Subsequently, we expanded equation (2.22) to incorporate both electric and magnetic fields, thus enhancing its scope and applicability:

$$C^2 = \left| \left(\frac{\iint_S (E_{x_1} H_{y_2} - E_{y_1} H_{x_2}) dS}{\sqrt{\iint_S (E_{x_1} H_{y_1} - E_{y_1} H_{x_1}) dS \cdot \iint_S (E_{x_2} H_{y_2} - E_{y_2} H_{x_2}) dS}} \right)^2 \right| \quad (2.23)$$

Sorting algorithm

In order to sort the modes we used test field functions (table A.1) in addition with overlap integral equations (2.21, 2.23). For example if in COMSOL multiphysics® we searched for 5 modes at 5 wavelengths then we have 25 solutions to work with. In *Results* branch of COMSOL multiphysics® we use *Global Evaluation* node so that we apply eq. (2.22) to all 25 solutions where E_{x_1} , E_{y_1} are test field functions of all listed LP modes and E_{x_2} , E_{y_2} are electric field components of given solution. On the output of this operation we have a 5 x 5 matrix for each of desired LP modes. Then if we take an index of row for each column where output value is bigger then other 4 then this index is belong to the mode which correspond to this 5 x 5 matrix at corresponded to column index wavelength as demonstrated in Table 2.4.

Table 2.4: Table with C^2 between test function and solved modes.

$\lambda_n, [\mu\text{m}]$ Mode $_m$	$\lambda_1 = 0.4$	$\lambda_2 = 0.45$	$\lambda_3 = 0.5$	$\lambda_4 = 0.55$	$\lambda_5 = 0.6$
$m = 1$	$6.7 \cdot 10^{-7}$ 	$1.7 \cdot 10^{-12}$ 	$1.6 \cdot 10^{-16}$ 	$6.9 \cdot 10^{-13}$ 	$1.0 \cdot 10^{-4}$ 
$m = 2$	$8.2 \cdot 10^{-8}$ 	$2.2 \cdot 10^{-11}$ 	$5.2 \cdot 10^{-13}$ 	$1.2 \cdot 10^{-12}$ 	$1.6 \cdot 10^{-3}$ 
$m = 3$	$4.2 \cdot 10^{-7}$ 	$8.8 \cdot 10^{-14}$ 	$2.3 \cdot 10^{-13}$ 	$4.9 \cdot 10^{-13}$ 	$1.8 \cdot 10^{-3}$ 
$m = 4$	$3.2 \cdot 10^{-9}$ 	$1.5 \cdot 10^{-9}$ 	$3.6 \cdot 10^{-11}$ 	$3.0 \cdot 10^{-10}$ 	0.921 
$m = 5$	0.955 	0.956 	0.954 	0.949 	$2.9 \cdot 10^{-3}$ 

In conclusion these various methodologies, applications, and intricacies collectively enable us to conduct rapid and reliable analyses of HCPCFs of diverse types. With these tools at our disposal, we can efficiently solve specific problems within minutes of computational time and explore broader approaches within a matter of hours.

2.2.3 Photonic band gap

In this section I will provide a comprehensive introduction to the theory and design of PBG fibers to illustrate the principle of photonic tight bonding model [14].

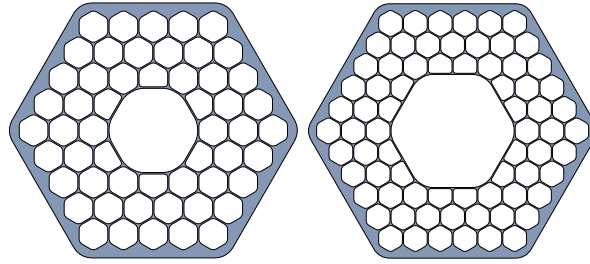


Figure 2.4: Geometries of conventional PBG HCPCF. 7-cell and 19-cell respectively.

For this aim, we start by using analytical equation (2.24) from [71] for propagation constant β of single rod as an Fig. 2.5 (left):

$$\beta^2 = (n_{co}k)^2 - \frac{U_\infty^2}{\rho^2} \frac{k^2}{(k + \frac{\eta}{\rho})^2} \quad (2.24)$$

where U_∞ is roots of Bessel function which correspond to the mode of interest, equal to 2.405 for the FM, $\eta = \frac{1-\Delta}{n_{co}\sqrt{2\Delta}}$, $\Delta = \frac{n_{co}^2 - n_{bkg}^2}{2n_{co}^2}$, $n_{co} = 1.45$ and $n_{bkg} = 1$ are refractive indexes of the rod and of background.

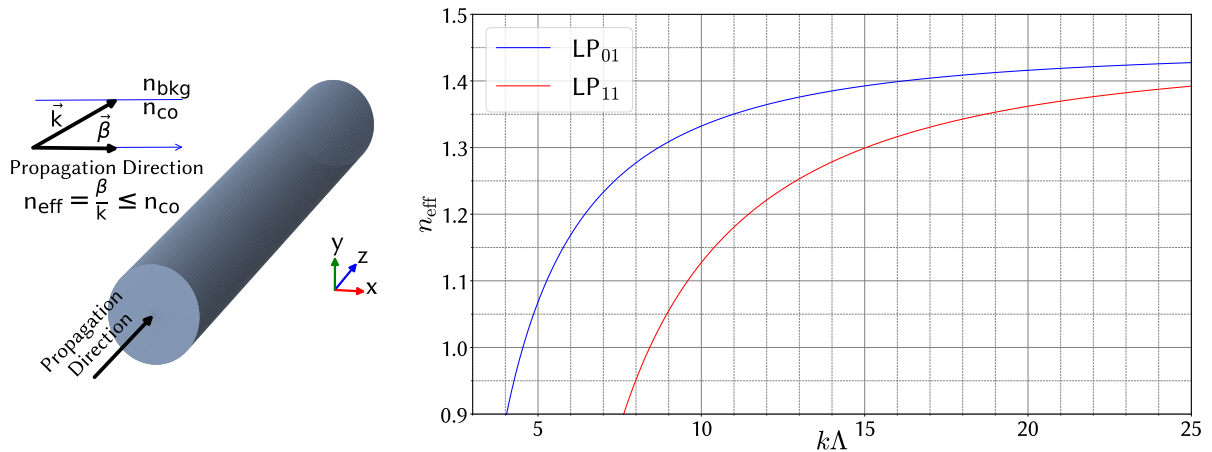


Figure 2.5: Visualisation of single silica rod in 3D (left). Dispersion curve for LP_{01} and LP_{11} of this structure (right).

We can obtain dispersion curve for several modes such as LP_{01} and LP_{11} displayed at Fig. 2.5 (right). If we apply similar approach as in [71] where equation for β was modified according to coupling with the neighbors rods:

$$\beta_j \Lambda = \beta \Lambda - 2\sqrt{(C\Lambda)^2} \cdot \cos\left(\frac{j\pi}{N+1}\right), j = 1, 2, \dots, N. \quad (2.25)$$

Where C - analytical coupling coefficient between two identical rods [72]. We can obtain

not only analytical dispersion curves but also, using FEM, numerical results showed in Figure 2.6 with green dots. The approximation is not that far from FEM results. In this section I will be using my numerical program as pedagogical tool to discuss the formation of PBG and assess the approximation of the tight binding model.

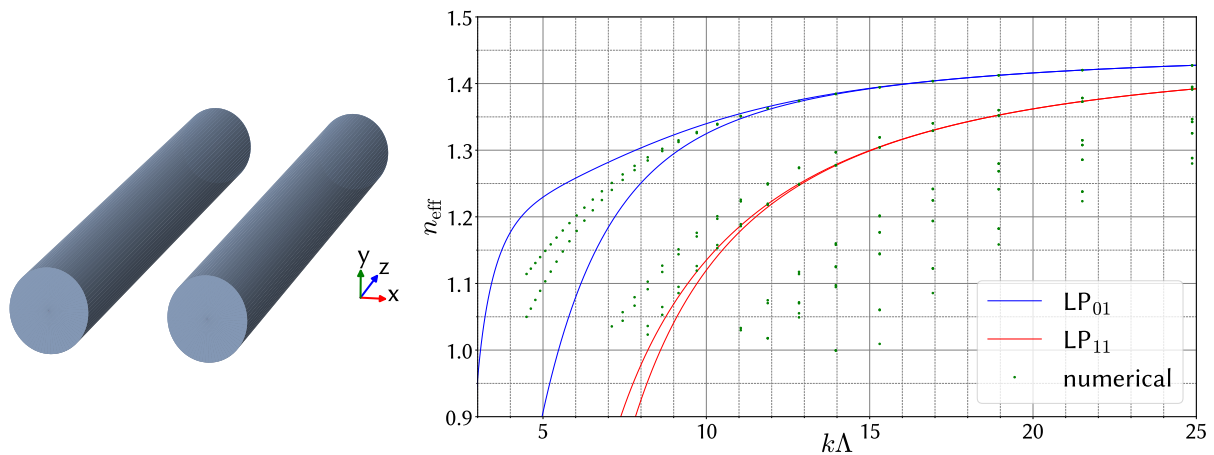


Figure 2.6: Visualisation of two silica rods array in 3D (left). Analytical dispersion curve for LP_{01} and LP_{11} (red and blue) and numerical simulation (with green dots) of this structure (right).

This trend continues to exist with increasing number of rods for 1D case (Figure 2.7).

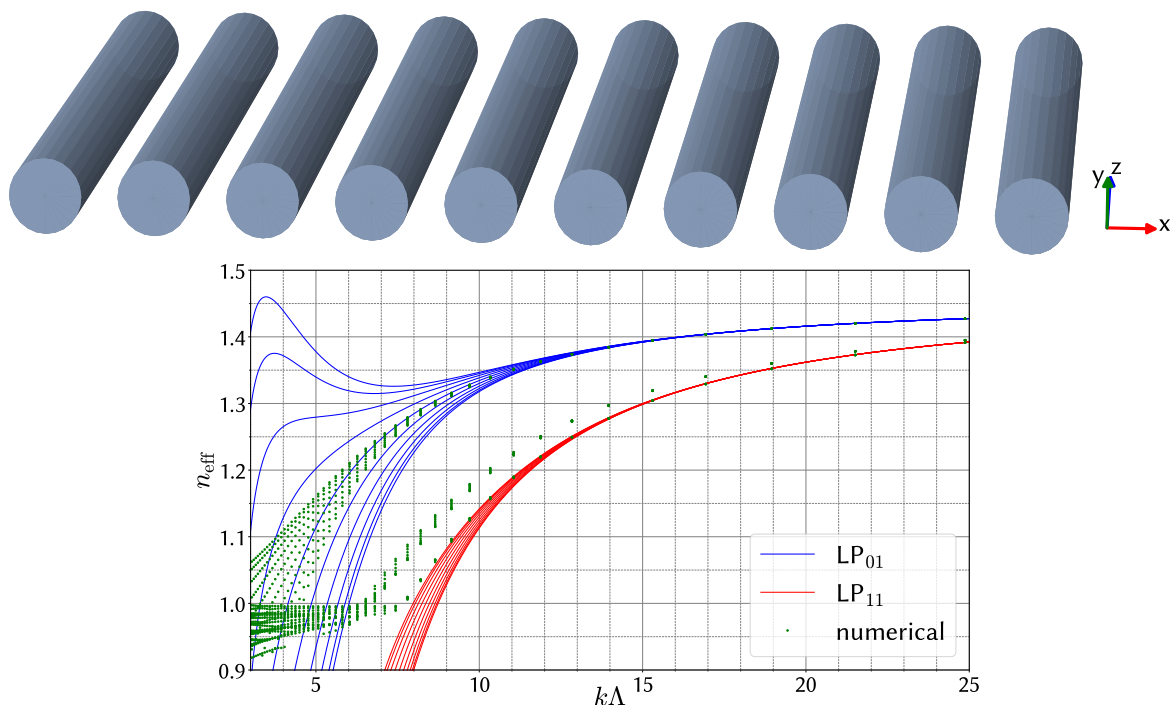


Figure 2.7: Visualisation of ten silica rods array in 3D (left). Analytical dispersion curve for LP_{01} and LP_{11} (red and blue) and numerical simulation (with green dots) of this structure (right).

From limited validity of equation (2.25) is clearly visible that analytical model compare to numerical simulation is inaccurate for case of more than one rods and require additional correction [73].

For 2D case of 36 rods spacing (Figure 2.8), the DOPS picture starts to look like in Figure 2.9.

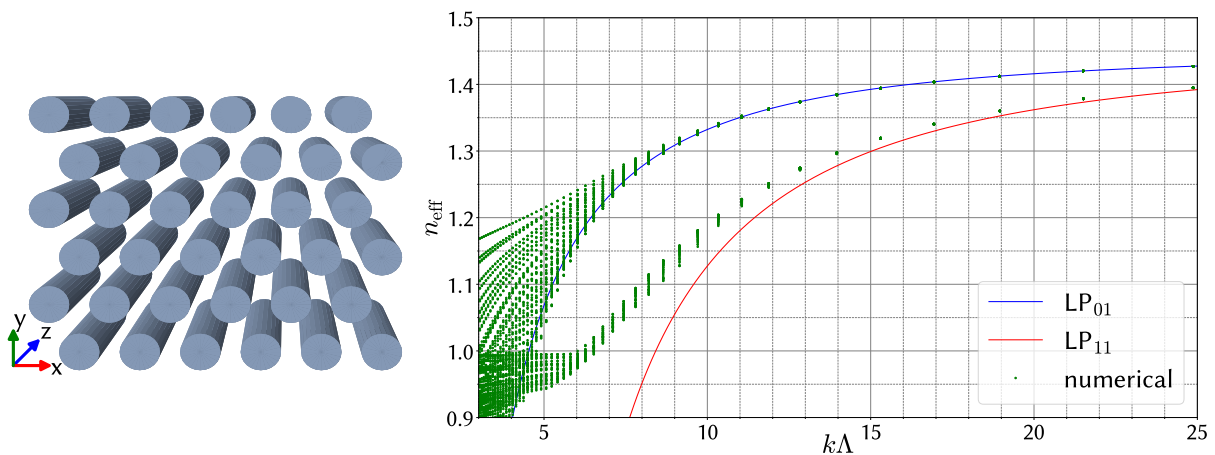


Figure 2.8: Visualisation of 36 silica rods triangular lattice in 3D (left). Analytical dispersion curve of a single rod for LP_{01} and LP_{11} (red and blue) and numerical simulation (with green dots) of this structure (right).

Here is described the principle of PBG from the very beginning with images at Figure 2.9. In Figure 2.9 (a), we can observe a continuum of modes when the refractive index of the material is $n_{\text{gl}} = 1.45$, and no modes are present above this threshold. However, if we increase the refractive index of the rod to $n_{\text{do}} = 1.5$ (doped), we can see an increase in the level of the mode continuum, as shown in Figure 2.9 (b). By introducing two materials into the structure, as seen in Figure 2.9 (c), we are able to explore the dispersion curves of available modes in such a structure. The black areas indicates $\text{DOPS} = 0$, which means no modes are present. Adding a 2D array of rods, as shown in Figure 2.9 (d), reveals the PBG DOPS (with an opened BG, meaning not an exact continuum of modes). Finally, by introducing a defect in the center of the 2D array, as shown in Figure 2.9 (e) (top), we are able to observe the blue dispersion curve of the fundamental mode of the defect region, as shown in Figure 2.9 (e) (bottom).

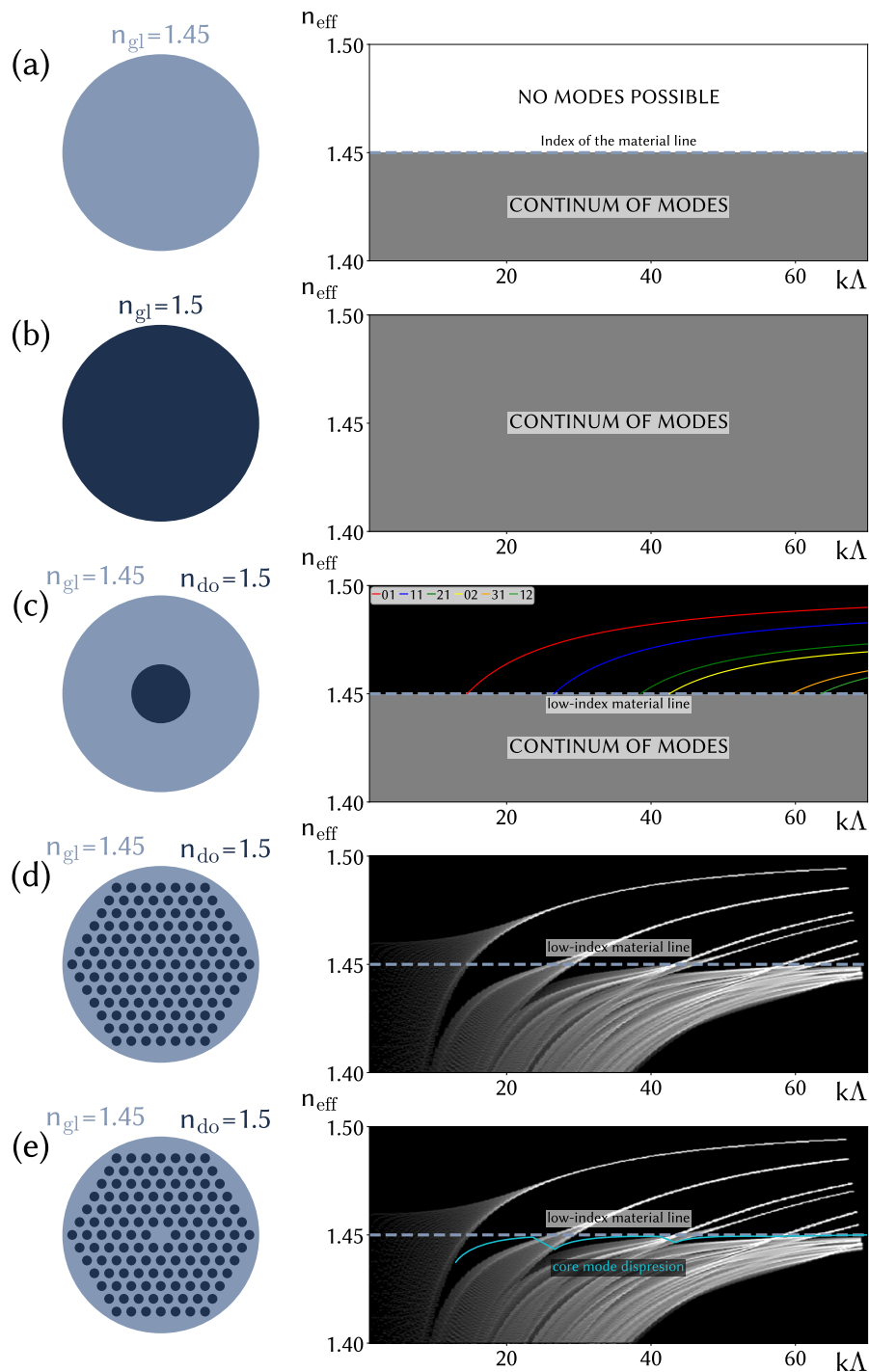


Figure 2.9: Left side of this figure represent a refractive index cross-sections under letters. Right part of this figure represent the DOPS of those structures in terms of $n_{\text{eff}}(k\Lambda)$ (a) A volume with glass $n_{\text{gl}} = 1.45$, (b) a volume with doped glass $n_{\text{gl}} = 1.5$, (c) a volume with glass and defect with doped glass rod $n_{\text{gl}} = 1.45$, $n_{\text{do}} = 1.5$, (d) a volume with glass and triangular lattice made of doped glass rods $n_{\text{gl}} = 1.45$, $n_{\text{do}} = 1.5$, (e) a volume with glass and triangular lattice made of doped glass rods and with defect in the center of this lattice $n_{\text{gl}} = 1.45$, $n_{\text{do}} = 1.5$.

2.2.4 Inhibited coupling

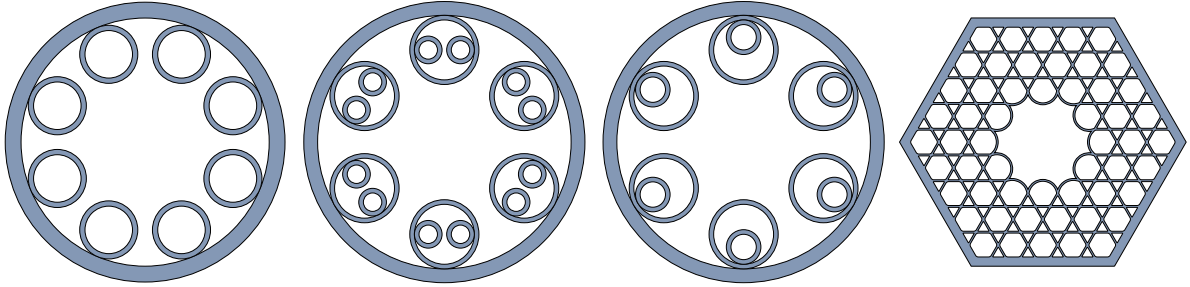


Figure 2.10: Examples of geometries of IC HCPCF.

As we already mentioned in chapter 1 the concept of IC guidance originated, with the aim of structuring the cladding and core so that cladding and core modes have the lowest possible overlap. Now we will see through the expression of the overlap integral that several engineering approaches are possible to achieve this. Here is the expression of field propagation for beginning:

$$\psi_{\text{core}}(r, \theta, z) = F_{\text{core}}(r, \theta) e^{i\phi_{\text{core}}(r, \theta)} e^{i\beta z} \quad (2.26)$$

where F_{core} - scalar function which represent spatial profile of transverse mode, β - propagation constant and ϕ_{core} - spatial transverse phase.

We need to take into account the phase matching in two components of the wave vector mode: k_{\parallel} along the propagation axis, and also k_{\perp} along the transverse axis to the direction of propagation z . It's allowing to eliminate the illogical nature of effective guidance, despite the fact that the main mode is surrounded by the cladding mode with the same effective index. It means that cladding mode and core mode could have equal β with saving different wave vectors ($k_{\text{core}} \neq k_{\text{clad}}$), which is necessary condition for modes not couple to each other.

Let's now look at the transverse phase and the approach to minimizing the coupling between two modes. We consider the dot product, overlap integral in other words, between the shell mode and the core mode and represent it in the following form:

$$\langle \psi_{\text{core}} | \Delta n^2 | \psi_{\text{clad}} \rangle = \sum_p \Delta n^2 \langle F_{\text{clad}}(r) | a_p(r) | F_{\text{core}}(r) \rangle \langle e^{i\phi_{\text{clad}}} | e^{im\theta} | e^{i\phi_{\text{core}}} \rangle \quad (2.27)$$

Here, we have introduced a radial index m to be able to write the scalar product

of the two modes as a combination of separable radial and azimuthal functions. This shows that reducing this scalar product would amount to minimizing any of the integrals:

$$\propto \iint F_{\text{core}}(r) \times F_{\text{clad}}(r) r dr d\theta \quad (2.28)$$

$$\propto \iint e^{i(\phi_{\text{clad}} - \phi_{\text{core}})} r dr d\theta \quad (2.29)$$

We introduce the local azimuthal index m , in order to put the key parameters in control of these integrals and write in the same manner as before, $e^{i\phi(r,\theta)} = \sum_m A_m R(r) e^{im\theta}$. Where A_m - constant and R - complex function dependent on r . Thus, the coverage integral reduces to a linear combination of integrals of the form:

$$\int_0^\infty R_{\text{core}}(r) R_{\text{clad}}(r) r \int_0^{2\pi} A_{m_1} A_{m_2} e^{-i\Delta m \theta} \quad (2.30)$$

where $\Delta m = m_{\text{clad}} - m_{\text{core}}$. There is two possible ways to make this integral approach zero. The one is to reduce spatial modes overlap listed $R_{\text{core}}(r)$ and $R_{\text{clad}}(r)$. The other is to obtain maximum possible phase mismatch, in other words, maximising Δm . Core mode usually considered as Gauss mode profile without azimuthal structure ($m = 0$), therefore maximising Δm also means maximising $m_{\text{clad}} = m$, it can be related with physical parameters of cladding as previously introduced in equation (1.2) in chapter 1.

The expression shows that as the length of the silica bridges increases and their thickness decreases, the transverse phase mismatch becomes more pronounced as we discussed in chapter 1. And the reduction of functions radials is ensured by working in the normalized high frequency regime $k\Lambda$ in other words in the large pitch regime (so that cladding modes strongly localised in silica)[14].

Also, the curvature makes it possible: to constrain the core mode to the hollow medium and to move it away from the cladding modes; to minimize the spatial overlap of the core mode with the silica pads of the contour of the core associated with a low azimuthal number, therefore a source of coupling and losses; to increase the value of one of the key geometrical parameters, L , which is found in the expression of the azimuthal number m [24]. For this last point, the increase in the curvature of the arches of the contour of the core implies an increase in the perimeter L and consequently an increase in m . Whilst these principles of IC guidance and the criteria for decreasing the IC fibers transmission loss are now known, there is thus far no analytical or semi-analytical expressions for core and cladding modes coupling. This, in turn strongly limits the prediction power in designing IC fibers and the explanation of their characteristics

properties such as scaling of CL with wavelength or the polarization dependence in the coupling between core and cladding modes. The next section is then motivated by the desire to fill, at least in part, this lack.

2.2.5 Fourier Decomposition

In collaboration with Pr. Luca Vincetti [44] we extend this idea of the role of m which was mentioned above and how to increase it using a semantically model. For that, we propose and develop an analysis method based on the azimuthal Fourier decomposition (AFD) of the fiber's modes. The AFD is a methodology based on Fourier analysis that can be used to decompose the fiber's modes along some specific elements of interest, such as the perimeter of the tubes composing the cladding of tubular lattice fiber (TLF) (see Fig. 2.11 (a)). Indeed, the latter and the knowledge of the expressions of a single tube dielectric modes [74] make such kind of fiber an ideal platform to develop such analytical or semi-analytical models of IC guidance.

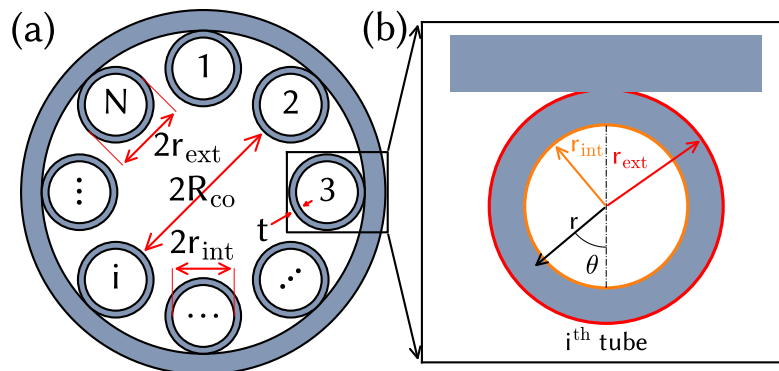


Figure 2.11: (a) Cross section of a 8 tubes TLF. (b) Local polar coordinated system (r, θ) centered at the center of the tube i -th. Red and orange lines highlight the outer and inner tube boundaries respectively.

In the context of the single isolated tube approximation, we consider a single tube with a local polar system (r, θ) with the origin at the center of the tube [75], as shown in Fig. 2.11 (b). Each component (radial, azimuthal and longitudinal) of core mode (CM) and cladding modes (CLM) electric fields is a periodic function of θ and thus representable in terms of an azimuthal Fourier series [76]:

$$E_{\text{co}_s}(r, \theta) = \sum_{m_{\text{co}}=-\infty}^{+\infty} (R_m^{\text{co}_s}(r) \cdot e^{jm_{\text{co}}\theta}) \quad (2.31)$$

$$E_{\text{cl}_s}(r, \theta) = \sum_{m_{\text{cl}}=-\infty}^{+\infty} (R_m^{\text{cl}_s}(r) \cdot e^{jm_{\text{cl}}\theta}) \quad (2.32)$$

where $s = r, \theta, z$, m is the azimuthal Fourier index, and

$$R_m^{\text{co/cl}_s}(r) = \frac{1}{2\pi} \int_0^{2\pi} E_{(\text{co/cl})_s}(r, \theta) e^{-jm_{\text{co/cl}}\theta} d\theta \quad (2.33)$$

Figure 2.12 shows an example of these Fourier Azimuthal Spectra hereinafter just “azimuthal spectra” $R_m^{\text{co}_r}(r)$, $R_m^{\text{co}_\theta}(r)$ of the radial and azimuthal component of the y-polarization of FM core mode computed at the inner ($r = r_{\text{int}}$) and outer ($r = r_{\text{ext}}$) boundaries of the tube numbered 1 in Fig. 2.11 (a). The spectra show a “low pass” feature since not negligible coefficients are observed only for low values of m_{co} . For $m_{\text{co}} = 0$, the radial component has its maximum, whereas the azimuthal one has a zero because of the odd symmetry.

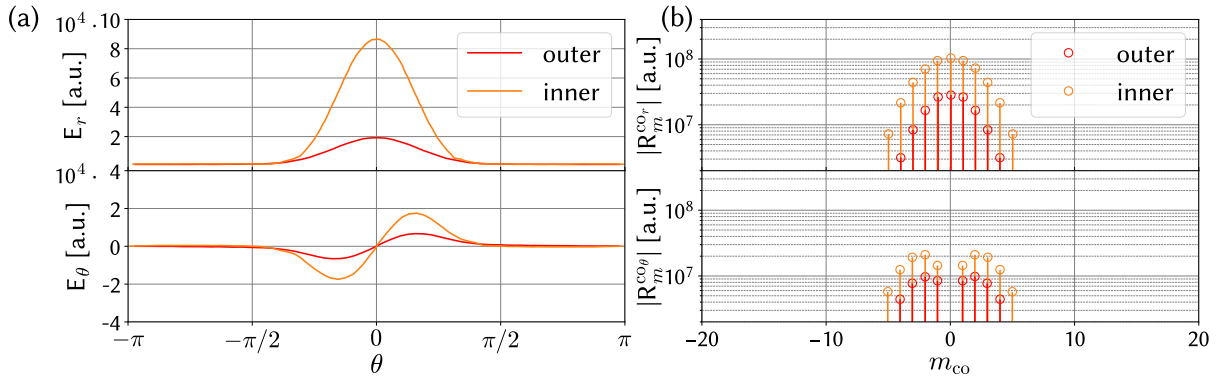


Figure 2.12: Fundamental core mode. Left: radial E_{co_r} (top) and azimuthal E_{co_θ} (bottom) electric field components along the inner (orange) and outer (red) tube boundaries. Right: modulus of the corresponding azimuthal spectra.

According with coupling mode theory, the loss due to the coupling between a core and a cladding leaky mode can be estimated as [77], [78]:

$$\Delta\alpha_p^{\mu,\nu} \propto A \frac{|K_p^{\mu,\nu}|^2}{\Delta\beta^2} \quad (2.34)$$

being $\Delta\beta = \frac{2\pi}{\lambda} (n_{\text{eff}_{\text{CM}}} - n_{\text{eff}_{\text{CLM}}})$ the constant phase difference and (μ, ν) respectively the azimuthal and radial indexes of the considered CLM ($p = \text{HE}, \text{EH}$). By taking into account the avoid crossing in the dispersion curve [77]:

$$n_{\text{eff}_{\text{CM}}} - n_{\text{eff}_{\text{CLM}}} \simeq \Delta n + \delta(F - F_{c_p}^{\mu, \nu}) \quad (2.35)$$

being F - normalized frequency, $F_{c_p}^{\mu, \nu}$ the phase matching frequency approximated with the cut-off one of CLM, Δn the effective index difference at phase matching frequency due to the avoid crossing, and δ the difference between the two dispersion curve slopes. Even though the values of Δn and δ should be set for each CLM, in this work for sake of simplicity, the following values have been used: $\Delta n = 1.7 \cdot 10^{-6}$ and $\delta\nu = \nu \cdot \delta_0$ with $\delta_0 = 5 \cdot 10^{-3}$. Finally, by taking into account all CLMs we can estimate the CL as (for more details about the equations and simplifications see our paper [79]):

$$\text{CL}(F) = A \sum_{\mu, \nu, p} \frac{|A_p^r R_{\mu}^{\text{co}_r}(r_{\text{int}}) + A_p^{\theta} R_{\mu}^{\text{co}_{\theta}}(r_{\text{int}})|^2}{(\Delta n + \delta_{\nu} (F - F_{c_p}^{\mu, \nu})^2)^2} \quad (2.36)$$

Here A is a global fitting constant, A_p^r and A_p^{θ} represents the azimuthal Fourier coefficient for the radial and azimuthal components of the CM, $R_{\mu}^{\text{co}_r}(r_{\text{int}})$ and $R_{\mu}^{\text{co}_{\theta}}(r_{\text{int}})$ are the azimuthal spectra of the radial and azimuthal component of the y-polarization of CM computed at the inner (r_{int}) boundaries of the tube, respectively.

Figure 2.13 compares the numerical results of the y-polarization FM CL of fiber (with parameters $t = 750$ nm, $r_{\text{ext}} = 6$ μm , $R_{\text{co}} = 13.6$ μm and $n_{\text{gl}} = 1.45$) with that obtained from eq. 2.36. Despite the approximations applied (computed only for 2 tubes of T8 TLF at $r = r_{\text{int}}$ from eqs. (8, 9) of [79]), the agreement is quite good in particular in describing the high loss regions' edges. The worst accuracy concerns the first transmission band because the corresponding very long wavelengths make less accurate the single isolated tube approximation. These results were submitted in 2022 [79]. Finally, this method could be used as an useful and effective theoretical tool for analyzing the impact of fiber non-idealities on the loss enhancement in real TLFs. The application of the approach for analyzing the impact of a non-constant thickness along the tubes perimeter has started to be studied and results have been submitted [80].

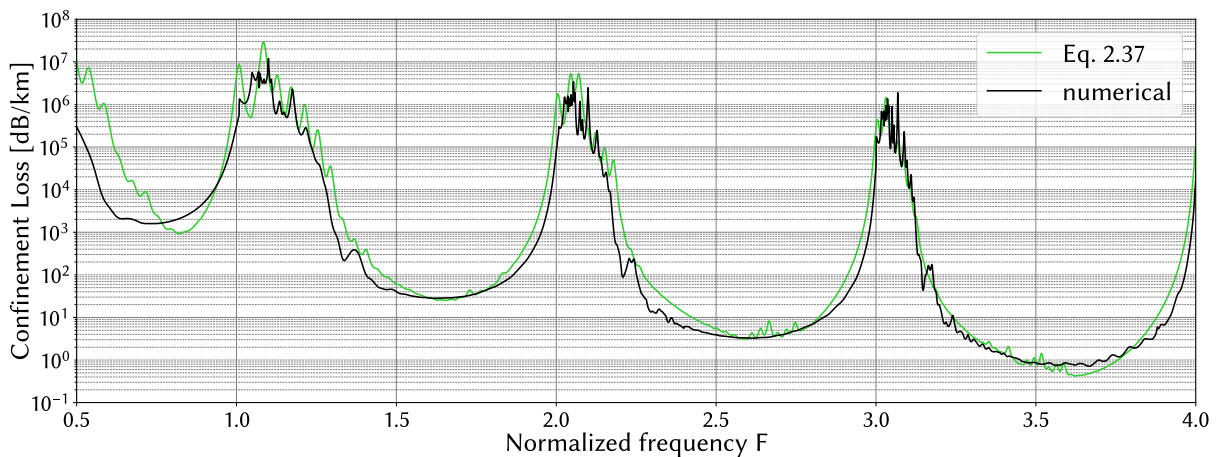


Figure 2.13: Comparison of CL spectrum of T8 TL HCPCF obtained with numerical simulation with $t = 750$ nm, $r_{\text{ext}} = 6$ μm , $R_{\text{co}} = 13.6$ μm , $\rho = 0.875$ and $n_{\text{gl}} = 1.45$ (black) and with Eq. 2.36 (green).

2.3 Conclusion

In this chapter, we have explored various numerical analysis methods, including the plane wave method, multipole method, finite difference method, and finite element method, to understand their applications in HCPCF. We delved into mode solving using FEM, examining the physics interface equations, eigenvalue problem, and mode analysis. To optimize simulations, we discussed the significance of geometry, symmetry, meshing, and mode recognition. Lastly, we analyzed two critical design concepts: photonic band gap and inhibited coupling.

By integrating our previous findings with new insights, we have demonstrated that the finite element method is a powerful tool for solving complex problems in HCPCF. The optimization techniques and design concepts discussed in this chapter can significantly enhance the performance and capabilities of these fibers as it will be now developed in chapter 3. Also, this deeper understanding of HCPCF will contribute to the development of cutting-edge technologies in many different applications. This will be used to tackle the surface roughness issue on HCPCF in chapter 4.

Finally, notice that despite that demonstrated method is a powerful tool it is still limited by two dimensions approximation. This will be discussed later on chapter 5 with the introduction of a (2D+1) model.

Chapter 3

Modeling of new designs of HCPCF for singlemodeness and ultra low loss

IN this chapter, the modeling of novel HCPCF designs with a primary emphasis on achieving a balance between ultra-low confinement loss and single-mode guidance is presented. The design approach involves the development of three distinct fiber designs, namely the hybrid Kagome, Snowman, and hybrid PBG fibers, each capitalizing on a fusion of diverse cladding structures and guidance mechanisms. The outcomes of these designs reveal up to four orders of magnitude enhancement in light confinement, coupled with unprecedented single-mode guidance capabilities when compared to the existing state-of-the-art HCPCF. Furthermore, the fabrication of two of these fibers has provided solid confirmation of the immense potential inherent in this innovative approach.

Table of content

3.1	Introduction	65
3.2	Design rationale	65
3.3	Design #1: hybrid Kagome	67
3.3.1	Performance of ideal design	67
3.3.2	Fabrication and characterisation of the fiber	74
3.4	Design #2: snowman	77
3.4.1	Performance of ideal design	78
3.4.2	Preliminary results of fabrication	81
3.5	Design #3: hybrid PBG	82
3.5.1	Performance of ideal design	83
3.6	Conclusion	86

3.1 Introduction

Throughout the historical development of HCPCFs, CL has stood out as the primary driving factor in their design. This focus on CL stems from its role as a robust indicator of the scientific validity of the guidance mechanism, whether based on PBG or IC principles. Consequently, since the inception of HCPCF research, substantial efforts have been devoted to understanding the underlying physics that govern guidance within these dielectric structures. These efforts have predominantly centered on minimizing CL, as it provides invaluable insights into the confinement of light within HCPCFs and lends credibility to various hypotheses. As a result of this effort, remarkable progress has been made in recent years, culminating in HCPCFs achieving CL values that are now comparable to those of conventional solid-core fibers, as presented in chapter 1. This accomplishment reflects the advancements made in HCPCF technology, positioning it favorably alongside its conventional counterparts.

However, this achievement came at the expense of other important performance indicators of an optical fiber, such as polarization maintenance, bend loss characteristics, and, notably, modal content. Particularly, IC HCPCFs have traditionally exhibited multimodal behavior, with no design hitherto achieving the sought-after objective of single-mode operation. This chapter is devoted to tackling this challenge through the exploration of an innovative approach that involves the amalgamation of various cladding structures.

3.2 Design rationale

Rigorously speaking, in IC-guiding fibers, single modedness is impossible because of the ubiquitous presence of higher-order modes in the fiber core. Indeed, because of the “gapless” nature of IC fiber’s cladding modal spectrum, one cannot use the concept of “cut-off wavelength” that is commonly used in conventional TIR fibers, which consists of reducing the effective index depth of the PBG so to allow a “index-bandwidth” to a single core mode. However, one can get closer to a truly singlemode operation if the loss extinction ratio between the lowest loss mode (typically, the core fundamental mode LP_{01}) and the second-lowest loss mode (typically LP_{11}) is sufficiently high. This was successfully achieved in six-tube single-ring (SR) tubular lattice (TL) HCPCFs thanks to the adequate ratio between the core and lattice tube diameters, $d_{\text{tubes}}/D_{\text{core}}$, to provide effective refractive index matching between the LP_{11} -like modes of the core (which are usually the main contaminating higher-order mode in the fiber modal content) and the

fundamental LP_{11} -like mode of the lattice tubes [81]–[83]. The Fig. 3.1 illustrates this effect where the coupling (between electromagnetic modes, i.e. HE_{11} and HE_{21}) is calculated to be maximized when ratio $d/D = 0.68$.

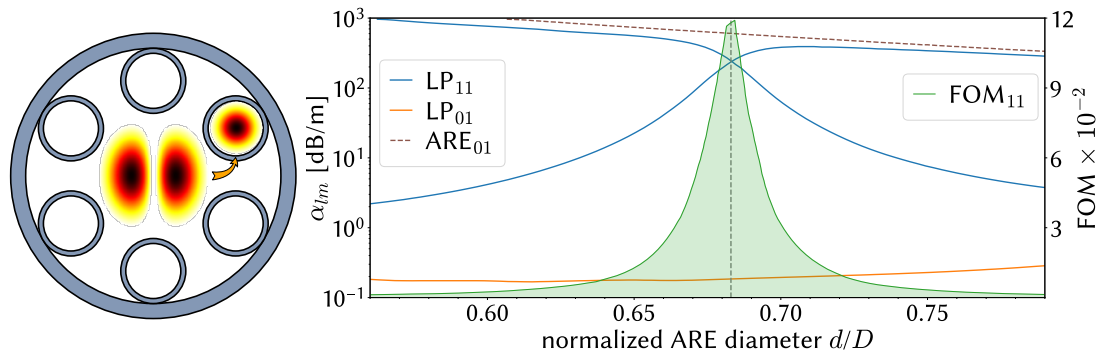


Figure 3.1: Demonstration of the coupling between LP_{11} -like of core to LP_{01} of tubes in T6 TLF design (left). Phase matching condition given by [83] (right).

However, this approach comes with a cost of high CL of T6 SR-TL HCPCF, typically ~ 500 dB/km at 1 μm for the fibers reported in the literature [84]. Other designs may have lower loss, despite this, the ratio of loss values between the fundamental and LP_{11} -like core modes is much lower than for the T6 SR-TL HCPCFs.

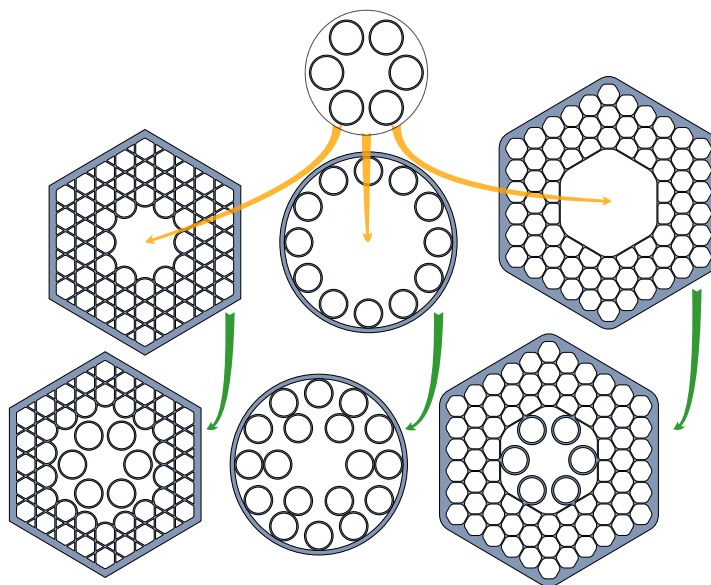


Figure 3.2: Illustration of the fiber design rationale proposed for single modedness and ultra low loss based on a hybrid fiber design made of Kagome and tubular cladding lattices.

In order to have best of two worlds, meaning achieving effective single-mode

operation and ultra low loss, we apply a novel approach patented by our group through number FR1912283 [85]. The core idea is to use two IC claddings to allow a decrease in CL while keeping the fiber core demarcated by a six-tube tubular lattice for effective single-mode operation. Fig. 3.2 illustrates schematically the principle for three fiber designs (see following sections), and which consists of integrating the T6 SR-TL as an inner cladding of the desired HCPCF, while the outer cladding could be made of Kagome lattice, another tubular lattice or even a PBG cladding lattice.

3.3 Design #1: hybrid Kagome

Figure 3.3 schematically depicts a cross-section profile of the HCPCF design for an ideal Hybrid Kagome structure. The fiber comprises an inner cladding composed of six isolated tubes, similar to the T6 SR-TL HCPCF, and an outer cladding constructed with a Kagome lattice structure. It's important to note that in this “ideal” configuration, the inner cladding tubes are suspended without attachment, although this may not be realistically achievable in fabrication. This design is studied to explore the feasibility of combining single-mode operation and achieving ultra-low CL [86].

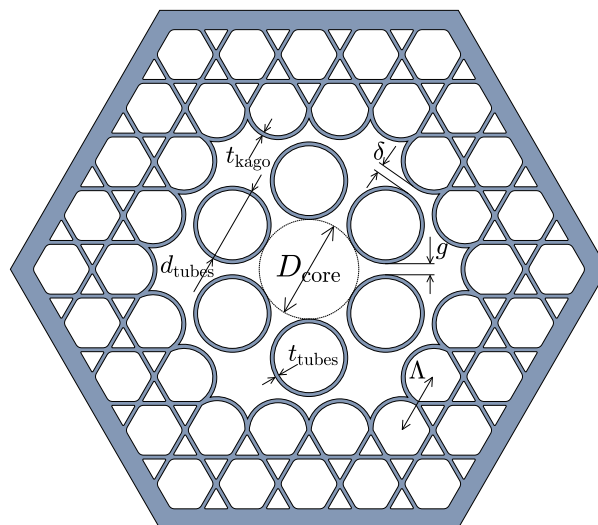


Figure 3.3: Cross-section profile of a hybrid Kagome HCPCF design

3.3.1 Performance of ideal design

The novel hybrid Kagome tubular (HKT) fiber design is numerically studied in this section by using the simulation tools developed in chapter 2. These calculations will allow us

to understand how to enhance the confinement capabilities when combining two IC cladding architectures but also found trade-offs which need to be considered for the fabrication process. For that, we start our analysis by considering an ideal version of the HKT HCPCF in which the tubular and Kagome lattices are not physically connected. Even though the ideal structure is unrealistic, this version acts as a pedagogical and pre-design tool that reveals the most important design elements and physical aspects of the proposed fiber architecture. The effect of the number of Kagome cladding layers, the impact of different thickness between the inner and outer claddings and finally the addition of connection between these two claddings are studied.

Confinement loss

• Impact of second cladding

In these simulations the core diameter (D_{core}), the distance between the cladding tubes (g), the distance between the tubular and Kagome lattices (δ), the Kagome cladding pitch (Λ), the curvature parameter (b , which indicates circular shaped boundary arcs), and the tube and Kagome lattice thicknesses (t_{tubes} and t_{kago}) were kept constant. In table 3.1 listed used dimensions for mentioned parameters.

Table 3.1: Table with geometrical parameters for HKT in Figure 3.4.

D_{core} , [μm]	g , [μm]	δ , [μm]	Λ , [μm]	t_{tubes} , [μm]	t_{kago} , [μm]	b	ξ
33.5	4.67	1.59	19.46	1.1		1	0 – 2

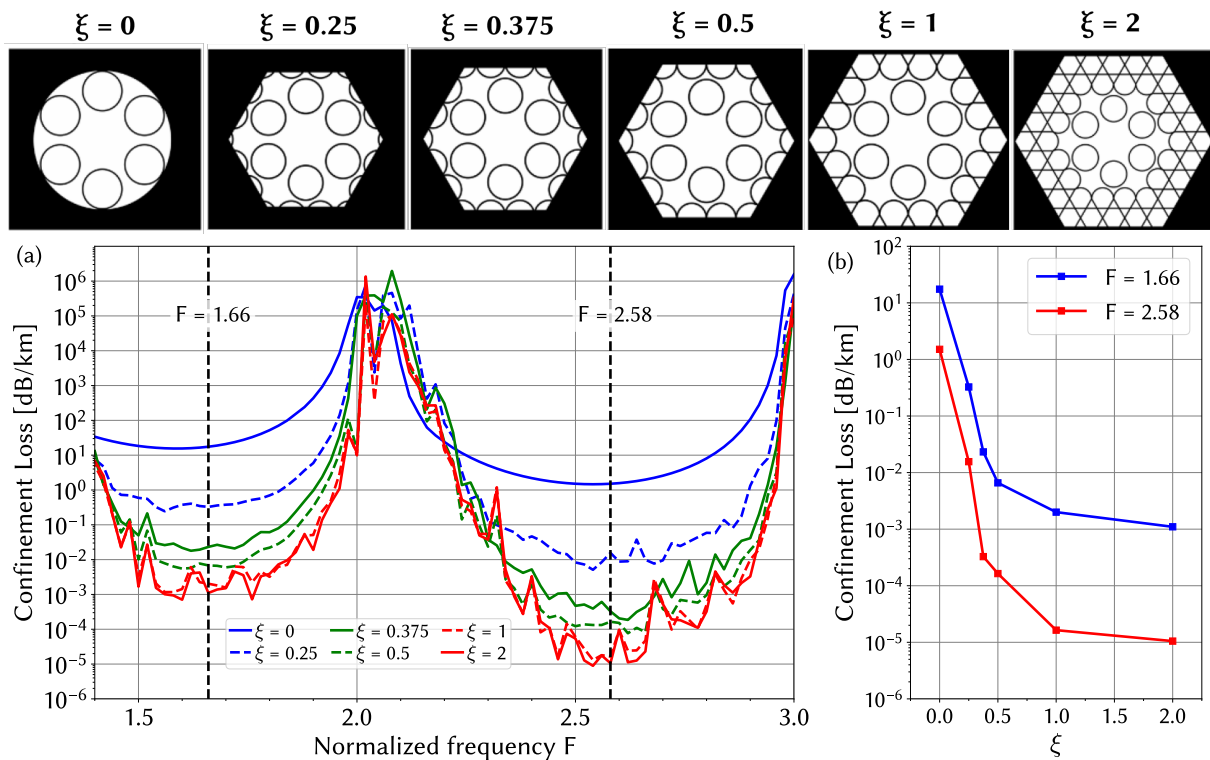


Figure 3.4: Study on the effect of adding the Kagome lattice around the tubular lattice in the HKT HCPCF design. (a) CL simulation results for fiber designs with different ξ values (see text for the definition). (b) CL values for two selected normalised frequency (F) values.

Figure 3.4 shows the CL when considering a 6-tube lattice structure and sequentially adding the Kagome structure around the tubular cladding layer by layer. For simplicity, we define a parameter ξ as the ratio between the thickness of the considered outer cladding in the simulations and the Kagome cladding pitch. In our analysis, ξ is varied from 0 (no Kagome cladding) to 2 (Kagome lattice composed of two rings of tubes), and the calculated CL values are presented in Fig. 3.4 (a). Figure 3.4 (b) shows the CL values for two representative normalised frequency values ($F = 1.66$ and $F = 2.58$).

The effect of adding the Kagome cladding on the CL drop rate is extremely drastic between $\xi = 0$ and $\xi = 0.5$ and gentler for $\xi > 1$. At $F = 1.66$, the CL is calculated to be 17.4 dB/km when $\xi = 0$ and $6.5 \cdot 10^{-3}$ dB/km when $\xi = 0.5$. At $F = 2.58$, the CL accounts for 1.5 dB/km when $\xi = 0$ and $1.6 \cdot 10^{-4}$ dB/km when $\xi = 0.5$. When $\xi = 1$ and $\xi = 2$, a further decrease, but at a slower rate, is observed in the CL values. At $F = 1.66$, the CL is calculated as $1.1 \cdot 10^{-3}$ dB/km when $\xi = 2$. At $F = 2.58$, the CL is calculated as $1.0 \cdot 10^{-5}$ dB/km when $\xi = 2$. Here, it is worth-noting that having a Kagome cladding formed by more than two rings of tubes (i.e., having $\xi > 2$) entails a marginal decrease in the CL. Indeed, while adding more cladding layers improves the confinement of the core

mode, it also leads to more cladding modes which the core mode is weakly coupled to. Therefore, the best CL is achieved by carefully balancing the number of photonic states in the cladding and the strength of confinement of the structure.

The CL of this optimized HKT HCPCF was then compared in Fig. 3.5 to three fibers made by the elements constituting the bases of the hybrid cladding and having the same core inner diameter ($35\ \mu\text{m}$), t ($1100\ \text{nm}$), and n_g (1.45). The first design (FD #1, purple line) consists of a jacketless 6-tube lattice structure whose minimum CL values are approximately $1650\ \text{dB/km}$, $20\ \text{dB/km}$, and $3\ \text{dB/km}$ in the fundamental, first-order, and second-order transmission bands, respectively. The second design (FD #2, green line) reproduces a 6-tube lattice SR-TL HCPCF. The results show that jacketing the suspended tubes impacts the CL spectrum mildly, with an increase in the above loss figures to approximately $1900\ \text{dB/km}$, $40\ \text{dB/km}$, and $5.5\ \text{dB/km}$, respectively. The third design (FD #3, blue line) is Kagome lattice HCPCF showing minimum CL figures around $440\ \text{dB/km}$, $50\ \text{dB/km}$, and $30\ \text{dB/km}$ in the three first transmission bands. We note for this fiber the oscillating structure in the CL spectrum due to connecting struts or nodes [13], which can either locally increase or decrease the CL compared to FD #1 and FD #2. Finally, the HKT HCPCF we propose herein is identified as FD #4. Although this is not a feasible fiber design, it communicates the potential of this novel design to achieve impressively low CL values - as low as $0.35\ \text{dB/km}$, $7 \cdot 10^{-5}\ \text{dB/km}$ and $8.6 \cdot 10^{-6}\ \text{dB/km}$ for wavelengths within the fundamental, first-order, and second-order transmission bands, respectively. It is noteworthy that the two latter values for this ideal structure are well below the current attenuation level of solid-core fibres, represented by the green dashed line in Fig. 3.5. Additionally, there is an expressive difference of five orders of magnitude between the CL of this new hybrid fiber and those calculated for the other designs.

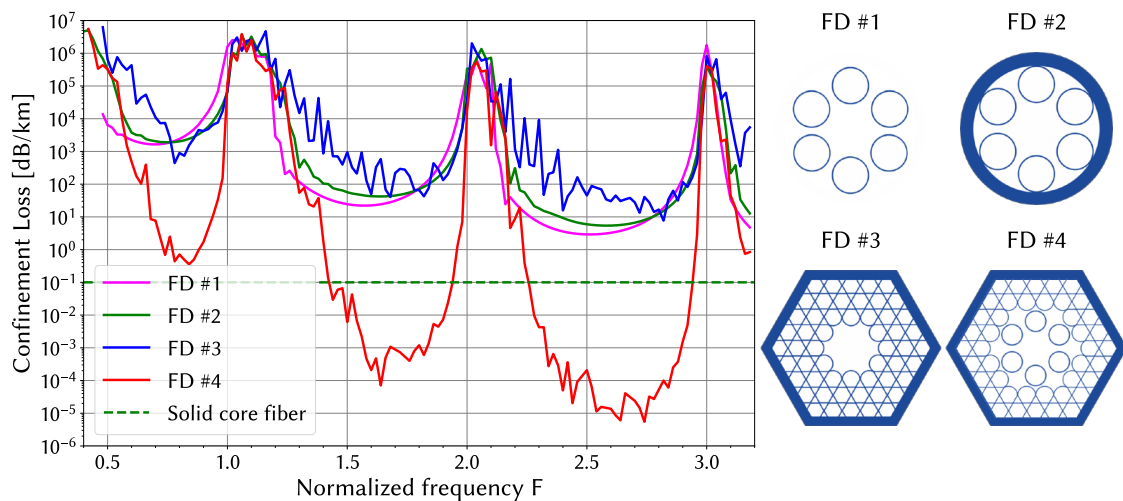


Figure 3.5: CL simulation results for different fiber designs. FD #1: jacketless tubular lattice; FD #2: jacketed tubular lattice; FD #3: Kagome lattice; FD #4: hybrid lattice. A comparison with solid-core fiber is added.

• **Impact of different thickness between t_{tubes} and t_{kago}**

The influence of varying the thickness of two claddings was also considered to anticipate the fabrication.

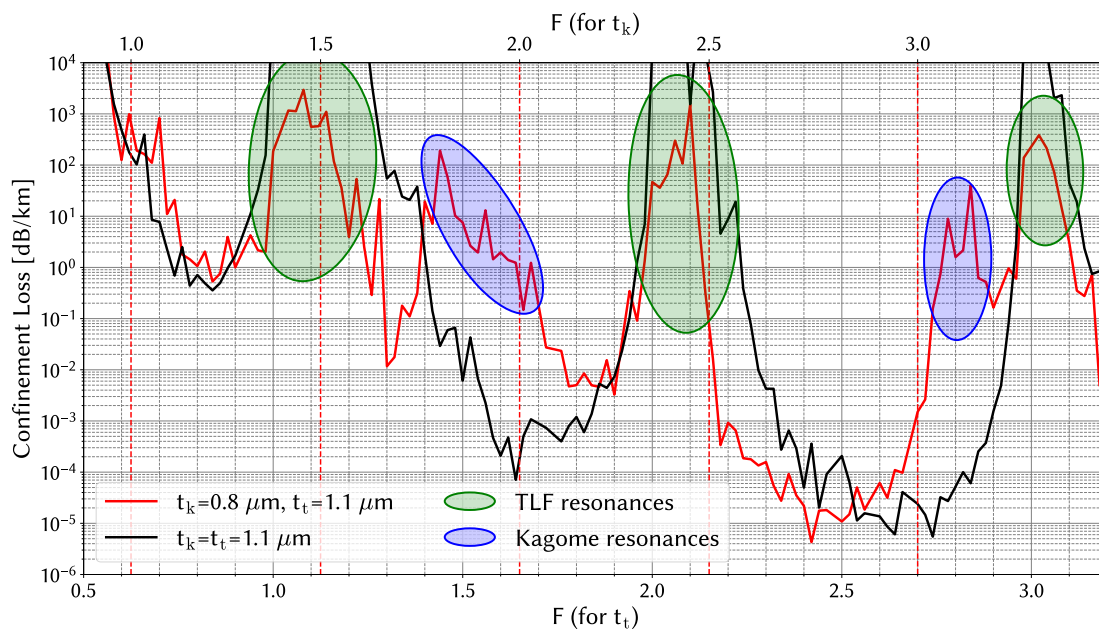


Figure 3.6: Effect on CL of having different glass thicknesses between the two cladding of HKT HCPCF.

Fig. 3.6 presents a comparison with the previous HKT HCPCF with a case where t_{kago} was reduced to 800 nm while keeping $t_{\text{tubes}} = 1100$ nm. As expected, multiple resonances appear in the different transmission bands which corresponds to the new cut-off wavelength positions according to the equation $F = \frac{2t}{\lambda} \sqrt{n_g^2 - 1}$. It also degrades the CL which is strongly increased at certain frequency by more than 4 orders of magnitude as for $F = 2$. The transmission bands are then less clearly identified and can result in a shift towards shorter wavelengths. Although these thickness variations have negative consequences, for a judicious choice of values it can serve as a strategy to make polarization maintaining HCPCF as it was recently reported in [87].

• Impact of connection between the two claddings

While the ideal HKT HCPCF design has suspended inner cladding tubes (therefore, it is not feasible), a realizable version of the HKT HCPCF has then been considered. Different type of connections between the two cladding have been simulated as shown in Fig. 3.7. The first is a direct touch between cladding tubes and the Kagome lattice (B, blue line), the second corresponds to the insertion of a circular connecting tubes (C, brown line) and the third the same but with a rectangular shape (D, pink line). As thinner the connection tubes are, the lower the CL values will be, we choose connecting tubes with a thickness of 640 nm (i.e., 58% of the cladding struts and tube thickness) as a reasonable value considering the HKT HCPCF fabrication.

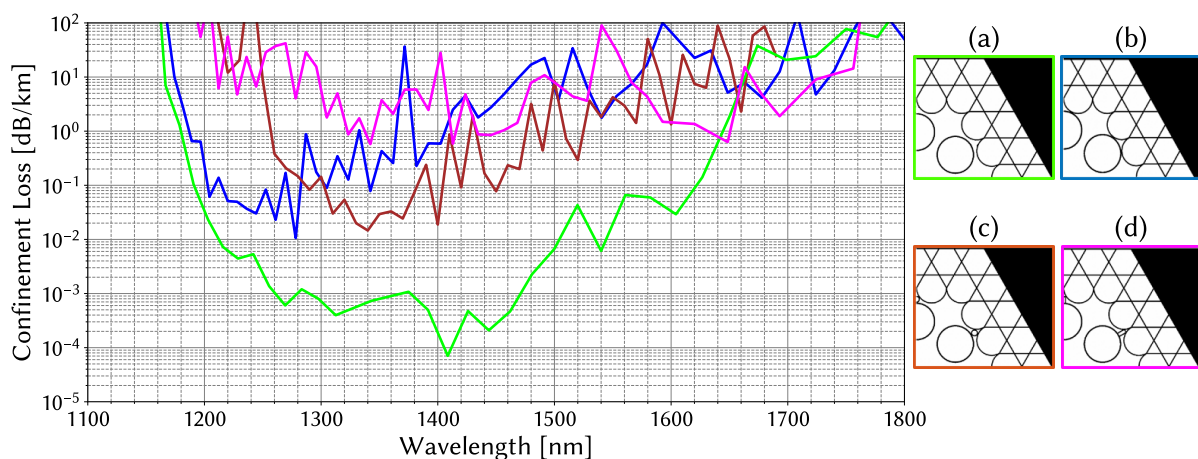


Figure 3.7: Fundamental mode CL simulation results for ideal and realizable hybrid fiber designs.

The results show that while the addition of the connections causes the CL to increase, the minimum CL of 10^{-2} dB/km in the telecom range remains reachable. Finally, the design using circular connecting tubes seems to be the best approach

for such wavelengths.

• State-of-the-art comparison

Finally, our HKT HCPCF was compared to the other state-of-the-art fiber designs. The Fig. 3.8 shows a comparative plot between the CL of the fundamental mode in the SR-TL HCPCF (I, dark green line), straight-bar (II, green line), nested-rod (III, grey line - [88]), conjoined tubes (IV, dark pink line - [28]), nested (V, pink line - [38]) and hybrid design proposed herein (VI and VII).

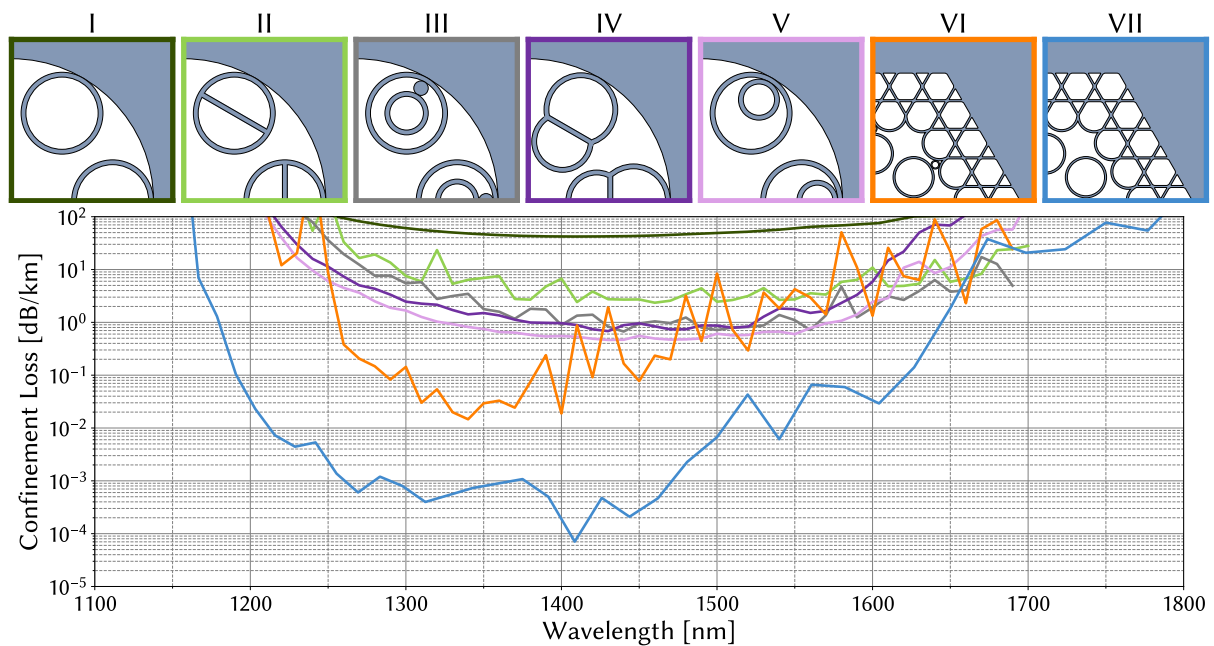


Figure 3.8: Fundamental mode CL simulation results for the (I) tubular, (II) straight-bar tubular, (III) nested-rod tubular, (IV) conjoined tubes, (V) nested tubular, (VI) hybrid with supporting tube and (VII) ideal hybrid fiber designs.

The data represent fibers with a core diameter of $30.5 \mu\text{m}$ and lattice tubes with an outer diameter and thickness of $22.1 \mu\text{m}$ and $1.1 \mu\text{m}$, respectively. In design V, the tubes in the second ring layer have a diameter of $26.4 \mu\text{m}$, and in designs II and IV, the nested tubes have a diameter of $12.17 \mu\text{m}$. The Kagome lattice pitch in designs VI and VII is set as $18 \mu\text{m}$. As seen in the plot, the improvement in performance is quite significant in comparison to other designs, with an improvement of around four orders of magnitude for the ideal case HKT HCPCF and with values 36 times lower for the realizable version.

Singlemode guidance (HOMER)

The higher-order mode (HOM) extinction ratio (HOMER) is a key metric that is used to evaluate the performance of optical fibers. It is defined as the ratio of the power of the HOMs to the power of the FM (the lowest loss mode):

$$\text{HOMER} = \frac{\alpha_{LP_{11}}}{\alpha_{LP_{01}}} \quad (3.1)$$

A high HOM extinction ratio means that the power of the HOMs is much lower than the power of the FM, resulting in a more stable and reliable single-mode operation. This HOMER has then been calculated for all the previous fiber design and results plotted in Fig. 3.9. As expected from our approach, the new hybrid design fiber demonstrates a high HOMER closed to 10^4 (value superior to 3 orders of magnitude compared to the nested and conjoined fibers), which confirms its improved single-mode behavior.

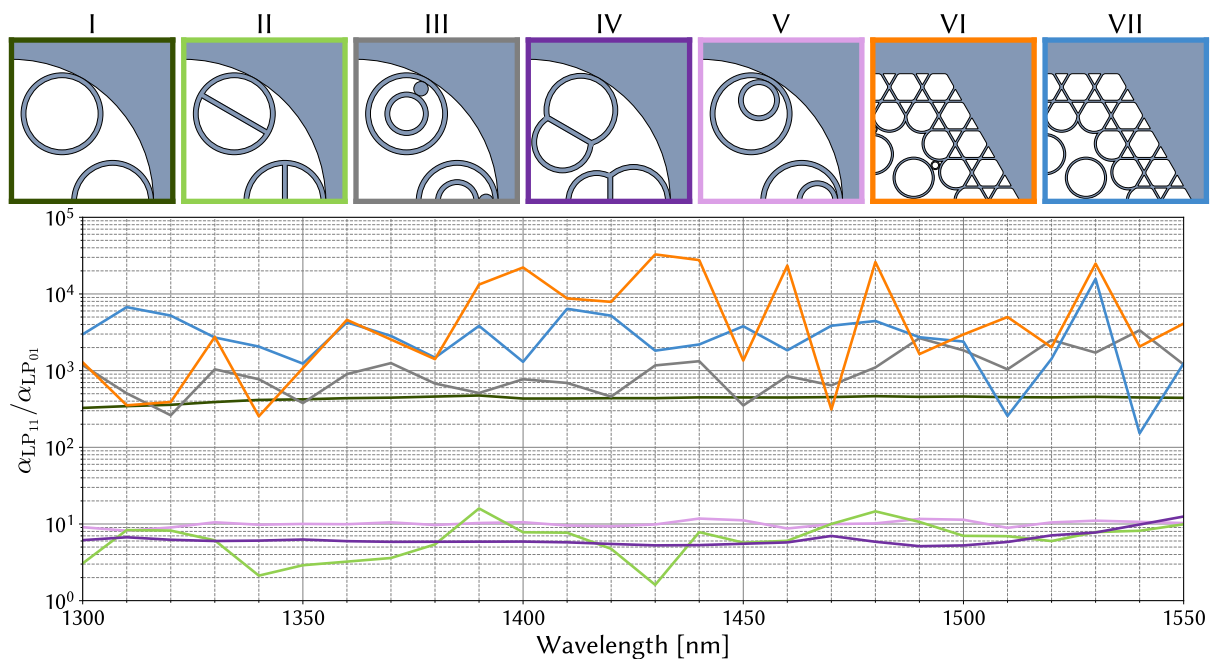


Figure 3.9: HOMER vs wavelength for the different studied fiber designs.

3.3.2 Fabrication and characterisation of the fiber

Due to the theoretical performances demonstrated, the fabrication of such HKT HCPCF has been investigated. The fiber was made by the stack and draw process and by using delicate strategies to independently pressurize the different air-holes sections,

i.e. hollow-core, connecting tubes and the two claddings. Figure 3.10 (a) presents the experimentally achieved of the first HKT HCPCF. The inner cladding tubes have a thickness of $1.27 \mu\text{m}$ and the fiber core diameter measures $37.1 \mu\text{m}$. The ratio between the core and cladding tubes diameters ($d_{\text{tubes}}/D_{\text{core}}$) was optimized during fiber fabrication to provide optimum coupling between the LP_{11} mode guided in the core and the fundamental mode of the cladding tubes, as previously explained. In this fabricated fiber with $d_{\text{tubes}} = 23 \mu\text{m}$ the ratio $d_{\text{tubes}}/D_{\text{core}} = 0.62$. A zoom on the core/cladding interface shows that the Kagome lattice struts have a uniform thickness of 720 nm , and the supporting tubes have a thickness of 370 nm . The loss of the HKT HCPCF (black curve) was then measured from a cutback technique using 120 m and 4 m long fiber pieces. Figure 3.10 (b) exposes the results where a minimum loss figure of 1.6 dB/km at 1050 nm is obtained, which was at date a record. The figure also presents the simulated CL and total loss of the fundamental mode ($\text{TL} = \text{CL} + \text{SSL}$). SSL is the surface scattering loss which was estimated by using the equation 1.5 presented in chapter 1 with $\eta = 0.25 \cdot 10^{-2}$, F_{00} is obtained from numerical simulation and $\lambda_0 = 1700 \text{ nm}$. More details on the SSL implementation will be given in chapter 4, which were calculated by taking into account the experimental structure.

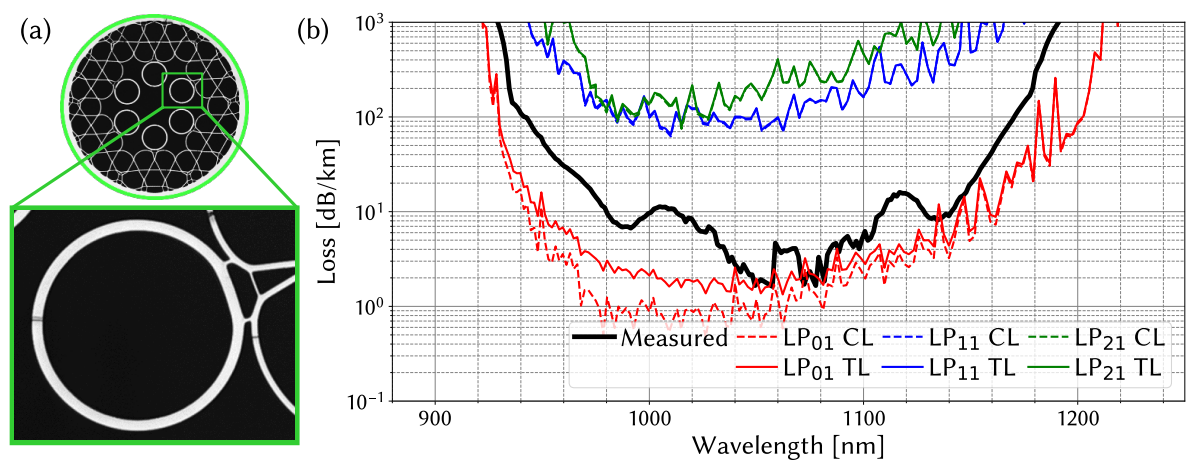


Figure 3.10: (a) Cross section of the fabricated hybrid Kagome-tubular HCPCF, with an enlarged view of the supporting tube region. (b) Cutback measurement results (black curve), simulated CL and TL for the fundamental mode (red dashed and red lines, respectively), and for the two first HOMs (blue and green lines).

Good similarity is observed between experimental and simulated data. The theoretical loss for the first HOM (electromagnetic modes of LP_{11} -like and LP_{21} -like mode, represented in blue and green respectively) was also studied. The HOM loss is found to be approximately two orders of magnitude higher than the loss of the fundamental mode, which suggests that quasi singlemode guidance could be achieved. To further

investigate it, we performed S^2 measurements¹ to assess the fiber modal content [89]. For optimized light launching conditions, the measurements show a HOM extinction ratio of 47 dB for a 10 m long fiber, which is a record-breaking result (see Figure 3.11 (a)). Finally, to show the fiber single-mode operation robustness, we examine the reconstructed near-field profile at the fiber output under different coupling conditions, i.e. by applying an offset in the input fiber position relative to the laser beam (here we used a laser at 1064 nm). The Figure 3.11 (b) shows a color map of the normalized power distribution with the associated near-field profiles in the insets (along the horizontal axis, along the vertical axis and at extreme positions). It is shown that over the $10 \times 10 \mu\text{m}^2$ area, the near-field profile remained fundamental-like with transmitted power higher than 60% of the maximum. All these results demonstrate the potential of our HKT design which provides a new path for the development of single modedness and ultra low loss HCPCFs, as illustrated by the comparative table 3.2.

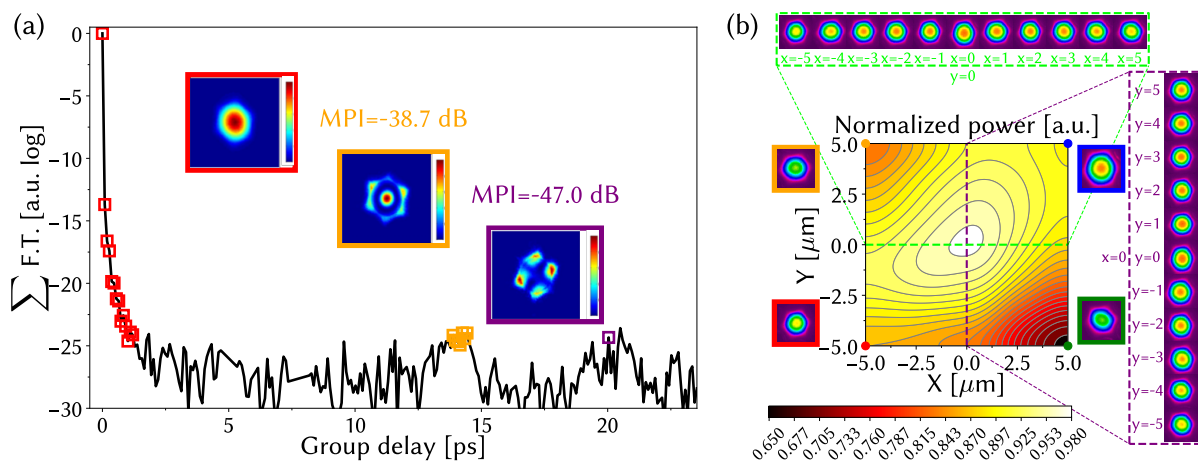


Figure 3.11: (a) S^2 measurement results for a 10 m long fiber. (b) Normalised power and near-field profiles at the fibre output at 1064 nm as a function of the input fiber offset.

¹Spatially and Spectrally resolved imaging of mode content in fibers, or more simply as S^2 imaging.

Table 3.2: Summary of the measured transmission loss figures and HOMER in representative HCPCFs.

Fiber design	Kagome lattice	SR-TL	Conjoined tube lattice	Nested tube lattice	HKT lattice
Minimum loss and working wavelength	8.5 dB/km @ 1030 nm [25]	500 dB/km @ 1000 nm (T6 TLF) [84] 7.7 dB/km @ 780 nm (T8 TLF) [90] 13.8 dB/km @ 539 nm (T9 TLF) [91]	2 dB/km @ 1512 nm [28]	0.28 dB/km @ 1550 nm [92] 2.5 dB/km @ 1000 nm [93]	1.6 dB/km @ 1050 nm [94]
Typical HOMER	20.2 dB for 5 m [25]	22.4 dB for 15 m (T8 TLF) [90]	>27 dB for 15 m [28]	~25 dB for 10 m [95]	47.0 dB for 10 m

Improvements to this first generation of HKT HCPCF to achieve lower transmission is now under consideration to achieve better control of the shapes and sizes of the connecting tubes between the tubular and Kagome lattices during the fiber draw. If this aspect can be obtained, a transmission loss reduction by more than one order of magnitude is expected at 1 μm . Also, by optimizing the thickness of the claddings and the core diameter, better losses than conjoined and nested fibers are expected in the telecom range as presented at the beginning. Moreover, further modifications to the fiber design, such as replacing some of the six tubes with others exhibiting different confining powers, will allow exploration of its potential as a polarization-maintaining waveguide.

3.4 Design #2: snowman

We've just seen that HKT HCPCF can for the first time combine single-mode operation and ultra low CL. However, the fabrication of such structure is complex and requires strong efforts to control all the parameters during the draw, which still in fact not completely reach. Then, an idea is to propose in parallel a second fiber design based on a more simple arrangement which can exhibits similar performances. To answer this call, we decide to investigate a design which consists to combine the previous

6 tubes ring to a second layer of tubular lattice as shown in Figure 3.12. For this configuration, 12 tubes are introduced of which one in two touches the first ring showing a pattern that resembles to a snowman (name that we decide to use). Compared to HKT HCPCF, the number of holes is then reduced by the half but more importantly the pressurization for the cladding can be made homogeneous which will reduce strongly the issue of inflation management.

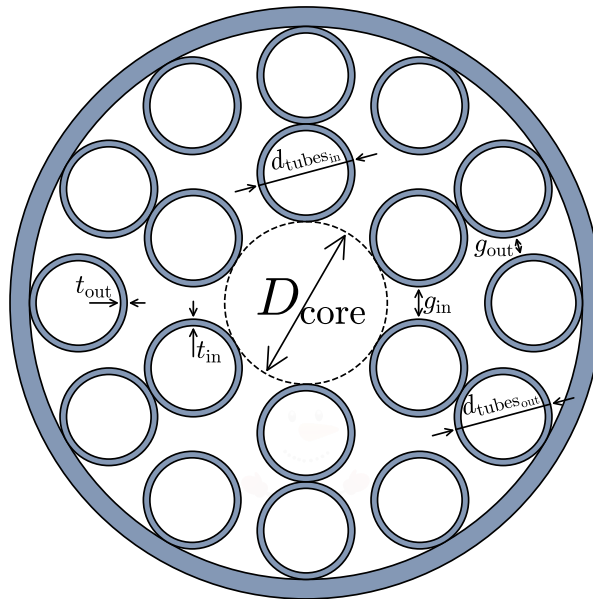


Figure 3.12: Cross section of the snowman fiber design with the associated geometrical parameters.

3.4.1 Performance of ideal design

A first set of simulations was carried out in order to compare the CL evolution of the snowman fiber versus the previous HKT HCPCF. The geometrical parameters were chosen to be as closed as possible between the fibers in term of core diameter, silica thickness and gap between of the holes. The table 3.3 summarizes the input data.

Table 3.3: Main geometrical parameters used for the snowman simulation in Fig. 3.13.

D_{core} , [μm]	g_{in} , [μm]	g_{out} , [μm]	$d_{tubes_{in}}$, [μm]	$d_{tubes_{out}}$, [μm]	t_{in} , [μm]	t_{out} , [μm]
31.86	7.025	4.349	17.268	17.128	1.1	

Notice that the ratio between the core and cladding tubes diameters ($d_{tubes_{in}}/D_{core}$) is

in this configuration complicated to set at 0.68. The impact on HOMER will be discussed later in this paragraph. The results are then plotted in Figure 3.13 with the ideal and realizable version of the HKT HCPCF. As expected, the curve of the snowman is closer the hybrid fiber with connecting tubes on the whole spectral range with a minimum in the telecom range around 10^{-1} dB/km.

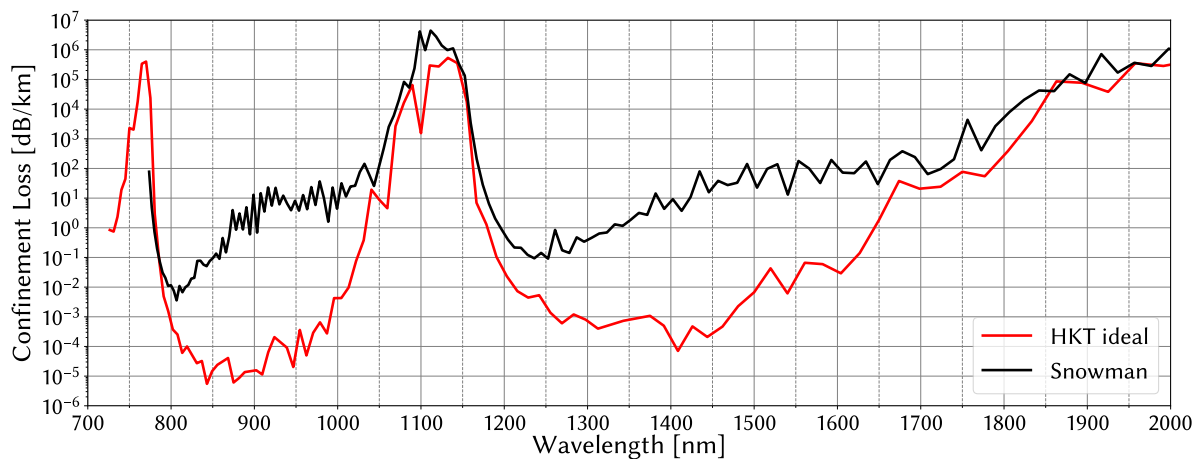


Figure 3.13: Fundamental mode CL simulation results for snowman fiber compared to the ideal HKT HCPCF.

A second run of simulations was made to cover a potential issue of fabrication. Indeed, usually during the fiber drawing process, melting-in of tubes in case of tubular lattice fibers is observed which might impact the performances. Geometrical parameters are listed in table 3.4. Two configurations were then studied. A first one corresponds to the ideal fiber case where we do not have overlap of the silica thickness between the two adjacent tubes and a second with overlap created at their outer silica lay interface as illustrated by Fig. 3.14 (a). This will also have the consequence to form a larger silica node which should supports more modes with low azimuthal number resulting in an increased of CL as discussed during chapter 1. The results plotted in Figure 3.14 (b) confirm this assumption with the minimum CL value increasing in the visible domain from 10^{-3} dB/km for no overlap to progressively up to the dB/km loss level when the overlap thickness is set to 30%. This evolution is found similar for the whole spectral range investigated. Also, more the overlap is, more pronounced the oscillations of the CL are.

Table 3.4: Main geometrical parameters used for the snowman simulation in Fig. 3.14 (b). Only parameters which are different from parameters in table 3.3 written here.

$D_{\text{core}},$ [μm]	31.86	31.868	31.9	31.978	32.05	32.13	32.236	32.368	32.528	32.69
$t_{\text{in}}, t_{\text{out}},$ [μm]	1.33									
$t_{\text{overlap}},$ [μm]	0	0.004	0.02	0.044	0.08	0.12	0.173	0.239	0.319	0.4

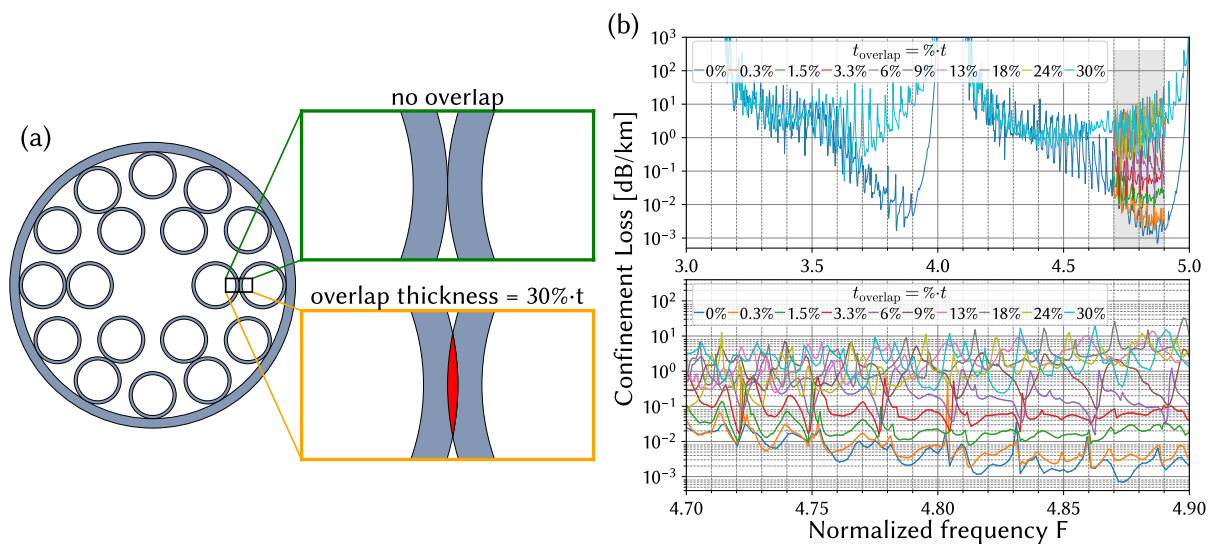


Figure 3.14: (a) Snowman fiber cross section with overlaps in red ovals and ideal design without overlap. (b) Corresponding evolution of CL for the fundamental mode for a set of overlap values ranging from 0 to 30%.

The field of the fundamental mode taken at $F = 4.87$ ($\lambda = 579.9$ nm) for the two extreme configurations, i.e. no overlap and 30% is shown in Fig. 3.15 (a) and (b) respectively which have $\Delta\text{CL} = 892$ dB/km, confirming that the contamination of loss is attributed to the expansion of the silica nodes. Hence, it is imperative to minimize this attachment during the fabrication process to mitigate the substantial increase in loss.

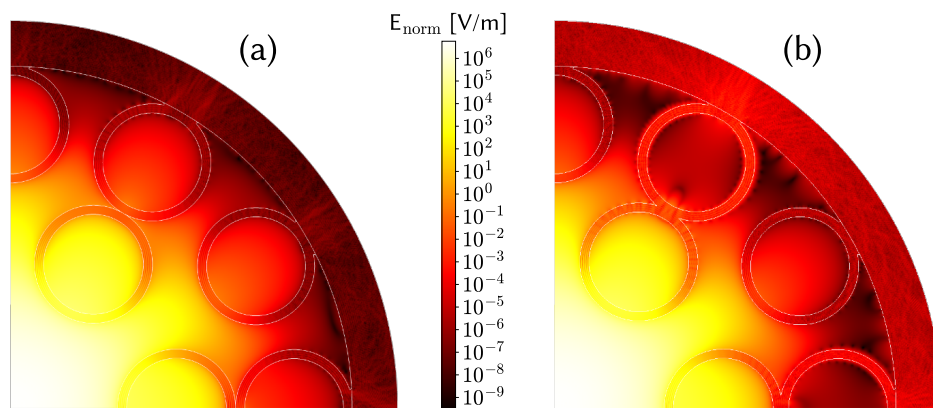


Figure 3.15: The fields of the fundamental mode at 579.9 nm for 0% (a) and 30% (b) overlap thickness cases are added. $E_{\text{norm}} = \sqrt{E_x \cdot E_x^* + E_y \cdot E_y^* + E_z \cdot E_z^*}$.

HOMER

Finally, the HOMER performance of this new fiber design is studied as before. The results for the ideal case (no overlap) and extreme overlap (30%) of the Snowman is plotted in Fig. 3.16 which demonstrate value lower than the ones achieved with the HKT HCPCF but still similar to the other competitive IC HCPCF for some wavelength ranges.

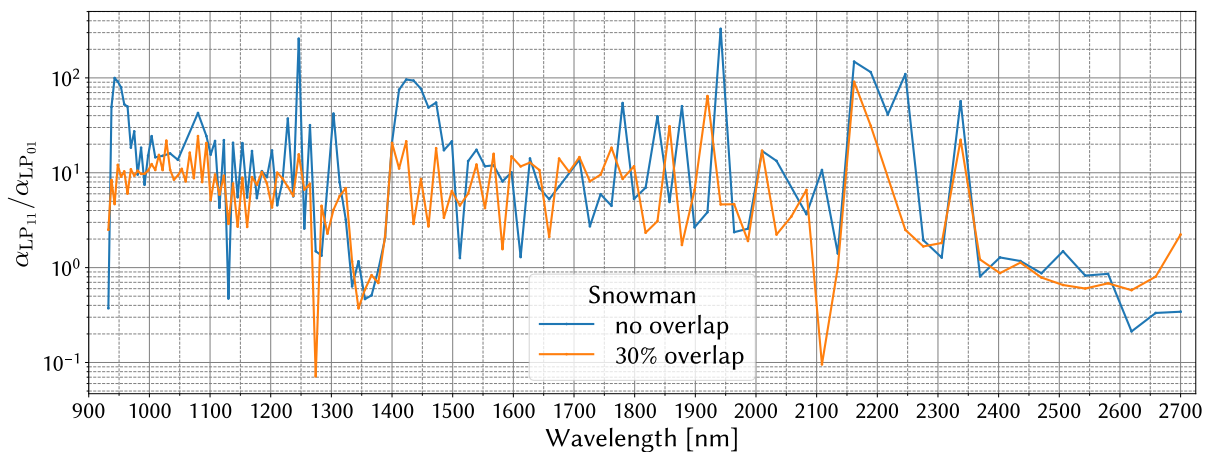


Figure 3.16: HOMER vs wavelength for the snowman fiber.

3.4.2 Preliminary results of fabrication

During the last months of my PhD, the fabrication of the snowman fiber began. A first realization is presented in Figure 3.17. The fiber has a core diameter of 33 μm , a

silica thickness of $1.33 \mu\text{m}$ which is almost similar for all the cladding tubes and a gap between the air-holes of the first ring of $5 \mu\text{m}$. A cut back was then made by using a 200 m long piece of fiber demonstrating losses around 50 dB/km in the telecom range with a minimum value of 20 dB/km around $1 \mu\text{m}$ and 800 nm. The CL simulations of the actual fiber profile are found in good agreement with the measure ones for the long spectral range (the difference for the shortest wavelength is attributed to the surface roughness, i.e. impact of SSL and MBL which are here not take into account and will be studied in the next chapter) and highlight the presence of strong oscillations in the spectrum. According to this, new fabrications are currently under progress by our group to improve these performances, especially by making a careful management of the holes overlap as it was anticipated. The linear characterizations in term of modal content and bending loss are also under investigations.

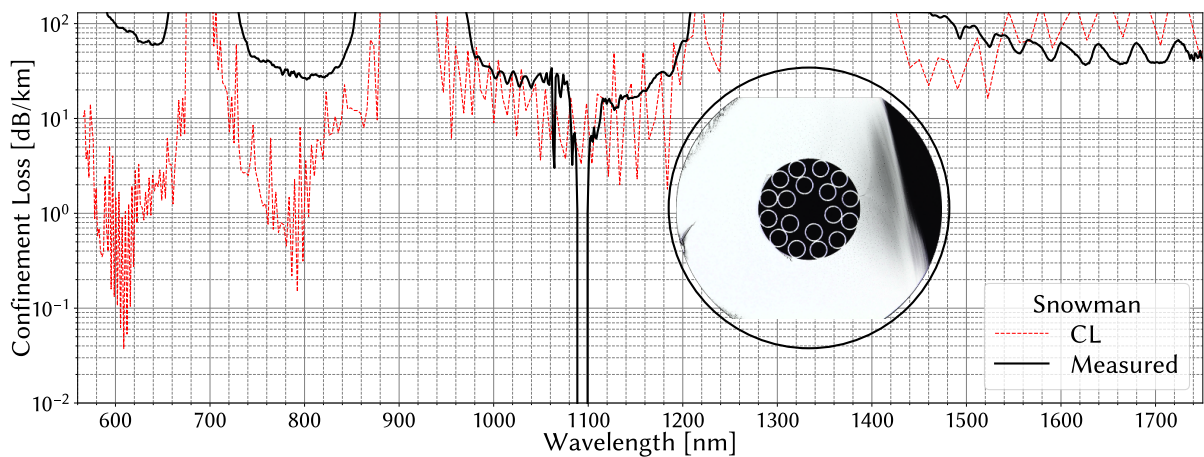


Figure 3.17: (a) Cross section of the fabricated snowman HCPCF. (b) Cutback measurement results (black curve) and simulated CL for the fundamental mode (red dashed and red lines, respectively).

3.5 Design #3: hybrid PBG

In this section, our previous idea to incorporate a IC tubular T6 ring for improving HOMER and reduce the optical overlap with the cladding is proposed into the second type of HCPCF, i.e. PBG as illustrated in Figure 3.18 with a comparison of a standard PBG HCPCF. This approach allows us to take advantage of the strengths of both guiding mechanisms, such as high resistance to bending in the case of the PBG lattice and improved single-mode operation and surface mode suppression in the case of the T6 fiber. Notice that improving on the PBG HCPCF single modedness has been already

investigated by using phase-matching coupling HOM to the cladding namely PRISM (for Perturbed Resonance for Improved Single Modedness) by Fini et al. in 2013 [96]). However, the loss was slightly degraded to 7.5 dB/km at 1590 nm whilst keeping the core diameter that of the record 19-cell defect design [19]. In our case, by combining hybrid cladding structure whereby the inner cladding confines the light in the core via IC mechanism and a PBG outer-cladding structure, we aim to achieve lower CL, low optical overlap with silica, single modedness and improvement in bend sensitivity. Furthermore, for implementation in applications such as telecommunications, it is desirable that the HCPCF core size is comparable to that of SMF. With our approach, a mode field diameter (MFD) in the range 6 – 8 μm while keeping ultra low CL became possible.

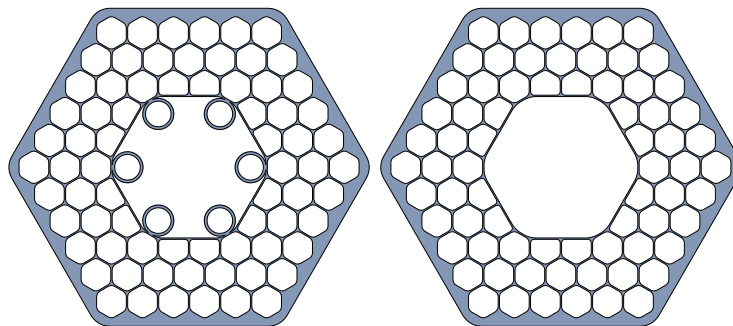


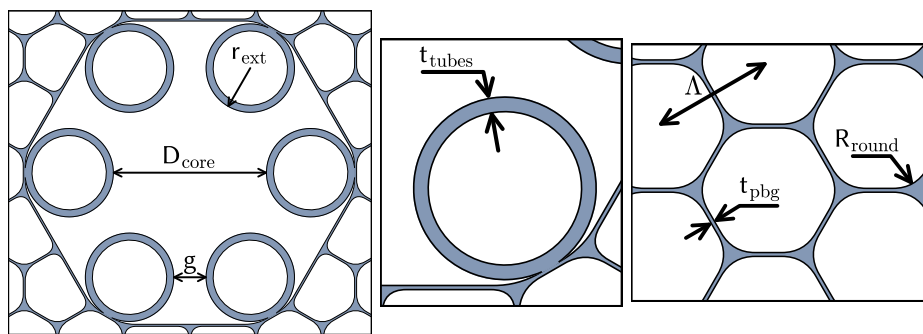
Figure 3.18: (a) Proposed hybrid PBG HCPCF cross section compared to (b) the classical 19-cell PBG HCPCF.

3.5.1 Performance of ideal design

Fig. 3.19 shows the transverse structure of the hybrid IC-PBG HCPCF with its key geometrical parameters. The fiber exhibits a triangular arrangement of packed hexagon-like air-holes with a pitch Λ of 4.7 μm and an air-filling fraction of $A_{\text{ff}} = 94.24\%$. The core is formed from 9 missing unit cells, and the cladding is formed by 6 ring of such unit cells. The hybrid IC-PBG HCPCF differs from the PBG HCPCF in that its core exhibits a 6 non-touching tubes. The pitch Λ and the thickness of the PBG structure t_{pbg} (94 nm) were kept constant for all the designs, as they were found to provide the best CL for the PBG structure. As we know that the thickness of the tubes t_{tubes} and the inter-tube gap spacing g of the first ring play a crucial role in the performances, it is essential to carefully study them.

Table 3.5: Main geometrical parameters used for the HPBG simulations in this section.

D_{core} , [μm]	8.68	10.012	11.344	12.68	14.012	15.344
g , [μm]	1	2	3	4	5	6
r_{ext} , [μm]	3.339	3.006	2.672	2.339	2.006	1.672
Λ , [μm]	4.7					
t_{tubes} , [μm]	0.2 / 0.5 / 1.0					
t_{pbg} , [μm]	0.094					
R_{round} , [μm]	$0.22 \cdot \Lambda$					

**Figure 3.19:** Key geometrical features of the hybrid PBG HCPCF.

Impact of thickness of the ring tubes

The proposed design was then numerically simulated for different thickness of the tubes $t = 200 \text{ nm}$, 500 nm and 1000 nm as shown in Fig. 3.20 (a). The results show that for the case of a thickness of 500 nm (black curve), the CL achieves a minimum value around 10^{-5} dB/km in the telecom band which is closed to one order of magnitude lower than the PBG fibers (dashed curves). In our simulation, the 7-cell fiber has 7 rings cladding structure in contrast with 6 for the 19-cell fiber. Through other simulations not shown here, we note that this optimal thickness value of the tubes is not always the same when the pitch Λ and the thickness of the PBG structure t_{pbg} are changed. Finally, the IC-PBG HCPCF exhibits an intensity profile with a MFD comparable to the 7-cell PBG fiber as illustrated by the field of the fundamental mode profile in Figure 3.20 (b). All these results confirm the improvement of CL by mixing PBG-IC guidance.

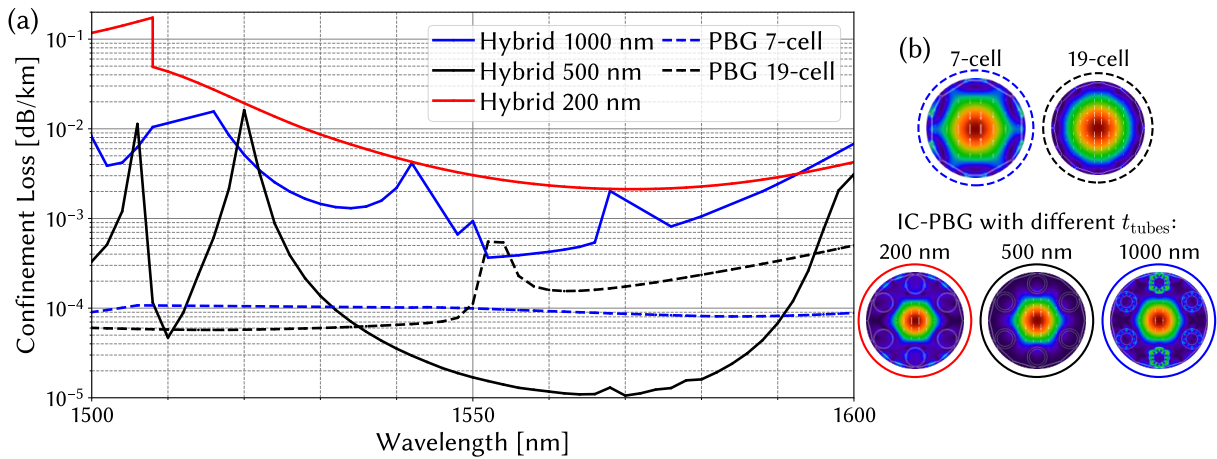


Figure 3.20: (a) CL of hybrid PBG fibers with inner cladding tube thickness (t_{tubes}) of 200 nm, 500 nm and 1000 nm compared to classical 7 cell and 19 cell PBG HCPCF. (b) Fundamental core mode profiles of the five fibers at 1550 nm.

Impact of the gap between the ring tubes

Another important aspect to optimize in our design was the gap between the small tubes g and the core size D_{core} . As these two features are related, we decided to adjust the value of g and conduct simulations for different values of g ranging from 1 to 6 μm . During these simulations the core size D_{core} also was varied between 8.68 μm and 15.344 μm . The results are presented in Fig. 3.21 (a). This also shows that the CL is minimized when the ratio g/D_{core} is increased (see Fig. 3.21 (b)).

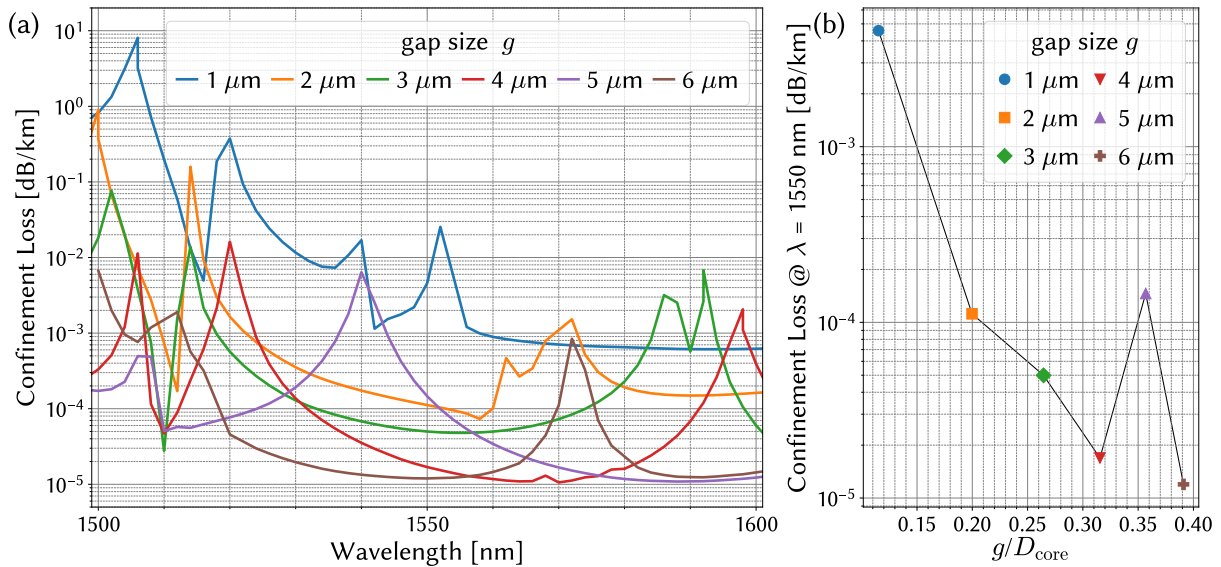


Figure 3.21: (a) CL for different gap size $g = 1 - 6 \mu\text{m}$. (b) Evolution of the CL at 1550 nm versus the ratio g/D_{core} .

HOMER

To ensure that the fiber design improves single-mode operation, simulations were also carried out to analyze the HOMs and compare them to the CL of FM by calculated the HOMER. Investigating the 500 nm tube thickness hybrid IC-PBG HCPCF further, Fig. 3.22 (a) shows respectively the CL of the lowest loss HOM (red colored curves) and the spectrum of the F (Fig. 3.22 (b)) for the hybrid fiber along with the 7 and 19 defect PBG fibers. Compared to the 19-cell PBG HCPCF, the results clearly demonstrate a much larger extinction ratio of 10^6 (i.e. 60 dB HOMER) between the FM and HOM for the IC-PBG HCPCF, record value for a PBG fiber. Also, the silica overlap F is reduced by a close-to-one order of magnitude in the vicinity of 1550 nm. These results confirmed that our new hybrid HCPCF design can present low CL, single modedness and small mode field diameter, properties combination that could be extremely useful for optical fiber telecommunications.

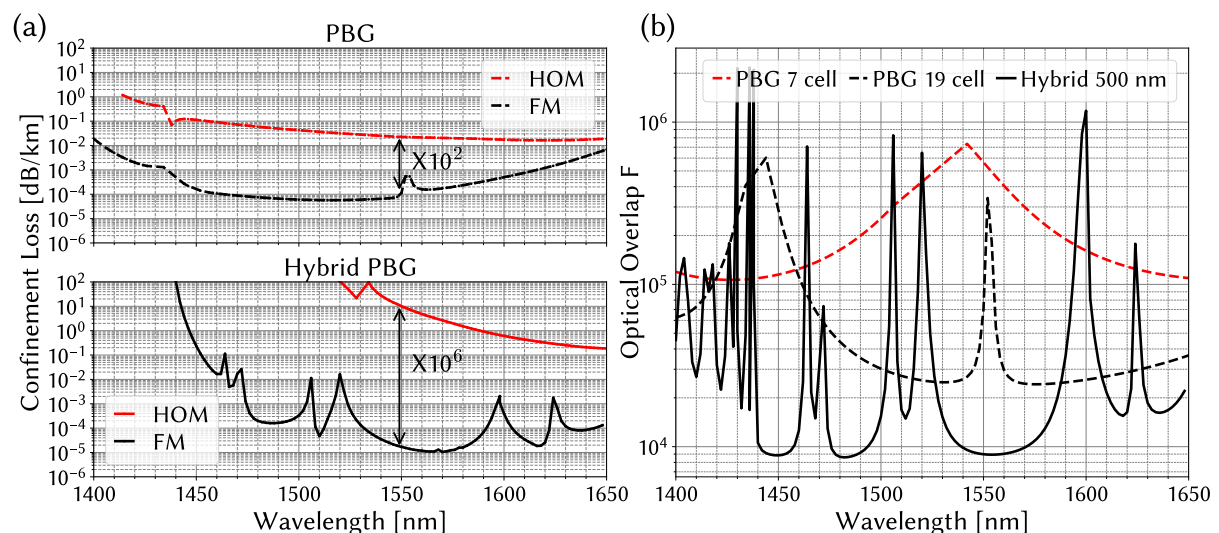


Figure 3.22: (a) CL for the FM (black color) and HOM (red color) for the 19-cell PBG HCPCF (dashed curves) and the hybrid IC-PBG HCPCF (solid curves). (b) spectrum of F for 7-cell (red dashed line), 19-cell (black dashed line) PBG HCPCF and hybrid IC-PBG HCPCF (black solid line).

3.6 Conclusion

In conclusion, this chapter presents an innovative design approach of hybrid fibers, combining the strengths of the two HCPCF guidance mechanisms, as well as mixing lattice structures. The simulations made on three new fiber designs have demonstrated

their potential to significantly impact both the CL and the single modedness. CL as low as 10^{-4} dB/km with HOMER larger than 40 dB became possible in the telecom range. Fabricated hybrid Kagome fiber showed an impressively low loss of 1.6 dB/km at 1050 nm and a record-breaking HOM extinction ratio of 47 dB for a fiber length of 10 m. This performance demonstrates the potential of the hybrid approach for developing next generation of low-loss single-mode HCPCFs.

Finally, The strong alignment between the simulation outcomes and experimental data, particularly in the long wavelength range (NIR), serves as a robust validation of our numerical tool. This validation instills confidence in the use of our numerical simulations for the ongoing optimization of hybrid fibers within this wavelength range. Such optimization endeavors hold the potential for substantial performance improvements and open up new possibilities, particularly in the domain of optical communications. Conversely, in the shorter wavelengths, certain disparities emerge, primarily attributed to the influence of SSL and MBL stemming from core surface roughness. These phenomena will be the focus of investigation in the upcoming chapters.

Chapter 4

Simulation and experimental control of surface roughness in HCPCF

IN this chapter, we explore surface roughness in HCPCF through a combination of numerical simulations and experimental investigations. We begin with an introductory overview of the surface roughness phenomenon induced by surface capillary waves in HCPCF. Subsequently, we introduce a theoretical model tailored for simulating HCPCF with surface roughness. Our numerical simulations unveil the confinement loss characteristics in HCPCF with surface roughness. Furthermore, we present the experimental findings from two novel HCPCF fabrication techniques designed to control surface roughness parameters like its RMS and power spectral density.

Table of content

4.1	Capillary wave in hollow core photonic crystal fiber	89
4.2	Surface roughness induced scattering and microbend transmission loss in HCPCF	93
4.3	Numerical modelling confinement loss in HCPCF with surface roughness	97
4.4	Fabrication and simulation of HCPCF with shear-stress induced surface roughness reduction	107
4.4.1	Principle of the shear-stress fabrication process	107
4.4.2	Experimental demonstration	110
4.4.3	New state-of-the-art for losses in the short wavelengths of the visible and ultraviolet spectrum	114
4.5	Opto-thermal process for the fabrication of HCPCFs	119
4.5.1	Fiber drawing set-up	124
4.5.2	Fabrication and characterization of the produced fibers	124
4.6	Conclusion	132

4.1 Capillary wave in hollow core photonic crystal fiber

In chapter 1, we observed that one of the most limiting factors in the performance of HCPCFs is surface roughness. The origin of this roughness is now established to be due to the formation of capillary waves when the glass of the fiber is in its viscoelastic state during the drawing process. Capillary waves are surface waves, much like those observed on the surface of water that can result in various impulses or forces [97]. In the case of HCPCF, the molten glass is viscoelastic media and the forces into play are gravity force, surface tension forces, and viscoelastic forces [98]. Analyzing the dynamics of these waves involves the spatial and temporal resolution of the Navier-Stokes elasticity equation for both fluids at the interface:

$$\rho \left(\frac{\partial \vec{v}}{\partial t} + (\vec{v} \cdot \nabla) \vec{v} \right) = -\nabla p - \eta \nabla (\nabla \vec{v} + (\nabla \vec{v})^T) + \nabla \cdot T_{\text{elast}} \quad (4.1)$$

Here, ρ represents the fluid density, v is the fluid velocity vector, η is the viscosity coefficient. ∇p denotes the pressure gradient created by the forces at play. Finally, the last term on the right-hand side of the equation pertains to the fluid's elasticity tensor. The resolution of this equation is complex and is beyond the scope of this work, especially given that a rigorous resolution of these equations entails faithfully replicating the dynamics of glass flow within the furnace, which is illustrated in Figure 4.1 (a). The figure schematically depicts an HCPCF during its drawing process, where the viscoelastic portion of the molten glass is confined to a region known as the “heat zone” of a length L . Beyond this zone, the glass is considered to be in a solid state. Additionally, at this stage, the fiber assumes an almost conical shape. It's worth noting that the tips of this “cone” move vertically downward at different speeds. Finally, we recall that the cladding of the HCPCF is microstructured, and all the air holes in the fiber are subject to pressurized gases. This is reminded to highlight the inherent complexity of a rigorous simulation. Nonetheless, it is possible to significantly simplify the problem while still achieving results that are consistent with the experimental results, as has been demonstrated in previous publications [19], where the approach was to treat the problem as if it were a free surface. Figures 4.1 (b) and (c) schematically illustrate this simplification. We begin by disregarding variations in the fiber's diameter within the furnace, as well as the fiber's microstructure, in order to reduce the problem to a tube of length L and very thin thickness t . Furthermore, this simplification can be taken a step further to reduce the problem to that of a membrane with the same thickness as the tube, with length L and width W , equivalent to the perimeter of the tube.

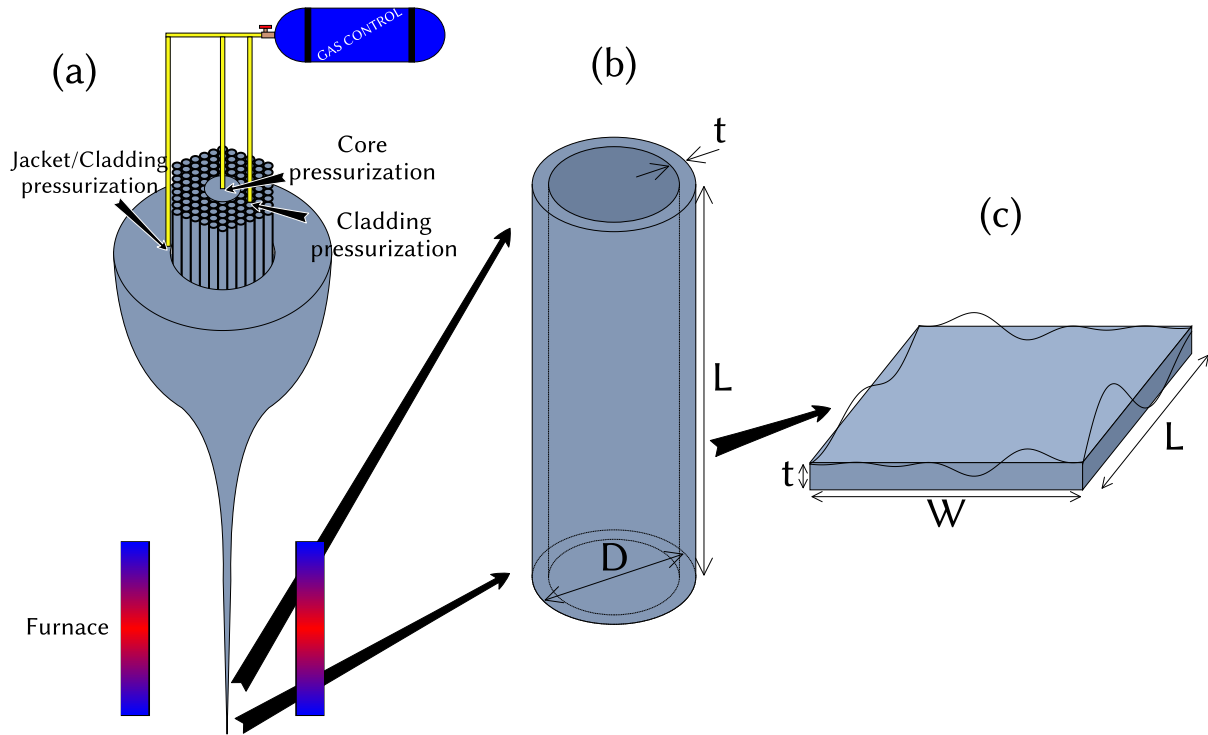


Figure 4.1: (a) Schematic of the drawing of an HCPCF, (b) a sheath tube, and (c) the membrane surface associated with this tube.

Finally, we can further simplify by approximately comparing the forces associated with surface tension, $F_{\text{surf}} = \gamma \cdot L \approx 3 \text{ mN}$, and viscosity, $F_{\text{vis}} = \eta \cdot W \cdot t \cdot \left(\frac{\partial v}{\partial x}\right)$. It's evident that gravity is negligible. Here, we've taken W to be $20 \text{ }\mu\text{m}$ and t to be $0.5 \text{ }\mu\text{m}$. Moreover, for a temperature range of $1700 - 2100^\circ\text{C}$, which is the working temperature range during HCPCF stretching, the viscosity coefficient is about $1 \text{ Mpa}\cdot\text{s}$, and the velocity gradient ranges between 10 and 100 s^{-1} . This results in a viscosity force ranging from 10 to a few hundred μN . Consequently, we can reduce the Navier-Stokes equation to two coupled equations in the Fourier space of lateral displacement, $h_x(x, t)$ and $h_y(y, t)$, of the surface along the x and y axes, respectively.

$$-\rho\omega^2 h_x(x, t) = -\gamma\nabla^2 h_x(x, t) - \eta\omega h_y(x, t) \quad (4.2)$$

$$-\rho\omega^2 h_y(x, t) = -\gamma\nabla^2 h_y(x, t) - \eta\omega h_x(x, t) \quad (4.3)$$

Consequently, by employing a modal decomposition, the expression of the surface

height $h(x, y, t)$ takes the following form:

$$h_{mn}(x, y, t) = h_{mn} \sin(q_m x) \sin(q_n y) e^{i\omega_{mn}t + \varphi_{mn}} \quad (4.4)$$

Here h_{mn} represents the amplitude of the capillary wave mode oscillating at the angular frequency ω and wave vectors q_m and q_n along the x and y axes, respectively. These wave vectors are discretized by the boundary conditions of a membrane with fixed edges and can thus be expressed as $q_m = \frac{m\pi}{L}$, $q_n = \frac{n\pi}{W}$. The complex dispersion of these capillary modes are given by [99]:

$$\omega_{mn} = \sqrt{\frac{\gamma}{\rho} q^3 + i \frac{\eta}{\rho} q^3} \quad (4.5)$$

The expression simplifies to the well-known dispersion relation of a capillary wave. $\omega_{mn}^2 = \left(\frac{\gamma}{\rho}\right) q^3$ in absence of the viscosity. Here $q = \sqrt{q_m^2 + q_n^2}$. Note that if the thickness and gravitational force are taken into account, this expression takes the following form, as derived from reference [100], [101], which was deduced in the case of a surface wave at the air-water interface of a water tank with depth t :

$$\omega^2 = \frac{(\rho - \rho')gk + \gamma q^3}{(\rho + \rho') \tanh(qt)} \tanh(qt) \quad (4.6)$$

Here, ρ and ρ' are the densities of the two fluids. Neglecting the density of air (ρ') yields the expression $\omega^2 = \left(gk + \left(\frac{\gamma}{g}\right) q^3\right) \tanh(qt)$. Notably, for HCPCF, the thickness t is on the order of a few hundred nanometers, whereas the period of capillary waves with the largest amplitudes is in the range of 1 – 10 μm . This implies $qt \ll 1$, allowing us to approximate $\tanh(qt) \approx qt$, and $\omega^2 = \left(gk + \left(\frac{\gamma}{g}\right) q^3\right) (qt)$. Thus, we obtain this results in the following dispersion relation in the absence of the gravitational effect: $\omega^2 = (qt) \left(\frac{\gamma}{g}\right) q^3$.

An estimate of the amplitude of the mode can be deduced by recalling that the source of energy for these capillary waves is provided by thermal fluctuations. Using the equipartition theorem of energy, each mode of the capillary waves possesses an average thermal energy of $\langle E \rangle = \frac{1}{2} k_B T$, with k_B being Boltzmann constant and T the temperature of the medium. Recalling that this energy is associated with the change in surface of the interface., $\delta E_s = \gamma dS$ we write $\langle E \rangle_s = \delta E_s = \gamma \left(\int_0^L \int_0^W \sqrt{1 + |\nabla h(x, y, t)|^2} dx dy - WL \right)$, which can be written for small surface height to $\frac{\gamma}{2} \int_0^L \int_0^W |\nabla h(x, y, t)|^2 dx dy$. The same approach can applied to gravity force and write $\langle E \rangle_g = \frac{\rho g}{2} \int_0^L \int_0^W h(x, y)^2 dx dy$. Consequently the total energy associated with the surface roughness formation is $\langle E \rangle = \langle E \rangle_s + \langle E \rangle_g$. Parseval theorem lead to following expression of energy of gravity-capillary

mode with a wavevector q :

$$\langle E \rangle = \sum_q \left(\frac{|h_q|^2}{q^2} + \frac{|h_q|^2}{l_c^{-2}} \right) \quad (4.7)$$

This yields an amplitude of a capillary mode with wave vector q , the following expression

$$\langle h_q^2 \rangle = \frac{k_B T}{\gamma} \frac{1}{LW} \frac{1}{q^2 + l_c^{-2}} \quad (4.8)$$

Here, we introduce the capillary length $l_c = \sqrt{\left(\frac{\gamma}{g\rho}\right)}$, and its associated wavevector magnitude $q_c = \sqrt{\left(\frac{g\rho}{\gamma}\right)}$.

The RMS is deduced by integration of the wavevector space:

$$\langle h^2(x, y) \rangle = \int_{q_{\min}}^{q_{\max}} \frac{dq}{(2\pi)^2} \int_{q_{\min}}^{q_{\max}} \frac{dq'}{(2\pi)^2} \langle h_q h_{q'} \rangle e^{i(q+q') \cdot r} \quad (4.9a)$$

$$= \frac{k_B T}{(2\pi)^2 \gamma} \int_{q_{\min}}^{q_{\max}} \frac{dq}{(2\pi)^2} \frac{1}{q^2 + l_c^{-2}} \quad (4.9b)$$

$$\approx \frac{k_B T}{2\pi \gamma} \ln \left(\frac{2\pi l_c}{\xi} \right) \quad (4.9c)$$

The associated auto-correlation is

$$\begin{aligned} g_h(x) &= \langle (h(x) - \langle h \rangle) (h(x+x') - \langle h \rangle) \rangle \\ &= \frac{k_B T}{2\pi \gamma} K_0 \left(\frac{x}{l_c} \right), \end{aligned} \quad (4.10)$$

where K_0 - modified Bessel function of second kind.

The lower limit of the integration is determined by $q_{\min} = 2\pi f_c = l_c^{-1} = \sqrt{\left(\frac{g\rho}{\gamma}\right)}$, corresponding to l_c . The upper limit is associated with the molecular length representing the cutoff for high spatial frequencies [102]. This expression can be deduced by applying the fluctuation-dissipation theorem, as reported in [103]. Sarlat *et al.* [102] estimated the RMS height to be 1.5 nm for fused silica with a capillary length of 4 mm, using $\gamma = 0.3 \text{ J}\cdot\text{m}^{-2}$ and $\rho \approx 2.2 \text{ kg}\cdot\text{m}^{-3}$, and a molecular length $\frac{\xi}{2\pi} = 0.5 \text{ nm}$. However, their AFM measurement yielded an RMS height of 0.43 nm, while Sarlat *et al.* [102] estimated it differently.

4.2 Surface roughness induced scattering and microbend transmission loss in HCPCF

The surface roughness induced scattering loss have emerged as a limiting factor in the effort to reduce HCPCF transmission losses. To illustrate the significance of surface roughness in the transmission performance of a HCPCF, it's important to recall that, in addition to the angles of incidence and scattering, the intensity scattered by a rough surface strongly depends on the power spectral density (PSD) of the surface roughness, $I_s \propto \tilde{h}(\kappa)/\lambda^4 I_i$ [104]. Here, $\tilde{h}(\kappa)$ represents the surface roughness PSD, and κ is the spatial frequency. Assuming random roughness with a normal distribution and a root mean square height (RMS) h_{rms} and a correlation length L_c , Elson *et al.* [104] found two asymptotic expressions for the magnitude of the scattered light: $I_s \propto (h_{rms}/\lambda)^2 I_i$ for $L_c \gg \lambda$ and $I_s \propto (h_{rms}^2 \cdot L_c^2)/\lambda^4$ for $L_c \ll \lambda$. In parallel, research on scattering loss in HCPCFs demonstrated a scaling law for the surface scattering loss (SSL), which follows the proportionality $I_s \propto \lambda^{-3} I_i$ [19], as previously mentioned in chapter 1. The expression of the SSL writes empirically as [105]:

$$SSL(\lambda) = \eta \cdot F_{oo}(\lambda) \left(\frac{\lambda_0}{\lambda} \right)^3 \text{ [dB/km]}, \quad (4.11)$$

where $\eta \propto h_{rms}^2$ is a factor that is proportional to the surface roughness RMS. give its the expression in function of $\tilde{h}(\kappa)$, η and λ_0 are two coefficients depending on roughness, and F_{oo} is the electric field at the dielectric interface parameter [105] (i.e. optical overlap in [38]):

$$F_{oo}(\lambda) = \sqrt{\frac{\varepsilon_0}{\mu_0}} \frac{\oint_{\Gamma_d} |\overline{E}|^2 d\Gamma}{\iint_{S_\infty} p_z dS} \quad (4.12)$$

Here Γ_d the air-dielectric interface, and \overline{E} and p_z the electric field and the Poynting vector axial component of the mode.

This expression illustrates the importance of having a low optical overlap of the guided mode with the cladding and a low surface roughness (i.e. small h_{rms} values). With regard to achieving low optical overlap, the IC HCPCFs represent by far the best candidates, and is the reasons of the recent achieved results [30], [94]. In parallel, surface roughness in HCPCF is still an active research topic. Figure 4.2. summarises the main results in this matter. The first observation linking the capillary wave induced

surface roughness scattering to the transmission loss was reported by [19]. In this work, the authors measured the surface roughness of a photonic band gap (PBG) guiding HCPCF using Atomic Force Microscope (AFM) on a spatial frequency range of $0.1 - 30 \mu\text{m}^{-1}$ and an RMS of $\sim 0.4 \text{ nm}$ (Fig. 4.2 (a)). They have also experimentally demonstrated the scaling λ^{-3} of the SSL (Fig. 4.2 (b)). In [106], the authors reproduced the measurement of a PBG HCPCF surface roughness using an optical profilometer, which allowed the extension of the spatial frequency range down to $0.01 \mu\text{m}^{-1}$. The results show that for spatial frequencies lower than $0.5 \mu\text{m}^{-1}$ -corresponding qualitatively to the spatial frequency of the fiber core perimeter-, the frequency scaling shows a crossover from $1/f$ scaling to $1/f^3$. The origin of such behavior is yet to be elucidated. In [37], the authors observe an anisotropy of the roughness with the roughness been smaller along the fiber draw. In a following section we explore this observation to develop a new drawing technique with lower longitudinal surface roughness height.

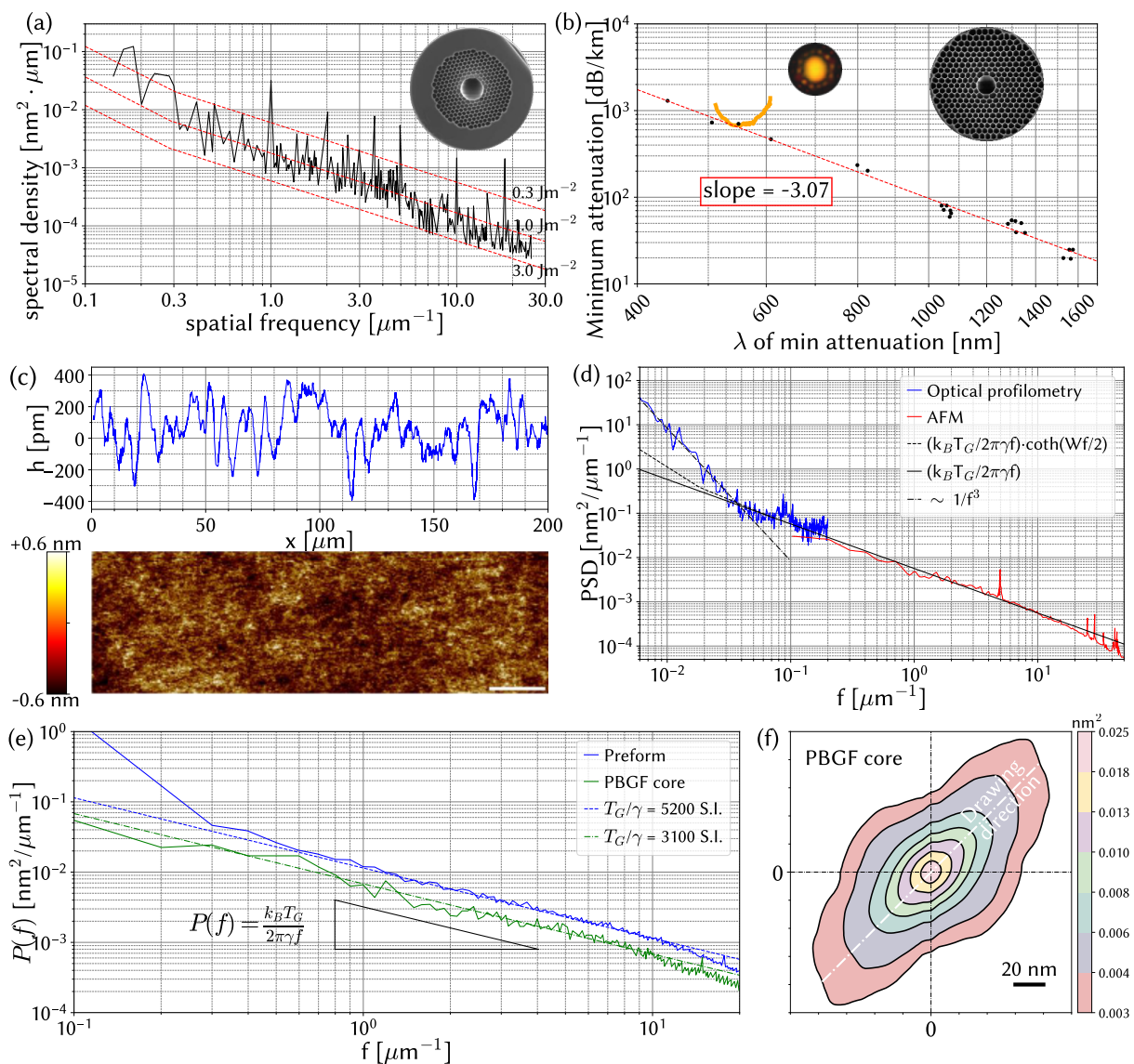


Figure 4.2: A summary of the main published work regarding surface roughness in hollow core fibers. Measured PSD (a) and minimum loss evolution with wavelength (b) of a PBG HCPCF from [19]. Surface roughness height profile (c) and associated PSD (d) of a PBG HCPCF from [106] PSD of a PBG HCPCF compared to that of its preform (e) and auto-correlation contour (f) from [37]

The above underscores the importance of thoroughly understanding surface morphology over sufficiently long lengths. For HCPCFs, the surface roughness over lengths greater than a millimeter is necessary to estimate the potential coupling of scattered light into higher-order modes of the HCPCF, its impact on confinement losses, or even on multiple-path interference (MPI), which is highly significant in telecommunications. For instance, the beat length between the fundamental mode (i.e., HE_{11} or approximately LP_{01}) and the first higher-order modes (i.e., LP_{11}), $L_{\text{beat}} = 2\pi/\Delta\beta$, covers a range

between 1 mm and 10 mm. Therefore, if the power spectral density of the roughness profile contains non-negligible components at spatial frequencies less than or equal to $L_{\text{beat}} = 2\pi/\Delta\beta$, surface scattering becomes a source of modal contamination. In the literature such coupling is historically associated with microbend loss (MBL). In conventional solid fibers, MBL is often attributed to slight deformations in the fiber's cross-section due to the random tilting of the fiber's longitudinal axis during the fabrication process and/or external mechanical stress resulting from activities such as fiber cabling. This definition raises questions regarding the distinction between MBL originating from surface roughness and additional mechanical stress induced by fiber handling. Up to now, there are no available data or experimental mechanisms to differentiate between these two sources of MBL. Therefore, while we will distinguish in our data processing and analysis SSL from MBL, we will rely on the empirical MBL formulas found in the literature. This approach is not only substantiated by the reasons mentioned earlier but also due to the limited availability of measured surface roughness data, which primarily extends to spatial frequencies of $10^{-3} \mu\text{m}^{-1}$. This range is significantly higher than the phase-matching range associated with MBL. Consequently, we adopt the MBL expression as presented in reference [44]:

$$\text{MBL} = \frac{1}{4} \left(\frac{2\pi}{\lambda} n_{\text{eff}}^{\text{FM}} \right)^2 R_0^2 \Phi(\Delta\beta) \text{ [dB/km]}, \quad (4.13)$$

with $n_{\text{eff}}^{\text{FM}}$ being the FM effective index, R_0 the FM field radius, $\Delta\beta$ the phase constant difference between FM and LP_{11} HOMs, and Φ the power spectral density (PSD) of the stochastic process describing the micro-bending, here due to unavailability Φ measurements, often next expression used $\Phi(\Delta\beta) = \frac{C_0}{\Delta\beta^2}$ [44], [107].

In conclusion, what we can gather from the above is that, despite the fundamental nature of surface roughness formation, and therefore the impossibility of eliminating it, reducing the SSL and MBL in HCPCF could be possible by either reducing surface roughness in HCPCF RMS by increasing the surface tension γ , or altering its PSD. For example, by noting that $\langle h_q^2 \rangle \propto q^2$ et $\langle h_q^2 \rangle \propto \frac{1}{LW}$, a mechanism that can exert control over the power spectral density (PSD) spectrum or boundary conditions can structure the spectrum and amplitude of the PSD in such a way as to minimize scattering losses. These are the drivers that motivate the work in this chapter.

Remarkably, the principle of controlling surface tension has been demonstrated in the field of hydrodynamics by Derks *et al.* [97] on the gas-liquid colloidal interface through shear flow. Based on this principle, Benabid *et al.* [85] proposed a new method for man-

ufacturing HCPCF to reduce surface roughness. Conversely Benabid [108] proposed a new drawing process based on photothermal effect that can control the surface roughness PSD parameters. Both of these techniques are detailed in the following sections.

4.3 Numerical modelling confinement loss in HCPCF with surface roughness

In this section we detail the numerical implementation of surface roughness and explore its impact on the CL of IC HCPCF. For this purpose we recall that the thermal fluctuation capillary wave induced surface roughness exhibits a stochastic and stationary process. Table 4.1 shows the mathematical expressions of auto-correlation function (ACF), structure function (SF), and PSD for two of the most common stochastic processes, namely the Gaussian and the exponential. The structure function (SF) or variance function represents the mean square of the expected height difference over all spatial distances. It quantifies the variability of the surface height as a function of the separation distance between data points. Unlike an autocorrelation function (ACF), which provides information about the strength and nature of the correlation between surface heights, the SF directly quantifies the magnitude of height variations. For stationary processes, SF is redundant with ACF. We note that the description of the process can be reduced to two parameters: the RMS height h_{rms} (i.e. σ in the following), and the correlation length L_c . This essentially represents the distance beyond which surface heights are no longer significantly correlated. This shows that if we measure the surface height at two points separated by a distance greater than L_c , the height variations between these two points will be largely random and uncorrelated. In other words, L_c indicates the distance at which the surface roughness properties begin to change significantly.

Table 4.1: Mathematical expressions of the Normalized Autocorrelation Function (ACF), Structure Function (SF), and Power Spectral Density (PSD) for Gaussian and exponential distributions.

Stochastic process	ACF	SF	PSD
Gaussian	$e^{-\left(\frac{r}{L_c}\right)^2}$	$\sigma^2 \left(1 - e^{-\left(\frac{r}{L_c}\right)^2}\right)$	$(\pi/2)\sigma^2 L_c^2 e^{-\left(\frac{fL_c}{2}\right)^2}$
Exponential	$e^{-\frac{ r }{L_c}}$	$\sigma^2 \left(1 - e^{-\frac{ r }{L_c}}\right)$	$\sigma^2 \frac{L_c}{1+(2\pi f L_c)^2}$

Figure 4.3 shows measured PSD for two different HCPCFs along with an exponential fit over a frequency range of $0.02 \mu\text{m}^{-1}$ and $10 \mu\text{m}^{-1}$. The HCPCFs are IC guiding single ring tubular cladding with 8 tubes (label T8 and green colored curve) and a PBG guiding

fiber (label PBG and orange colored curve), respectively. The T8 fiber has a fiber core diameter of $39.4 \mu\text{m}$ and a cladding tube diameter of $15.99 \mu\text{m}$. The PBG fiber has a fiber core diameter of $10.35 \mu\text{m}$ and cladding hole diameter of $3.5 \mu\text{m}$. We note that the exponential expression doesn't fit fully the experimental curves for higher spatial frequency. The measured PSD show steeper slope, indicative of stronger correlated roughness profile. This demonstrated with the fit with a power-law behavior at higher frequency of (i.e. pink noise) $\propto 1/f^{2H+1}$, with H being the Hurst exponent [109] which was found to be around 0.875 in our fit (red curve). However in our following simulations we will be considering an exponential process for the impact of the surface roughness PSD high spatial frequency range is much smaller than the lower range. Furthermore, in our simulation we consider the transverse surface roughness, which we assume to have the same PSD as the longitudinal roughness profile.

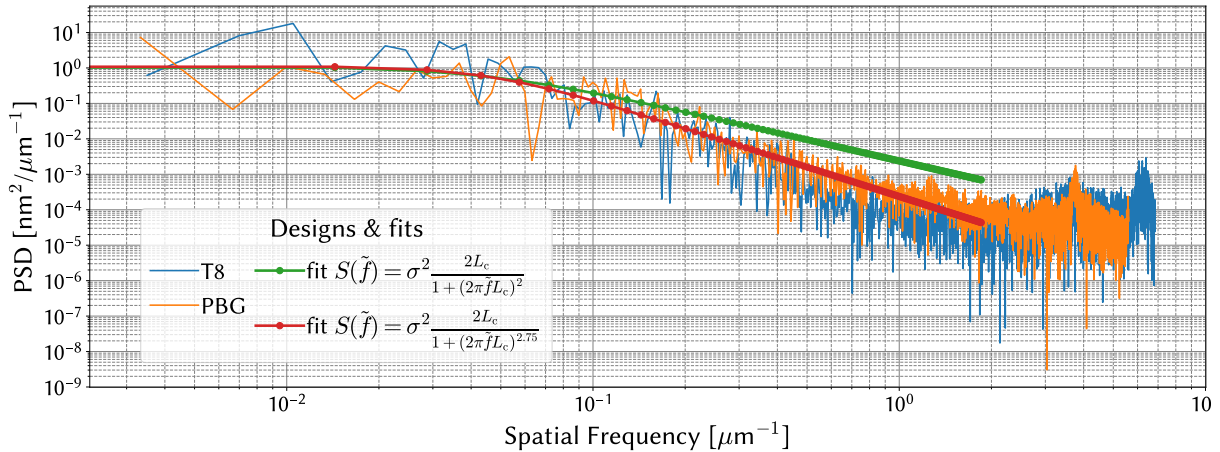


Figure 4.3: Measured PSD and their fits using the expression of the exponential process (green curve) and the expression of a modified exponential (red curve).

In order to investigate the impact of surface roughness on confinement loss, we start with the profile of the cross section of a tube waveguide affected by random small variations that deviate from the ideal circular line Figure 4.4 (left, middle).

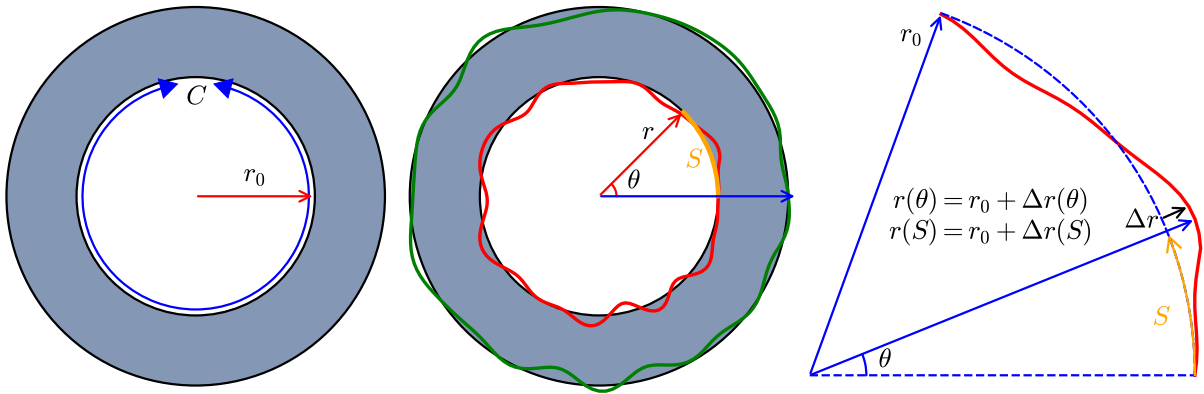


Figure 4.4: SR. S curvilinear abscissa, θ azimuthal angle, C circumference

Using this approach we can apply the roughness to both surfaces of the tubes capillary surfaces. Since the path is along a circumference, it is better using the polar coordinates system. The roughness is represented as deviation from r_0 as Δr . As illustrated in Figure 4.4, r_0 is the radius of the circumference $C = 2\pi r_0$. Considering a vector, rotating by an azimuthal angle θ and tracing the curvilinear abscissa s . The rotating vector presents the displacement $\Delta r(s) = \Delta r(s + C)$, clearly periodical in C .

This structural roughness implies a perturbation in the material refractive index, which is given by the variation in the permittivity as:

$$\Delta\varepsilon_{\text{real}}^T(x, y) = \Delta\varepsilon_{\text{real}}^T(x, y) - \Delta\varepsilon_{\text{ideal}}^T(x, y) = \sum_{p=1}^{N_T} \Delta\varepsilon_r^p(x, y)((x\hat{i} + y\hat{j}) - \overline{C}_p), \quad (4.14)$$

where $\overline{C}_p = ((R_{\text{clad}} - r_{\text{ext}}) \cdot \cos(\frac{2\pi}{N} \cdot p) \cdot \hat{i} + (R_{\text{clad}} - r_{\text{ext}}) \cdot \sin(\frac{2\pi}{N} \cdot p) \cdot \hat{j})$ and depicted in Figure 4.5

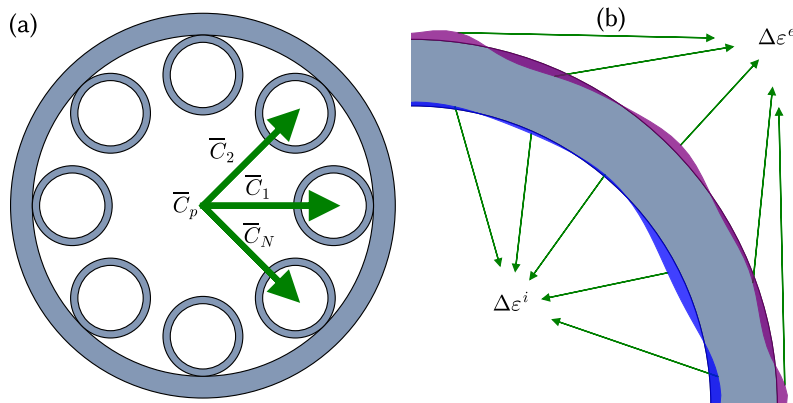


Figure 4.5: (left) A cross-section of the SR-TL HCPCF, where the vector C_p represents the shift from the reference system of a local single tube to the reference system of the fiber. (right) Visual representation of the external and internal contributions affecting the perturbation $\Delta\varepsilon$.

We defined auto-correlation function of the radius variation as:

$$R(\xi) = \langle \Delta r(s) \Delta r(s + \xi) \rangle \quad (4.15)$$

Because we assume that investigated random process is stationary and ergodic.

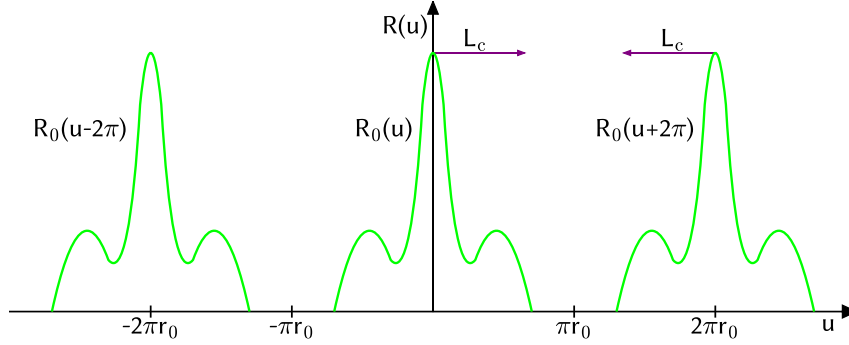


Figure 4.6: Auto-correlation function and Correlation length, periodic of $2\pi r_0$

Figure 4.6 shows that $R(\xi)$ is periodic with respect to ξ . Auto-correlation is the correlation of a signal with a delayed copy of itself. $R(\xi)$ usually decreases as ξ increases, and the range over which it varies describes how much the random function is correlated at different positions. The range known as the correlation length (L_c) gauges the correlation between the height displacements of adjacent points on the surface.

The Power Spectral Density $S(\tilde{f})$ can be obtained by applying the Fourier transform to the auto-correlation function $R(\xi)$, which is related to the spatial frequencies contained in the sinusoidal function. The Wiener-Khinchin theorem is valid in this case.

$$R(\xi) = \int_0^{+\infty} S(\tilde{f}) e^{i2\pi\tilde{f}\xi} d\tilde{f} \quad (4.16)$$

$$S(\tilde{f}) = \int_0^{+\infty} R(\xi) e^{-i2\pi\tilde{f}\xi} d\xi \quad (4.17)$$

Assuming that the auto-correlation function $R(\xi)$ does not depend on ξ :

$$R(0) = \int_0^{+\infty} S(\tilde{f}) d\tilde{f} = \langle \Delta r^2(s) \rangle = \sigma^2 \quad (4.18)$$

where $\sigma = \sqrt{\sigma^2} = \sqrt{\langle \Delta r^2(s) \rangle}$ is the root mean square of the stochastic process.

With the information stated earlier, we can now provide a mathematical representation of SR that is more practical for our numerical simulation. As mentioned before, since the variation in surface height $\Delta r(s)$ is periodic with a period of C , the transverse

roughness can be expressed as a sum of an infinite number of cosine waves with different spatial frequencies \tilde{f} . These cosine waves are statistically independent of each other and continue indefinitely.

$$\Delta r(s) = A \sum_{n=1}^{\infty} \sqrt{S(n\tilde{f}_0)} \cos(n\tilde{f}_0 s + \phi_{0n}) \quad (4.19)$$

The equation describes the mathematical representation of roughness. It is composed of a sum of infinite and independent cosine functions with spatial frequencies, denoted by \tilde{f} . The variable ϕ_{0n} is randomly and uniformly distributed between 0 and 2π . The fundamental spatial frequency is $\tilde{f}_0 = 1/C$, and the generic spatial frequency is $\tilde{f}_n = n\tilde{f}_0 = n/(2\pi r_0)$, where n is any integer and r_0 is the radius of the fiber. The coefficient A normalizes the function. The function $\Delta r(s)$ needs to be discretized at spatial intervals for numerical analysis, using the discrete Fourier transform (DFT). The coefficient A can be obtained if express $\Delta r(s)$ in eq. (4.19) in terms of $\langle \Delta r^2(s) \rangle$:

$$\langle \Delta r^2(s) \rangle = \frac{A^2}{2} \sum_{n=1}^{\infty} |S(n\tilde{f}_0)| \Rightarrow A = \frac{\sigma}{\sqrt{\sum_{n=1}^{\infty} |S(n\tilde{f}_0)|}} \quad (4.20)$$

Also we replacing the infinity number of harmonics with N which is should high enough value which depends by the fiber geometry and the normalized spatial cut-off frequency. This leads us to the the equation of SR which we used in our simulations for [110]:

$$\Delta r(\theta) = \frac{\sigma}{\sqrt{\sum_{n=1}^N |S(\frac{n}{2\pi r_0})|}} \sum_{n=1}^N \left(\sqrt{S(\frac{n}{2\pi r_0})} \cos(n\theta + \phi_{0n}) \right) \quad (4.21)$$

With this equation the roughness can be controlled by only 2 parameters. The first is σ - RMS of the controlling SR which control height of the PSD (see Fig. 4.7 (b)). The second is \tilde{f}_c . Expressing \tilde{f}_c as the frequency where the power spectral density reaches half of its maximum value, which is denoted by $S_{\max}/2$, we have:

$$\tilde{f}_c = \frac{1}{2\pi L_c} = \frac{P}{2\pi C} \quad (4.22)$$

We reduces control by \tilde{f}_c to control by parameter P . In terms of P , the correlation

length L_c is given by:

$$L_c = \frac{C}{P} = \frac{2\pi r_0}{P} \quad (4.23)$$

meaning that the variation fits its maximum displacement (i.e. $2\pi r_0$) for a unitary normalized cut-off spatial frequency. Since the correlation length L_c must be shorter than C : $P \geq 1$. Moreover, since the cut-off spatial frequency \tilde{f}_c is greater than the fundamental one \tilde{f}_0 , so that

$$\tilde{f}_c = \frac{P}{2\pi C} \geq \tilde{f}_0 = \frac{1}{C} \quad (4.24)$$

Expressing the fact that the variation fits its maximum displacement for a unitary normalized cut-off spatial frequency (i.e. $P = 1$), we have the variation corresponds to its maximum displacement (i.e. $2\pi r_0$) when the normalized cut-off spatial frequency is equal to one. Additionally, the correlation length L_c must be shorter than C , which implies that P is greater than or equal to one. Also, since the cut-off spatial frequency \tilde{f}_c is greater than the fundamental frequency \tilde{f}_0 , we have:

$$\tilde{f}_c = \frac{P}{2\pi C} \geq \tilde{f}_0 = \frac{1}{C} \quad (4.25)$$

it takes to: $P \geq 2\pi$. As mentioned in equation (4.21), the functions $\Delta r(\theta)$ are determined by the PSD of the auto-correlation function $S(\tilde{f})$, which we take to be exponential as mentioned earlier. Figure 4.7 depicts the shape of the PSD that corresponds to this, with a constant value at low spatial frequencies defined by σ , and a $\frac{1}{f^2}$ trend beyond the cut-off spatial frequency \tilde{f}_c . Technological control can be exerted over σ , while \tilde{f}_c is dependent on the fiber core and cladding tube diameter.

Notice that assuming assuming a minimum detectable value for the PSD amplitude of 10^{-4} , the roughness can be represented by a minimum number of harmonics, which is:

$$S\left(\frac{n}{2\pi r_0}\right) = 10^{-4} S_{\max} \rightarrow N = 10^2 \frac{P}{2\pi} \quad (4.26)$$

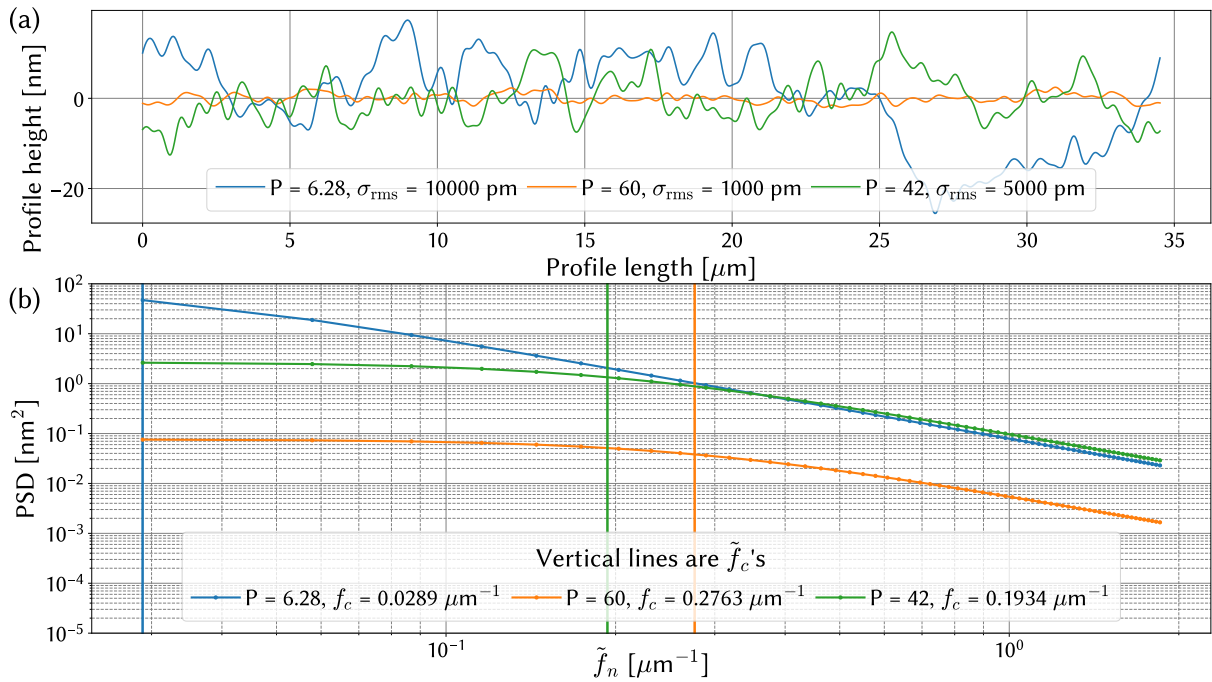


Figure 4.7: (a) Example of generated transverse roughness with $\sigma = 1, 5, 10 \text{ nm}$ and $P = 2\pi, 42$ and 60 . (b) The PSD of the given SR profiles.

Now, before performing the simulations I developed a *Python* class (GitLab repository [111]) based on the equation (4.21) in order to have flexible tool for generation and analysis of artificial roughness. This tool generating the files which can be imported to the COMSOL multiphysics® as a geometry with already applied surface roughness similar to the one presented on Figure 4.5 (b) with parameters summarized in Table 4.2.

Table 4.2: Table with geometrical parameters for T8-TL HCPCF in Figure 4.8.

$D_{\text{core}}, [\mu\text{m}]$	$g, [\mu\text{m}]$	$d_{\text{tubes}}, [\mu\text{m}]$	$t_{\text{tubes}}, [\mu\text{m}]$
27	3.565	11	0.6

Figures 4.8 (a) and 4.8 (b) show the confinement loss and the power overlap factor for different σ and P ranging from 0.4 nm to 1 nm and 2π to 20 respectively. Notice that each curve corresponds to an average of 10 simulations which implies a running time around a day for each fiber parameter.

The results indicate that, for wavelengths longer than 1000 nm , surface roughness does not appear to have a noticeable influence on the CL (Figure 4.8 (a)). Similarly, the spectrum of the optical overlap (Figure 4.8 (b)) and the dispersion of the fundamental mode (Figure 4.8 (c)) remain relatively unchanged relative to the surface roughness free fiber. However, for wavelengths shorter than 600 nm , the CL spectra show a

slight increase in CL, with this increase becoming more pronounced as the wavelength decreases. Figure 4.9 shows a close-up of the CL over the 3rd and 4th transmission bands. It shows, as expected that the loss increases with the increasing σ . It also shows that for a fixed sigma, the loss increasing with increasing the cut-off spatial frequency. Thus indicating that the RMS parameter is not the sole parameter that affect the impact of the surface roughness on the CL.

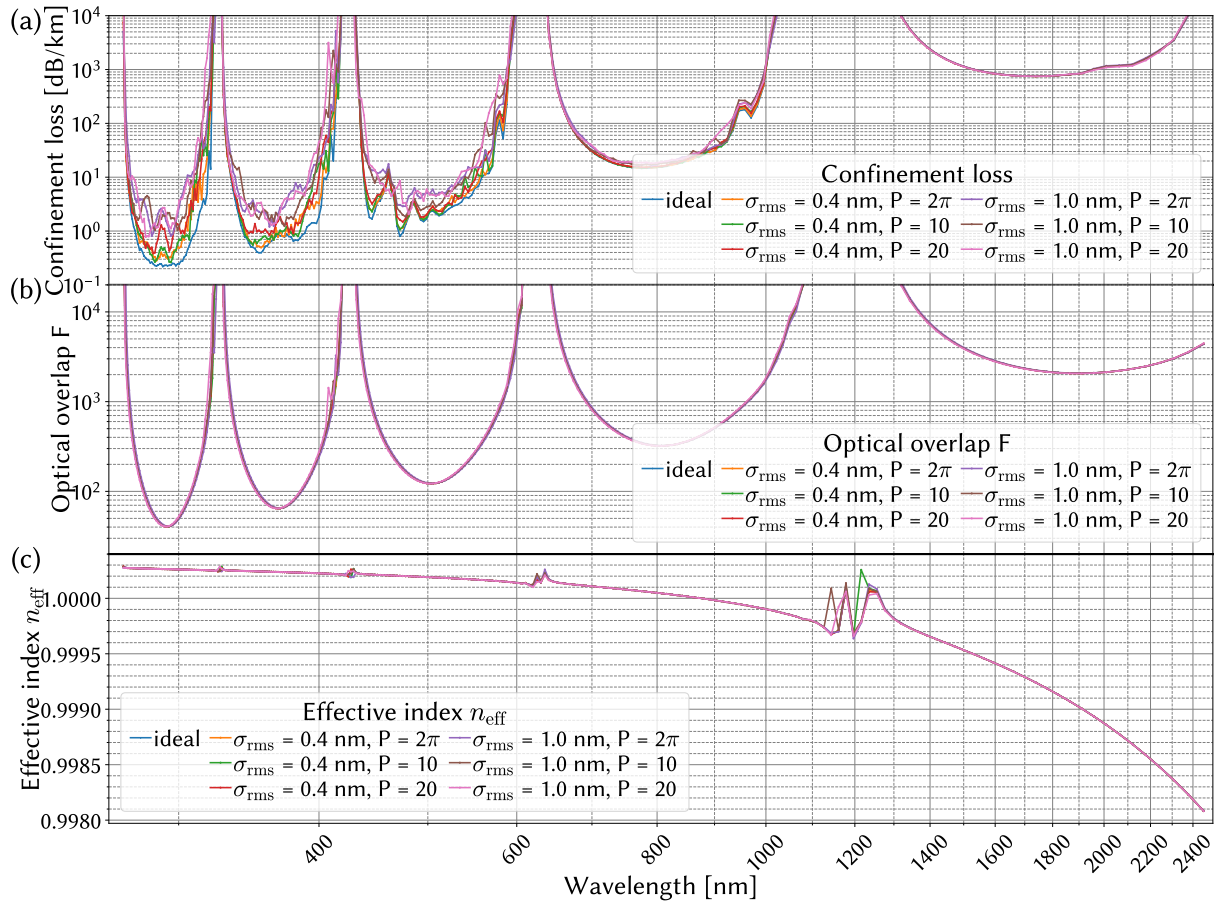


Figure 4.8: Comparison of (a) CL, (b) optical overlap F_{00} and (c) n_{eff} of LP_{01} with different parameters of surface roughness.

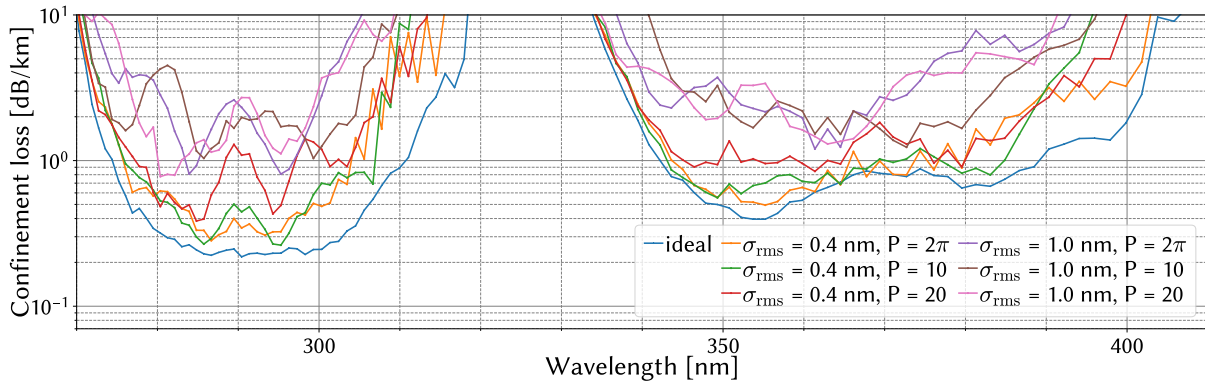


Figure 4.9: Close-up of the CL over the 3rd and 4th transmission bands of Fig. 4.8 (a)

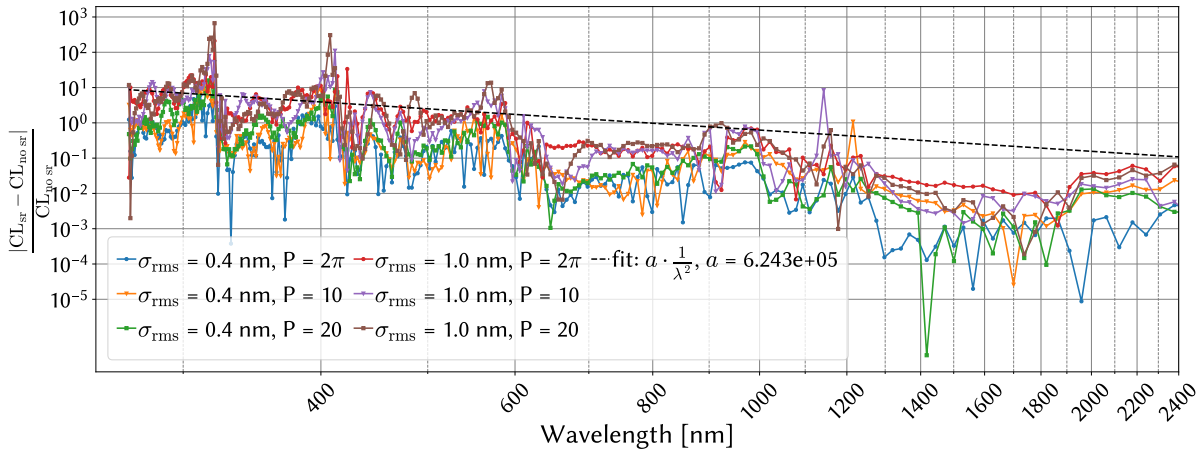


Figure 4.10: Relative difference of CL with SR according to CL without SR for different parameters of SR.

Figure 4.10 shows the spectrum of CL relative change for the different fibers. The results show more clearly the stronger impact of the surface roughness in the short wavelength range where the loss can increase by a factor of ten for wavelength shorter than 400 nm, while it only increases by less than 1%. The relative increase in CL with wavelength follows approximately a λ^{-2} .

Because MBL is influenced by the propagation constant difference, $\Delta\beta$, between the fundamental mode LP_{01} and the higher order mode LP_{11} , any alteration in $\Delta\beta$ due the surface roughness will result in changes in MBL between fibers with different surface roughness. Figure 4.11 examines this effect, by displaying the spectrum of the effective index difference between the LP_{01} and LP_{11} modes (Figure 4.11(a)). Notably, the figure demonstrates that surface roughness has a minimal impact. This is further highlighted in the MBL spectra depicted in Figure 4.11(b), where it is evident that MBL remains relatively unchanged despite the surface roughness-induced alterations in $\Delta\beta$.

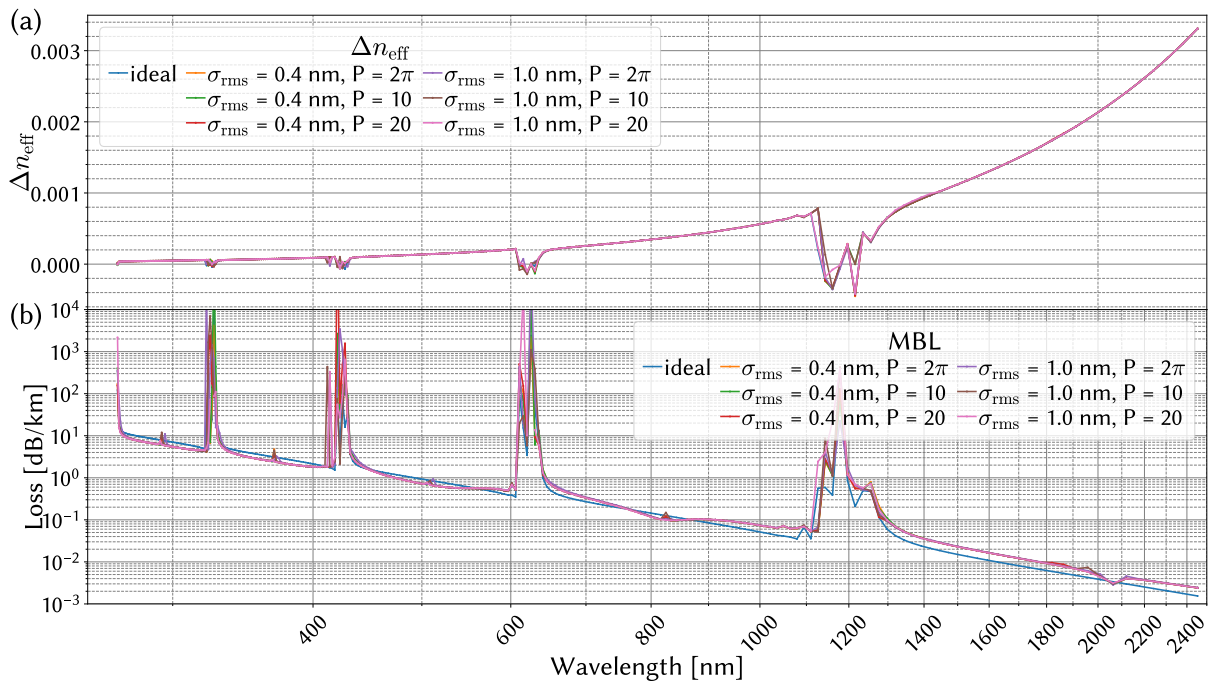


Figure 4.11: MBL with different parameters of surface roughness.

We finish this investigation of the impact of surface roughness on CL by comparing it with SSL and MBL using the empirical equations 4.11 and 1.7.

Figure 4.12 presents the spectra of the CL, SSL and MBL for $\sigma = 0.4 \text{ nm}$ and $P = 2\pi$ alongside the CL without SR for comparison. The data distinctly indicates that the CL increase induced by surface roughness has minimal impact, particularly when contrasted with the dominant effects of SSL and MBL, especially at shorter wavelengths where both SSL and MBL significantly outweigh the contributions from a surface roughness-free CL.

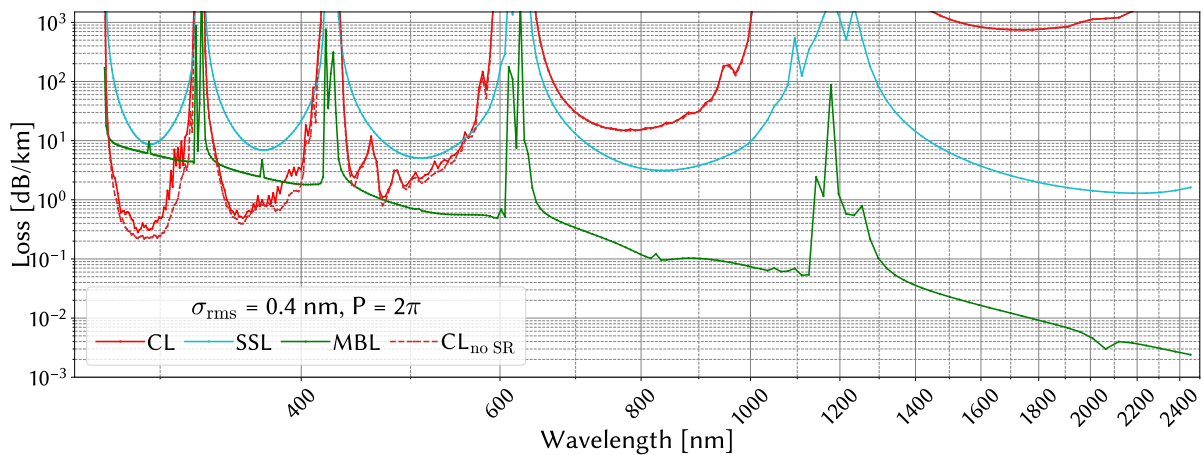


Figure 4.12: CL, SSL and MBL for SR with parameters $\sigma = 0.4 \text{ nm}$ and $P = 2\pi$ compare to CL of ideal design.

It's important to highlight that the introduction of SSL and MBL in the previous discussion was empirical, meaning that it did not consider the complete spectral structure of both transverse and longitudinal surface roughness. Additionally, considering that both spectral structure and RMS height affect CL, it is reasonable to assume that similar effects may apply to SSL and MBL. To thoroughly investigate these effects, numerical simulations involving both transverse and longitudinal surface roughness, as well as light propagation along the z-direction are required. This will be the subject of chapter 5 and 6.

4.4 Fabrication and simulation of HCPCF with shear-stress induced surface roughness reduction

4.4.1 Principle of the shear-stress fabrication process

As mentioned above, the inherent glass surface roughness arises from thermal fluctuations induced capillary waves, with an RMS value of ~ 0.4 nm at thermodynamic equilibrium [103]. In 2006, Derks *et al.* [97] proposed a technique relying on applying shear stress at the interface between two fluids to reduce the surface roughness RMS below the thermodynamic limit. To describe this effect on their sheared system, the authors introduced the concept of effective surface tension, given below:

$$\gamma_{\text{eff}}(\kappa) = \gamma_0 + \Phi(\kappa) \quad (4.27)$$

Here γ_0 is the interfacial tension at zero shear, and $\Phi(\kappa)$ is a positive function that increases with the shear rate denoted as κ . For the case of glass-air interface, $\Phi(\kappa)$ writes as

$$\Phi(\kappa) = \left(\frac{3k_{\text{B}}T}{4\pi} \right) \left[\frac{(\mu_{\text{air}} + \mu_{\text{glass}})\kappa}{\gamma_0 L_{\text{cap}}} \right] \sqrt{\left[\frac{[(\mu_{\text{air}} + \mu_{\text{glass}})\kappa L_{\text{cap}}]^2}{\gamma_0} \right] - 1} \quad (4.28)$$

where μ_{glass} and μ_{air} are the viscosities of glass and air, and L_{cap} is the capillary length, given by $\sqrt{\frac{\gamma_0}{g(\rho_{\text{glass}} - \rho_{\text{air}})}}$ where g is the acceleration due to gravity, ρ_{glass} and ρ_{air} are the densities of glass and air, respectively. Since the root mean square roughness $\langle h^2 \rangle$ (described in the previous paragraph) is inversely proportional to the interfacial tension, Derks *et al.* demonstrated that the amplitude of capillary waves can be expressed as:

$$\langle h^2 \rangle(\kappa) = \left[\frac{\gamma_0}{\gamma_{\text{eff}}(\kappa)} \right] \langle h^2 \rangle(\kappa = 0) \quad (4.29)$$

where $\langle h^2 \rangle_{(\kappa = 0)}$ is the root mean square roughness for zero shear. This expression indicates that we can expect the amplitude of a sheared surface to be reduced by a factor of $\frac{\gamma_{\text{eff}}}{\gamma_0}$ compared to that of the original surface. Such reduction of interfacial fluctuations has also been studied by other groups [112]–[114]. In particular, Smith *et al.* [113], [114] conducted simulations on laterally driven surface dynamics and concluded that applying shear results in a reduction of interfacial width. They showed that shear acts as an effective confinement force in the system, to the extent of even eliminating interfacial capillary wave fluctuations. In the context of optical fibers, the behavior of glass surface roughness was studied by Bresson *et al.* on air/silica tubes [37]. By evaluating the surface profiles of such tubes with typical diameters of 220 μm and thicknesses of 15 μm , the authors demonstrated that surface roughness levels can be reduced during the drawing process due to the attenuation of capillary surface waves in the drawing direction (i.e., from the top of the drawing tower to the bottom). More specifically, they observed anisotropic height correlations in the manufactured capillaries, showing that the glass surfaces retain a structural signature of the flow direction that occurred during fiber fabrication (see Figure 4.2). However, it is important to note that the attenuation of surface capillary waves studied in this research (i.e., the tension experienced by the fiber during manufacturing) results from various drawing parameters such as furnace temperature, drawing speeds, dimensions of the fiber to be drawn, and the preform. While this allowed the authors to correlate the reduction in surface roughness with the drawing process, it was challenging to delve deeper into the analysis, given that the reduction found in roughness was relatively moderate. Therefore, with the aim of amplifying this phenomenon and applying it to our case of smaller hollow-core fibers, we have proposed a novel approach based on the use of counterflow pressure within the preform during manufacturing. This process has been filed for a patent under the number FR1912283 [85]. In this context, we initially proposed a simplified model that relates the gas pressures used within the preform to the shear rate one can expect in the resulting hollow-core fiber. To achieve this, we applied the Navier-Stokes equations and the continuity relations to the flow of gas inside a tube of length L and variable radius r , where $r(z) = r_0 e^{-\beta z}$ and r_0 is the initial radius of the preform, as shown in Figure 4.13 (a) [115]. It is worth noting that this model does not consider any glass flow, as in our case, the axial velocity of the glass is significantly lower than the gas velocity inside the fiber (the ratio between the axial velocities of gas and glass flow is estimated at 30). Additionally, we do not consider glass collapse or dilation. This assumption is valid because we control the pressure levels inside the fiber to prevent glass collapse, and although we use pressure to inflate the microstructure holes during our drawing,

the rate of such expansion is low. These considerations allow us to accurately use the negative exponential to describe the shape of the preform-fiber transition region.

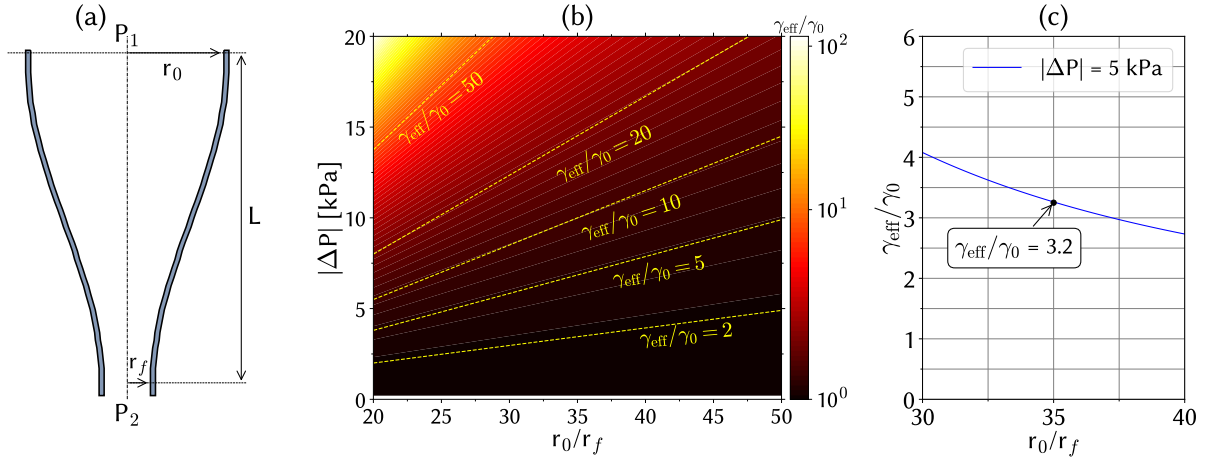


Figure 4.13: Proposed model to study the shear rate that could be achieved on the silica walls surrounding the air core of the fiber. (a) Diagram of the transition zone (or cone) between the preform and the fiber. P_1 and P_2 represent the pressure in the preform and in the fiber, while r_0 and r_f represent the radius. L is the length of the preform-fiber transition. (b) Diagram presenting the attainable values of the $\frac{\gamma_{\text{eff}}}{\gamma_0}$ ratio as a function of different pressure gradients $|\Delta P|$ and the ratio of fiber radius to preform radius $\frac{r_0}{r_f}$, expression is derived using equations (4.27, 4.32). (c) Specific case for $|\Delta P|$.

In the case of laminar flow (an applicable assumption here, as the Reynolds number calculated for the gas flow under study is on the order of 10^{-4}) and for a structural transition from the preform to the fiber following an exponential shape, the gas velocity established along the axis of fiber drawing (z -direction) denoted as u_z can be expressed as:

$$u_z = \frac{\Delta P}{4\mu_{\text{air}}L} \left[r_0^2 e^{-2\xi\left(\frac{z}{L}\right)} - r^2 \right] \quad (4.30)$$

where $\Delta P = P_1 - P_2$ is the pressure difference between the preform and fiber regions (P_1 and P_2 , respectively), L is the length of the preform-fiber transition, r is the radial coordinate, and a parameter ξ is defined as:

$$\xi = \ln\left(\frac{r_0}{r_f}\right) \quad (4.31)$$

where r_0 and r_f are respectively the radius of the preform and the fiber [116], [117]. Equation 4.29 then allows the calculation of the volumetric flow rate at a certain position z and subsequently the shear rate κ associated with such flow. The resulting expression is:

$$\kappa = \frac{|\Delta P| r_0 \exp\left(-\frac{\xi z}{L}\right)}{2\mu_{\text{air}}L} \quad (4.32)$$

Finally, by using Equation 4.29, we can estimate the effective interfacial tension of the sheared surface of the tube wall. Figure 4.13 (b)) illustrates the evolution of the $\frac{\gamma_{\text{eff}}}{\gamma_0}$ ratio for different pressure gradients $|\Delta P = P_1 - P_2|$ and the ratio of fiber radius to preform radius r_0/r_f . Here, the following parameters were used to obtain the curve: $T = 2300^\circ\text{K}$, $L = 2 \text{ cm}$, $\mu_{\text{air}} = 5.817 \cdot 10^{-5} \text{ Pa}\cdot\text{s}$, $\mu_{\text{glass}} = 6.165 \cdot 10^3 \text{ Pa}\cdot\text{s}$, $\gamma_0 = 0.3 \text{ N/m}$, $\rho_{\text{air}} = 0.199 \text{ kg/m}^3$, and $\rho_{\text{glass}} = 2200 \text{ kg/m}^3$.

The results indicate that the smaller the aspect ratio of the preform-fiber transition, the stronger the shear effect, especially when the applied pressure gradient increases. Based on what can be achieved during manufacturing, a limited parameter space is identifiable.

In particular, on Fig. 4.13 (c) we present an example which will be used later where $|\Delta P|$ is fixed at 5 kPa. We can then see that for the ratio $\frac{r_0}{r_f} = 35$, typical value for our fabrication of tubular lattice IC HCPCFs, we obtain a reduction ratio on the values $\langle h^2 \rangle$ of $\frac{\gamma_{\text{eff}}}{\gamma_0} = 3.2$. This result will be compared to the upcoming experimental measurements.

4.4.2 Experimental demonstration

The manufacturing of HCPCF is based on the “stack-and-draw” method, thoroughly documented in the literature [1]. In our case, in order to establish a shear-stress during the draw we apply fiber hole pressurization in the way schematically shown in fig 4.14 (a). Traditionally, these gas flows are applied in the same direction following the axis of glass flow during stretching (co-directional forces). In order to achieve a shear effect, we proposed to modify the process by using a set of reverse gas flows, namely, a first pressure applied in the air holes of the cladding in the stretching direction (an overpressure for the cladding), and a second pressure in the core with a direction opposite to the flow (a vacuum for the core) to create counter-directional forces with the draw direction (see Figure 4.14 (a)). Figure 4.14 (b) provides a close-up view of the silica membrane surrounding the air core with the forces at play.

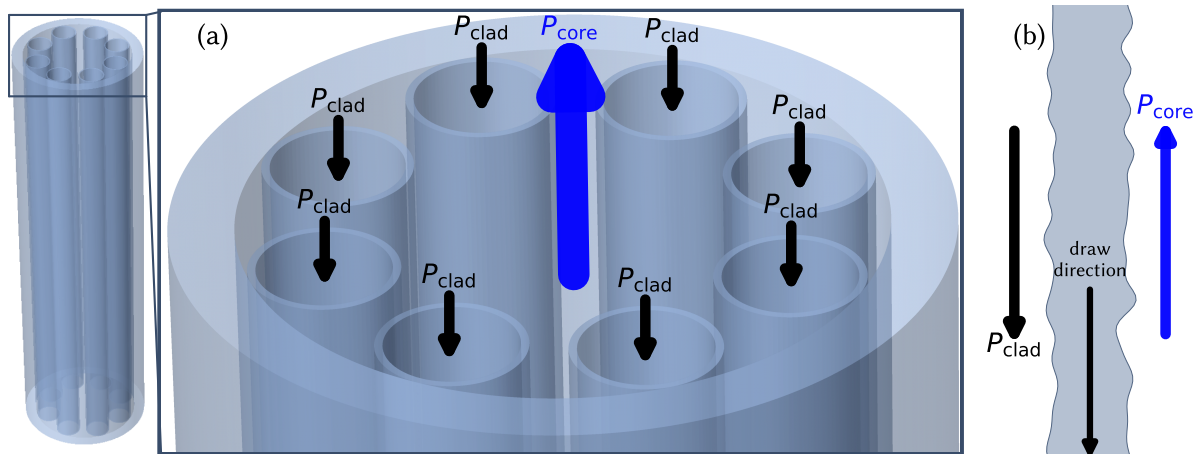


Figure 4.14: (a) The diagram illustrates the pressure distribution in the fiber preform during the fabrication with shear process. The pressure applied in the fiber core is represented as P_{core} , while the pressure in the cladding tubes is depicted as P_{clad} . (b) The diagram shows the interfaces between the surfaces of the cladding tubes, the internal region of the tubes, and the fiber core.

To demonstrate whether a reduction in roughness can be achieved through this approach, we manufactured a series of IC HCPCFs based on an 8-tube cladding. Several geometric parameters were included in this study by varying the air core diameter (25 μm to 42 μm) and the silica thickness (300 nm to 1220 nm). Finally, the performance of these fibers (referred to as G#2) was compared to similar fibers (referred to as G#1) that followed the traditional fabrication method (i.e., overpressure applied for P_{clad} and P_{core}), and for which we aimed to maintain comparable geometric dimensions. Table 4.3 provides details of the structures created for all of the two groups, G#1 and G#2, which correspond to a selection of fifteen T8 IC HCPCFs.

Table 4.3: Geometrical parameters of the fibers manufactured by the two techniques grouped under the nomenclature G#1 and G#2. Particular fiber from G#2 is indicated in blue color and fiber from G#1 in purple because they will be studied in more detail later.

Fiber code	G#1						G#2								
	I	II	III	IV	V	VI	VII	VIII	IX	X	XI	XII	XIII	XIV	XV
t , [nm]	230	415	465	500	545	600	300	305	360	600	720	900	1050	1080	1120
D_{tubes} , [μm]	15.6	13.0	11.2	10.8	16.0	10.2	10.6	10.7	8.5	11.2	15.6	18.0	14.7	14.1	14.0
D_{core} , [μm]	41.5	41.5	32.0	34.5	39.9	37.0	28.0	29.5	25.0	27.0	35.0	42.0	41.0	40.0	42.0

The roughness of the silica cladding surrounding the air core for the fibers in groups

G#1 and G#2 was then measured along the fiber propagation axis (z -axis) using the picometric-resolution optical profilometer developed by Dr. Ali Al Dhaybi. Figure 4.15 shows a typical surface profile for a fiber from G#1 (fiber V, left curve) and another fiber from G#2 (fiber X, right curve), measured at the outer interface of the silica wall (i.e., on the air core side). It is evident that the G#2 fiber exhibits reduced peak-to-peak values compared to G#1, with a maximum amplitude decreasing from 1.5 nm to approximately 0.5 nm.

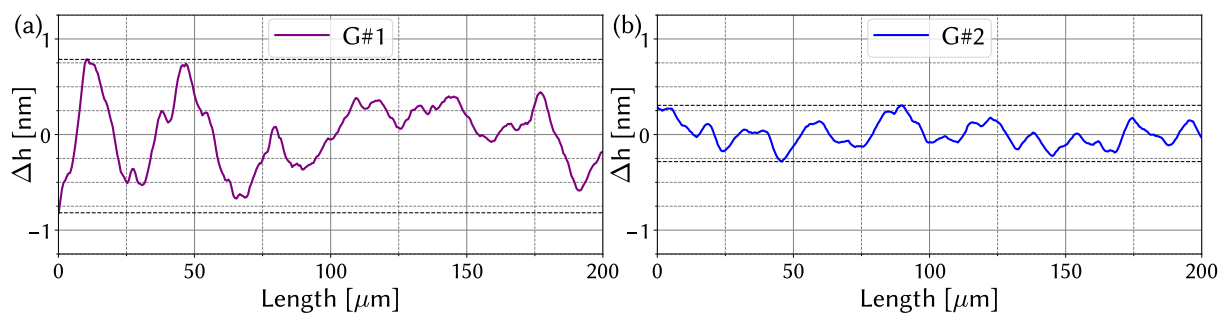


Figure 4.15: Typical profiles of roughness along the axis of the fiber.

Figure 4.16 presents the associated PSD plots for these two fibers, which were obtained by combining roughness measurements made by the optical profilometer (over a length of 200 μm) and by AFM (over a length of 6 μm). At spatial frequencies below $10^{-1} \mu\text{m}^{-1}$, a reduction in the PSD values is observed for the G#2 case, which is in line with the direct surface profile measurement since we know that these low spatial frequencies predominantly affect roughness.

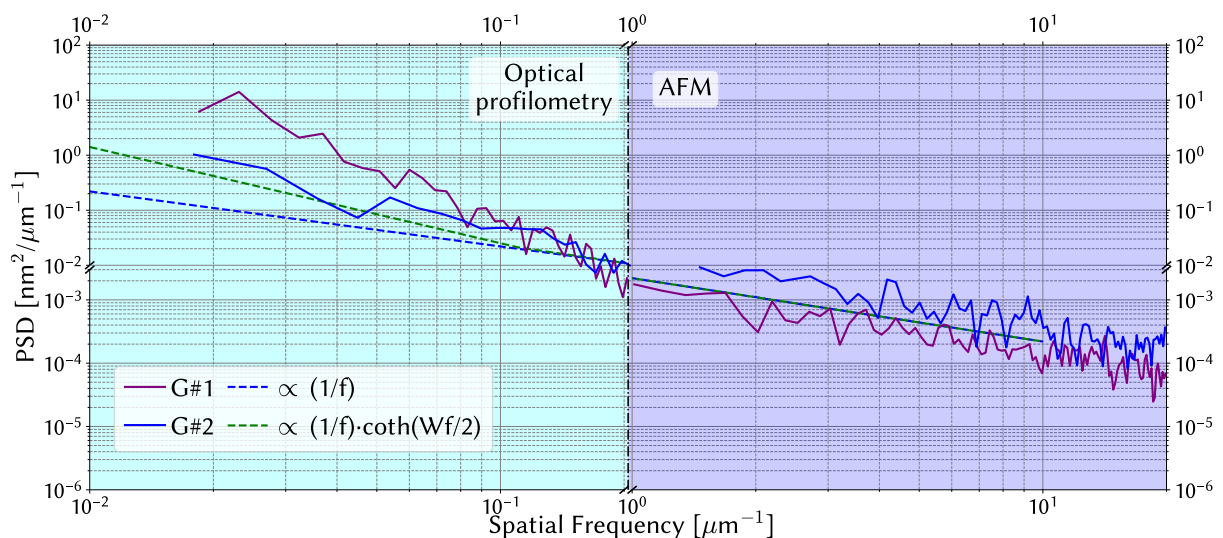


Figure 4.16: PSD for fibers in G#1 and G#2.

Furthermore, as mentioned in chapter 1 with previous works [19], [97], [106] and shown in Figure 4.2 (d), a $1/f$ trend for PSD functions at high spatial frequencies (i.e., greater than $1 \mu\text{m}^{-1}$) is confirmed. The dotted blue curve was obtained using the equation 4.33 from [19].

$$|H_{\text{scw}}(f)|^2 = \frac{k_{\text{B}}T_{\text{G}}}{2\pi\gamma f} \quad (4.33)$$

In this context, we employed $T_{\text{G}}/\gamma = 2000 \text{ Km}^2/\text{J}$, where k_{B} is the Boltzmann constant, and γ is the surface tension. This choice is consistent with the values reported in [19] for the case of silica capillary stretching. As an additional comparison, we added a modified trend to Figure 4.16 (dashed green line) obtained by multiplying Equation 4.33 by $\coth(\frac{\xi}{2})$. Here, ξ is the perimeter of the air holes forming the cladding, which equals $15 \mu\text{m}$ in this example. This trend modulated by the hyperbolic cotangent term appears to better fit the evolution of the PSD at low spatial frequencies for the G#2 fiber. Conversely, for the G#1 fiber, a deviation from this trend is observed, resulting in a $1/f^3$ behavior, similarly to what has been shown in recent studies [106], [118]. While the $1/f$ behavior directly results from the freezing of surface capillary waves, the deviation at lower frequencies for the G#1 case still requires further explanation.

Finally, surface profile measurements using the optical profilometer were applied to all the fibers in the study, and the root mean square (RMS) roughness values were deduced. Figure 4.17 shows the RMS results obtained for G#1 fibers (left side) and G#2 fibers (right side). It is evident that G#1 fibers exhibit RMS roughness values varying around 0.40 nm , as expected with the scenario of capillary wave fluctuations at thermodynamic equilibrium. In contrast, G#2 fibers show a reduced average RMS roughness value around 0.15 nm . These results demonstrate the success of using the shearing technique to improve the quality of the surface surrounding the air core. In this case, a factor of 2.7 reduction in RMS roughness is achieved, which is in relatively good agreement with the expectations from our model that predicted a reduction ratio on $\langle h^2 \rangle$ of $\gamma_{\text{eff}}/\gamma_0 = 3.2$.

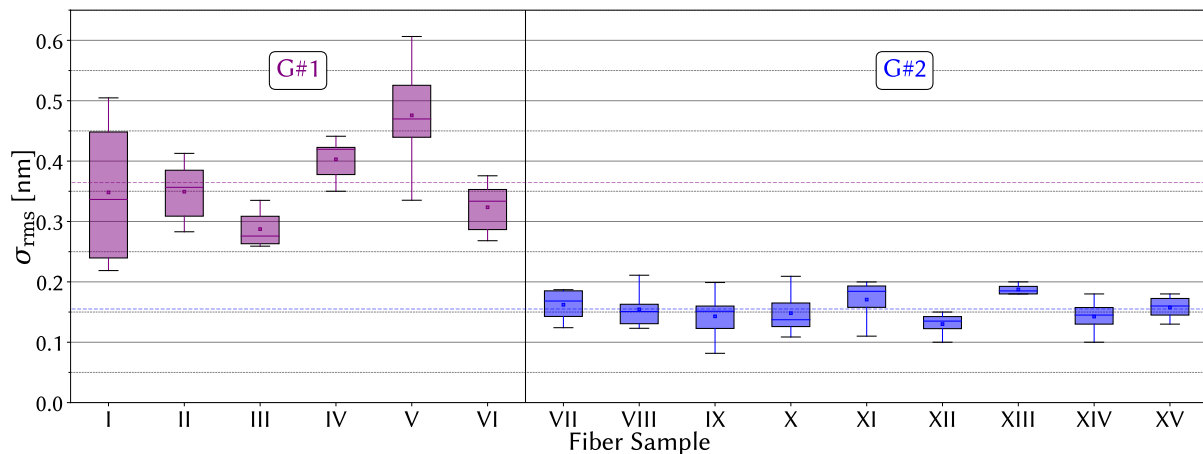


Figure 4.17: Measurement of the inner and outer roughness of the silica membrane surrounding the air core for 5 G#2 fibers manufactured using the shearing technique.

4.4.3 New state-of-the-art for losses in the short wavelengths of the visible and ultraviolet spectrum

As it was presented above, such a reduction in the levels of silica surface roughness should result in a decrease in scattering losses (SSL). In this context, the manufactured fibers were characterized in terms of linear attenuation using the cut-back method. This technique involves measuring the transmission spectrum for a long length of fiber (L_1) and then for a shorter length (L_2) without changing the injection conditions. Attenuation is then determined by taking the difference between the two transmission measurements divided by the value $L_2 - L_1$ and is expressed in dB/km. In our study, a first white light source of the supercontinuum type (a nonlinear PCF fiber associated with a nanosecond pulsed laser emitting at 1064 nm) was used to cover the spectral range from 400 nm to the infrared, along with an optical spectrum analyzer (Ando). For wavelengths below 400 nm, a plasma lamp (Energetiq EQ-99X-FC series) was used as the light source, and the transmitted signal was measured by a spectrometer (Stellarnet). During the measurements, the fiber lengths varied between 100 m and 500 m, depending on the fabrication, and were arranged in loops with a 1 m radius to minimize bending losses. Additionally, the coupling conditions at the fiber input were carefully adjusted using free-space optics to obtain modal content dominated by the fundamental mode. Finally, the fibers were thoroughly inspected to identify and remove scattering points resulting from fabrication defects, thereby minimizing their impact on the measured losses. Figure 4.18 (a) provides an example of measured losses

for two fibers from the two groups with similar tube thicknesses ($t \approx 0.6 \mu\text{m}$). As the core diameters were slightly different ($40 \mu\text{m}$ for fiber V in group G#1 compared to $27 \mu\text{m}$ for fiber X in group G#2, see Table 4.3), a normalization according to the R_{co}^4 rule was applied for a fair comparison to minimize the impact of confinement losses on total losses [105], as shown in Figure 4.18 (b). From these curves, it is evident that there is a clear reduction in losses for the case of G#2, with a tendency to increase for wavelengths below 600 nm. This results in a decrease from 280 dB/m losses for G#1 to a record of 50 dB/km for G#2, a difference of around two orders of magnitude, indicating a significant reduction in SSL, as expected from roughness measurements. To confirm this result, we first looked at the impact of surface roughness on confinement losses alone. This was done by simulating the G#2 fiber for an ideal case (i.e., without surface roughness, shown as a dashed line in Figure 4.18 (c) and for a case that best approximates the fiber X in G#2 (i.e., by including transverse RMS roughness of 0.15 nm on the inner wall of the air tubes, which had been previously measured, shown in red on Figure 4.18 (c)). We note that, although we did not measure the roughness in the transverse direction of the tubes, we assume that variations in transverse surface height follow the characteristics of the roughness measured along the axis of the fiber since its formation is a stochastic process. The results in Figure 4.18 (c) confirm that transverse roughness levels have little impact on CL values in our HCPCF, as we already studied in the previous section of this chapter (see Figure 4.10). Therefore, we can disregard this influence in our subsequent analyses.

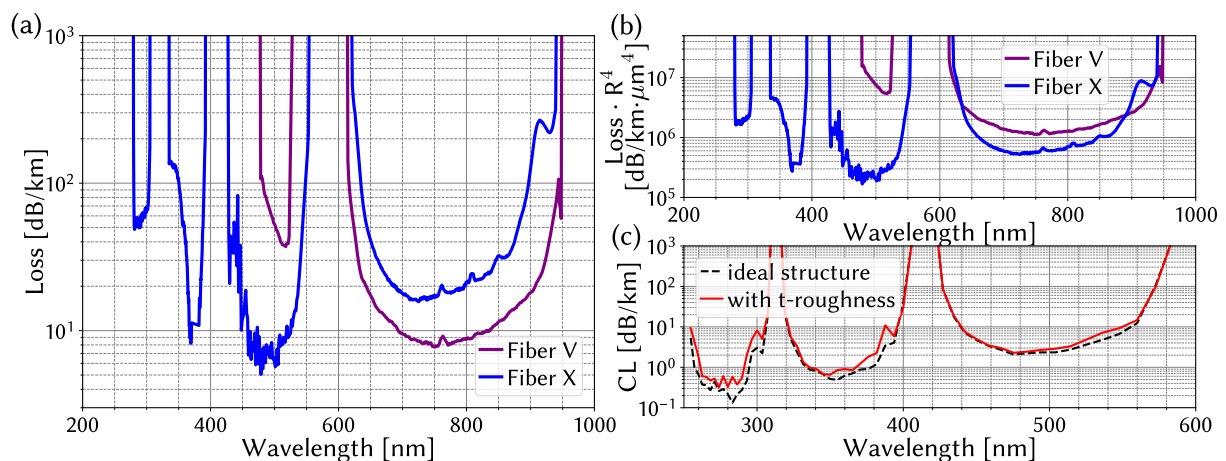


Figure 4.18: (a) Comparison of measured losses for a fiber from G#1 (here fiber VI) and G#2 (here fiber X) presenting an identical silica thickness of 600 nm. (b) Curves normalized by the air core size. (c) Study of the impact of transverse roughness on the CL (dashed line represents ideal structure i.e., without roughness and solid line with an RMS roughness of 0.15 nm).

Therefore, we ultimately sought to determine the contribution of each of the different

sources of loss detailed in chapter 1, namely, CL, SSL, MBL, and $TL = CL + SSL + MBL$ (in this case, BLs are neglected due to the experimental measurement being performed with $R_c = 1$ m). This was done while considering the example of the same two fibers from groups G#1 and G#2. For this purpose, new simulations were conducted in collaboration with the team of Professor Luca Vincetti at the University of Modena in Italy. All the results are presented in Figure 4.19 (a) (fiber from G#1) and Figure 4.19 (b) (fiber from G#2), where experimentally measured losses are shown as solid lines, and curves from simulations for each of the contributions are represented as dashed lines. It should be noted that in simulating SSL losses, we adjusted the parameter denoted as η in the equation 4.11 to best match the calculated total losses to the measured losses. As a result, it appears that between the two fibers from G#1 and G#2, this factor changed from $\eta_{G\#1} = 8.0 \cdot 10^{-3}$ to $\eta_{G\#2} = 1.1 \cdot 10^{-3}$, which corresponds to a reduction by a factor $\sqrt{\frac{\eta_{G\#1}}{\eta_{G\#2}}} \approx 2.7$. This result is highly convincing because it aligns with the experimentally measured reduction in surface roughness between these two fibers. Ultimately, these findings confirm that at short visible and ultraviolet wavelengths, the major contributions to losses are governed by SSL and MBL, which are mechanisms associated with surface roughness. Therefore, by improving surface quality, we can expect to achieve new records of losses in this short-wavelength domain, as demonstrated in Figure 4.19 (b) (or in Figure 4.20 (a), depicted differently with a focus on the spectral region of interest), as well as in another example shown in Figure 4.20 (b).

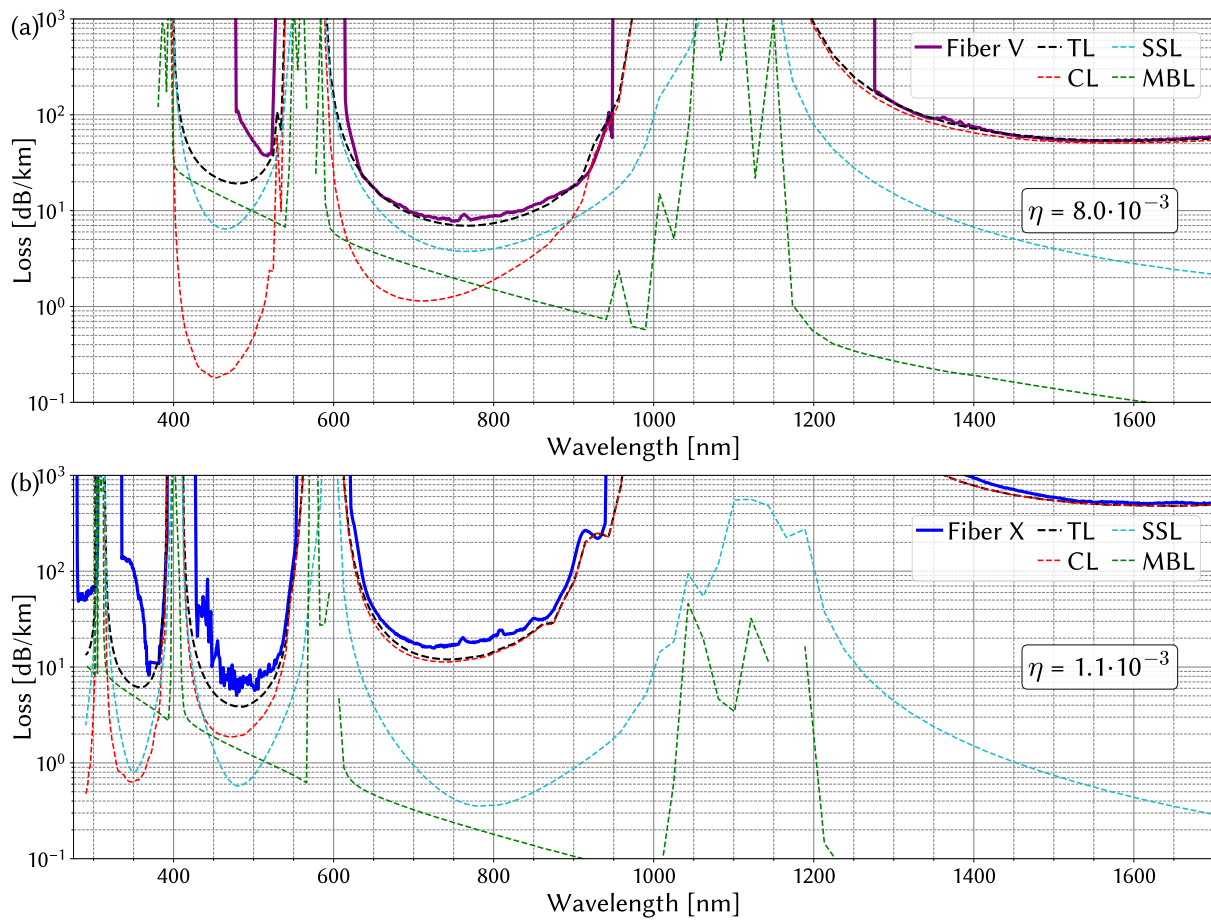


Figure 4.19: Numerical calculations under Comsol to evaluate the weight of each of the loss sources namely CL, MBL, SSL, and TL (here the curvature losses are neglected) in the case of (a) standard fabrication (G#1) and (b) when the shearing technique is applied (G#2, fiber X).

For the first case (fiber X), the measured losses exhibit minima at 50.0 dB/km at 290 nm, 9.7 dB/km at 369 nm, and 5.0 dB/km at 480 nm. In the second fiber (fiber XII), the core diameter was increased to 42 μm , with slightly thicker silica bridges ($t \approx 0.9 \mu\text{m}$), resulting in very low losses at new wavelengths, namely 0.9 dB/km at 558 nm and 1.8 dB/km at 719 nm.

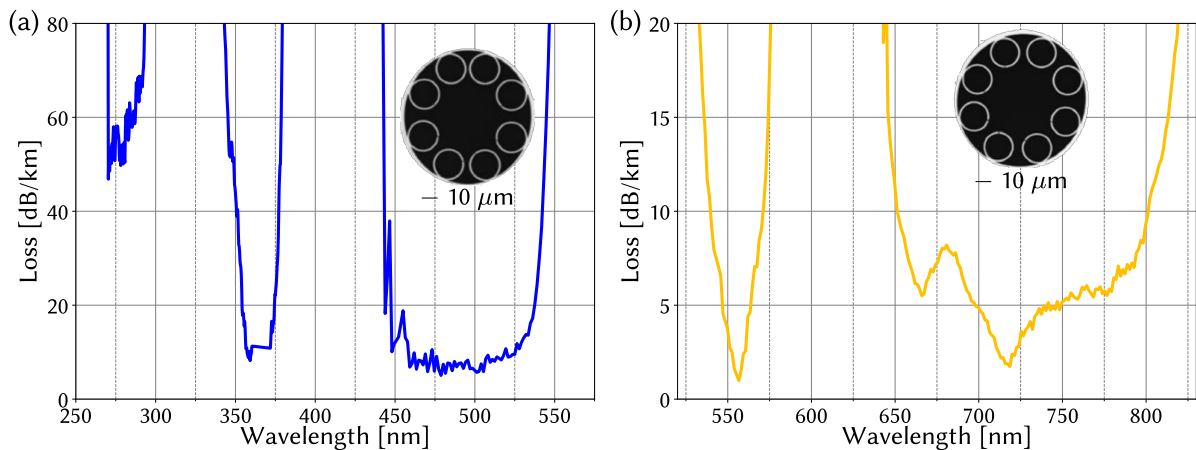


Figure 4.20: Experimental loss curves for two record fibers with low surface roughness (a) fiber X and (b) fiber XII. An image of their cross-section is provided as an insert.

Finally, Figure 4.21 provides context by comparing these values to the best-performing IC HCPCFs in the state-of-the-art for the spectral range from 250 nm to 900 nm. Additionally, the Rayleigh scattering limit of silica (SRSL) is included in Figure 4.21. The measured losses in our two low surface roughness IC HCPCFs represent record-breaking values for short visible and UV wavelengths and are below the SRSL limit, which represents the fundamental limit for losses in silica solid-core fibers. These results have been published in the high impact journal *Nature Communications* [43].

It is worth noting that this new state-of-the-art has been demonstrated using a relatively simple fiber architecture (8-tube lattice), suggesting that light confinement could be further improved with more complex structures (such as hybrid or nested lattice IC HCPCF), potentially achieving losses below the dB/km threshold in the UV.

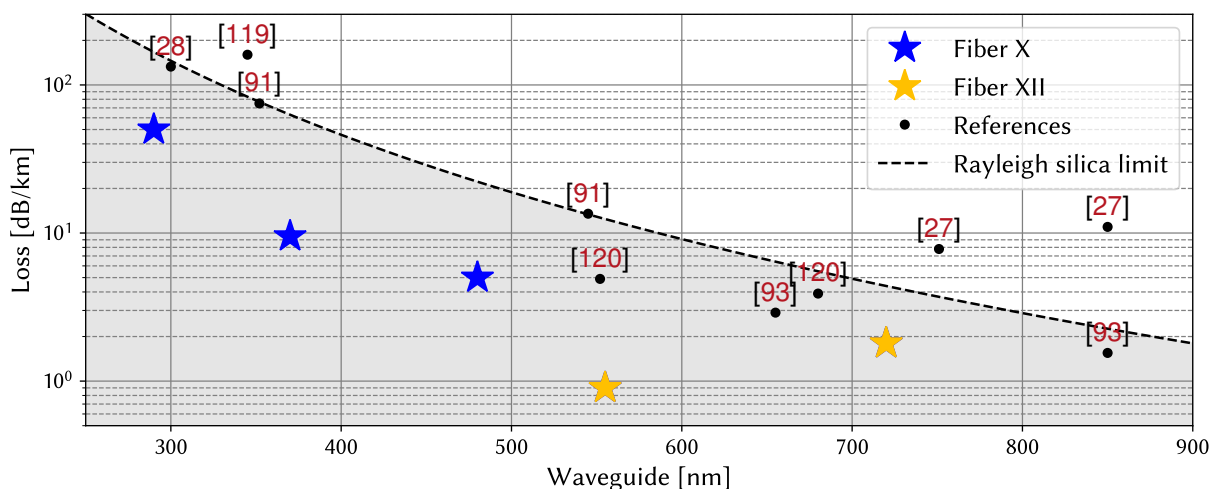


Figure 4.21: Plot of the performance achieved by the two fibers in comparison with the state of the art of IC HCPCFs and the fundamental Rayleigh limit of solid core silica fibers.

4.5 Opto-thermal process for the fabrication of HCPCFs

We saw that the root mean square (RMS) of surface roughness can be reduced by increasing the surface tension through the application of shear stress [43]. Here we explore a novel technique [108], based on the control of the spectral structure of roughness. In our case, this control is achieved by exciting materials with a laser to act on the surface through the photoelastic effect. Figure 4.22 schematically illustrates its principle. In this setup, a laser beam is applied to the fibers within the fiber drawing furnace (i.e., during the molten phase of silica). The power absorbed by the viscoelastic medium's surface undergoes a geometric deformation induced by a change in temperature, through the phenomenon of thermoelasticity, itself induced by photo-absorption and thermal expansion. In other words, we have $\Delta h/h = \alpha_{th}\Delta T$, where α_{th} is the coefficient of thermal expansion, ΔT is the change in temperature, and $\Delta h/h$ is the relative change in the length of the medium. Practically, the temperature variation is a temperature modulation, which can be achieved through the photo-absorption of a laser modulated in power. This can be expressed as a modulation of the change in length: $\frac{\Delta h}{h} \propto \alpha_{th}P_{abs} \cos(2\pi\nu_{mod}t)$, where P_{abs} is the laser power absorbed by the medium. It's worth noting that these phenomena are distinct from those associated with the inscription of a Bragg grating in fibers (e.g., photosensitivity), which involve electronic restructuring and result in a change in the medium's refractive index [121].

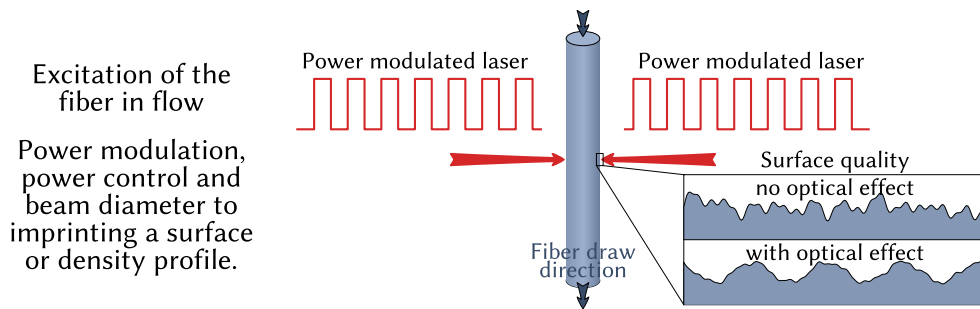


Figure 4.22: Illustration of the second process called “opto-thermal” to control the surface quality during the fiber draw.

Revisiting the linearized Navier-Stokes equation introduced in the first section of the chapter in the case of the presence of a harmonic excitation in the form of $F \cos(\omega_{at})$, we can express the equation for the surface roughness height as follows:

$$\frac{\partial^2 h(x, t)}{\partial t^2} + \Gamma \frac{\partial h(x, t)}{\partial t} = -g\nabla^2 h(x, t) + F \cos(\omega_{at}) + \xi(x, t) \quad (4.34)$$

with Γ the damping coefficient of the capillary wave is $\xi(x, t)$ is the term representing

thermal fluctuations, so $\langle \xi(x, t)\xi(x', t') \rangle = 2k_B T \Gamma \delta(x - x')\delta(t - t')$. Without resorting to solving this equation rigorously, we can write the solution in Fourier space as a sum of two terms representing the displacement due to the external force, $h_F(q)$, and to thermal fluctuations $\tilde{h}(q, \omega)$:

$$\tilde{h}(q, \omega) = h_{PT}(q)\delta(\omega - \omega_d) + \tilde{h}_t(q, \omega) \quad (4.35)$$

This expression clearly shows that the spectral structure of the roughness can be modified. It is also important to note that the finite diameter of the laser beam alters the boundary conditions, which can affect both the spectral structure of the PSD and the amplitude of the capillary modes. Additionally, by carefully choosing the amplitude and frequency of this external force, one can control the oscillation regime. For example, you can achieve a critical regime, underdamped or overdamped, for a specific capillary mode. For more details on this new technique, please refer to the Benabid patent [108]. Here, we'll only highlight the key control parameters required to successfully control the surface profile of silica membranes in HCPCFs. To do this, we remind you that the total laser power, P , is given by:

$$P = P_0 + P_m \sin(2\pi\nu_{\text{mod}}t) \quad (4.36)$$

Here, ν_{mod} is the modulation frequency of the laser power. P_0 represents the continuous or DC part. P_m is the modulated power. The expression of P as a function of the total (or maximum) power can also be written in the form:

$$P = P_T \left[1 - \frac{P_m}{P_T} (1 - \sin(2\pi\nu_{\text{mod}}t)) \right] \quad (4.37)$$

The ratio P_m/P_T represents the modulation depth. The amplitude of the surface deformation induced by the photo-thermal effect in the case of a collimated (non-focused) laser, power-modulated at frequency ν_{mod} and normally incident on the surface, can be quantified by its response function (in length units), provided below [108]:

$$h_{PT}(\nu) = \sqrt{\frac{2}{\pi}} \frac{\alpha_{\text{th}}}{\kappa} (1 + \sigma) \begin{cases} \frac{\langle P_{\text{abs}} \rangle \nu_c}{\nu} & \text{if } \nu \gg \nu_c \\ \langle P_{\text{abs}} \rangle & \text{if } \nu \ll \nu_c \end{cases} \quad (4.38)$$

Here, α_{th} , κ , and σ represent the coefficient of thermal expansion, thermal conductivity, and Poisson's ratio of the medium (e.g., glass), respectively. $\nu_c = (2\pi^{-1})\sqrt{\kappa/\rho C w_0^2}$, where ρ and C are the density and heat capacity of the heated medium, and w_0 is the effective laser radius. For silica, this cutoff frequency can be expressed as $\nu_c = 2\text{Hz} \frac{100\mu\text{m}}{\omega_0}$,

which results in a cutoff frequency of 2 Hz for a laser with an effective diameter of 200 μm . $\langle P_{\text{abs}} \rangle$ is the average laser power absorbed by the stretched preform. This is determined by both the absorption coefficient of the medium at the laser wavelength and the parameters P_0 , P_m/P_T mentioned earlier. In this case, the characteristic times for photo-absorption are much faster than to be affected by the value of $\langle P_{\text{abs}} \rangle$. This gives us :

$$\langle P_{\text{abs}} \rangle = \alpha_{\text{abs}} \sqrt{P_0^2 + \frac{P_m^2}{2}} \quad (4.39)$$

We note that in the case of maximum modulation depth (i.e. $P_0 = 0$ and $P_m = P_T$), we have $\langle P_{\text{abs}} \rangle = \alpha_{\text{abs}} P_m / \sqrt{2}$. Thus, for small values of $P_m/P_T \approx 0$, we have $\langle P_{\text{abs}} \rangle = \alpha_{\text{abs}} P_0$. Consequently, in the case of no modulation, there is a constant and “static” deformation of

$$h_0 \approx \sqrt{S_{PT}(\nu \rightarrow 0)} \approx \frac{1}{\pi} \left(\frac{\alpha_{th}}{\kappa} \right) (1 + \sigma) \alpha_{\text{abs}} P_0 \quad (4.40)$$

For silica, the thermomechanical values are given in the table 4.4:

Table 4.4: Thermomechanical properties of silica.

Density : ρ , [$\text{kg}\cdot\text{m}^{-3}$]	2201
Thermal expansion coefficient : α_{th} , [K^{-1}]	$4.8 \cdot 10^{-7}$
Thermal conductivity : κ , [$\text{Wm}^{-1}\text{K}^{-1}$]	2.7
Heat capacity : C_p , [$\text{J/kg}\cdot\text{K}$]	1052
Viscosity : η , [$\text{Pa}\cdot\text{s}$]	$10^{6.2}$ at 1734 °C 10^3 at 2354 °C
Surface tension : γ , [$\text{J}\cdot\text{m}^{-2}$]	0.3

Table 4.5 summarizes the impact of laser parameters on surface structuring:

Table 4.5: Impact of laser parameters on surface profile control.

Continuous power (P_0)	1. Primary surface profile (long range)
Modulation frequency ν_{mod}	1. Selective excitation of short-range CWs 2. Control of the scattering length
Modulation depth	1. Control of the amplitude of short-range CWs
Beam size	1. Control of the relaxation time of CWs 2. Control of the boundary conditions of the CWs (i.e., control of the phases of the CWs)
Laser-furnace distance	1. Adjusting to the viscoelastic state of the CWs induced by thermodynamic noise in the thermal furnace. 2. Control of the boundary conditions of the CWs (i.e., control of the phases of the CWs)

From these results, it becomes possible to establish operating conditions for shaping the surface of glass subjected to thermally induced CW (generalizable to volume). Dimensioning our device can be achieved by establishing a hierarchy among the characteristic times (or equivalently: characteristic lengths) associated with the different effects underlying the generation of surface capillary waves. The table below (Table 4.6) summarizes the characteristic times for given conditions:

Table 4.6: Characteristic times of the different underlying effects generating the CWs for the following operating conditions ($w_0 = 100 \mu\text{m}$, $v_d = 10 \text{ m/min}$, $10 \text{ Hz} < \nu_{\text{mod}} < 1 \text{ kHz}$).

Characteristic Time	Associated Phenomenon	Expression	Range
Cooling time (τ_{cool})	The cooling time of a heated glass exiting the furnace	$\frac{\rho C_p}{\kappa} \frac{V}{A} 2w_0$	1 ms - 60 ms
Laser-material interaction time (τ_{int})	The interaction time with the laser of a glass (e.g. fiber) moving at a uniform speed v_d	$\frac{2w_0}{v_d}$	100 μs – 10 s
Laser-material modulation time (τ_{las})	The interaction time with the laser of a glass (e.g., fiber) moving at a uniform speed v_d	$\frac{1}{\nu_{\text{mod}}}$	1 ms – 10 s
Thermal relaxation time (τ_{therm})	The cooling time of a glass heated by photo-absorption	$\frac{\rho C_p}{\kappa} w_0^2$	8 ms – 3 s
Correlation time of a CW (τ_{CW})	The time associated with the correlation length of a CW	$\frac{\sqrt{\gamma/\rho g}}{c_s}$	0.7 μs – 1 μs

From this set of trends, we can deduce initial operating conditions to be followed during the fabrication of fibers using the “opto-thermal” technique, which are detailed in Table 4.7.

Table 4.7: Operating conditions of the laser system for surface shaping.

Description of the condition	Condition on the device parameters
The dominant CW amplitude induced by photo-elasticity must be greater than the dominant CW amplitude by thermal noise. This condition is imposed in order to shape the surface through photo-elasticity.	$P_0 \geq 45 \text{ W}$
The furnace-laser beam distance, d , must be sufficiently short so that the temperature of the fiber at the furnace exit, T_h , remains above the softening temperature. A condition for the CWs induced in the furnace to remain dynamic and not solidified (or frozen).	$d \leq v_d \tau_{\text{cool}} \ln \left(\frac{T_h}{T_{\text{soft}}} \right)$ For silica $d \leq 10 \text{ mm}$ for $v_d = 10 \text{ m/min}$
The transit time of the fiber/preform in the laser beam must be sufficiently long for the photo-elasticity phenomenon to establish itself over the entire volume of the glass (mislead) in the laser beam.	$\tau_{\text{int}} \geq \max(\tau_{\text{las}}, \tau_{\text{therm}})$
One of the strategies to dampen the amplitude of the CWs induced by thermal noise in the furnace is to neutralize them by interference with the CWs generated by photo-elasticity. This implies that the frequency range of the CWs induced by photo-elasticity is the same as that of the CWs induced by thermal noise. This, consequently, determines a range for the laser modulation frequency.	$\nu_{\text{mod}} \in 2\pi^{-1} \left[g \sqrt{\frac{\rho h}{\gamma}}, \sqrt{\frac{\gamma}{\rho h^3}} \right]$ For silica $\nu_{\text{mod}} \in [10 \text{ Hz}, 8 \text{ kHz}]$
Another strategy to flatten the roughness is to exploit the wave properties of the CWs and their boundary conditions to set their amplitude to zero by superimposing the position of the valley of a CW with the edge of the laser beam area. This condition can be achieved by controlling the laser diameter (see opposite) and/or the position of the latter.	$k_{cw} \cdot 2\omega_0 = (2n + 1)\pi$ For the dominant CW $2\omega_0 \sqrt{\frac{\rho g}{\gamma}} = (2n + 1)\pi$ (here n an integer). For silica $2\omega_0 = (2n + 1) \cdot 11 \text{ mm}$

4.5.1 Fiber drawing set-up

In order to implement the opto-thermal technique during the fiber drawing process, a new opto-thermal furnace was designed and sized¹. This furnace is a modified conventional thermal furnace that can accommodate laser beams within it. A detailed description of the furnace cannot be provided in this manuscript for intellectual property reasons.

Figure 4.23 summarizes the operation of this furnace. It schematically shows the optical excitation (top and left of the figure). The system includes a laser beam directed towards the fiber inside the furnace. The transmitted power is measured by a power meter positioned as shown in the diagram. A camera is used for aligning the laser with the flowing fiber (bottom left of the figure). The laser is a continuous-wave laser emitting at a wavelength of 1064 nm, and its power can be set to a maximum value of 400 W. Finally, the beam size is controlled by a telescope.

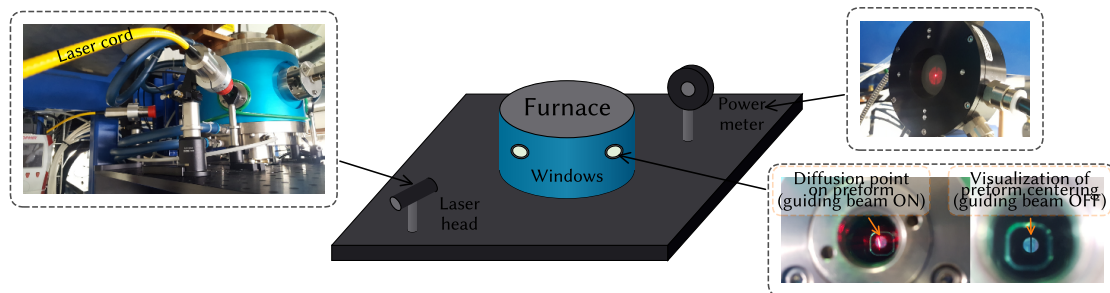


Figure 4.23: Experimental configurations of the opto-thermal manufacturing device.

4.5.2 Fabrication and characterization of the produced fibers

A series of HCPCF fabrication were carried out, focusing on the design of IC HCPCFs with 8 tubes, which was used in my previous studies. The geometric parameters in terms of core diameter ($40\ \mu\text{m}$), hole size ($15\ \mu\text{m}$), gap ($3 - 5\ \mu\text{m}$), and the value of the silica bridge thickness ($1\ \mu\text{m}$) were chosen to be as close as possible to facilitate result analysis.

Opto-thermal Process versus thermal Process

In this context, initial studies were conducted using a single laser beam. During each fiber draw, a standard fiber to serve as a reference (i.e., laser OFF) and an “opto-thermal” fiber (i.e., laser ON) were fabricated. Laser parameters were chosen based on

¹The design and sizing of the opto-thermal furnace were carried out by F. Benabid.

theoretical conclusions, with an average power greater than 45 watts and a modulation frequency in the range of several tens of Hertz. A typical example of the fabrication process is summarized in Table 4.8.

Table 4.8: Laser parameters used for the manufacturing of 8-tube IC HCPCFs noted $F_{\text{opto}\#1}$, (D_{ext} : external diameter, P_1 : power of laser 1, and F_1 : modulation frequency of laser 1).

$F_{\text{opto}\#1}$	Shear process	D_{ext} (μm)	P_1 [W]	F_1 [Hz]
$F_{\text{opto}\#1-0}$	no	260	-	-
$F_{\text{opto}\#1-1}$	no	260	145	60

Figure 4.24 summarizes the structural and optical characteristics, including a cross sectional image of the fiber, loss measurements using the cut-back technique over a 100 m segment, and a surface profile obtained by the optical profilometer with the associated PSD curve². The results show a difference in the spectral profile between the fiber made using conventional process and the one with laser assistance. It is observed that even though the RMS roughness of the surface has slightly increased, transmission losses have significantly decreased for wavelengths shorter than 1 micron. This can be explained by the spectral structure of the PSD, where the PSD amplitude of the components at the lower range of spatial frequency are lower compared to the case of conventional process (see Figure 4.24 (d)), which should imply a reduction in scattering loss.

²All the surface roughness measurements carried out by Ali Al Dhaybi.

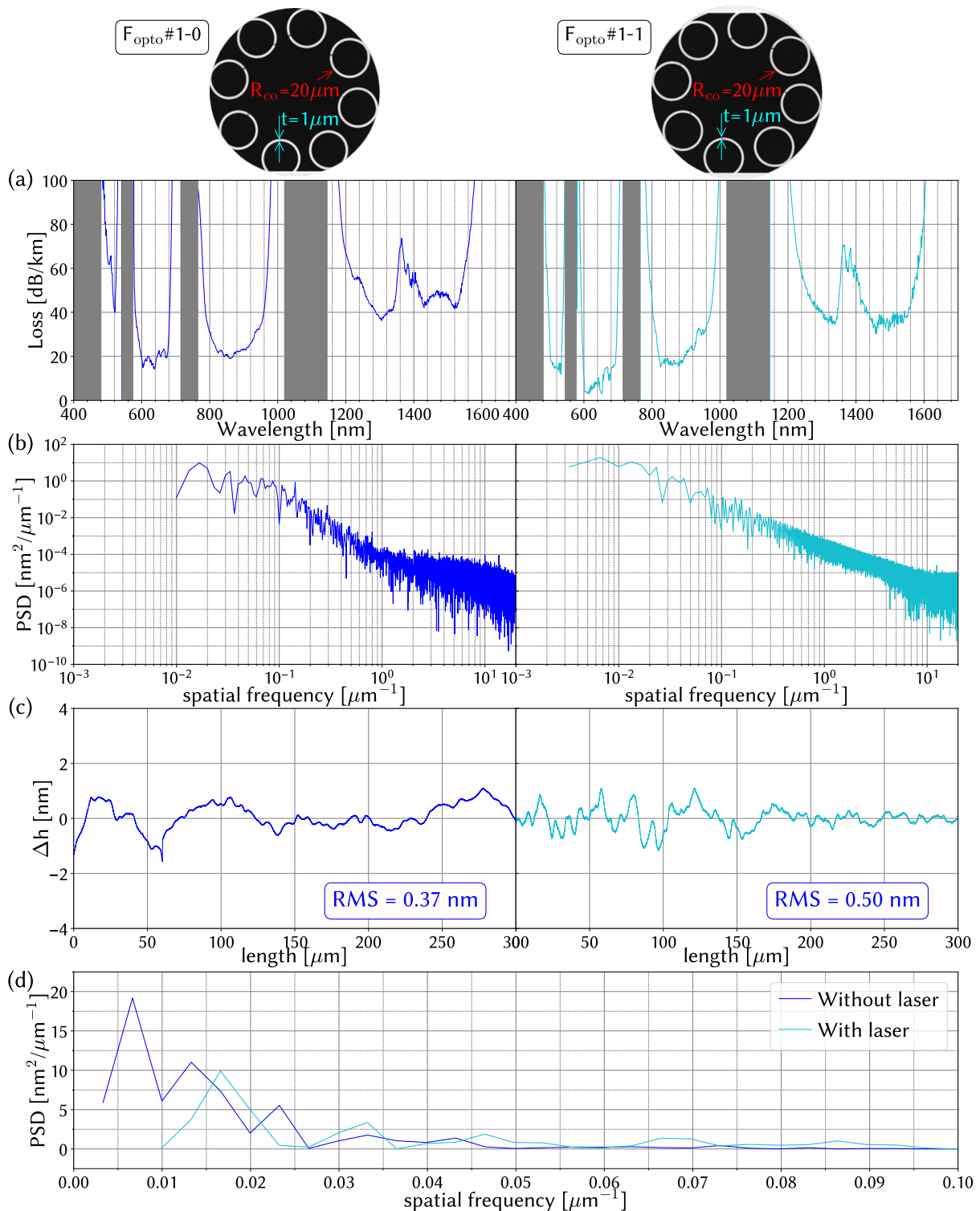


Figure 4.24: Linear characterization of fibers $F_{\text{opto}} \#1-0$ (laser OFF) and $F_{\text{opto}} \#1-1$: (a) measured loss, (b) roughness profiles, (c) Evolution of the PSD (d) in linear scale.

After these promising results, a second study was then initiated. This time we

combine the shear process with the opto-thermal approach. Similarly, a table and a figure present the results obtained.

Table 4.9: Laser parameters used for the manufacturing of 8-tube IC HCPCFs noted as $F_{\text{opto}\#2}$, in the presence of the shear process.

$F_{\text{opto}\#2}$	Shearing process	D_{ext} [μm]	P_1 [W]	F_1 [Hz]
$F_{\text{opto}\#2-0}$	yes	260	-	-
$F_{\text{opto}\#2-1}$	yes	260	65	5

Firstly, we note that the reduction in surface roughness obtained through the use of shear is well observed when comparing the two reference fibers $F_{\text{opto}\#1-0}$ and $F_{\text{opto}\#2-0}$, as we go from an RMS of 0.37 nm to 0.2 nm. Then, by carefully examining the surface profile of the fiber $F_{\text{opto}\#2-1}$, unlike the previous case, the surface roughness deviate strongly from a stochastic profile and exhibits a slight modulation at a spatial frequency of 15 μm , which is also associated with an increase in amplitude by a factor of 8.

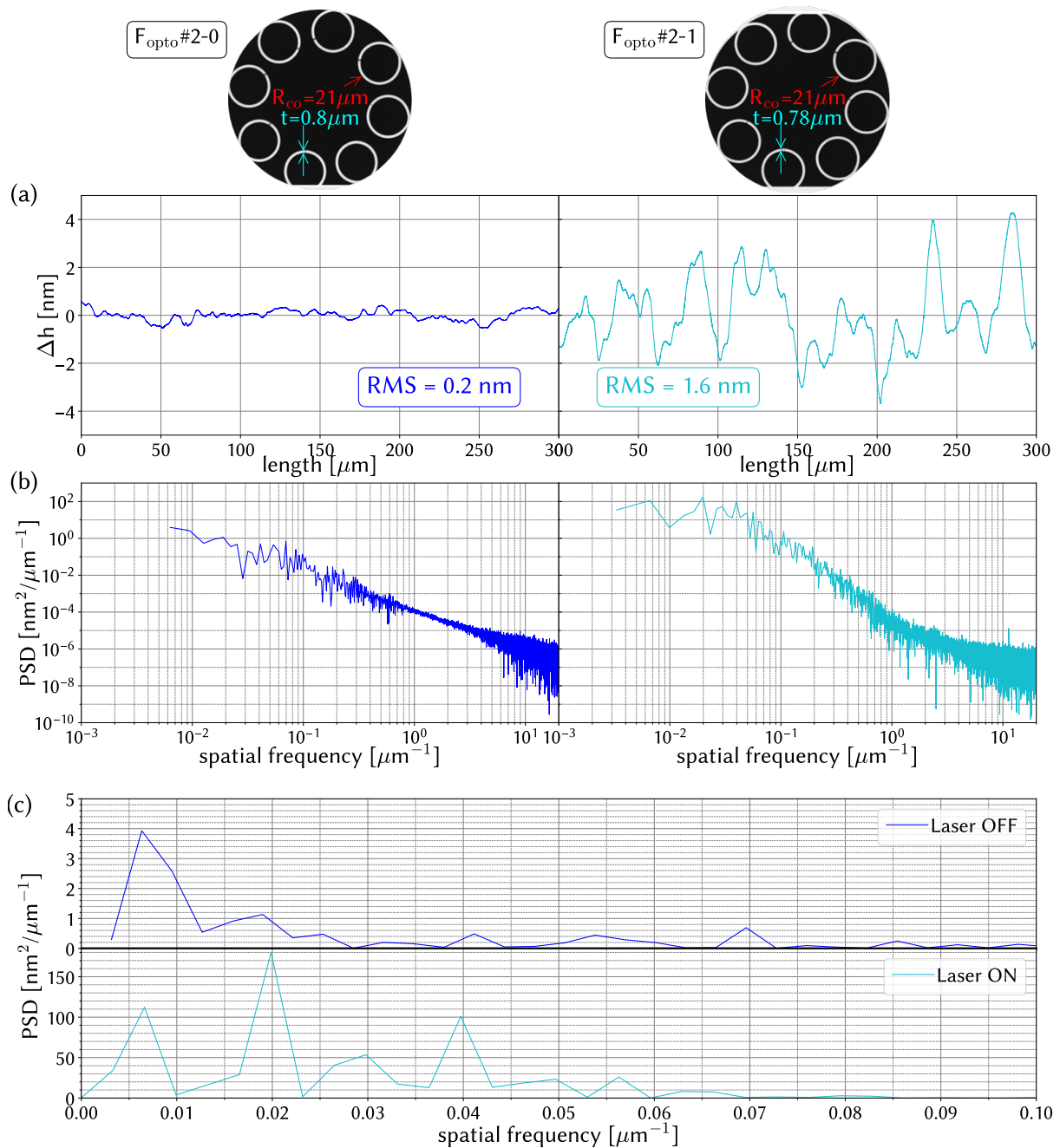


Figure 4.25: Linear characterization of the fibers F_{opto}#2-0 (laser OFF) and F_{opto}#2-1 (laser ON): (a) roughness profiles, (b) evolution of the PSD and (c) evolution of the PSD in linear scale.

Effect of power modulation frequency

Due to this result, in the very last months of my thesis, additional studies were initiated based this time on the use of 2 laser beams to see if the phenomenon observed previously could be reproduced or even amplified. For this, we decided to use a first

unmodulated laser to soften the glass associated to a second laser which will use the same modulated powers of a hundred Watts but with frequencies that we will choose to vary. Table 4.10 summarizes the configurations studied.

Table 4.10: Laser parameters used for the manufacturing of 8-tube IC HCPCFs noted $F_{\text{opto}}\#3$.

$F_{\text{opto}}\#3$	Shear process	D_{ext} , [μm]	P_1 , [W]	F_1 , [Hz]	P_2 , [W]	F_2 , [Hz]
$F_{\text{opto}}\#3-0$	yes	260	-	-	-	-
$F_{\text{opto}}\#3-1$	yes	260	115	CW	85	2
$F_{\text{opto}}\#3-2$	yes	260	115	CW	85	50
$F_{\text{opto}}\#3-3$	yes	260	115	CW	85	100
$F_{\text{opto}}\#3-4$	yes	260	115	CW	85	400

The characterizations of surface roughness are plotted in Fig. 4.26 (a) for each fiber. A modulation of the surface profile according to the axis of analysis (or fiber propagation) is this time clearly observed. A link between the modulation frequency of laser 2 and this oscillation seems to be demonstrated here, as for the case of $F_{\text{opto}}\#3-1$ a period of 160 μm is measured while it changes to 24 μm for $F_{\text{opto}}\#3-2$ as expected by the applied change in modulation frequency. For modulations increased to a hundred Hz, the same effect is present but the plots are less convincing due to the spatial resolution of our optical profilometer's measurement limited to few microns. It remains to mention that the increase in this oscillation is associated with an increase in the amplitude of the roughness which goes from 0.18 nm to more than 10 nm.

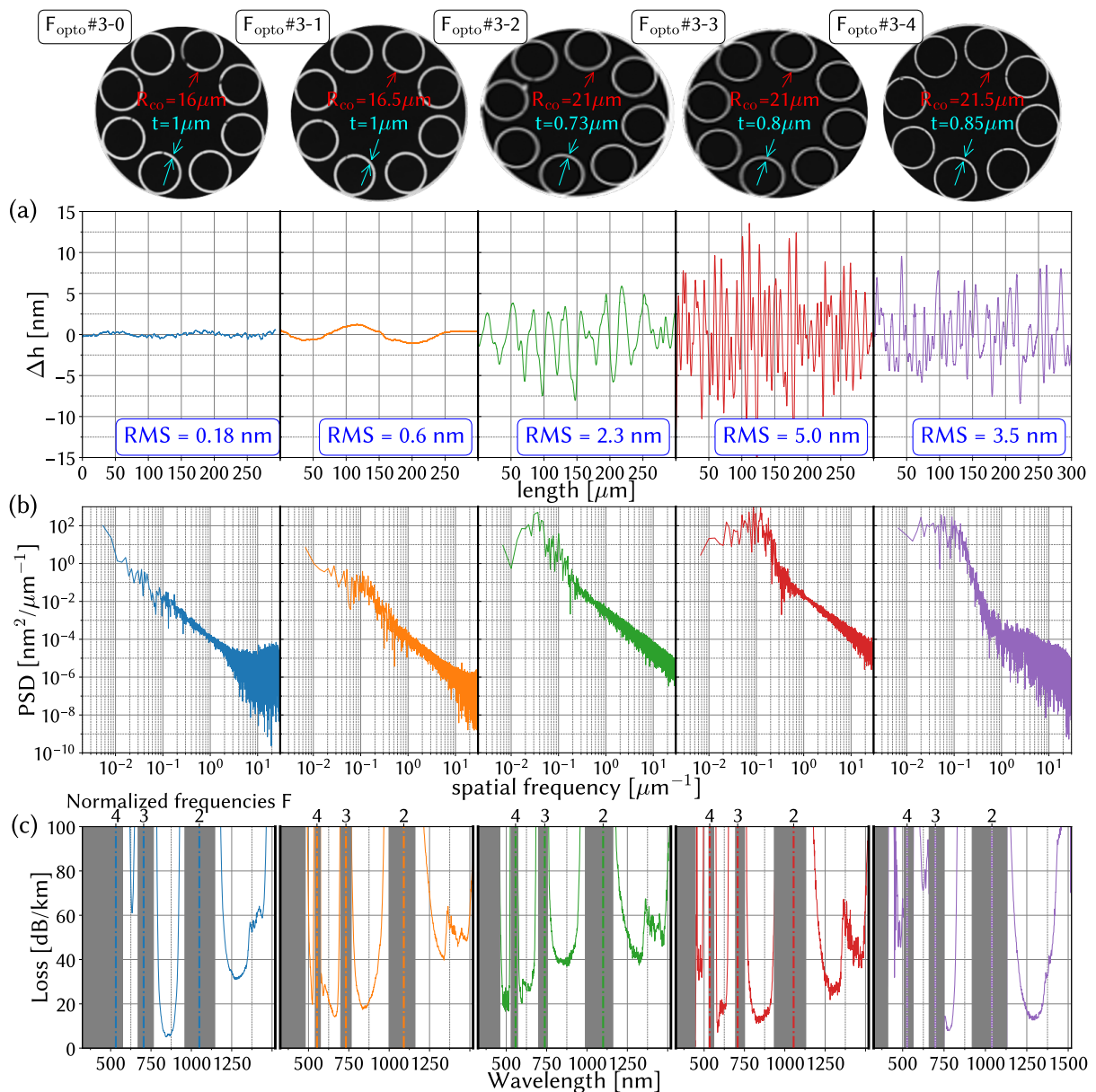


Figure 4.26: Linear characterization of fibers F_{opto} #3-0 (laser OFF), F_{opto} #3-1 (laser 1 ON CW and laser 2 ON modulation at 2 Hz), F_{opto} #3-2 (laser 1 ON CW and laser 2 ON modulation at 50 Hz), F_{opto} #3-3 (laser 1 ON CW and laser 2 ON modulation at 100 Hz), and F_{opto} #3-4 (laser 1 ON CW and laser 2 ON modulation at 400 Hz): (a) roughness profiles, (b) evolution of the PSD and (c) measured loss.

The losses were then measured for all the fibers. For the case of the F_{opto} #3-0 where shear is applied alone, minimum losses of 5 dB/km around 850 nm are measured which once again confirms the impact of the shear method. In addition, it should also be noted that for the F_{opto} #3-1, F_{opto} #3-2, and F_{opto} #3-3 fibers, the losses at short visible wavelengths are slightly improved with values reduced around 20 dB/km at 500 nm.

This point seems to be further confirmed by the analysis of the PSD which shows that by increasing the modulation frequency of the laser, the number of peaks becomes much dense with a more pronounced presence at higher spatial frequencies. Indeed, as shown in Fig. 4.27 (b), the $F_{\text{opto}} \#3-0$ presents a single peak centered

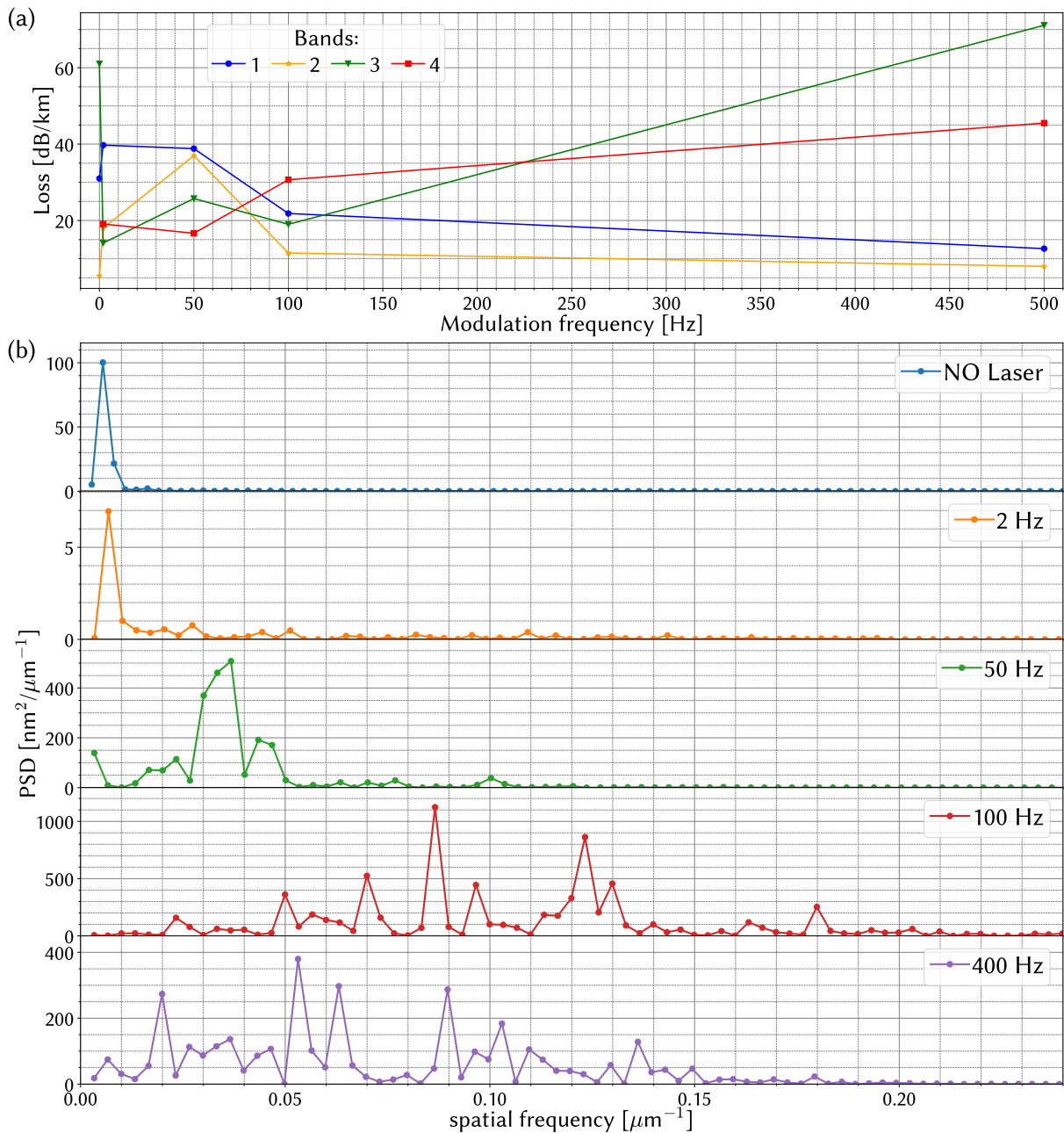


Figure 4.27: (a) Loss at minimum of different transmission band vs modulation frequency. (b) Evolution of the PSD in linear scale for the fibers $F_{\text{opto}} \#3-0$ (laser OFF), $F_{\text{opto}} \#3-1$ (laser 1 ON CW and laser 2 ON modulation at 2 Hz), $F_{\text{opto}} \#3-2$ (laser 1 ON CW and laser 2 ON modulation at 50 Hz), $F_{\text{opto}} \#3-3$ (laser 1 ON CW and laser 2 ON modulation at 100 Hz), and $F_{\text{opto}} \#3-4$ (laser 1 ON CW and laser 2 ON modulation at 400 Hz).

at $0.0054 \mu\text{m}^{-1}$ with an amplitude of $100 \text{ nm}^2/\mu\text{m}^{-1}$. When the laser system is activated with a modulation frequency of 2 Hz at laser 2, the peak frequency is shifted slightly to $0.006 \mu\text{m}^{-1}$ with an amplitude reduced to $7 \text{ nm}^2/\mu\text{m}^{-1}$ ($F_{\text{opto}} \#3-1$). This phenomenon is then amplified for the case of the $F_{\text{opto}} \#3-2$ where a maximum of $500 \text{ nm}^2/\mu\text{m}^{-1}$ is obtained at the spatial frequency of $0.036 \mu\text{m}^{-1}$. When the modulation frequency reaches a hundred Hz ($F_{\text{opto}} \#3-3$), a multitude of peaks appear in the range from $0.025 \mu\text{m}^{-1}$ to $0.18 \mu\text{m}^{-1}$ with a maximum exceeding $1000 \text{ nm}^2/\mu\text{m}^{-1}$, all shifted to higher spatial frequencies. Finally, for the F_{opto} fiber #3-4, a similar behavior is observed but this time with an inverted shift towards short spatial frequencies. This last observation could explain that the loss curve of the $F_{\text{opto}} \#3-4$ approaches that of the $F_{\text{opto}} \#3-0$. Although it is difficult to really give a conclusion, it seems that using too much power modulation is not beneficial. It is therefore important to emphasize that at this stage the optimum fiber parameters have not yet been determined. Thus, even if these first results are most encouraging because they demonstrate for the first time that it is possible to control the roughness profile during fiber drawing by making it non-stochastic, efforts must be continued to be able to achieve better performances.

4.6 Conclusion

In this chapter, we delve into the ongoing challenge of surface roughness in HCPCF. The initial section provides a concise overview of surface capillary waves, which are responsible for generating silica roughness during the fiber drawing process. We then introduce models to incorporate these phenomena into numerical mode-solving simulations. Notably, we propose a method for generating transverse perturbations to mimic roughness profiles, employing coupling coefficients between core/cladding modes and leveraging discrete Fourier transform techniques.

Our simulations involve HCPCF with transverse roughness, and we investigate its impact on confinement loss. In the subsequent part, we explore two novel fabrication processes aimed at reducing and controlling roughness during fiber drawing. One approach involves inducing shear stress by using counter-directional gas and glass flows, leading to a remarkable threefold reduction in surface roughness. This method results in the production of tubular-lattice IC HCPCFs with exceptional low-loss properties, including 50 dB/km at 290 nm, 9.7 dB/km at 369 nm, 5.0 dB/km at 480 nm, 0.9 dB/km at 558 nm, and 1.8 dB/km at 719 nm. These achievements are theoretically substantiated through scaling formulas and have been published in Nature Communications.

Finally, we introduce a second process known as “opto-thermal” and initiate its

exploration. A new furnace, compatible with laser beam systems, has been designed and integrated into the fiber drawing tower. By adjusting laser powers and modulation frequencies, promising results have been observed, leading to the generation of non-stochastic roughness profiles. These findings represent a compelling avenue for my thesis work, with the potential application of this process to novel hollow-core fibers, particularly in the realm of optical telecommunications.

Chapter 5

Development of (2D + 1) model for confinement and scattering

IN this chapter, we present an innovative approach for simulating light propagation within HCPCF. This novel technique, referred to as the “2D+1 numerical simulation”, leverages mode coupling theory and the previously described mode solver to estimate the surface scattering loss (SSL). This approach provides a quick and simple tool for 3D light propagation in HCPCF. The 2D+1 numerical simulation methodology takes into account both the core-guided modes as solved numerically and the coupling coefficient between the core mode with different surface roughness profile. While the 2D+1 approach is approximate in nature, the results obtained are highly promising as they successfully replicate the spectral structure of SSL. This suggests that the 2D+1 simulation method holds great potential for accurately capturing the effects of surface roughness on light propagation in HCPCF.

Table of content

5.1	Introduction or problem framing	135
5.2	Basic principle	136
5.3	Fiber twist and tilt induced loss	138
5.4	Scattering point	143
5.5	Surface roughness	146
5.6	Conclusion	154

5.1 Introduction or problem framing

All the simulations performed so far are based on 2D mode solving FEM approach. This means that the fiber structure is uniform along its propagation axis. Indeed, 2D simulations do not give us information on the propagation dynamic because z-axis is uniform due to the fundamental assumption ($\frac{\partial}{\partial z} = 0$). Consequently, effects such as mode coupling, surface scattering loss or microbending loss couldn't be simulated with a 2D mode solver. So far SSL and MBL are added to the transmission loss using empirical analytical expressions. Furthermore, chapter 4 showed that the surface roughness profile must be taken fully to have rigorous results, and thus indicating that 3D simulations are required.

Several 3D techniques have been developed in the past decades, with the prominent being Finite-Difference Time-Domain (FDTD) technique, 3D Finite Element Method (FEM), Beam Propagation Method (BPM) and Mode Expansion Methods (MEM). The FDTD is a full-vector, 3D electromagnetic simulation technique that can model light propagation in microstructured optical fibers with high accuracy. It can handle complex geometries and structural variations along the z-axis, making it suitable for a wide range of fiber designs. However, FDTD simulations are computationally intensive and require significant computational resources and time. FEM is a versatile numerical technique in simulating optical waveguides and fibers. However, like FDTD, 3D-FEM simulations can be computationally demanding. The BPM is a numerical method used for simulating light propagation in waveguides, including microstructured optical fibers. It's based on the split-step approach and can handle both 2D and 3D simulations, depending on the specific implementation. BPM is computationally less demanding than FDTD or 3D-FEM, however, it is limited to a very limited spatial modes and it is thus challenging to use it to simulate the dynamic of scattered light and its coupling to different guided modes. In FEM we can expand the field distribution into a set of guided modes and calculating the evolution of mode coefficients along the fiber's length. This approach is particularly useful for modeling the behavior of specific modes and their interactions. However, its implementation is too complex and prone to mistakes for it requires prior assumptions on the propagating modes.

Because of the above shortcomings, semi-analytical approaches, which combine analytical techniques with numerical calculations to simulate light propagation in microstructured optical fibers, were developed as a means to balance between accuracy and computational efficiency.

In this chapter, we explore a semi-numerical approach grounded in mode coupling

theory to simulate SSL. The chapter is structured as follows. We begin with a section introducing the foundational principles of the 2D+1 approach. We then apply this approach to the case of a fiber tilt and twist. We then delve into the analysis of optical loss when encountering well-defined scattering points along the core surround. Finally, we implement the 2D+1 approach to study the effects of arbitrary surface roughness, particularly in the context of SSL.

From our hand we propose a novel 2D+1 approach based on coupled modes theory (CMT).

5.2 Basic principle

Waveguide modes can couple to each other when phase matching and field overlap are fulfilled [122]–[124]. Figure 5.1 illustrates this phenomenon for two different configurations. The first one is the so-called co-directional coupler, and which consists of two parallel waveguides that are sufficiently closed to each other so their the fields of their respective guided modes overlap, leading to power exchange between the two waveguides. The second configuration, coined butt-coupling scheme, consists of two waveguides arranged in series. Here the field of mode of one waveguide is transferred to that of a mode of the second waveguide.

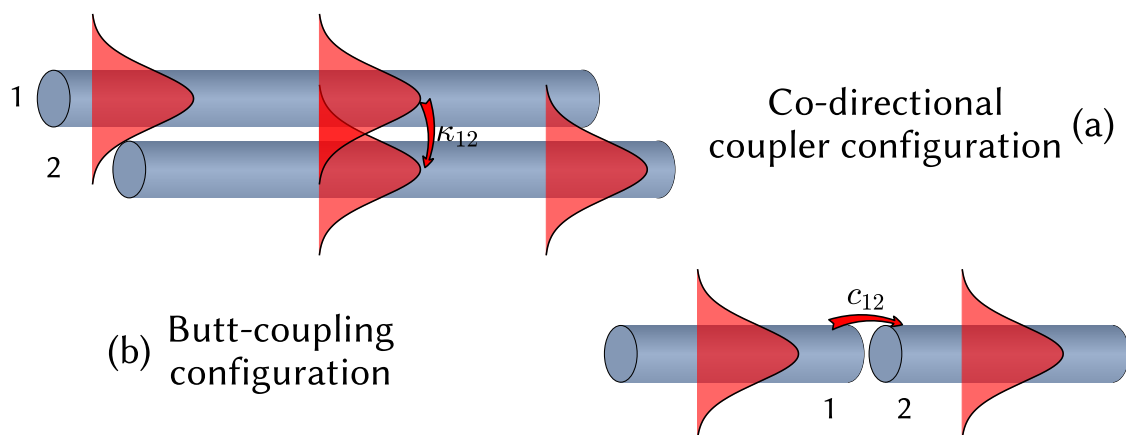


Figure 5.1: Schematics of modes coupling in the co-directional coupling configuration (a) and butt-coupling configuration (b).

The latter situation can be generalised to a single waveguide which exhibits non-uniformities along the propagation axis. It is this property that we explore to estimate the propagation loss deduced by the presence of a perturbation along the length of the fiber such as twist, scattering point or surface roughness.

The coupled waveguide system can be analyzed using Maxwell's equations and boundary conditions to derive supermodes. Alternatively, and akin to tight-binding model in condensed matter, CMT simplifies this analysis by starting with individual waveguide mode fields and explore their evolution in the presence of others. This evolution is described by a set of coupled first-order differential equations evolving the mode amplitudes, providing an intuitive understanding of power exchange. The solution shows that supermodes are combinations of individual waveguide modes. Variational analysis using a linear combination of waveguide fields yields similar results as CMT.

The assumption is made that the combined guided field in the coupled structure can be expressed as the summation of the individual waveguide modes. Each waveguide is assumed to have a single mode:

$$\begin{aligned}\vec{E}(x, y, z) &= A(z)\vec{E}_1(x, y)e^{-j\beta_1 z} + B(z)\vec{E}_2(x, y)e^{-j\beta_2 z} \\ \vec{H}(x, y, z) &= A(z)\vec{H}_1(x, y)e^{-j\beta_1 z} + B(z)\vec{H}_2(x, y)e^{-j\beta_2 z}\end{aligned}\quad (5.1)$$

The amplitudes of the propagating mode in Waveguide 1 (WG_1) and Waveguide 2 (WG_2) are denoted by $A(z)$ and $B(z)$ respectively. Here, for simplicity and without losing generality, we limit the model to the propagation along a single direction. The transverse mode field profiles of the individual waveguides, denoted as $\vec{E}_1(x, y)$, $\vec{H}_1(x, y)$ and $\vec{E}_2(x, y)$, $\vec{H}_2(x, y)$ are assumed to remain unchanged in the presence of the second waveguide. This the only approximation taken here. The corresponding propagation constants are β_1 and β_2 , often expressed in terms of an effective index n_{eff} , where $\beta = k_0 n_{\text{eff}}$ and $k_0 = 2\pi/\lambda$.

The amplitudes $A(z)$ and $B(z)$ are related to each other by the so-called generalized coupled-mode equations:

$$\begin{aligned}\frac{dA}{dz} + c_{12}\frac{dB}{dz}e^{-j(\beta_2-\beta_1)z} + j\chi_1 A + j\kappa_{12}B e^{-j(\beta_2-\beta_1)z} &= 0 \\ \frac{dB}{dz} + c_{21}\frac{dA}{dz}e^{-j(\beta_2-\beta_1)z} + j\chi_2 B + j\kappa_{21}A e^{-j(\beta_2-\beta_1)z} &= 0\end{aligned}\quad (5.2)$$

Here, the parameters $\chi_{(1,2)}$, $c_{(12,21)}$ and $\kappa_{(12,21)}$ are respectively the change in propagation constant, butt coupling coefficient and mode coupling coefficient respectively [122]–[124]. They are expressed as follows:

$$\kappa_{12} = \frac{\omega \varepsilon_0 \int_{-\infty}^{+\infty} \int_{-\infty}^{+\infty} (\varepsilon_{r,1} - \varepsilon_{r,2}) \vec{E}_1^* \cdot \vec{E}_2 \, dx dy}{\int_{-\infty}^{+\infty} \int_{-\infty}^{+\infty} \hat{z} \cdot (\vec{E}_1^* \times \vec{H}_1 + \vec{E}_1 \times \vec{H}_1^*) \, dx dy} \quad (5.3)$$

$$c_{12} = \frac{\int_{-\infty}^{+\infty} \int_{-\infty}^{+\infty} \hat{z} \cdot (\vec{E}_1^* \times \vec{H}_2 + \vec{E}_2 \times \vec{H}_1^*) \, dx dy}{\int_{-\infty}^{+\infty} \int_{-\infty}^{+\infty} \hat{z} \cdot (\vec{E}_1^* \times \vec{H}_1 + \vec{E}_1 \times \vec{H}_1^*) \, dx dy} \quad (5.4)$$

$$\chi_1 = \frac{\omega \varepsilon_0 \int_{-\infty}^{+\infty} \int_{-\infty}^{+\infty} (\varepsilon_{r,1} - \varepsilon_{r,2}) \vec{E}_1^* \cdot \vec{E}_1 \, dx dy}{\int_{-\infty}^{+\infty} \int_{-\infty}^{+\infty} \hat{z} \cdot (\vec{E}_1^* \times \vec{H}_1 + \vec{E}_1 \times \vec{H}_1^*) \, dx dy} \quad (5.5)$$

Here, χ_2 is deduced by interchanging the under-suffix 1 and 2 in the expression of χ_1 . Based on the considerations outlined above, and for the case of the problem we would like to solve, we can deduce the loss induced in a HCPCF by a perturbation $P(z)$ located at z by numerically solving the expression of the fields $\vec{E}_1(x, y)$, $\vec{H}_1(x, y)$ and $\vec{E}_2(x, y)$, $\vec{H}_2(x, y)$ and deducing the coefficient c_{12} . In order to extract the associated propagation loss coefficient, a characteristic length is necessary to be introduced. Despite its inherent approximation, this 1+2D technique offers notable advantages in terms of computational efficiency, making it a practical alternative to 3D methods for extracting propagation loss coefficients in HCPCFs.

5.3 Fiber twist and tilt induced loss

In this study, we use the above 2D+1 for the case of a twist and a tilt of a HCPCF that can occur at given position along its length. Fig. 5.2 shows schematically this type of deformations. The figure shows that a single length of HCPCF can be represented as a succession of butt-coupled segments.

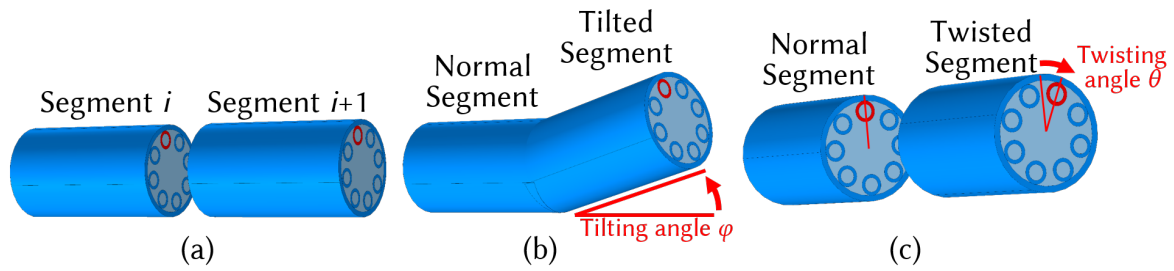


Figure 5.2: Schematic representation of the multistage approach. (a) Decomposition of the fiber into segments. (b) Fiber tilting. (c) Fiber twisting.

In the context of the two distinct deformations under investigation—namely, tilting of the fiber axis (Fig. 5.2 (b)) and a twisting of the cladding tubes around the fiber axis (Fig. 5.2 (c)), the fields $\vec{E}_1(x, y)$, $\vec{H}_1(x, y)$ and $\vec{E}_2(x, y)$, $\vec{H}_2(x, y)$ refer to the fields at the ends of two facing segments. The interface plane between any two segments signifies a discontinuity, leading to the transfer of power from the fundamental mode (FM) that escapes from the i -th segment to all modes of the subsequent segment or simply scattered. This power transfer arises from the interaction between the modes, which can generally be measured through the overlap integral, as depicted in the equation (2.23) or (5.4). Specifically, indexes 1 and 2 denote the FM of two successive segments, C_{FM}^2 signifies the power that is transferred from the FM back to itself, while $1 - C_{FM}^2$ indicates the power that is transferred to all other modes. Within the context of an effectively single mode regime, the power transferred to the higher order modes (HOM) can be deemed as lost, hence $1 - C_{FM}^2$ serves as an estimate of the FM power loss induced by deformations. In the fiber twist and tilt, The fields could easily be deduced by a transverse rotation of θ or projection of the field over a plane making an angle φ with z -axis. However, and in order to ensure rigorous results, all the fields were calculated numerically using the 2D solver¹.

In light of this, we evaluated the fields for FM-FM (i.e., LP_{01} mode from segment i to LP_{01} of segment $i+1$) and FM-HOM butt couplings across a range of wavelengths corresponding to transmission windows. We considered various magnitudes of perturbations and focused on the lowest loss HOM. This assessment allowed us to quantify the optical loss in FM by examining the value of $1 - C_{FM}^2$, and determining the power coupled from FM to the most significant contributing HOMs. To gain insight into how key geometric parameters affect these losses, we conducted comprehensive 2D FEM simulations on a variety of fibers with different cross-sectional parameters. The fibers in our study exhibited a tube count N ranging from 6 to 9, a tube thickness t of 750 nm, and a gap

¹This evaluation were undertaken in collaboration with Prof. Vincetti team at the university of Modena

between tubes varying from 1.4 to 7.6 μm . Additionally, the core radius R_{core} spanned from 10 to 23 μm , and the cladding tube radius r_{ext} ranged between 4.4 and 7.5 μm .

Fig. 5.3 plots FM-FM butt coupling C_{FM}^2 when the fiber is twisted with different rotation angles. The fiber used is a single ring tubular HCPCF with 8 cladding tubes (T8-TLF), and is schematically shown in Fig. 5.4 (a). The results clearly show that it fits the fact that T8-TLF exhibits 8-fold azimuthal symmetry, as shown by maximum drop in C_{FM}^2 at 22.5° and 67.5° .

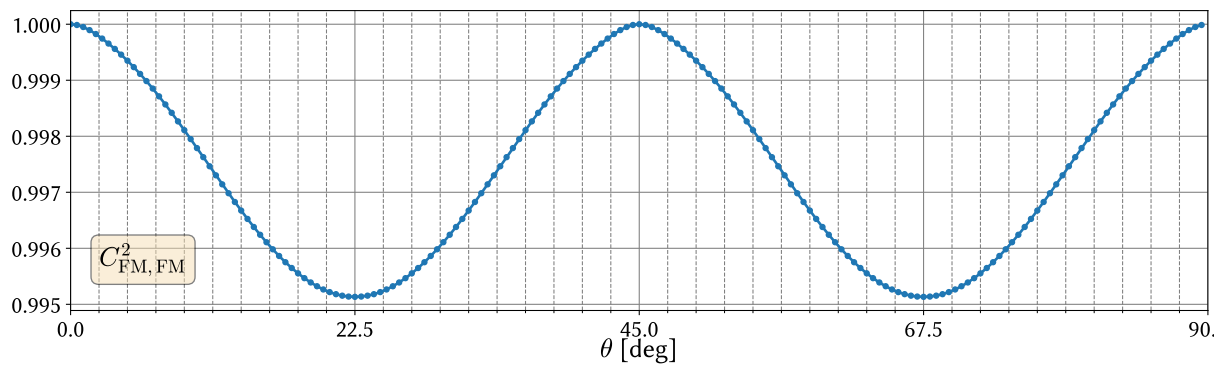


Figure 5.3: Butt coupling coefficient C^2 of FM-FM vs angle of rotation.

The results show that a maximum loss, $1 - C_{\text{FM}}^2$, of $5 \cdot 10^{-3}$, i.e. 0.02 dB per a twist of 22.5° . For very small twist angle θ , the loss per twist can be written as $2 \cdot 10^{-3} \theta / \pi$. For fabricated fibers, we can have an estimate of an effective twist of an angle θ that can be deduced from the surface roughness peak to peak of typically 0.5 nm. This gives $\theta \approx 5 \cdot 10^{-4}$ rad for a fiber radius of 10 μm , which in turn gives a loss per twist of approximately $3 \cdot 10^{-6}$ dB.

In order to explore how such twist-induced loss evolves with fiber geometrical parameters, we have carried out the above calculation for different fiber core radius and gaps. Upon analyzing the trends in our results, we discerned the loss's dependence on wavelength, angle θ , and geometric parameters, leading to the derivation of several scaling laws for both tilting (φ) and twisting deformations.

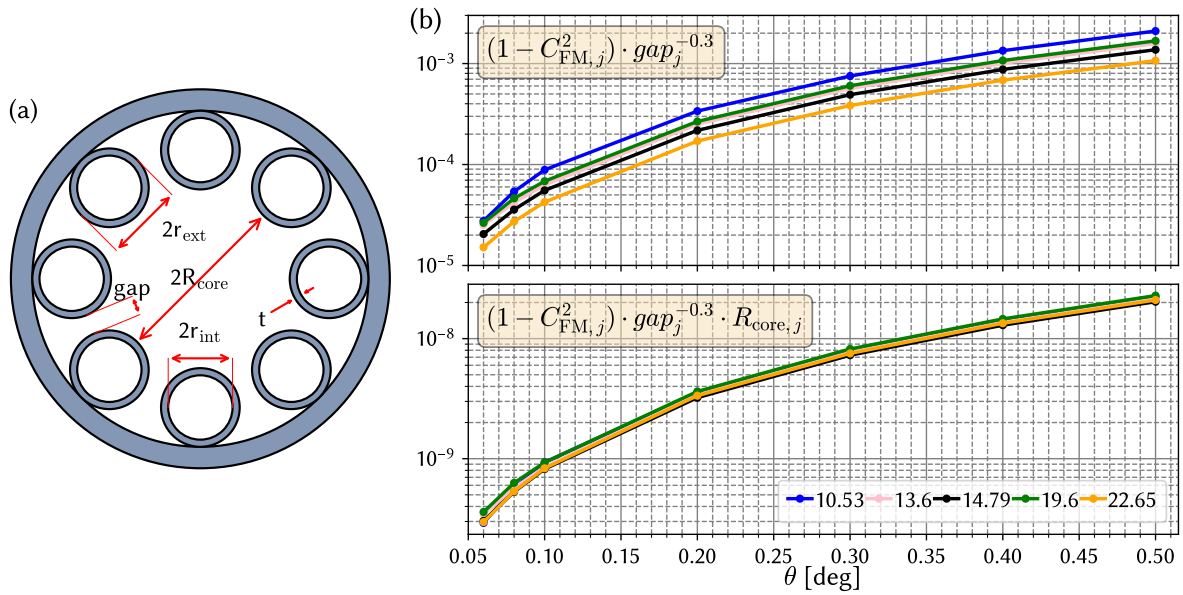


Figure 5.4: (a) T8-TLF geometry with the key parameters (θ shown in Fig. 5.2 (c)). (b) Normalized twist induced loss evolution with the twist angle for different fiber radius.

Fig. 5.4 (b) shows the evolution of the twist-induced loss for an angle range from 0.05° to 0.5° for different values of gap and the core. The top of the figure shows this loss normalized to the gap size. The results show that the loss follows a θ^2 power law and its decreases with core radius increase. The bottom of the figure shows the same data when the loss is normalized with both the gap size and the core radius. Consequently we can write that the twist induced loss as $1 - C_{\text{FM}}^2 \propto \theta^2 \text{gap}^{0.3} R_{\text{core}}^{-1}$. In addition, we observed that the twist-induced loss doesn't depend on the wavelength nor on the changes in N and r_{ext} . Table 5.1 summarises this scaling law.

Fig. 5.5 shows the tilt induced loss with wavelength. For tilting angles φ under 1° , we discovered that the power loss from the FM scales as $1/\lambda^2$ and as φ^2 . We also found that changes in N , gap , and r_{ext} do not significantly affect the loss, while a quadratic dependence on R_{core} is evident. This is confirmed by the figure, which shows that when $1 - C_{\text{FM}}^2$ is multiplied by R_{core}^2 , the curves coincide. See Table 5.1 for summary.

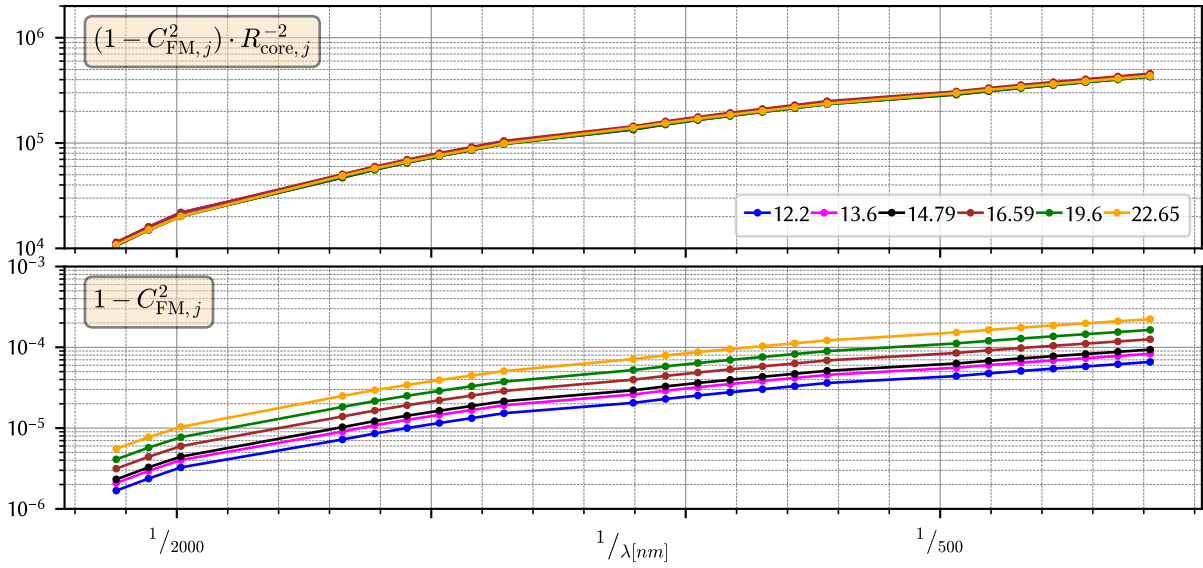


Figure 5.5: Scaling laws for tilting ($\varphi = 0.01^\circ$), showing CL and core radius law effect.

Finally, it is important to understand the proportion of power lost due to tilting that couples to HOMs. This is simply deduced by the value of $C_{FM,HOM}^2$, which we write as C^2 . Fig. 5.6 shows C^2 versus the normalised frequency for the modes LP_{02_x} , $LP_{11_{bx}}$, $LP_{21_{bx}}$, $LP_{12_{bx}}$, $LP_{31_{bx}}$. The results show that most of the lost power is coupled to LP_{02_x} , which more than two orders of magnitude larger than the power coupled to other HOMs. Furthermore, we observe a trend $C^2 \propto F^2$ for modes $LP_{11_{bx}}$, $LP_{12_{bx}}$, $LP_{31_{bx}}$. While for Modes $LP_{21_{bx}}$, LP_{02_x} the trend is $C^2 \propto F^4$.

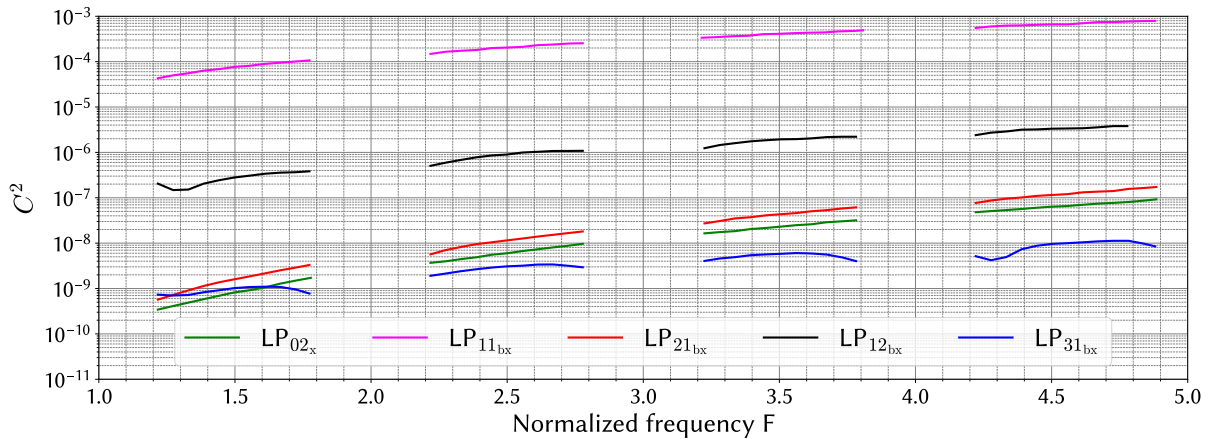


Figure 5.6: C^2 vs F for HOMs LP_{02_x} , $LP_{11_{bx}}$, $LP_{21_{bx}}$, $LP_{12_{bx}}$ and $LP_{31_{bx}}$.

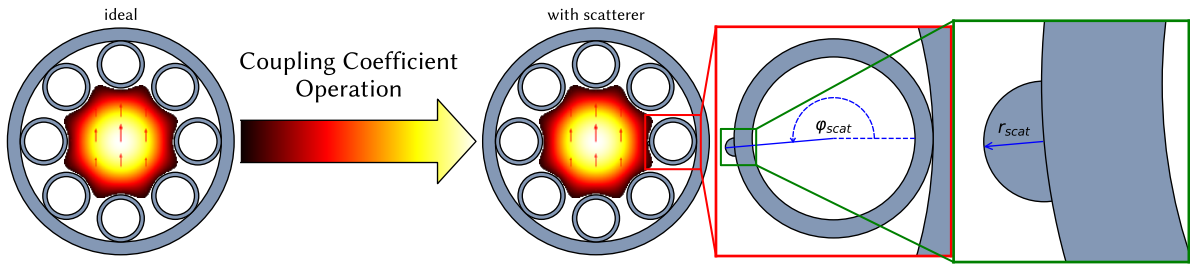
In conclusion, the above tilt-perturbed and twist-perturbed coupling analysis can be summarized in table 5.1.

Table 5.1: Scaling laws of C^2 coupling for tilt and twist perturbations.

Perturbation type	Dependency on angle (φ or θ)	Dependency on F	Dependency on R_{core}	Dependency on gap
Tilting	$\propto \varphi^2, \propto \varphi^4$	$\propto F^2, \propto F^4$	$\propto R_{\text{core}}$	NO
Twisting	$\propto \theta^2$	NO	$\propto \frac{1}{R_{\text{core}}}$	$\propto \sqrt{gap}$

5.4 Scattering point

In this section, we investigate the influence of a small scatterer located on the core surround on the butt coupling coefficient. The position of the scatterer is schematically depicted in Fig. 5.7, and it is represented as a fraction of a cylindrical rod radius r_{scat} positioned on the surface of one of the small tubes of the T8-TLF. The scatterer is oriented at an angle φ_{scat} relative to a reference frame with its origin at the center of the cladding tube containing the scatterer. The fiber used for this investigation is the same as for fiber X from chapter 4 and has been listed in table 4.2.


Figure 5.7: Schematic of butt coupling between 2 designs.

As a first step of the simulation, we performed the calculation of $1-C_{\text{FM}}^2$ for a fixed normalized frequency $F = 4.5$ ($\lambda = 294.29$ nm) and mapped over values of r_{scat} and φ_{scat} between 10 and 300 nm and between 44° and $\sim 315^\circ$ respectively. This simulation took 44 hours, ~ 40 GB of RAM in peak and ~ 300 GB of storage. The results plotted in Figure 5.8 shows the results of these calculations. The results show that the scatterer induced loss is maximum for $\varphi_{\text{scat}} = 180^\circ$ and is strongly dependent on the scatterer azimuthal position. Indeed, the value of $1-C_{\text{FM}}^2$ reaches a maximum $\sim 6 \cdot 10^{-5}$ (i.e. $\sim 2 \cdot 10^{-5}$ dB loss) and drops to below 10^{-8} for angle outside the range of 120° and 250° . Conversely, the results show a strong dependence with the scatterer size. The loss remains less than 10^{-8} for $r_{\text{scat}} < 40$ nm. It reaches a maximum at a radius of 125 nm and exhibits an oscillatory behaviour. This oscillatory behaviour is not here investigated.

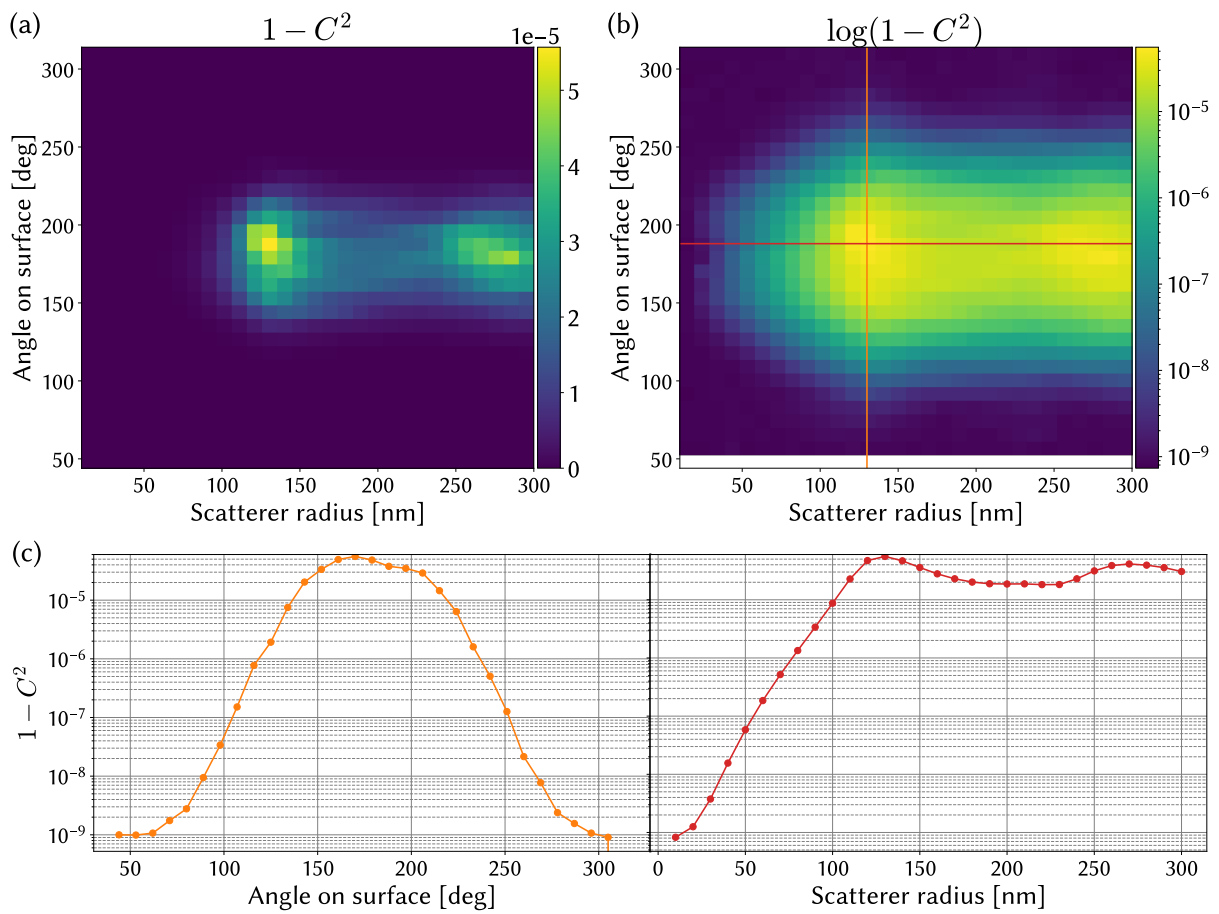


Figure 5.8: Fraction of the lost power $1 - C^2$ in linear scale (a) and in logarithmic scale (b). Orange and red lines on (a) are depicted as curves $1 - C^2$ vs φ_{scat} and $1 - C^2$ vs r_{scat} respectively on (c). Only fundamental mode (FM) in those simulations considered.

The green curves in Fig. 5.9 show the 2D+1 calculated transmission loss spectra for two different configurations of the scatterer point. In the first configuration we have $r_{\text{scat}} = 130$ nm and $\varphi_{\text{scat}} = 190^\circ$, and the second configuration relates to a scatterer with $r_{\text{scat}} = 65$ nm and $\varphi_{\text{scat}} = 190^\circ$. Each of those two simulations took ~ 40 hours, ~ 40 GB of RAM in peak and ~ 250 GB of storage. Here the spectrum range from $F = 1$ to $F = 5$, and the fiber used still the same fiber X as before. Here, the loss per unit length was deduced by considering an effective propagation length to be equal to r_{scat} . Remarkably the results show a very good agreement with the total loss (i.e. the sum of CL and SSL) as calculated using the numerically calculated CL and the empirical expression of SSL (equation 1.5). Here, the η in SSL expression was taken as be $2 \cdot 10^{-3}$.

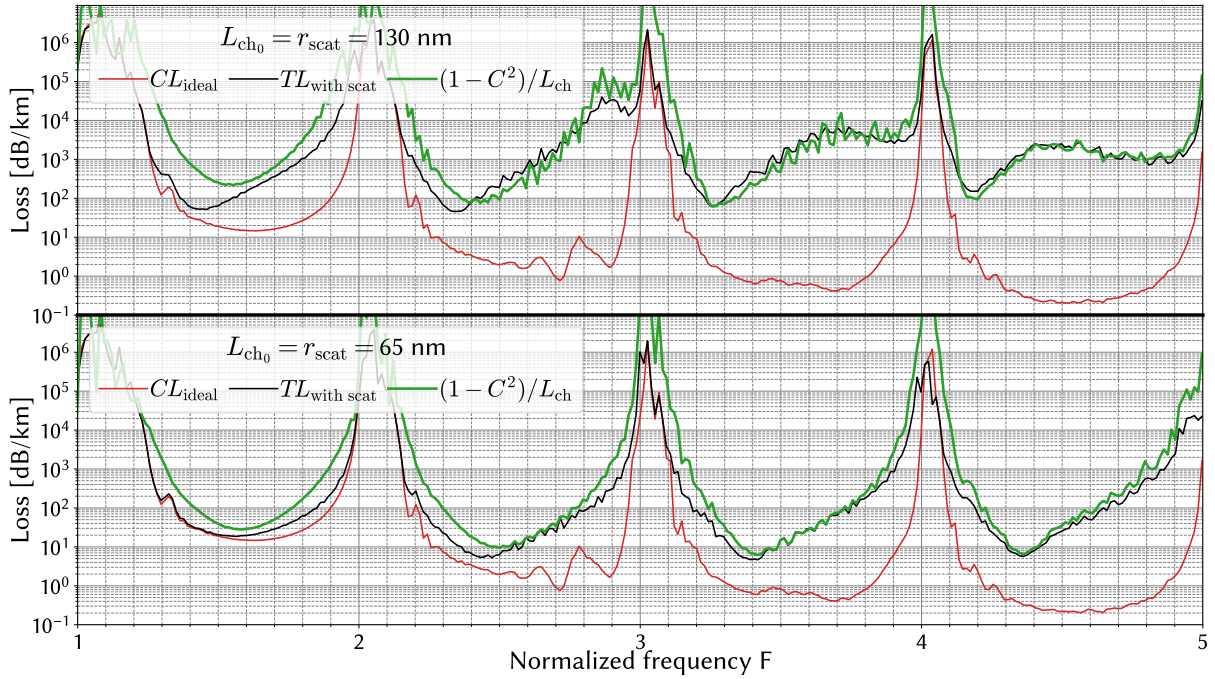


Figure 5.9: 2D+1 computed transmission loss spectrum (green curves) versus the sum of CL and SSL (black curve). The red curve represents the confinement loss of a scatterer-free T8-TLF (fiber X)

The core contour profile with a scatterer point can be presented in the same way as a stochastic profile and in the same way as described in section 4.3 of chapter 4 (see for example Fig. 4.7 (a),(b)). Consequently, we can obtain PSD, σ and RMS for such a profile height with a single bump of radius r_{scat} as demonstrated on Fig. 5.10. This approach gives an RMS of 0.5393 nm for $r_{\text{scat}} = 130$ nm, and 0.1910 nm for $r_{\text{scat}} = 65$ nm. Recalling the expression of SSL loss coefficient, $\alpha_{\text{SSL}} = \eta \cdot F_{00}(\lambda) \cdot \left(\frac{\lambda_0}{\lambda}\right)^3$, and that $\eta \propto \text{RMS}^2$, we can write $\eta = C_\eta \cdot \text{RMS}^2$. Here C_η is a constant. It has been empirically deduced for an RMS of 0.4 nm. This means that $C_\eta = 0.7 \cdot 10^{-4}$.

Based on the above we can deduce the value of η and hence of α_{SSL} for the core contour profile with a single scatterer. Finally, in order to convert the but coupling loss $1 - C_{\text{FM}}^2$ in the propagation loss, we introduce empirically a characteristic length, which represents the effective propagation length during the scattering process. By recalling that the height of capillary wave write as $\langle h_q^2 \rangle \propto \frac{1}{q^2}$, we can write the characteristic length as:

$$L_{\text{ch}} = L_{\text{ch}_0} \cdot \frac{f_0}{f} = L_{\text{ch}_0} \cdot \frac{\lambda}{\lambda_0} \quad (5.6)$$

where $f_0 = \frac{1}{\lambda_0}$, $f = \frac{1}{\lambda}$ and L_{ch_0} - fit parameter. For example on Figure 5.9 $L_{\text{ch}_0} = 130$ nm and 65 nm. Also calculated earlier RMS has been used for obtaining TL curve.

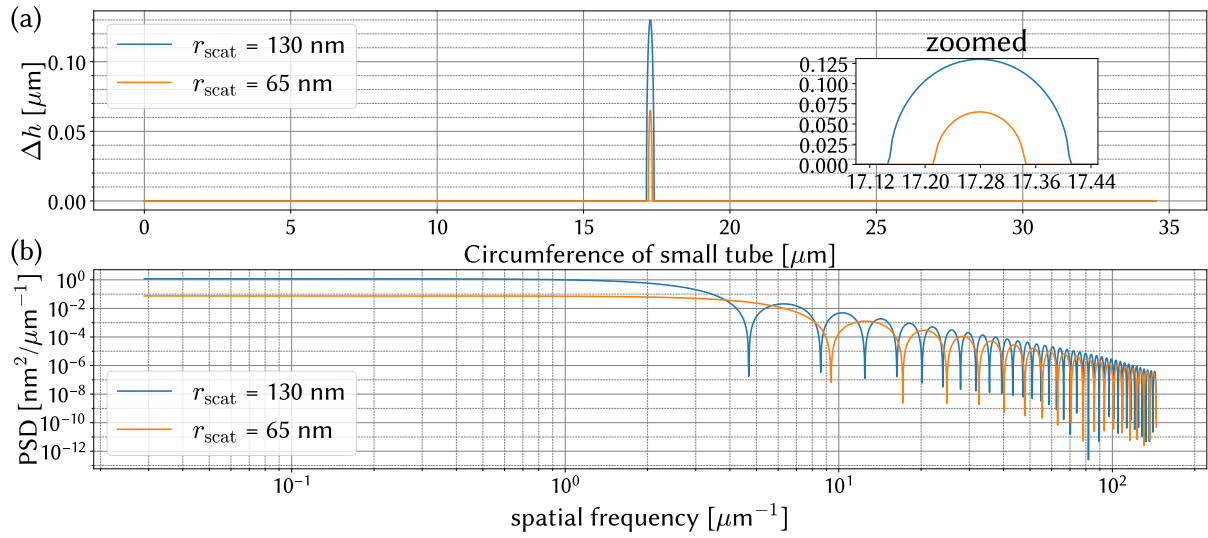


Figure 5.10: (a) Δh profile and (b) PSD of the profile

In conclusion, the good consistency between the results obtained with $\alpha_{TL} = \alpha_{CL} + \alpha_{SSL}$ and with the 2D+1 approach indicates that the latter is a very promising alternative to 3D simulations.

5.5 Surface roughness

In this section we extend the 2D+1 approach to HCPCF with core contour exhibiting surface roughness. The HCPCF structure and dimensions are the same as above. We have carried out 2D simulation over 3×3 to obtain nine different over the first order transmission band (i.e. normalized frequency spans from $F = 1$ to $F = 2$). Table 5.2 summarises the parameters of these nine surface roughness profiles. We have taken three different $\sigma = 0.4, 1, 2$ nm. For each value σ we set three cut-off frequencies f_c controlled with parameter $P = 2\pi, 10, 20$. For each pair of σ and P is associated a value of RMS. Similarly to what has been described in section 4.3, the surface roughness was applied to both external and internal side of the cladding tubes surfaces.

Table 5.2: Parameters of nine surface profiles configuration.

σ , [nm]	0.4			1.0			2.0		
P	2π	10	20	2π	10	20	2π	10	20
f_c , [μm^{-1}]	0.0289	0.0461	0.0921	0.0289	0.0461	0.0921	0.0289	0.0461	0.0921
RMS, [nm]	0.0727	0.07515	0.0787	0.1817	0.1879	0.1966	0.3634	0.3757	0.3932

As demonstrated in the previous section, the azimuthal placement of a scatterer exerts a significant influence on the scattering loss (see Fig. 5.8). This implies that relying solely on a surface roughness profile is insufficient to accurately predict scattering loss. Indeed, when applying a single surface roughness profile characterized by σ and P to a tube contour, the azimuthal position is not fixed. Therefore, using the same surface roughness profile can result in significantly different scattering losses due to its strong dependence on the azimuthal location of specific surface features. To mitigate the effect of this azimuthal dependency, we introduce a "phase shift" to each surface roughness profile, allowing us to control the azimuthal position of a particular feature (see equation 4.19). In this context, we conducted for every surface profile (i.e. for a given pair of σ and P) 10 different CL simulations, each with different randomly generated phase shifts. We then deduce the average CL extracted from the 10 CL spectra, and which we consider as the most representative CL for a HCPCF with this surface roughness profile. Gathering this data required 90 simulations, which took 24 days to achieve them using ~ 40 GB of RAM in peak and ~ 70 GB of storage per simulation.

Fig. 5.11 (a) shows a set of 10 CL spectra of a HCPCF corresponding to different phase-shifts for the surface roughness of $\sigma = 2$ nm and $P = 20$. These spectra are compared to that of a surface roughness-free fiber, which we refer to as the "Ideal" case. The wavelength range considered for this comparison is 600 nm to 1000 nm, corresponding to the first-order transmission band of the HCPCF. As anticipated, the CL loss exhibits variation with phase-shift. Each colored curve represents a different phase-shift, while the red square-symbol curve represents the average CL spectrum for the 10 realizations. The blue-colored region corresponds to the CL minimum-maximum range. The results show that this range is less than 40 – 100dB/km for wavelengths shorter than 700 nm, and can achieve a range of 100 – 800 dB/km for wavelength longer than 900 nm.

Fig. 5.11 (b) shows the average CL for the 9 distinct surface roughness profiles. We note that for $\sigma = 0.4$ nm (i.e RMS in the range on 73 pm and 79 pm) CL remains

relatively constant. Conversely, for $\sigma = 2$ nm (i.e RMS in the range on 363 pm and 393 pm) the CL increases significantly relative to the surface roughness free fiber. Furthermore, the cut-off frequency impacts the CL even when the RMS is kept constant. This observation corroborates the point made in chapter 4, emphasizing that RMS alone is insufficient to quantify SSL. Fig. 5.11 (c) shows the total loss by adding the SSL to the CL. We observe the same trend as with CL, indicating that reducing the RMS to a level of 70 – 80 pm could mitigate the SSL contribution, making it insignificant in the context of propagation loss.

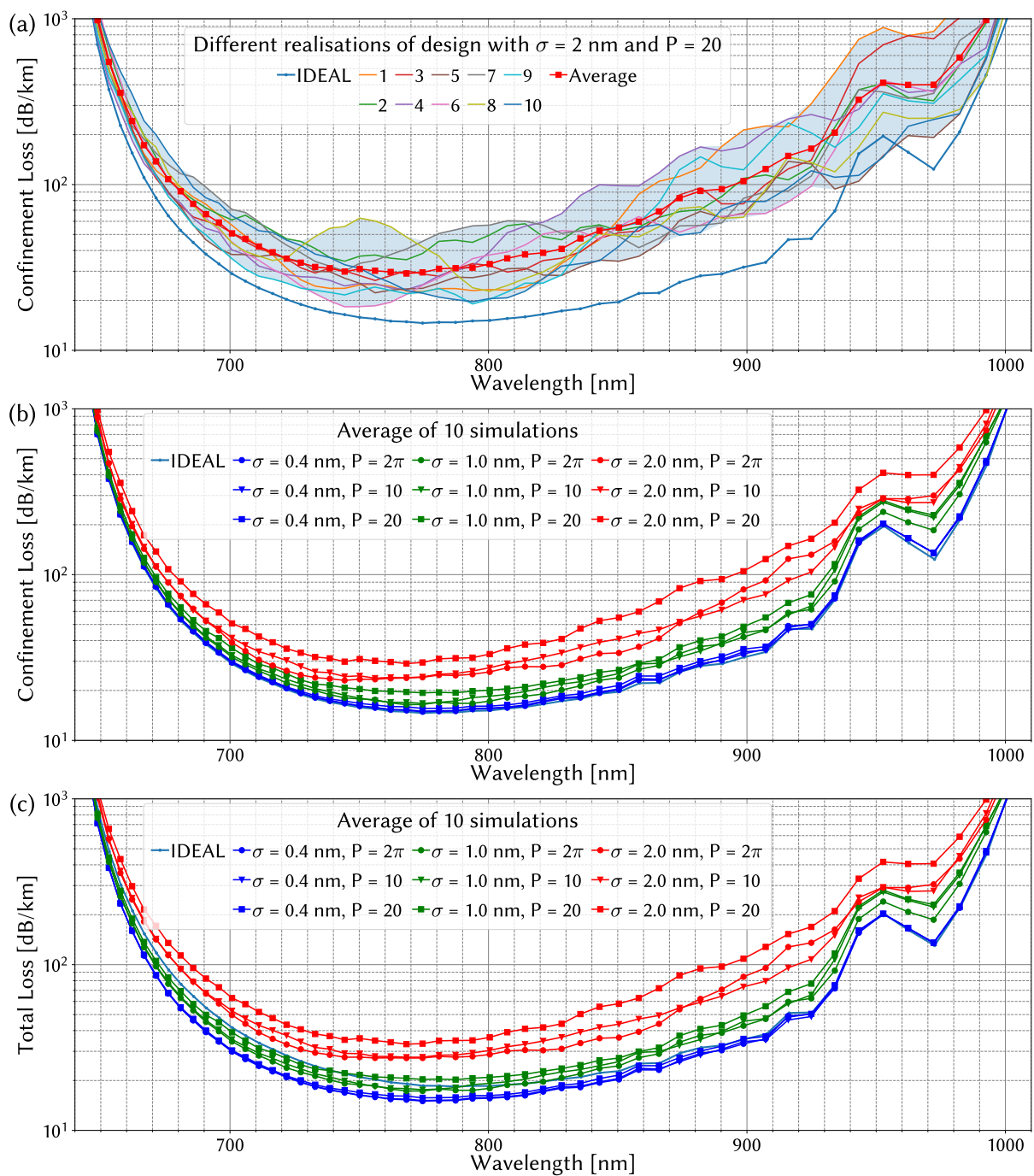


Figure 5.11: (a) CL of 10 realisations of SR with $\sigma = 2$ nm and $P = 20$. (b) CL and (c) TL of 90 simulations averaged over each group of SR properties.

In order to analyze the potential trends in how the CL and TL evolve with varying surface roughness characteristics, we have generated statistical distributions of the minimum CL and TL values for different combinations of σ and f_c . As depicted in Fig. 5.12 (a), we observe that for fixed σ , the average of the minimum CL increases with

higher values of f_c . Conversely, when f_c is held constant, the minimum CL increases with increasing σ . Fig. 5.12 (b) presents a similar analysis for TL, and the results exhibit the same patterns as observed for CL. This analysis allows us to gain insights into how changes in surface roughness parameters influence both CL in HCPCF.

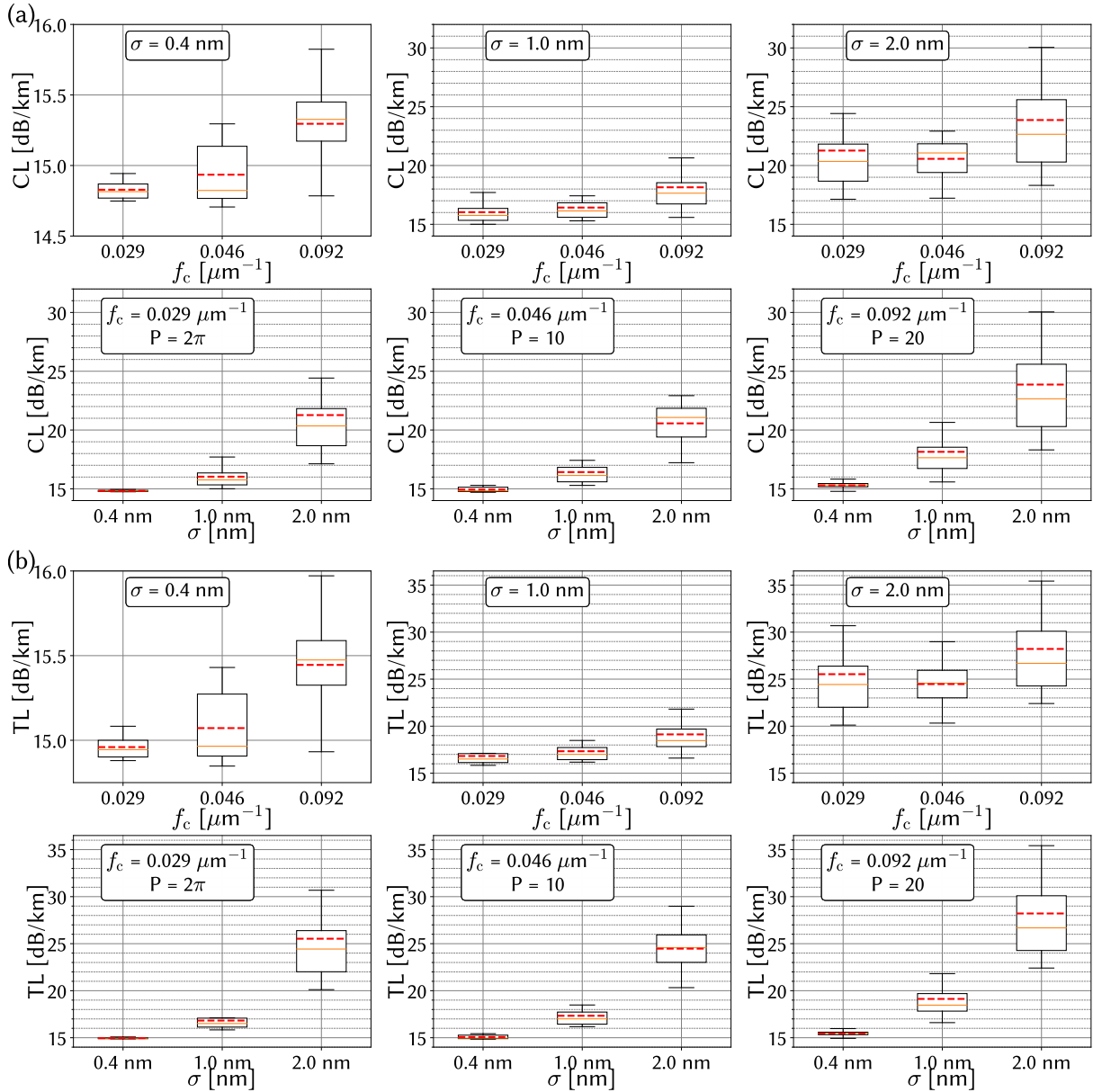


Figure 5.12: 90 simulations statistics data at minimum loss wavelengths for the (a) CL and (b) TL.

Now that we have successfully completed the 2D simulations, we have obtained the field profiles of the fundamental mode (FM) for each of the 90 different fibers considered in our study. With these field profiles in hand, we are equipped to employ the 2D+1

technique to calculate $1-C^2$ for butt-coupling scenarios between a surface roughness-free HCPCF and one with a surface roughness profile selected from the pool of 90 profiles we have at our disposal. Fig. 5.13 (a) presents the results of this analysis. Similar to Fig. 5.12, it shows the evolution of $1-C^2$ with surface roughness parameters. In contrast with CL $1-C^2$ decreases with increasing f_c for fixed σ . The values of the coupling loss was found to be in the range of 10^{-7} (i.e. $4 \cdot 10^{-7}$ dB) for $\sigma = 0.4$ nm (i.e RMS in the range on 73 pm and 79 pm) and increases by two orders of magnitude for $\sigma = 2$ nm (i.e RMS in the range on 363 pm and 393 pm). As expected, the coupling loss increases quadratically with σ . Nevertheless, it is important to note that the rate of increase in coupling loss depends on the value of f_c . This relationship between surface roughness parameters and coupling loss is crucial for understanding the impact of surface roughness on the transmission characteristics of the HCPCF. Fig. 5.13 (b) plots $1-C^2$ with RMS. The results clearly show that the coupling loss increase with the RMS. The blue curve represents a quadratic fit to the data. These findings align reasonably well with the empirical proportionality of $SSL \propto h_{rms}^2$, considering the significant influence of the azimuthal position of surface features, as discussed earlier.

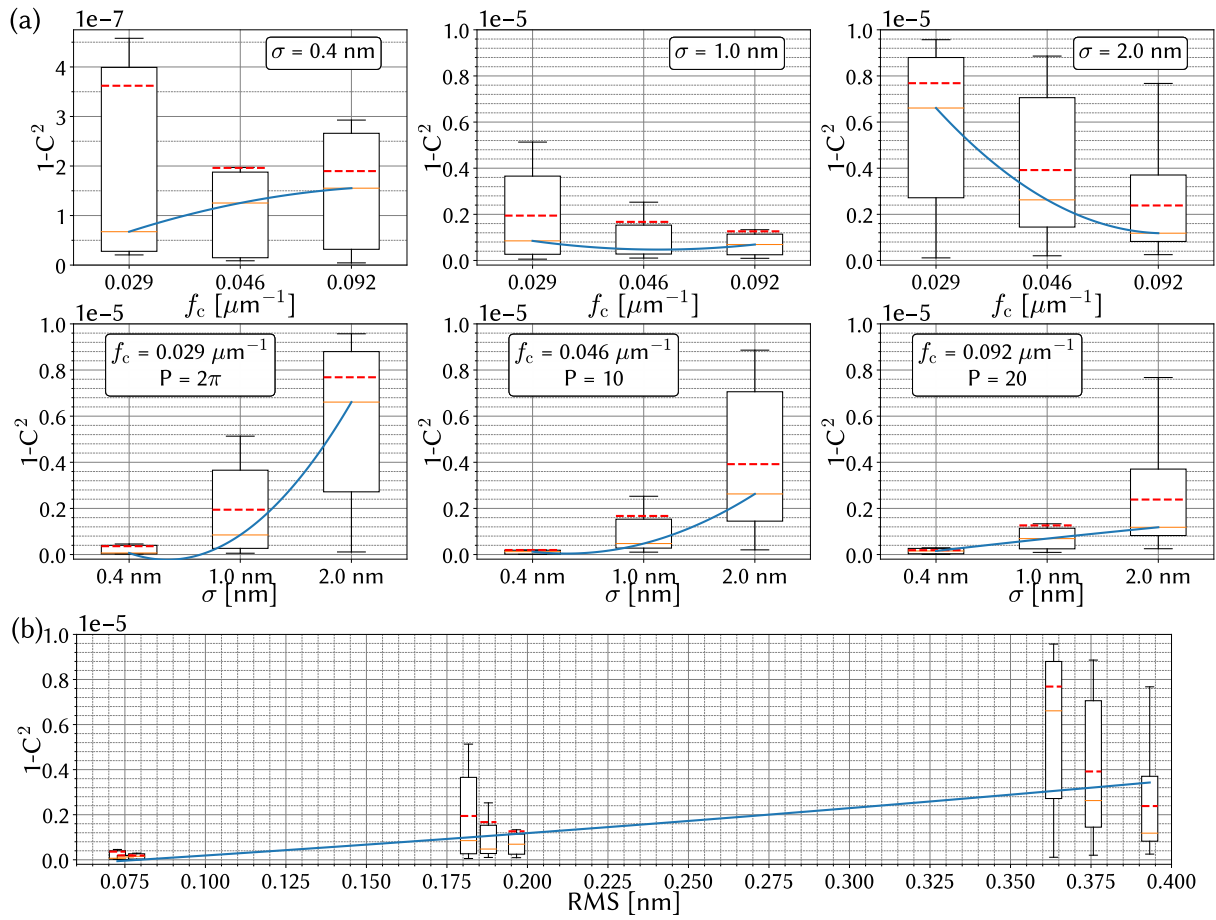


Figure 5.13: 90 simulations statistics data at minimum loss wavelengths for the fraction of lost power $1-C^2$.

Finally, we utilize the characteristic length L_{ch} introduced earlier to establish a connection between the coupling loss coefficient $1-C^2$ and the propagation loss. To achieve this, we computed the TL spectrum by summing the contributions of SSL and CL over the normalized frequency range F spanning from 1 to 5. We then compared these TL spectra with those using the expression $(1-C^2) \frac{1}{L_{\text{ch}}}$. In this context, L_{ch_0} is used as a fit parameter. This parameter was adjusted to obtain the best agreement between the calculated TL spectra and the expression $(1-C^2) \frac{1}{L_{\text{ch}}}$. This approach allows us to link the coupling loss coefficient to the propagation loss and gain insights into the impact of surface roughness on the transmission characteristics of the HCPCF.

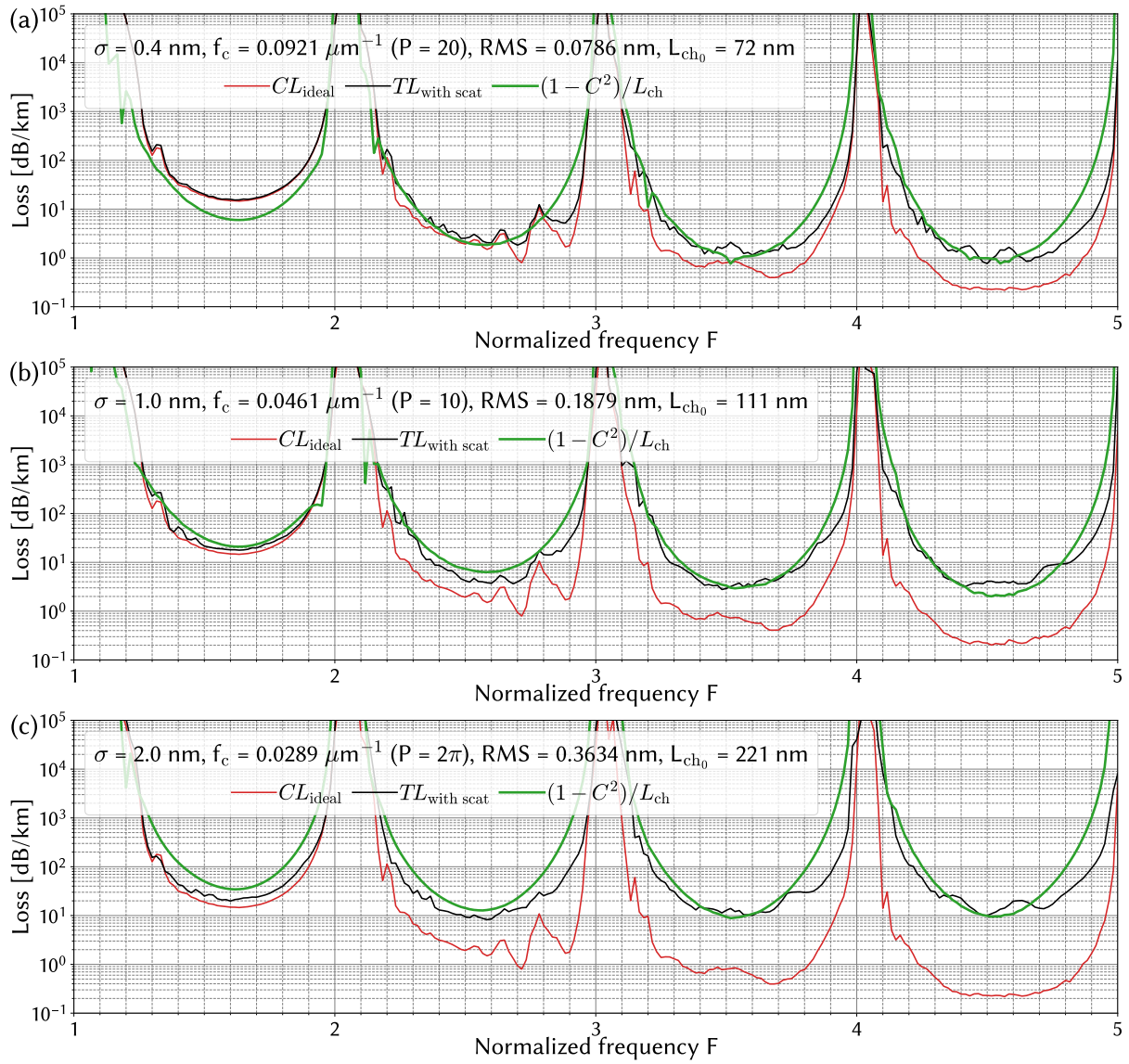


Figure 5.14: Spectra of α_{TL} and $\alpha_{2\text{D}+1}$ with fitted L_{ch_0} for some of the SR configurations listed in table 5.2 (a) $\sigma = 0.4 \text{ nm}$, $P = 20$, (b) $\sigma = 1.0 \text{ nm}$, $P = 10$, (c) $\sigma = 2.0 \text{ nm}$, $P = 2\pi$.

Summarised results are presented in table 5.3, extended version of previous table 5.2.

Table 5.3: Results on fit parameter L_{ch_0} for different SR configurations.

σ , [nm]	0.4			1.0			2.0		
P	2π	10	20	2π	10	20	2π	10	20
f_c , [μm^{-1}]	0.0289	0.0461	0.0921	0.0289	0.0461	0.0921	0.0289	0.0461	0.0921
RMS, [nm]	0.0727	0.07515	0.0787	0.1817	0.1879	0.1966	0.3634	0.3757	0.3932
L_{ch_0} , [nm]	40	135	72	413	111	67	221	34	29

Fig. 5.14 illustrates a comparison of loss spectra obtained through the two different techniques: 2D+1 and CL+SSL, for three distinct surface roughness profiles. The green curve correspond to the propagation loss using the 2D+1 approach, the black curves correspond to $\alpha_{CL} + \alpha_{SSL}$, and the red curves are the CL of roughness-free HCPCF. The results show a very good agreement both in the spectral structure and in the loss values. This, however, was achieved by fitting parameter L_{ch_0} that doesn't show a clear a trend with the surface parameters (see table 5.3). Thus indicating that the effective propagation length in the scattering process requires a better definition. Despite this limit, the 2D+1 approach has proved to be a very promising alternative to 3D simulations. Furthermore, the requirement of introducing an effective propagation length is not necessary if we extend the calculation of $1-C^2$ to a series of segments. However, because of time and computing power constraints, this simulation is not in this work scope.

5.6 Conclusion

In summary we described a new technique to simulate the propagation loss in IC HCPCF in the presence of deformation along the fiber propagation axis using butt-coupling approach. We tested this 2D+1 technique by introducing different scenarios. We have calculated the loss induced by a twist or a tilt of a fiber along with scaling law with parameters such the fiber core radius, cladding tube radius, gap, frequency and the twit or tilt angle. This study allowed to draw useful scaling laws. They reveal that in the case of tilting, the power loss scales as $1/\lambda^2$, with θ^2 and R_{core}^2 , and is unaffected by other fiber parameters. Conversely, in the case of twisting, the power loss is not influenced by the wavelength, but it increases with $1/R_{core}$ and with $gap^{0.3}$. We have then considered the coupling with a fiber with a well defined scattering point located on

the fiber core-contour. By introducing a characteristics length to represent the effective propagation during the scattering process. The agreement with $\alpha_{CL} + \alpha_{SSL}$ was found to be very good. Finally, we have simulated a HCPCF with 9 different surface profiles with each 10 different azimuthal positions to explore both the impact of roughness on CL and to validate our 2D+1 technique. The results show good agreement between $\alpha_{CL} + \alpha_{SSL}$ and $(1-C^2)L_{ch}^{-1}$. However, work is still required to better define L_{ch} . As a future work, one could apply 2D+1 technique to a series of interface couplings. This would provide a propagation loss without the need for an effective length. Conversely a better knowledge on the surface roughness profile and the mechanism of scattering would be useful to define a more accurate characteristic length.

Chapter 6

3D beam propagation modeling and concluding prospects

IN this chapter we delve into the intricacies of advancing from traditional 2D and 2D+1 described in chapter 5 to sophisticated 3D simulations by exploring a technique called beam envelop method (BEM). We begin by presenting preliminary results on beam propagation in a HCPCF, and sharing insights into the technical challenges we encountered during the implementation of this 3D simulation technique. In the latter part of the chapter, we offer a comprehensive summary of the outcomes achieved throughout this doctoral research and shed light on potential avenues for future investigations.

Table of content

6.1	Introduction	157
6.2	Beam Envelop Method 3D simulation	158
6.2.1	Principle and implementation	158
6.2.2	Beam propagation in HCPCF	162
6.2.3	Surface roughness perturbation	165
6.2.4	Discussion	170
6.2.5	Work Summary	171
6.2.6	Directions for future work	174

6.1 Introduction

It becomes evident from our exploration in previous chapters that 2D simulations of mode solving pose a significant limitation in fully capturing the complex dynamics of light propagation within HCPCF. Moreover, the 2D+1 approaches, while valuable, rely on initial assumptions and approximations that inevitably constrain the accuracy and comprehensiveness of the results they can offer. This underscores the necessity of 3D simulations to thoroughly investigate scattering, mode coupling, and light leakage or confinement in HCPCF. It is crucial to assess and understand the sensitivity of these phenomena to structural features and to elucidate the interconnections between them. Figure 6.1 schematically illustrates the intricacy of this light dynamics, and which cannot be simulated with 2D techniques or 2D+1 techniques. For example the presence of micro-scaled surface roughness induces light to scatter and to be lost via coupling to cladding radiation modes or to be back-coupled to core guided modes in the forward or backward direction. Thus altering not only the modal content, it creates undesirable back reflection and increases the propagation loss. Additional structural perturbations to the already complex structure of the cladding impact its confinement power (see Fig. 6.1 (a)). Conversely, a macroscopic bend could also be considered as a structural perturbation which affect the leakage, the modal content and the scattering (see Fig. 6.1 (b)). Consequently, one has to be able to simulate simultaneously microscopic and macroscopic features while capturing all the optical phenomena listed above.

In chapter 5 we listed the most prominent techniques that have been investigated, and which all require extensive computing power and time. During this research, we have explored several techniques including FDTD, however, their implementation were incompatible with our computing resources. Here, we introduce a 3D simulation technique, called beam envelop method (BEM), which is much less computing intensive as FDTD or 3D FEM [125]. The chapter structure is broken down into two main parts. The first is a description of BEM principles, a proof-of-concept of beam propagation dynamics in a straight and perturbation-free HCPCF, and an attempt to investigate beam propagation in a HCPCF with a deformation along the propagation axis. This part will conclude with a discussion on the performance of BEM and its suitability for HCPCF design and science. The second part of the chapter serves as a comprehensive conclusion, summarizing the body of work conducted throughout this doctoral research endeavor. Additionally, this part of the chapter sets the stage for future directions in HCPCF science and technology by examining both the accomplishments and constraints

encountered in this research.

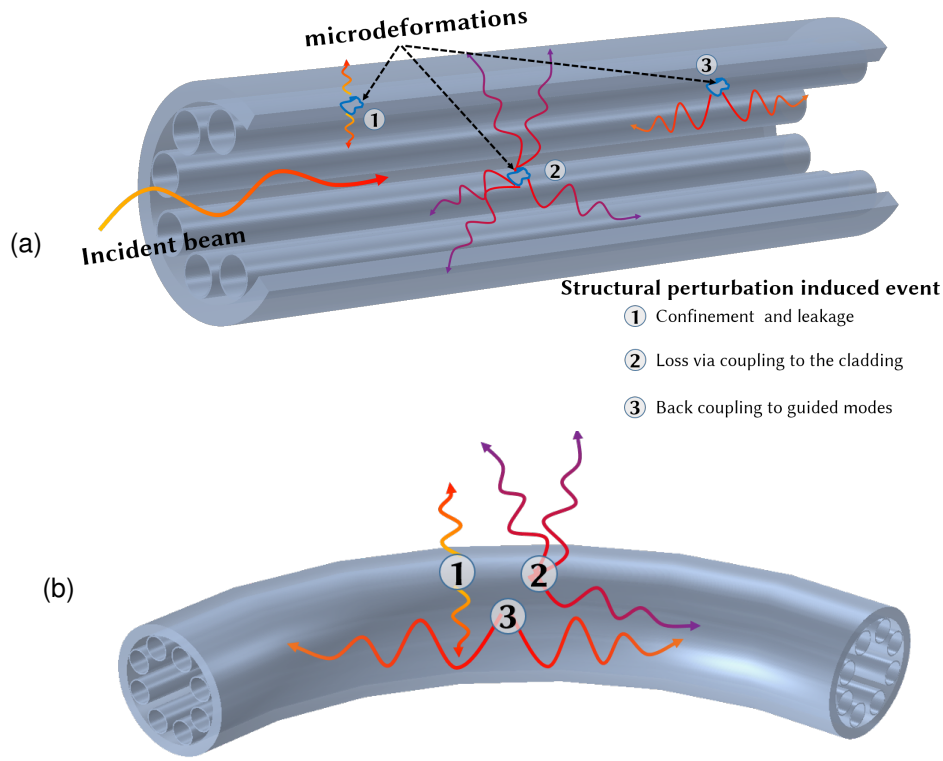


Figure 6.1: (a) Schematic representation of the impact on fundamental mode (FM) propagation of microdeformations in an HCPCF. (b) Appearance in 3D space of bent fiber.

6.2 Beam Envelop Method 3D simulation

6.2.1 Principle and implementation

The core principle of the BEM is to write the field as $\vec{E} = \vec{E}_1 e^{-ik_1 \cdot \vec{r}}$, with \vec{k}_1 being a given wave vector whose z component we set to be equal to propagation to be solved. The vector \vec{E}_1 is the unknown electric field envelope represented in Fig. 6.2 [125]. Under these assumptions, the equation to be solved is:

$$(\nabla - \vec{k}_1) \times (\mu_r^{-1} (\nabla - \vec{k}_1) \times \vec{E}_1) - k_0^2 \epsilon_r \vec{E}_1 = 0 \quad (6.1)$$

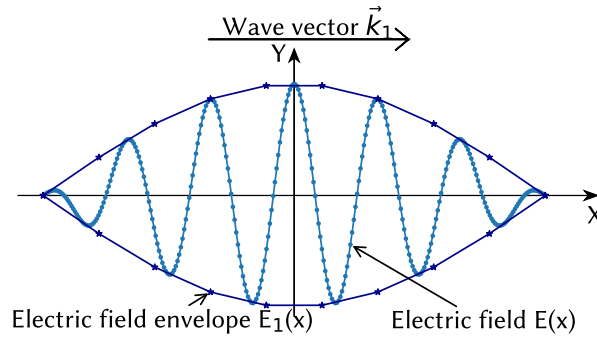


Figure 6.2: Field approximation description.

The field propagation dynamics is resolved by solving the equation sequentially every step Δz along the z -axis. At each z -step the propagation constants and the eigenmodes are solved. It is noteworthy that when \vec{k}_1 is accurately given as an initial condition, longer propagation ($> 100 \mu\text{m}$) can be covered with modest mesh. Otherwise meshing needs to be increased to resolve the beat wavelength ($\lambda_b = \frac{2\pi}{\Delta_c k_0}$, Δ_c - fraction of difference of \vec{k}_1 from the target wave-vector \vec{k}_0).

One of the initial stages in simulating 3D beam propagation within a HCPCF involves constructing a suitable mesh. Fig. 6.3 presents a typical 3D meshing arrangement for a straight HCPCF. In this example, the fiber structure is divided into contiguous segments of a specified length, and the meshing is confined to the transverse plane. This meshing approach offers the advantage of computational efficiency.

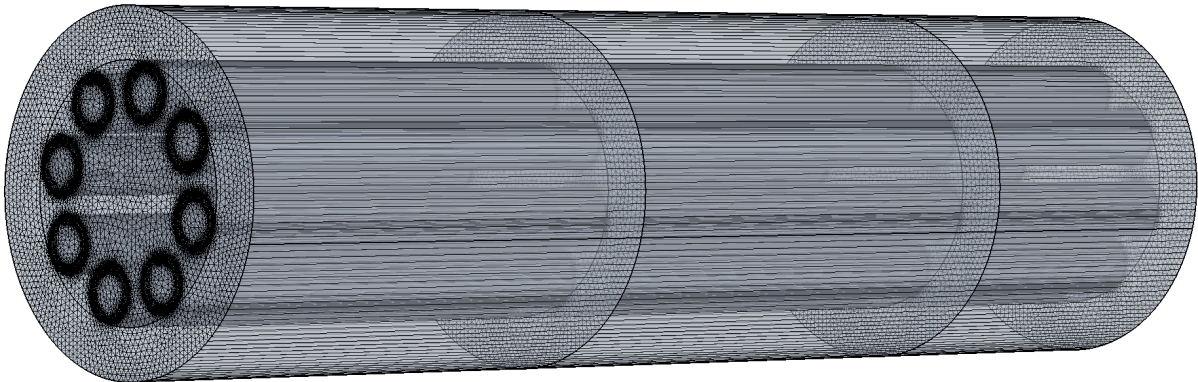


Figure 6.3: Appearance of meshed in 3D HCPCF.

Secondly, in order to account for a propagation along the fiber axis that can have an arbitrary curved line, we introduce the spatial propagation phase, which writes as $\phi = \beta \cdot z$ for a straight fiber, and takes the following expression for a bend fiber:

$$\phi = \beta \cdot (R_{\text{bend}} \cdot \text{atan2}(z, y + R_{\text{bend}}) + L_{\text{in}}). \quad (6.2)$$

Here, atan2 is a function of four-quadrant inverse tangent (see COMSOL multiphysics® manual). It gives the angle by which the center of the domain is shifted upon a bend of radius of curvature R_{bend} . L_{in} is length of domain before bend domain. Last domain after bending must be straight in the same way as the start domain. This is implemented by having a quarter of one coil conjoint to straight domain. The latter axis is parallel to one of the axes (here y -axis is oftenly used), and its associated phase is expressed as:

$$\phi = \beta \cdot (-y + R_{\text{bend}} \cdot \frac{\pi}{2} + L_{\text{in}}) \quad (6.3)$$

It is noteworthy that in practice the bend fiber section is shorter than a “quarter coil” to keep the computational resources to a manageable level. To this end, I developed equation for phase evolution in a such straight domain (displayed in blue on Fig. 6.4 (bottom)) of the fiber after bending length L_{bend} :

$$\phi = \beta \cdot (A \cdot (a \cdot (z - z_{b_0}) + b \cdot (y - y_{b_0}))) + L_{\text{bend}} + L_{\text{in}} \quad (6.4)$$

where $L_{\text{bend}} = \varphi_b \cdot R_{\text{bend}}$ is the length of the bent domain marked as yellow on figure 6.4 (bottom), L_{in} is the length of straight domain marked as green on figure 6.4 (bottom), y_{b_0} and z_{b_0} are coordinates of the center position gradient, and they are at equal position from domain ends, $R_{\text{bend}} \cdot (\cos(\varphi_b) - 1)$ and $R_{\text{bend}} \cdot \sin(\varphi_b)$ respectively. The parameters a and b are set to control the gradient direction and they are equal to $\sin(\frac{\pi}{4} - \varphi_b) + \cos(\frac{\pi}{4} - \varphi_b)$ and $\sin(\frac{\pi}{4} - \varphi_b) - \cos(\frac{\pi}{4} - \varphi_b)$ respectively. The parameter $A = \frac{1}{\sqrt{2}}$ is a normalisation factor for compensation of grow rate of gradient term. Also, it was necessary to develop equations for z , y coordinates of the end of the line (L_{out}) in ZY -plane. Appendix A.3 gives the details of the expressions of these coordinates. This line is normal to the cross-section of the end of the domain with bending (L_{bend}) as displayed with on figure 6.4 (top).

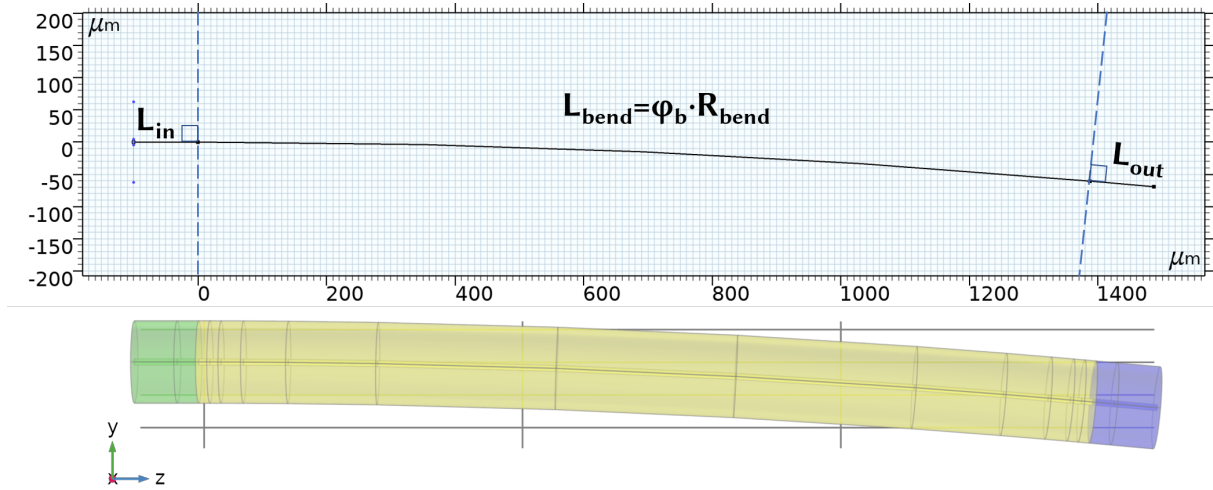


Figure 6.4: (Top) ZY -plane which show the line along which 2D cross-section of the fiber will be extruded. (Bottom) Fiber in 3D already extruded with 3 domains color-coded. Where green is input domain, yellow is bended domain and blue is straight domain after bending.

Finally, the design of a 3D phase-matching layer (PML) is crucial in ensuring accurate results because the boundaries are extremely sensitive to material index change and to the optical field structure at that interface. We developed an approach to imitate PML with imaginary part of material refractive index which represents the attenuation of the field inside PML [61], [62]:

$$n_{\text{in PML}} = n_{\text{mat}} - j \cdot \alpha$$

$$\alpha = \frac{(m+1) \cdot \lambda}{4\pi \cdot n_{\text{mat}} \cdot d_{\text{PML}}} \cdot \left(\frac{\rho}{d_{\text{PML}}} \right)^m \cdot \ln \left(\frac{1}{R_{\text{PML}}} \right). \quad (6.5)$$

Here, $n_{\text{in PML}}$ and n_{mat} are the index of the PML and of the material respectively. m is an integer, usually equal to 3, λ - wavelength used for simulation, d_{PML} - thickness of the PML, R_{PML} - reflectance of the PML which approaching 0 and better to be $\ll 10^{-100}$, ρ is called the distance function of the PML. This distance function ρ is a key parameter and is strongly dependent to the phase ϕ . Consequently, ρ must be adequately defined for all target domains, namely longitudinally, transversely and inter-sectional. The expressions of ρ for the different configurations are detailed in Appendix A.5. Fig. 6.5 shows an example of the α for a bend section of a HCPCF. Also note here that in 3D we do not consider anisotropy of the material index.

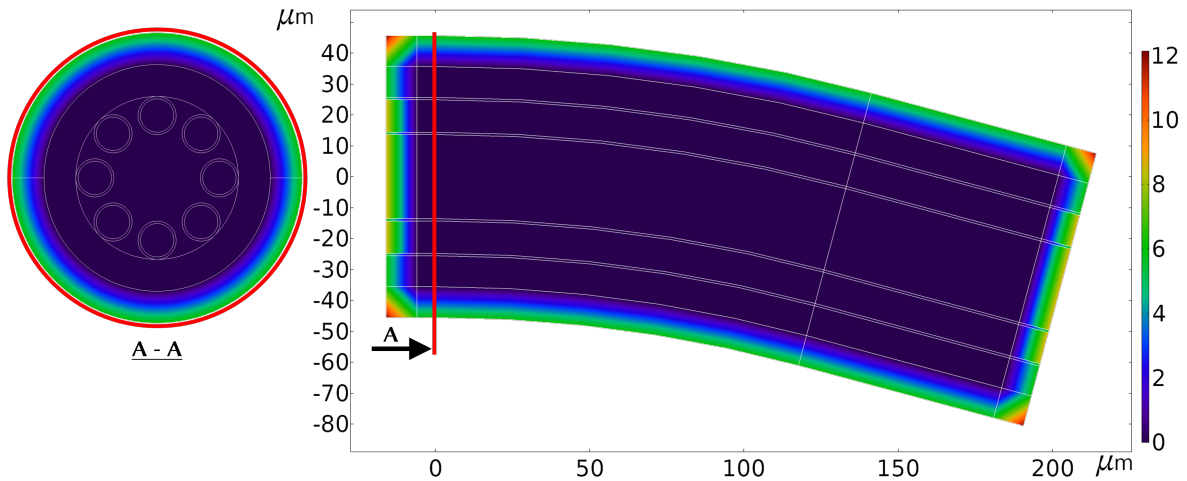


Figure 6.5: Plots of α for $R_{\text{PML}} = 10^{-200}$. (Left) A-A cross section is XY -plane at $Z = 0$. (Right) ZY -plane.

6.2.2 Beam propagation in HCPCF

Once the HCPCF's 3D structure, mesh, and perfectly matched layer (PML) settings have been appropriately configured, we can proceed with beam propagation simulations. In these simulations, we set the initial field to match the characteristics of the mode LP_{01_y} , specifically ensuring that $E_x = 0$, $E_z = 0$. The wave-vector \vec{k}_1 was set to be aligned with z -axis (i.e. $k_{1_x} = k_{1_y} = 0$) and its magnitude was taken from solved mode for the plane at $Z = 0$. In our case, and in order to gain accuracy and the computing time efficiency, we take the z -component of \vec{k}_1 equal to the propagation constant of the fundamental mode of the fiber as calculated from a 2D solver, i.e. $k_{1_z} = \beta_{(\text{LP}_{01})}$. A list of the different test functions employed in setting the initial field can be found in Appendix A.4 for reference. The fiber explored is T8 HCPCF described in table 4.2

Fig. 6.6 (a) presents a longitudinal cross-section of the guided beam propagating through a straight HCPCF with a length of $100 \mu\text{m}$. Fig. 6.6 (b) illustrates the different components of the electric field of the beam at positions $z = 0$ and $z = 100 \mu\text{m}$. It is evident to observe that the transverse field profile undergoes changes during the $100 \mu\text{m}$ propagation, resulting in a stronger overlap with the cladding. Fig. 6.7 shows the fractional power distribution among the HCPCF core modes and its evolution along the the fiber length. The distribution was deduced via the coupling coefficient C introduced in chapter 2 and 5 (see also A.1). The results show that the initial field can be decomposed chiefly into LP_{01} (80% of the total power), LP_{02} (20%) and LP_{03} (7%). The relatively strong power in LP_{02} (20%) and LP_{03} (7%) is attributed to the fact their intensity profile

peaks in the center of the fiber core. A comparison of this modal distribution with that of $z = 100 \mu\text{m}$ shows that although the overall modal distribution remains stable, there is a slight power loss in the LP_{01} mode, accompanied by an increase in optical power distributed among the higher-order modes (HOMs).

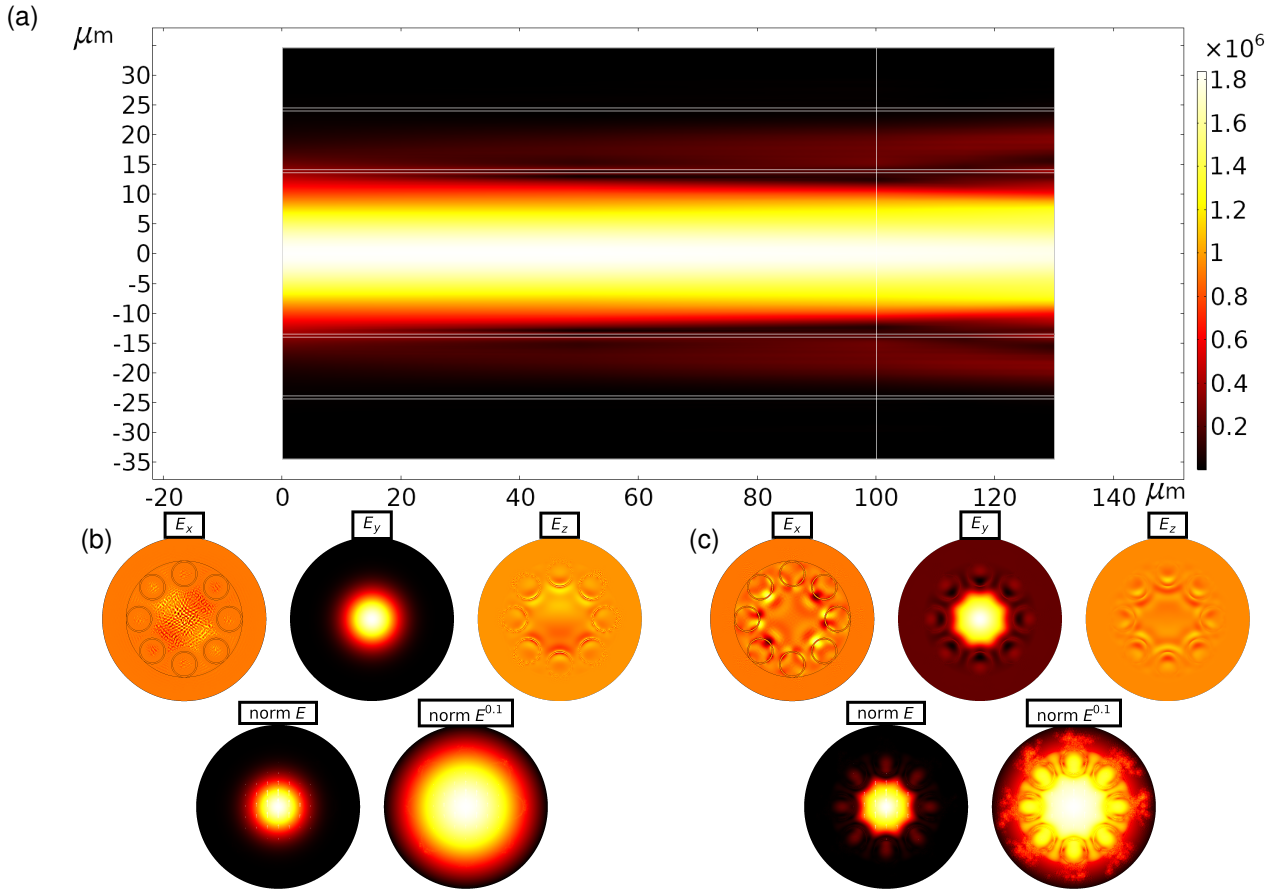


Figure 6.6: (a) Demonstration of E_{norm} in ZY -plane of ideal T8-TLF. Different components of electric field and E_{norm} at (b) $L = 0 \mu\text{m}$ and (c) $L = 100 \mu\text{m}$ at $\lambda = 581.7 \text{ nm}$.

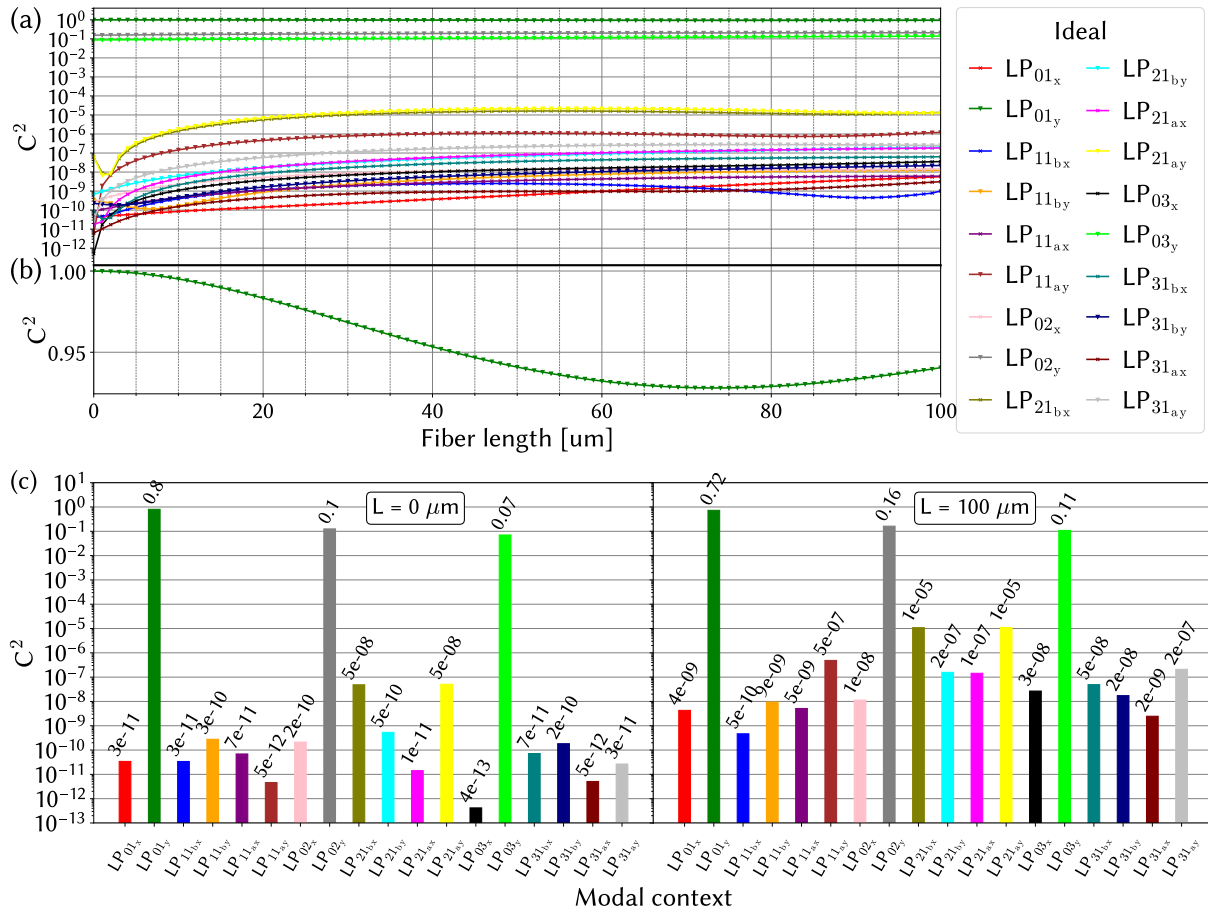


Figure 6.7: Mode distribution distribution and evolution with propagation. (a) coupling coefficient C^2 versus fiber length for different HCPCF modes. (b) A close-up of the fractional power in LP_{01} mode. (c) The modal power distribution at $L = 0 \mu\text{m}$ and $L = 100 \mu\text{m}$ at $\lambda = 581.7 \text{ nm}$. Note an approximation used in the equation (2.23) mentioned in the appendix A.1.

To validate the 3D technique, we conducted a comparison of propagation loss calculations with those obtained using a 2D mode solver. The propagation loss coefficient α_{3D} was determined using the scattering matrix approach, with the input and output being the two ends of the $100 \mu\text{m}$ long HCPCF. This coefficient is calculated as follows:

$$\alpha_{3D} = -\frac{10}{L_{\text{fiber}}} \log_{10} (|S_{21}|^2) \quad (6.6)$$

where S_{21} is the forward transmission coefficient of the S -matrix. Expressed in optical powers, α_{3D} writes as:

$$\alpha_{3D} = -\frac{10}{L_{\text{fiber}}} \log_{10} \left(\frac{P_{\text{out}}}{P_{\text{in}}} \right) \quad (6.7)$$

Here in its turn $P_{in\backslash out}$ can be defined from Pointing vector z component or field intensity at area $A_{in\backslash out}$:

$$P_{in\backslash out} = \int_{A_{in\backslash out}} \left(\frac{1}{2} \text{Re} [H_y^* \cdot E_x - H_x^* \cdot E_y] \right) \text{ or} \quad (6.8)$$

$$P_{in\backslash out} = \int_{A_{in\backslash out}} \left(\frac{cn\epsilon_0}{2} \left| \sqrt{E_x \cdot E_x^* + E_y \cdot E_y^* + E_z \cdot E_z^*} \right|^2 \right) \quad (6.9)$$

Fig. 6.8 shows the confinement loss spectrum as measured using a 2D mode solver (blue curve), and the present 3D technique (orange curve). The 3D results are consistent with the 2D ones over the calculated wavelength range of ~ 420 nm and ~ 620 nm. This is a very good proof that the PML and meshing are adequately implemented.

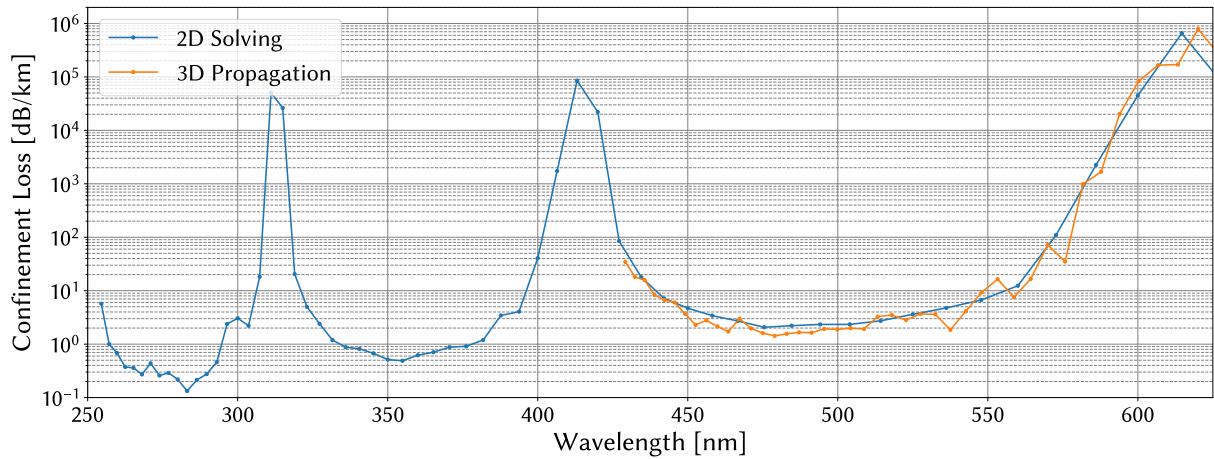


Figure 6.8: Losses obtained from 2D simulation and 3D Simulation (FM only).

It is noteworthy, however, to recall that the computing time for the 2D CL spectrum from 250 nm – 620 nm was around 2 hours, it took over 4 hours to compute α_{3D} for the fraction of the spectral bandwidth. Furthermore, the straight fiber configuration allowed to use very few longitudinal mesh elements compatible with our current servers. We develop further the computing requirement for more complex fiber configuration in a following section.

6.2.3 Surface roughness perturbation

Now that we have confirmed the accuracy of the mesh and implemented the PML, we proceed to investigate a fiber with structural deformations. Fig. 6.9 shows the 3D meshed structure of such a fiber. It is the same HCPCF considered so far but exhibits a deformation present on of the cladding tube outer surface. The deformation takes

the form of a half-circle shape that runs along length of the tube. The deformation is located $z = 50 \mu\text{m}$, with its convex side facing the center of the fiber. The radius of the half-circle is $0.5 \mu\text{m}$. This structural feature introduces a perturbation in the tube's geometry, which can affect its optical properties and light propagation characteristics.

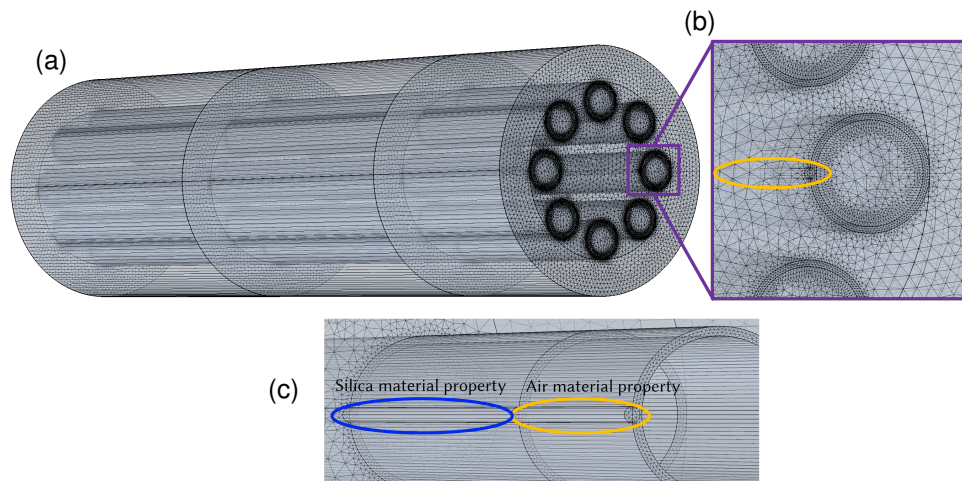


Figure 6.9: Mesh of T8-TLF with a rod.

Fig. 6.10 shows a longitudinal cross-section of the guided beam propagating through the $100 \mu\text{m}$ long HCPCF with the perturbation defined above. At first glance, there may appear to be no noticeable change compared to the perturbation-free fiber, as shown in Fig. 6.6. However, a closer examination of the modal fractional power and distribution, as depicted in Fig. 6.11, clearly reveals the impact of the rod-shaped perturbation. This impact is evident in the sudden power drop observed at $z = 50 \mu\text{m}$ in higher-order modes such as LP_{11} , as well as in the abrupt increase in power in the fundamental mode. These observations indicate that simple deformations can be effectively implemented in the BEM, allowing for the study of their effects on beam propagation.

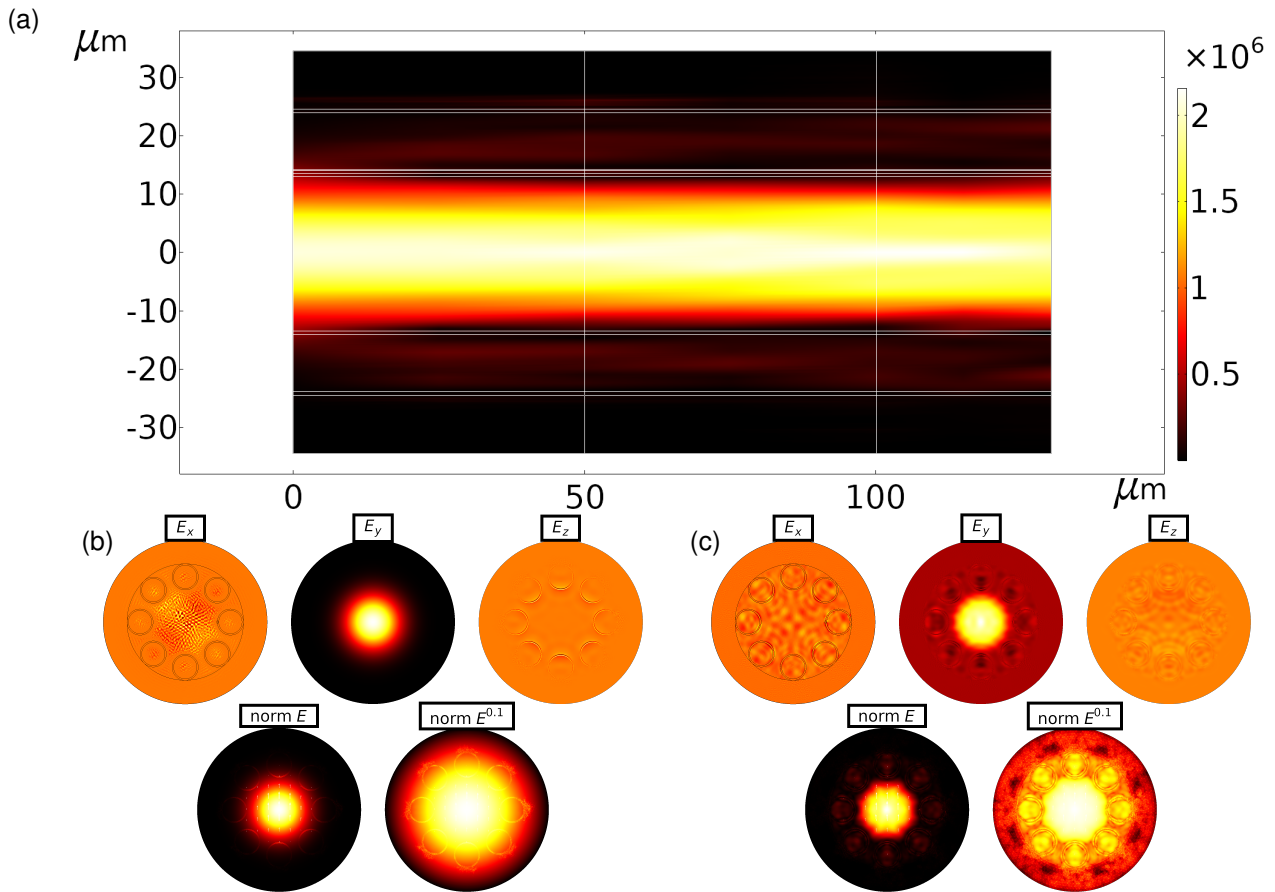


Figure 6.10: (a) Demonstration of E_{norm} in ZY -plane of perturbed T8-TLF. Different components of electric field and E_{norm} at (b) $L = 0 \mu\text{m}$ and (c) $L = 100 \mu\text{m}$ at $\lambda = 581.7 \text{ nm}$.

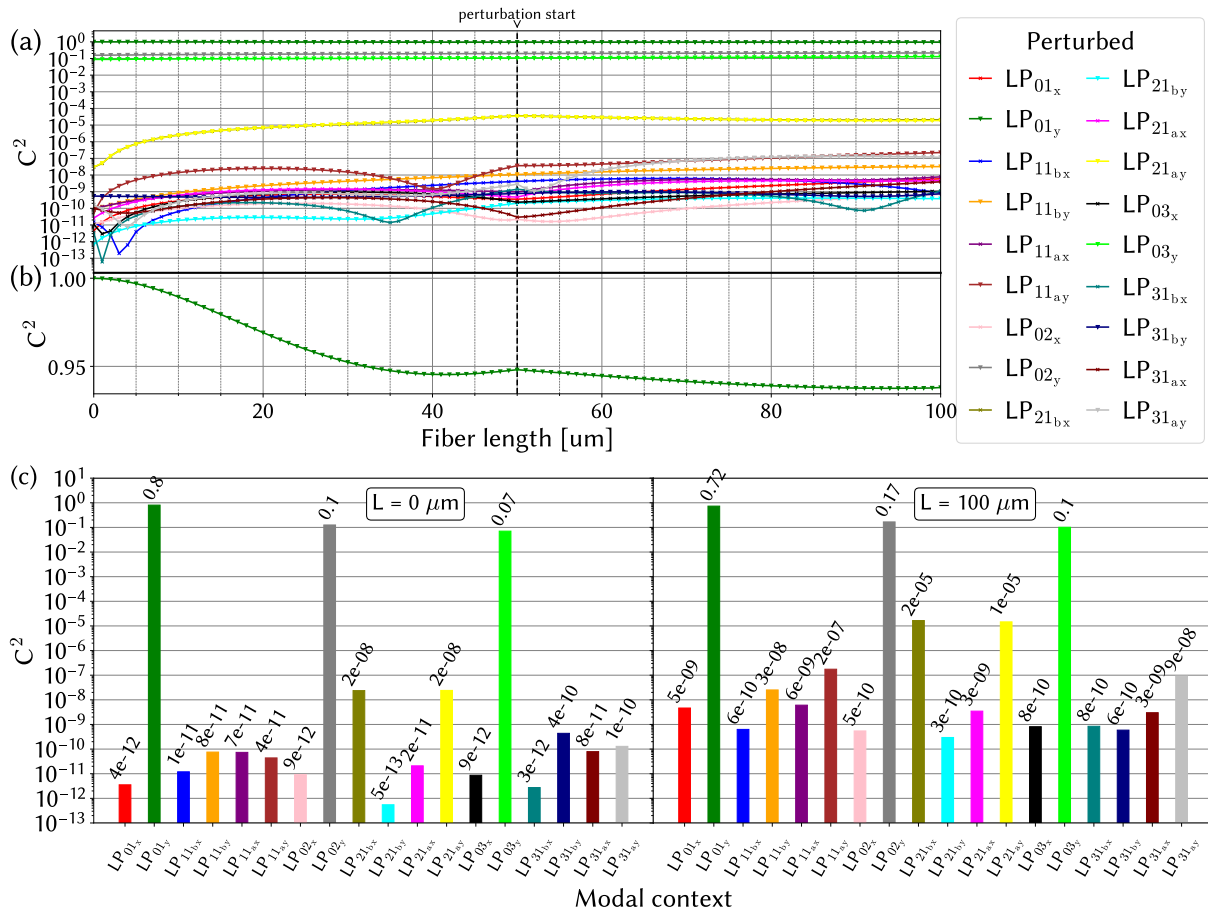


Figure 6.11: Mode distribution distribution and evolution with propagation in perturbed T8-TLF. (a) coupling coefficient C^2 versus fiber length for different HPCPF modes. (b) A close-up of the fractional power in LP_{01} mode. (c) The modal power distribution at $L = 0 \mu\text{m}$ and $L = 100 \mu\text{m}$ at $\lambda = 581.7 \text{ nm}$. Note an approximation used in the equation (2.23) mentioned in the appendix A.1.

This section pertains to explore the implementation of arbitrary surface roughness or fiber microbend. As previously detailed in Chapter 4, a *Python* library for generating roughness profiles was developed [111]. In this library, the class *GenerateRoughness* was set to accommodate 3D-structure. This gives 3 array-objects (L_s, R_x, R_y). Here, L_s represents the length along the propagation axis, while R_x and R_y correspond to the x and y coordinates of the deformation, respectively. This 3D roughness profile is schematically illustrated in Figure 6.12 by taking the example of the deviation of the fiber core centre from a given reference. Figure 6.13 plots this deviation in a 3D space. Several parameters can be controlled to build a roughness profile, including the length of propagation in meters, the RMS value of roughness in meters, the parameter P (which was previously discussed in chapter 4), the number of cosinusoidal components $\geq 100 \cdot P/(2\pi)$, and the number of elements in length.

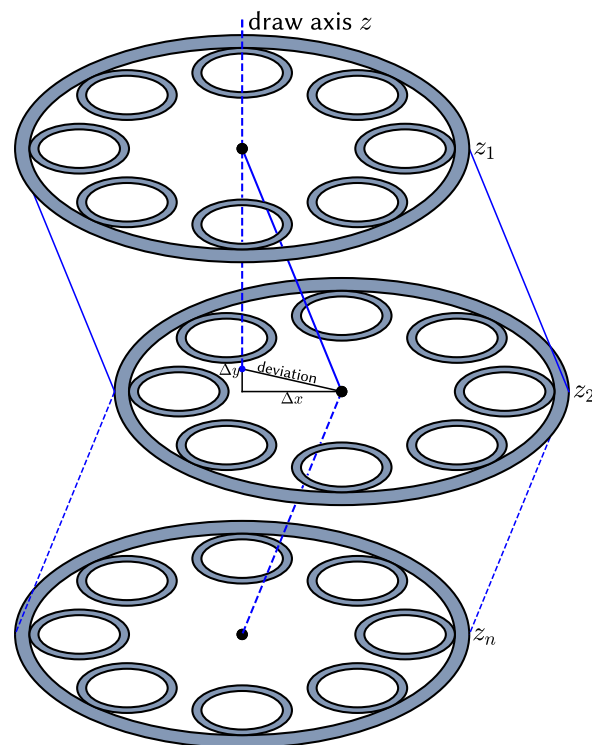


Figure 6.12: Schematic representation of 3D roughness proposed.

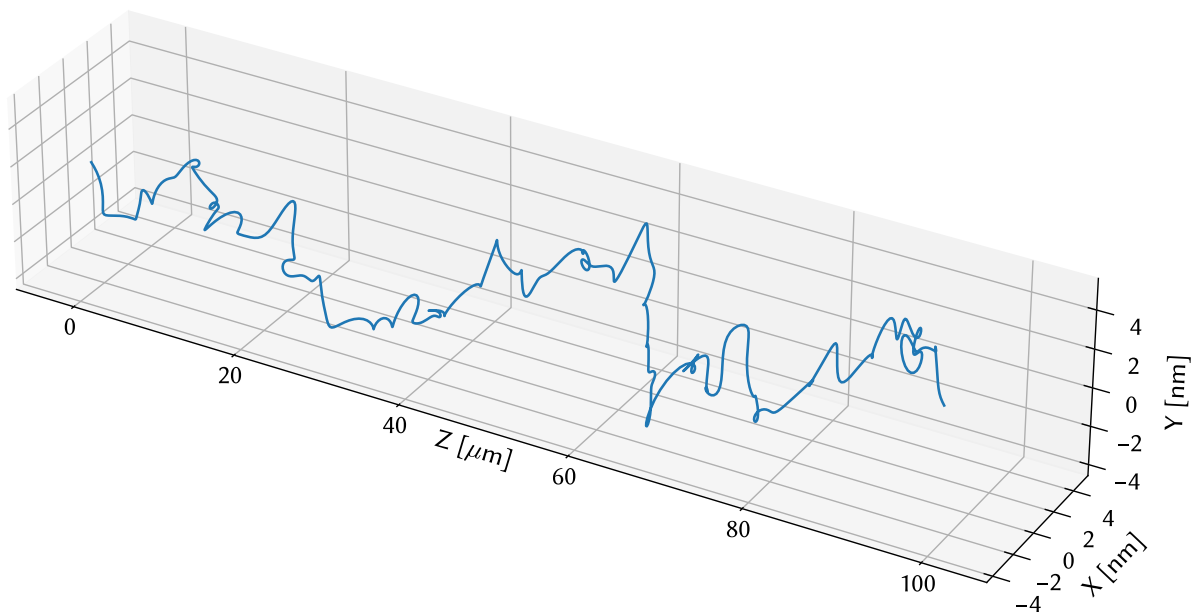


Figure 6.13: Plotted 3D roughness line with length of propagation $100 \mu\text{m}$, RMS value of roughness $\sigma = 2 \text{ nm}$, $P = 10$, number cosinusoidal components equal to 64 (for demonstration condition $\geq 100 \cdot P/(2\pi)$ is not respected) and number of elements in length equal to 800.

6.2.4 Discussion

The above work served as a demonstration of assessing the potential utility of 3D BEM in studying 3D beam propagation dynamic in HCPCF. While some results are very promising, this progress was not without challenges and limitations. One of the primary difficulties encountered was establishing the propagation phase ϕ for such complex structures, particularly in curved configurations. To tackle this issue, we implemented the beam envelope approximation available from COMSOL multiphysics® software and supplemented it with external programming components written in *Python*, *Java*, and *C*. Additionally, we addressed the formulation of the PML equations and implemented perturbations due to surface roughness.

Furthermore, we conducted a comparative analysis between 2D and 3D simulations, focusing on confinement loss in a straight fiber configuration, constrained by the available RAM at the time (see table 2.2). The observed evolution of the loss was found to be in good agreement for a fiber length of 100 μm , confirming the potential of 3D BEM as a robust tool for analyzing fibers in 3D. This paves the way for investigating perturbation effects that may occur during the propagation in HCPCF, such as bending and surface roughness, in the near future.

However, one of the primary concerns with the 3D BEM lies in the substantial computational resources required to model HCPCF with sub-micrometer resolution deformations, such as surface roughness or bent fibers. For instance, when dealing with bent fibers, especially those with “longitudinal” SR, we need to resolve a significantly higher number of longitudinal elements. As an example, for a longitudinal mesh with several hundred elements combined with a relatively “coarse” transverse mesh, we encountered RAM consumption exceeding 2 TB for a bent fiber design. In the case of designs with SR, each element in the line from Figure 6.13 must be represented as a longitudinal mesh element, resulting in RAM consumption exceeding 5 – 10 TB under promising scenarios. While we at the GPPMM group are still actively exploring solutions to address this limitation and enhance the efficiency of our simulations, we can conclude that 3D BEM, like the other computationally intensive 3D techniques, won’t be an adequate tool in HCPCF designs, but can be essential in investigation specific 3D propagation problems or phenomena.

We recall that this doctoral research work is an integral part of a larger-scale project of F. Benabid research group GPPMM. It is aimed at establishing a comprehensive framework for advancing the technology and science of HCPCF; the necessary milestones to develop next generation HCPCF and to address the pending scientific and

technological topics in this field. The project comprises three main pillars. The first pillar is dedicated to the innovation and implementation of novel fabrication processes and state-of-the-art facilities to explore new designs of HCPCF or improve on their optical and structural properties. The second pillar revolves around the meticulous and exhaustive characterization of HCPCF, encompassing both optical and structural aspects. The last pillar is a robust and versatile numerical platform designed to seamlessly integrate with two other key pillars of this ambitious project. The primary focus of my research endeavor was the development of such a numerical platform and assist on both the HCPCF fabrication process and characterization. It is thus within the broader context of these interconnected endeavors that the outcomes of this work is set for it is an essential component to the overarching goal of advancing HCPCF technology and science. In the next section, we present a concise and thorough overview of the key findings and insights obtained from the preceding chapters. Following that, we explore in another section potential directions for further research and innovation in the field of hollow-core photonic crystal fibers, taking into account both our accomplishments and the challenges we have faced.

6.2.5 Work Summary

The field of Inhibited Coupling guiding HCPCF has made significant progress over the past two decades and continues to be a subject of active research, drawing interest from industrial sectors like telecommunications, lasers, and laser material microprocessing, as well as fundamental research. It is within this context that the current doctoral research was conducted. Of particular timely significance are two key aspects: Firstly, the need for the advancement of fast and efficient numerical mode-solving tools, enabling the exploration of novel HCPCF designs and the characterization of fabricated HCPCF with improved efficiency compared to existing methods. Moreover, because Inhibited Coupling mechanism is not fully understood or explored, a faster numerical mode-solvers would be a tool to fill the knowledge gap. Secondly, there is a pressing need to deepen our understanding of the impact of surface roughness on the optical properties of HCPCF, but also on how this surface forms so to develop strategies for its control. In chapter 2, we used a commercially available 2D mode solver based on FEM, with a primary focus on ensuring its reliability for various HCPCF designs while developing suitable PML. Our secondary goal was to enhance its computational efficiency. To achieve this, we implemented modal discrimination techniques, enabling us to specifically target particular modes and significantly accelerate the processing of data generated by the

2D mode solver. We exploited the 2D mode solver to deepen our understanding of the Inhibited Coupling guidance mechanism, particularly through the development of a local azimuthal Fourier decomposition of the core-guided field, which, however, due to time constraints and the aim of maintaining a concise manuscript, we provided a brief description of this approach. In chapter 3, we leveraged the 2D mode solver to address a timely challenge: the design of a HCPCF that offers a combination of ultra-low transmission loss and single-mode guidance. Historically, efforts were primarily focused on achieving ultra-low confinement loss, resulting in substantial progress, as evidenced by transmission losses now falling within the range of 1 – 0.1 dB/km. As a result, the HCPCF research community has shifted its attention towards developing fibers with low loss and single-mode characteristics. In this context, we introduced three novel fiber designs (hybrid Kagome, Snowman, and hybrid PBG) by employing an approach that combines two different cladding structures, and even different guidance mechanism for one of them (i.e. hybrid PBG). The results exhibited a remarkable improvement in light confinement, achieving confinement losses as low as 10^{-4} dB/km in the telecom range, along with unprecedented single-mode guidance (HOMER of 10^4) compared to state-of-the-art HCPCFs. Fabrication processes have commenced, and for the hybrid Kagome fiber, we achieved a record-breaking HOM extinction ratio of 47 dB over a fiber length of 10 m, with losses of 1.6 dB/km at 1050 nm. Chapters 4 to 6 are dedicated to addressing another critical challenge in the field, namely surface roughness of the glass web that form the HCPCF cladding, which has proven to be a significant limitation in achieving ultra-low loss HCPCFs, particularly for wavelengths shorter than 1 μm . Despite the discovery of this phenomenon two decades ago as a major obstacle to unlocking the full potential of HCPCFs, a viable solution has remained elusive, and research into the physics of its generation and characterization has been relatively limited. Chapter 4 encompasses both numerical and experimental efforts aimed at comprehending the impact of surface roughness on transmission loss by introducing it into the structural profile of simulated HCPCFs. Additionally, it explores endeavors to develop fabrication processes for its control. Two novel HCPCF fabrication techniques were conducted to control surface roughness parameters like its RMS and power spectral density. In a first approach, a shear stress due to counter-directional gas and glass flows was induced to successfully improve on the quality of the fiber core surfaces. New state-of-the-art HCPCFs for short wavelengths exhibiting loss of 50 dB/km at 290 nm, 9.7 dB/km at 369 nm, 5.0 dB/km at 480 nm, 0.9 dB/km at 558 nm and 1.8 dB/km at 719 nm were reported and theoretically confirmed through scaling formulas. A second process, known as the "opto-thermal" method, was subsequently initiated by designing and integrating

a new furnace into the drawing tower, which comprise laser beam systems. Through precise adjustments of laser powers and modulation frequencies, this approach yielded a remarkable outcome: the observation of a non-stochastic roughness profile. While the identification of the optimal fiber draw parameters for showcasing groundbreaking performance records in HCPCF transmission is still ongoing, the initial results undeniably underscore the viability and innovative potential of this novel technique. The implications of this discovery have the potential to revolutionize the field of fiber photonics, and could impact other field in material nanoprocessing. A second process named “opto-thermal” was then initiated with the implementation in the drawing tower of a new furnace compatible with laser beam systems. By adjusting laser powers and modulation frequencies, for the first time a non-stochastic roughness profile was observed. Although the optimum fiber draw parameters have not yet been identified to demonstrate new record performances, the results already show the soundness of this original technique, and they hold revolutionary potential for this technique.

Finally, chapters 5 and 6 addressed the extension of 2D mode analysis to the propagation axis by exploring both 2D+1 and 3D simulations. Novel 2D+1 simulation technique have been proposed. This method allowed to simulate the impact of deformations along the fiber propagation axis on the coupling loss, scattering and mode coupling, and provide useful scaling laws. We have introduced a characteristic length L_{ch} to transcribe the coupling loss due surface roughness into a transmission loss. Future work to validate and improve on this method includes the extension of butt-coupling to a stack of interfaces, which will give provide the transmission loss and, at the same time, distinguish the contribution of SSL from the CL. In this chapter, we paved the ways to explore the practicality of 3D technique and to capture the full picture of the beam propagation dynamics in HCPCF. The results, using a BEM, show that we successfully replicated the CL obtained with 2D mode solver, while additionally tracking the evolution of modal content during propagation. Moreover, we achieved the implementation of arbitrary 3D surface roughness profiles. However, it is essential to acknowledge that the significant computational demands of 3D techniques pose a substantial obstacle to their utilization as a general-purpose platform for HCPCF design.

In conclusion, the research presented here has the potential to significantly impact the development of next generation low-loss single-mode fibers, further advancing the downward trend in losses and enhancing the capabilities of hollow-core optical fibers for new applications and at unconventional wavelength ranges.

6.2.6 Directions for future work

Within the overarching objective of developing a comprehensive science and technology platform to enable the design and realization of next-generation HCPCFs and to deepen our comprehension of the fundamental principles in both the light guidance within these photonic microstructures and in their microfabrication, in particular the surface roughness formation, this work unveiled the challenges and the several promising avenues for future exploration and innovation.

The progress made in this research highlights the critical significance of advancing our comprehension and mastery of surface roughness in HCPCF. This understanding is pivotal for the development of HCPCFs that can significantly reduce losses in UV and DUV spectral ranges, thereby unlocking exciting possibilities in a wide array of applications, including telecommunications, quantum communication, and gas-filled HCPCFs. Furthermore, this pursuit involves pioneering explorations into innovative fabrication processes, such as opto-thermal techniques, which hold immense potential but demand thorough investigation into the intricacies of rheology and surface profile formation. Simultaneously, the ongoing quest to design HCPCFs with improved specifications like reduced propagation loss, single-mode operation, and bend insensitivity, remains a paramount objective within the HCPCF field. Achieving these goals implies further research across the various components of the HCPCF development chain, encompassing numerical simulations, fabrication processes, fiber characterization, and advanced design methodologies. This holistic approach is essential to drive progress in HCPCF technology and its myriad applications.

In the realm of numerical tools, 2D simulations have reached a high level of reliability and computational efficiency. Future efforts should focus on creating user-friendly interfaces to make these tools accessible to fiber designers, fabricators, and users. The emerging 2D+1 techniques offer interesting prospects, and further research is needed to enhance their reliability and explore their potential applications, such as investigating transmission loss and mode coupling during beam propagation by extending the developed technique in chapter 5 to conjoined interfaces. The concept of characteristic length also warrants in-depth exploration, investigating into the mechanisms of scattering by surface roughness.

While 3D techniques offer a comprehensive platform for studying beam propagation dynamics and optical phenomena like scattering, microbend, mode coupling, and interference, their current demands on computational resources make them less suitable as a general-purpose HCPCF design and characterization tool. However, they can comple-

ment 2D+1 techniques, either by bolstering the development of reliable 2D+1 methods or by providing data that 2D+1 simulations cannot yield, particularly in understanding the dynamics of scattering, microbend, and modal interactions.

The physics of light guidance in HCPCFs remains a dynamic area of research, with ongoing investigations into the Inhibited Coupling guidance mechanism. Future work should aim to distinguish the effects of IC and tunnelling phenomena, explore fiber designs that achieve full inhibition between core and cladding modes, and delve into the polarization properties of IC HCPCFs, offering possibilities for designing HCPCFs with controlled polarization.

In the domain of fiber design, there is a push to develop HCPCFs with well-characterized polarization properties, enhanced single-mode operation, and improved bend tolerance. These endeavors are intrinsically linked to the conceptual tools developed in this research for creating novel fibers with specific characteristics.

In conclusion, this doctoral work serves as a foundation for future research spanning a wide range of areas, from numerical simulations and fiber design to the physics of light guidance and surface roughness control. The successful exploration of these avenues promises exciting prospects for advancing the science and technology of HCPCFs over the next 5 – 10 years and beyond.

A

Appendix

Table of content

A.1	Couple coefficients	177
A.2	Script for the λ from normalized frequency	179
A.3	Coordinates of the point which is at length of L from tangent point on tangent line to the circle	184
A.4	Mode field test functions	186
A.5	Distance function inside 3D PML	187

A.1 Couple coefficients

Overlap integral computation involves two solutions: $(\bar{E}_1, \bar{H}_1), (\bar{E}_2, \bar{H}_2)$:

$$C = \frac{\iint_S \frac{1}{2} \left(\bar{E}_{t_1} \times \bar{H}_{t_2}^* \right) \cdot \hat{z} dS}{\sqrt{P_{z_1}} \sqrt{P_{z_2}}} \quad (\text{A.1})$$

$$P_{z_i} = \iint_S \frac{1}{2} \left(\bar{E}_{t_i} \times \bar{H}_{t_i}^* \right) \cdot \hat{z} dS$$

where S is cross section with PMLs excluded, \bar{E}_{t_i} is transverse component of the electric field, \bar{H}_{t_i} is transverse component of the magnetic field, $i = 1, 2$. In the framework of LP modes approximations (acceptable for hollow core fibers [126]) we can write:

$$\bar{H} \simeq \frac{n_{\text{eff}}}{\eta_0} \hat{z} \times \bar{E}, \text{ where } \eta_0 = \sqrt{\frac{\mu_0}{\varepsilon_0}} \approx 377 \Omega \quad (\text{A.2})$$

$$\begin{aligned} P_{z_i} &= \iint_S \frac{1}{2} \left(\bar{E}_{t_i} \times \bar{H}_{t_i}^* \right) \cdot \hat{z} dS \\ &= \frac{n_{\text{eff}_i}}{\eta_0} \iint_S \frac{1}{2} \left(\bar{E}_{t_i} \cdot \bar{E}_{t_i}^* \right) dS \\ &= \frac{n_{\text{eff}_i}}{\eta_0} \iint_S \frac{1}{2} |\bar{E}_{t_i}|^2 dS \end{aligned}$$

$$\begin{aligned} C &= \frac{\iint_S \frac{1}{2} \left(\bar{E}_{t_1} \times \bar{H}_{t_2}^* \right) \cdot \hat{z} dS}{\sqrt{P_{z_1}} \sqrt{P_{z_2}}} \quad (\text{A.3}) \\ &= \frac{\frac{n_{\text{eff}_2}}{\eta_0} \frac{1}{2} \iint_S \left(\bar{E}_{t_1} \cdot \bar{E}_{t_2}^* \right) dS}{\sqrt{P_{z_1}} \sqrt{P_{z_2}}} \\ &= \frac{\frac{n_{\text{eff}_2}}{\sqrt{n_{\text{eff}_1} n_{\text{eff}_2}}} \iint_S \left(\bar{E}_{t_1} \cdot \bar{E}_{t_2}^* \right) dS}{\sqrt{\iint_S |\bar{E}_{t_1}|^2 dS} \sqrt{\iint_S |\bar{E}_{t_2}|^2 dS}} \end{aligned}$$

In order to simplify the equation and using the fact that factor $\frac{n_{\text{eff}_2}}{\sqrt{n_{\text{eff}_1} n_{\text{eff}_2}}}$ approaching 1, especially for the same modes - we approximate it to 1:

$$\begin{aligned}
C^2 &= \frac{\left| \iint_S (\overline{E}_{t_1} \cdot \overline{E}_{t_2}^*) dS \right|^2}{\iint_S |\overline{E}_{t_1}|^2 dS \iint_S |\overline{E}_{t_2}|^2 dS} & (A.4) \\
&= \frac{\left| \iint_S (E_{x_1} E_{x_2}^* + E_{y_1} E_{y_2}^*) dS \right|^2}{\iint_S (|E_{x_1}|^2 + |E_{y_1}|^2) dS \iint_S (|E_{x_2}|^2 + |E_{y_2}|^2) dS} \\
&= \frac{\left| \iint_S (E_{x_1} E_{x_2}^* + E_{y_1} E_{y_2}^*) dS \right|^2}{(\iint_S |E_{x_1}|^2 dS + \iint_S |E_{y_1}|^2 dS)(\iint_S |E_{x_2}|^2 dS + \iint_S |E_{y_2}|^2 dS)}
\end{aligned}$$

C^2 - should be the fraction of the power transmitted from E_{t_1} to E_{t_2} , then $1-C^2$ it is loosed fraction of power.

A.2 Script for the λ from normalized frequency

Since equation for normalized frequency F is:

$$F = \frac{2t}{\lambda} \cdot \sqrt{n_{glass}(\lambda)^2 - n_{gas}(\lambda)^2}$$

We can't directly get λ from F in general case when Refractive index of medium dependent on λ .

$$n_{glass} = \sqrt{1 + \frac{0.6961663\lambda^2}{\lambda^2 - 0.0684043^2} + \frac{0.4079426\lambda^2}{\lambda^2 - 0.1162414^2} + \frac{0.8974794\lambda^2}{\lambda^2 - 9.896161^2}} \quad (\text{A.5})$$

$$n_{air} = 1 + \frac{0.05792105}{238.0185 - \lambda^{-2}} + \frac{0.00167917}{57.362 - \lambda^{-2}} \quad (\text{A.6})$$

I developed the script which iteratively solves this problem.

```

1 #include <math.h>
2 #include <stdlib.h>
3 #include <string.h>
4 #include <stdbool.h>
5
6 #ifndef _MSC_VER
7 #define EXPORT __declspec(dllexport)
8 #else
9 #define EXPORT
10 #endif
11
12 static const double xenon(const double wl, const double p, const double
    t) {
13     double calc = 1 + 0.00322869/(46.301 - 1.0 / pow(wl, 2)) +
        0.00355393/(59.578 - 1.0 / pow(wl, 2)) + 0.0606764/(112.74 - 1.0 /
        pow(wl, 2));
14     const double p0 = 1.0;
15     const double t0 = 293.15;
16     calc = sqrt(1+(pow(calc, 2) - 1)*(p/p0)*(t0/t));
17     return calc;
18 }
19
20 static const double air(const double wl) {
21     double calc = 1.0 + (0.05792105 / (238.0185 - 1.0 / pow(wl, 2))) +
        (0.00167917 / (57.362 - 1.0 / pow(wl, 2)));
22     return calc;
23 }

```

```

24
25 static const double glass(const double wl) {
26     double calc = sqrt(1 + (0.6961663 * pow(wl, 2)) / (pow(wl, 2) - pow
        (0.0684043, 2)) + (0.4079426 * pow(wl, 2)) / (pow(wl, 2) - pow
        (0.1162414, 2)) + (0.8974794 * pow(wl, 2)) / (pow(wl, 2) - pow
        (9.896161, 2)));
27     return calc;
28 }
29
30 static const double from_wl_to_f(const double t, const double wl) {
31     double calc = 2 * t / wl * sqrt(pow(glass(wl), 2) - pow(air(wl), 2));
32     return calc;
33 }
34
35 static const double from_wl_to_f_xenon(const double t, const double wl,
        const double pressure, const double temperature) {
36     double calc = 2 * t / wl * sqrt(pow(glass(wl), 2) - pow(xenon(wl,
        pressure, temperature), 2));
37     return calc;
38 }
39
40 static const double from_f_to_wl_wrong(const double t, const double f) {
41     double calc = 2 * t / f * sqrt(pow(1.45, 2) - 1);
42     return calc;
43 }
44
45 static const void optimisation(long long *i, double *temp_F, double *
        F_real, const double *F, double *delta_F_1){
46     if (*i % 2 != 0 && *i > 0){ // # every odd index we take delta F
47         *temp_F = *F_real - *F;
48         *delta_F_1 = (*temp_F) > 0 ? *temp_F : (*temp_F) * -1;
49     }
50     if (*i % 2 == 0 && *i > 0) {
51         *temp_F = *F_real - *F;
52         double delta_F_2 = (*temp_F) > 0 ? *temp_F : (*temp_F) * -1;
53         *i += (long long)(delta_F_2 / (*delta_F_1 - delta_F_2));
54         if (*i % 2 != 0)
55             *i--;
56     }
57 }
58
59 static const double solve_good_wl_for_F(const double F, const double t)
        {

```

```

60 double min_value = 1e-10; // accuracy of 1e-10
61 double wl_wrong = from_f_to_wl_wrong(t, F);
62 double F_real = from_wl_to_f(t, wl_wrong);
63 long long i = 0;
64 bool initial_cond = (F_real - F) > 0;
65 double m = initial_cond ? 1. : -1.; // sign definition;
66 double delta_F_1 = 0;
67 double temp_F;
68 while (initial_cond ? (F_real > F) : (F_real < F)) {
69     i++;
70     F_real = from_wl_to_f(t, wl_wrong + min_value * i * m);
71     optimisation(&i, &temp_F, &F_real, &F, &delta_F_1);
72 }
73 return wl_wrong + min_value * i * m;
74 }
75
76 const double solve_good_wl_for_F_xenon(const double F, const double t,
77     const double pressure, const double temperature) {
78     double min_value = 1e-10; // accuracy of 1e-10
79     double wl_wrong = from_f_to_wl_wrong(t, F);
80     double F_real = from_wl_to_f_xenon(t, wl_wrong, pressure, temperature)
81     ;
82     long long i = 0;
83     bool initial_cond = (F_real - F) > 0;
84     double m = initial_cond ? 1. : -1.; // sign definition;
85     double delta_F_1 = 0;
86     double temp_F;
87     while (initial_cond ? (F_real > F) : (F_real < F)) {
88         i++;
89         F_real = from_wl_to_f_xenon(t, wl_wrong + min_value * i * m,
90             pressure, temperature);
91         optimisation(&i, &temp_F, &F_real, &F, &delta_F_1);
92     }
93     return wl_wrong + min_value * i * m;
94 }
95
96 static const char *error = NULL;
97 static const char *author = "Author: Kostiantyn Vasko";
98 char *F_error;
99
100 EXPORT int init(const char *str) {
101     return 1;

```

```

100 }
101
102 EXPORT const char *getLastError() {
103     return error;
104 }
105
106 EXPORT int eval(const char *func,
107               int nArgs,
108               const double **inReal,
109               const double **inImag,
110               int blockSize,
111               double *outReal,
112               double *outImag) {
113     int i, j;
114     asprintf(&F_error, "F is too small, something wrong.\n Recompile dll
115                 in order to make it work.\n%s", author);
116
117     if (strcmp("get_good_wl", func) == 0) {
118         if (nArgs != 2) {
119             error = "Two argument expected.\n";
120             free(F_error);
121             return 0;
122         }
123         double t0;
124         for (i = 0; i < blockSize; i++) {
125             double F = inReal[0][i];
126             double t = inReal[1][i];
127             if (F < 1e-2){
128                 error = F_error;
129                 free(F_error);
130                 return 0;
131             }
132             // t it's thickness, must be in [um]
133             // usually t given in [m]
134             // so to transform to [um] we need to multiply by 1e6
135             t0 = t * 1e6;
136             // output of solve_good_wl_for_F given in [um]
137             // dont need to transform to [m]
138             // !BUT! need to use '[um]' after usage of this function
139             outReal[i] = solve_good_wl_for_F(F, t0);
140         }
141         free(F_error);
142     }
143     return 1;

```

```

142 }
143 else {
144     if (strcmp("get_good_wl_xenon", func) == 0) {
145         if (nArgs != 4) {
146             error = "Four argument expected.\n";
147             free(F_error);
148             return 0;
149         }
150         double t0_2;
151         for (i = 0; i < blockSize; i++) {
152             double F_2 = inReal[0][i];
153             double t_2 = inReal[1][i];
154             double pressure = inReal[2][i];
155             double temperature = inReal[3][i];
156             if (F_2 < 1e-2){
157                 error = F_error;
158                 free(F_error);
159                 return 0;
160             }
161             // t it's thickness, must be in [um]
162             // usually t given in [m]
163             // so to transform to [um] we need to multiply by 1e6
164             t0_2 = t_2 * 1e6;
165             // output of solve_good_wl_for_F given in [um]
166             // dont need to transform to [m]
167             // !BUT! need to use '[um]' after usage of this function
168             outReal[i] = solve_good_wl_for_F_xenon(F_2, t0_2, pressure,
169             temperature);
170         }
171         free(F_error);
172         return 1;
173     }
174     else {
175         error = "Unknown function.\n Available functions: get_good_wl,
176         get_good_wl_xenon.";
177         free(F_error);
178         return 0;
179     }
180 }

```

Listing A.1: Full code for the algorithm which can be used for COMSOL multiphysics®

A.3 Coordinates of the point which is at length of L from tangent point on tangent line to the circle

Firstly we need to get equation of line tangent to the circle with radius R_{bend} at angle φ_b . Also worth to mention that in equations (A.7, A.8, A.10, A.11) parameters $R = R_{\text{bend}}$ and $\varphi = \frac{\pi}{2} - \varphi_b$. For the circle in the center of the coordinates ($x_0 = 0; y_0 = 0$), equation is next:

$$y = -\cot(\varphi) \cdot x + R \cdot \csc(\varphi) \quad (\text{A.7})$$

For the circle in the center of the coordinates ($x_0 \neq 0; y_0 \neq 0$), equation of line tangent to the circle is next:

$$y = \frac{-x \cdot (R \cdot \cos(\varphi) - x_0) - x_0^2 - y_0^2 + x_0 \cdot R \cdot \cos(\varphi) + y_0 \cdot R \cdot \sin(\varphi) + R^2}{R \cdot \sin(\varphi) - y_0}$$

$$y = k \cdot x + m \quad (\text{A.8})$$

$$k = -\frac{R \cdot \cos(\varphi) - x_0}{R \cdot \sin(\varphi) - y_0}$$

$$m = \frac{-x_0^2 - y_0^2 + x_0 \cdot R \cdot \cos(\varphi) + y_0 \cdot R \cdot \sin(\varphi) + R^2}{R \cdot \sin(\varphi) - y_0}$$

Equation for distance we can express as:

$$L_{\text{out}} = \sqrt{(z_{b_1} - z_{b_0})^2 + (y_{b_1} - y_{b_0})^2} \quad (\text{A.9})$$

We already know z, y coordinates of the start of the line which are equal to z_{b_0} and y_{b_0} respectively also we have L_{out} known. Next we write equation A.8 into equation A.9 and after some math I got equation in form of square equation:

$$a \cdot x^2 + b \cdot x + c = 0$$

$$a = -k^2 - 1 \quad (\text{A.10})$$

$$b = 2 \cdot R \cdot \cos(\varphi) - 2 \cdot k \cdot (m - R \cdot \sin(\varphi))$$

$$c = L^2 - (m - R \cdot \sin(\varphi))^2 - (R \cdot \cos(\varphi))^2$$

Then we solve our square equation A.10 for $x_{1,2}$ and set result into equation A.8:

$$\begin{aligned}
 D &= b^2 - 4ac \\
 x_{1,2} &= \frac{-b \pm \sqrt{D}}{2a} = z_{b_{11,2}} \\
 y_{1,2} &= k \cdot x_{1,2} + m - R = y_{b_{11,2}}
 \end{aligned}
 \tag{A.11}$$

There is two solutions but in my case positive discriminant was the correct solution. Much later during finishing writing of the thesis I asked chatGPT to optimise this equations and it end up with those:

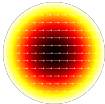
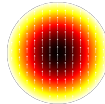
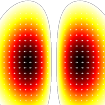
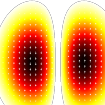
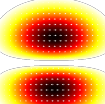
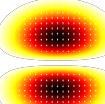
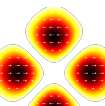
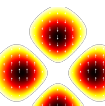
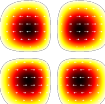
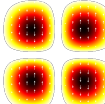
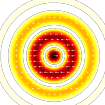
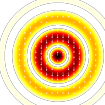
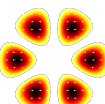
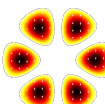
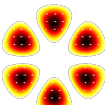
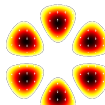
$$\begin{aligned}
 x &= x_0 + R \cdot \cos(\phi) + L \cdot \sin(\phi) \\
 y &= y_0 + R \cdot \sin(\phi) - L \cdot \cos(\phi)
 \end{aligned}
 \tag{A.12}$$

After verification of the given equations I decide to let them here because they require much less math operations for the computer.

A.4 Mode field test functions

For recognition of the solved modes was used test field functions listed in table (A.1)

Table A.1: Table with test functions

Mode name	Equations	Field	Equations	Field
LP_{01}^x , LP_{01}^y	$E_x = e^{-\frac{x^2+y^2}{R^2}}$ $E_y = 0$		$E_x = 0$ $E_y = e^{-\frac{x^2+y^2}{R^2}}$	
$LP_{11}^{a\ x}$, $LP_{11}^{a\ y}$	$E_x = \sin\left(\frac{2\pi x}{4R}\right) e^{-\frac{x^2+y^2}{R^2}}$ $E_y = 0$		$E_x = 0$ $E_y = \sin\left(\frac{2\pi y}{4R}\right) e^{-\frac{x^2+y^2}{R^2}}$	
$LP_{11}^{b\ x}$, $LP_{11}^{b\ y}$	$E_x = \sin\left(\frac{2\pi y}{4R}\right) e^{-\frac{x^2+y^2}{R^2}}$ $E_y = 0$		$E_x = 0$ $E_y = \sin\left(\frac{2\pi x}{4R}\right) e^{-\frac{x^2+y^2}{R^2}}$	
$LP_{21}^{a\ x}$, $LP_{21}^{a\ y}$	$E_x = \sin\left(\frac{\pi \frac{x+y}{\sqrt{2}}}{R}\right) \sin\left(\frac{\pi \frac{x-y}{\sqrt{2}}}{R}\right) \cdot e^{-\frac{x^2+y^2}{R^2}}$ $E_y = 0$		$E_x = 0$ $E_y = \sin\left(\frac{\pi \frac{x+y}{\sqrt{2}}}{R}\right) \sin\left(\frac{\pi \frac{x-y}{\sqrt{2}}}{R}\right) \cdot e^{-\frac{x^2+y^2}{R^2}}$	
$LP_{21}^{b\ x}$, $LP_{21}^{b\ y}$	$E_x = \sin\left(\frac{\pi x}{R}\right) \sin\left(\frac{\pi y}{R}\right) e^{-\frac{x^2+y^2}{R^2}}$ $E_y = 0$		$E_x = 0$ $E_y = \sin\left(\frac{\pi x}{R}\right) \sin\left(\frac{\pi y}{R}\right) e^{-\frac{x^2+y^2}{R^2}}$	
LP_{03}^x , LP_{03}^y	$E_x = \cos\left(\frac{3\pi\sqrt{x^2+y^2}}{\frac{4}{3}R}\right) e^{-\frac{x^2+y^2}{R^2}}$ $E_y = 0$		$E_x = 0$ $E_y = \cos\left(\frac{3\pi\sqrt{x^2+y^2}}{\frac{4}{3}R}\right) e^{-\frac{x^2+y^2}{R^2}}$	
$LP_{31}^{a\ x}$, $LP_{31}^{a\ y}$	$E_x = \sin\left(\frac{\pi x}{R}\right) \sin\left(\frac{\pi \frac{x+\sqrt{3}y}{2}}{R}\right) \cdot \sin\left(\frac{\pi \frac{x-\sqrt{3}y}{2}}{R}\right) e^{-\frac{x^2+y^2}{R^2}}$ $E_y = 0$		$E_x = 0$ $E_y = \sin\left(\frac{\pi x}{R}\right) \sin\left(\frac{\pi \frac{x+\sqrt{3}y}{2}}{R}\right) \cdot \sin\left(\frac{\pi \frac{x-\sqrt{3}y}{2}}{R}\right) e^{-\frac{x^2+y^2}{R^2}}$	
$LP_{31}^{b\ x}$, $LP_{31}^{b\ y}$	$E_x = \sin\left(\frac{\pi y}{R}\right) \sin\left(\frac{\pi \frac{y+\sqrt{3}x}{2}}{R}\right) \cdot \sin\left(\frac{\pi \frac{y-\sqrt{3}x}{2}}{R}\right) e^{-\frac{x^2+y^2}{R^2}}$ $E_y = 0$		$E_x = 0$ $E_y = \sin\left(\frac{\pi y}{R}\right) \sin\left(\frac{\pi \frac{y+\sqrt{3}x}{2}}{R}\right) \cdot \sin\left(\frac{\pi \frac{y-\sqrt{3}x}{2}}{R}\right) e^{-\frac{x^2+y^2}{R^2}}$	

A.5 Distance function inside 3D PML

Straight longitudinal

For straight longitudinal configuration, the associated PML is lying in negative z space but ρ must be growing and positive. Also an offset $L_{in\ wg}$ used because input domain of this length starting in negative part of the z coordinate in space. The equation of ρ is then given by:

$$\rho(z) = -(z + L_{in\ wg}) \quad (\text{A.13})$$

Tilted longitudinal

In the presence of a tilt, the equation needs to present a dependency of 2 coordinates according to the bending radius as indicated below:

$$\begin{aligned} \phi_b &= \frac{L_b}{R_{bend}} - \text{is total angle of bended domain.} \\ \phi_a &= \frac{\pi}{4} - \phi_b - \text{is angle for gradient to aim it.} \\ z_c &= R_{bend} \cdot \cos\left(\frac{\pi}{2} - \phi_b\right) \\ y_c &= R_{bend} \cdot \left(\sin\left(\left(\frac{\pi}{2} - \phi_b\right)\right) - 1\right) \\ a &= \sin(\phi_a) + \cos(\phi_a) \\ b &= \sin(\phi_a) - \cos(\phi_a) \\ \rho(z, y) &= \frac{b \cdot (y - y_c) + a \cdot (z - z_c)}{\sqrt{2}} - L_{out\ wg} \end{aligned} \quad (\text{A.14})$$

Straight transverse

For the transverse PML, ρ have dependency on the 2 coordinates for straight case:

$$\rho(x, y) = \sqrt{x^2 + y^2} - R_{jacket} \quad (\text{A.15})$$

Bend transverse

When a bending is applied in this transverse plane, the 3 coordinates (x, y, z) are involved. For this purpose we introduce the point $(O_x = 0, O_y = R_{bend} \cdot (\sin(\frac{\pi}{2} - \phi_b(z, y)) - 1),$

$O_z = R_{\text{bend}} \cdot \cos\left(\frac{\pi}{2} - \phi_b(z, y)\right)$, where d the distance function writes as:

$$\begin{aligned} d(x, y, z) &= \sqrt{(x - O_x)^2 + (y - O_y)^2 + (z - O_z)^2} \\ \rho(x, y, z) &= d(x, y, z) - R_{\text{jacket}} \end{aligned} \quad (\text{A.16})$$

Tilted transverse

For tilted case in transverse there is dependency on 3 coordinates as well. We have coordinates of the point O in the center of tilted domain:

$$\begin{aligned} L_p(z, y) &= \frac{b \cdot (y - y_c) + a \cdot (z - z_c)}{\sqrt{2}} \\ O_x &= 0 \\ O_y &= R_{\text{bend}} \cdot \sin\left(\frac{\pi}{2} - \phi_b\right) - L_p(z, y) \cdot \cos\left(\frac{\pi}{2} - \phi_b\right) - R_{\text{bend}} \\ O_z &= R_{\text{bend}} \cdot \cos\left(\frac{\pi}{2} - \phi_b\right) + L_p(z, y) \cdot \sin\left(\frac{\pi}{2} - \phi_b\right) \end{aligned} \quad (\text{A.17})$$

where ϕ_b , y_c and z_c are taken from Tilted longitudinal ρ formulation. So distance from center to any point at plane:

$$\begin{aligned} d(x, y, z) &= \sqrt{(x - O_x)^2 + (y - O_y)^2 + (z - O_z)^2} \\ \rho(x, y, z) &= d(x, y, z) - R_{\text{jacket}} \end{aligned} \quad (\text{A.18})$$

Intersection

It is also worth mentioning that in cases where domains intersect, we need to sum the longitudinal and transverse PML-like attenuation. This implies that the refractive index for these domains will be expressed as:

$$n_{\text{in PML intersect}} = n_{\text{mat}} - j \cdot (\alpha_z + \alpha_{xy}) \quad (\text{A.19})$$

B

BIBLIOGRAPHY

Table of content

References	190
Scientific contributions	204

References

- [1] B. Debord, F. Amrani, L. Vincetti, F. Gérôme, and F. Benabid, “Hollow-core fiber technology: the rising of ‘gasphotonics’,” *Fibers*, Feb. 2019. [Online]. Available: <https://doi.org/10.3390/fib7020016> (cit. on pp. 17, 19–21, 24, 29, 110).
- [2] S. John, “Strong localization of photons in certain disordered dielectric superlattices,” *Phys. Rev. Lett.*, vol. 58, pp. 2486–2489, 23 Jun. 1987. [Online]. Available: <https://doi.org/10.1103/PhysRevLett.58.2486> (cit. on p. 17).
- [3] E. Yablonovitch, “Inhibited spontaneous emission in solid-state physics and electronics,” *Phys. Rev. Lett.*, vol. 58, pp. 2059–2062, 20 May 1987. [Online]. Available: <https://doi.org/10.1103/PhysRevLett.58.2059> (cit. on p. 17).
- [4] E. Yablonovitch, “Photonic band-gap structures,” *J. Opt. Soc. Am. B*, vol. 10, no. 2, pp. 283–295, Feb. 1993. [Online]. Available: <https://doi.org/10.1364/JOSAB.10.000283> (cit. on p. 17).
- [5] T. Birks, J. Roberts, P. Russell, D. Atkin, and T. Shepherd, “Full 2-d photonic bandgaps in silica/air structures,” *Electronics Letters*, vol. 31, pp. 1941–1943, Nov. 1995. [Online]. Available: <https://doi.org/10.1049/el:19951306> (cit. on pp. 17, 22).
- [6] R. Cregan, B. Mangan, J. Knight, *et al.*, “Single-mode photonic band gap guidance of light in air,” *Science (New York, N.Y.)*, vol. 285, pp. 1537–1539, Oct. 1999. [Online]. Available: <https://doi.org/10.1126/science.285.5433.1537> (cit. on p. 17).
- [7] T. A. Birks, J. C. Knight, and P. S. J. Russell, “Endlessly single-mode photonic crystal fiber,” *Opt. Lett.*, vol. 22, no. 13, pp. 961–963, Jul. 1997. [Online]. Available: <https://doi.org/10.1364/OL.22.000961> (cit. on p. 17).
- [8] B. J. Mangan, F. Couny, L. Farr, *et al.*, “Slope-matched dispersion-compensating photonic crystal fibre,” in *Conference on Lasers and Electro-Optics/International Quantum Electronics Conference and Photonic Applications Systems Technologies*, Optica Publishing Group, 2004, CPDD3. [Online]. Available: <https://opg.optica.org/abstract.cfm?URI=CLEO-2004-CPDD3> (cit. on p. 17).
- [9] J. Knight, T. Birks, R. Cregan, P. Russell, and J.-P. de Sandro, “Large mode area photonic crystal fibre,” *Electronics Letters*, vol. 34, no. 13, pp. 1347–1348, Jun. 1998. [Online]. Available: <https://doi.org/10.1049/el:19980965> (cit. on p. 17).
- [10] J. M. Dudley, G. Genty, and S. Coen, “Supercontinuum generation in photonic crystal fiber,” *Rev. Mod. Phys.*, vol. 78, pp. 1135–1184, 4 Oct. 2006. [Online]. Available: <https://doi.org/10.1103/RevModPhys.78.1135> (cit. on p. 17).

- [11] G. S. Wiederhecker, C. M. B. Cordeiro, F. Couny, *et al.*, “Field enhancement within an optical fibre with a subwavelength air core,” *Nature Photonics*, vol. 1, no. 2, pp. 115–118, Feb. 2007. [Online]. Available: <https://doi.org/10.1038/nphoton.2006.81> (cit. on p. 17).
- [12] F. Benabid, J. C. Knight, G. Antonopoulos, and P. S. J. Russell, “Stimulated raman scattering in hydrogen-filled hollow-core photonic crystal fiber,” *Science*, vol. 298, no. 5592, pp. 399–402, 2002. [Online]. Available: <https://doi.org/10.1126/science.1076408> (cit. on pp. 17, 23).
- [13] F. Couny, F. Benabid, P. J. Roberts, P. S. Light, and M. G. Raymer, “Generation and photonic guidance of multi-octave optical-frequency combs,” *Science*, vol. 318, no. 5853, pp. 1118–1121, 2007. [Online]. Available: <https://doi.org/10.1126/science.1149091> (cit. on pp. 17, 19, 23, 70).
- [14] F. Couny, F. Benabid, P. J. Roberts, M. T. Burnett, and S. Maier, “Identification of bloch-modes in hollow-core photonic crystal fiber cladding,” *Opt. Express*, vol. 15, no. 2, pp. 325–338, Jan. 2007. [Online]. Available: <https://doi.org/10.1364/OE.15.000325> (cit. on pp. 19, 21, 22, 53, 59).
- [15] J. von Neumann and E. P. Wigner, “Über das verhalten von eigenwerten bei adiabatischen prozessen,” in *The Collected Works of Eugene Paul Wigner: Part A: The Scientific Papers*, A. S. Wightman, Ed. Berlin, Heidelberg: Springer Berlin Heidelberg, 1993, pp. 294–297. [Online]. Available: https://doi.org/10.1007/978-3-662-02781-3_20 (cit. on p. 20).
- [16] P. S. Light, F. Couny, Y. Y. Wang, N. V. Wheeler, P. J. Roberts, and F. Benabid, “Double photonic bandgap hollow-core photonic crystal fiber,” *Opt. Express*, vol. 17, no. 18, pp. 16 238–16 243, Aug. 2009. [Online]. Available: <https://doi.org/10.1364/OE.17.016238> (cit. on p. 22).
- [17] R. F. Cregan, B. J. Mangan, J. C. Knight, *et al.*, “Single-mode photonic band gap guidance of light in air,” *Science*, vol. 285, no. 5433, pp. 1537–1539, 1999. [Online]. Available: <https://doi.org/10.1126/science.285.5433.1537> (cit. on p. 22).
- [18] N. Venkataraman, M. Gallagher, C. Smith, *et al.*, “Low loss (13 db/km) air core photonic band-gap fibre,” in *2002 28TH European Conference on Optical Communication*, vol. 5, 2002, pp. 1–2. [Online]. Available: <https://ieeexplore.ieee.org/document/1601381> (cit. on pp. 22, 29).
- [19] P. J. Roberts, F. Couny, H. Sabert, *et al.*, “Ultimate low loss of hollow-core photonic crystal fibres,” *Opt. Express*, vol. 13, no. 1, pp. 236–244, Jan. 2005.

- [Online]. Available: <https://doi.org/10.1364/OPEX.13.000236> (cit. on pp. 22, 23, 28, 83, 89, 93–95, 113).
- [20] G. Humbert, J. C. Knight, G. Bouwmans, *et al.*, “Hollow core photonic crystal fibers for beam delivery,” *Opt. Express*, vol. 12, no. 8, pp. 1477–1484, Apr. 2004. [Online]. Available: <https://doi.org/10.1364/OPEX.12.001477> (cit. on p. 23).
- [21] M. Duguay, Y. Kokubun, T. Koch, and L. Pfeiffer, “Antiresonant reflecting optical waveguides in sio₂-si multilayer structures,” *Applied Physics Letters*, vol. 49, pp. 13–15, Aug. 1986. [Online]. Available: <https://doi.org/10.1063/1.97085> (cit. on p. 23).
- [22] Y. Y. Wang, F. Couny, P. J. Roberts, and F. Benabid, “Low loss broadband transmission in optimized core-shape kagome hollow-core pcf,” in *Conference on Lasers and Electro-Optics 2010*, Optica Publishing Group, 2010, CPDB4. [Online]. Available: <https://doi.org/10.1364/CLEO.2010.CPDB4> (cit. on p. 25).
- [23] Y. Y. Wang, N. V. Wheeler, F. Couny, P. J. Roberts, and F. Benabid, “Low loss broadband transmission in hypocycloid-core kagome hollow-core photonic crystal fiber,” *Opt. Lett.*, vol. 36, no. 5, pp. 669–671, Mar. 2011. [Online]. Available: <https://doi.org/10.1364/OL.36.000669> (cit. on p. 26).
- [24] B. Debord, M. Alharbi, T. Bradley, *et al.*, “Hypocycloid-shaped hollow-core photonic crystal fiber part i: arc curvature effect on confinement loss,” *Opt. Express*, vol. 21, no. 23, pp. 28 597–28 608, Nov. 2013. [Online]. Available: <https://doi.org/10.1364/OE.21.028597> (cit. on pp. 26, 59).
- [25] M. Maurel, M. Chafer, A. Amsanpally, *et al.*, “Optimized inhibited-coupling kagome fibers at yb-nd:yag (8.5 db/km) and ti:sa (30 db/km) ranges,” *Opt. Lett.*, vol. 43, no. 7, pp. 1598–1601, Apr. 2018. [Online]. Available: <https://doi.org/10.1364/OL.43.001598> (cit. on pp. 26, 77).
- [26] A. D. Pryamikov, A. S. Biriukov, A. F. Kosolapov, V. G. Plotnichenko, S. L. Semjonov, and E. M. Dianov, “Demonstration of a waveguide regime for a silica hollow - core microstructured optical fiber with a negative curvature of the core boundary in the spectral region $> 3.5 \mu\text{m}$,” *Opt. Express*, vol. 19, no. 2, pp. 1441–1448, Jan. 2011. [Online]. Available: <https://doi.org/10.1364/OE.19.001441> (cit. on p. 26).
- [27] B. Debord, A. Amsanpally, M. Chafer, *et al.*, “7.7 db/km transmission loss at 750 nm inhibited-coupling guiding hollow-core photonic crystal fibers,” in *2017 European Conference on Lasers and Electro-Optics and European Quantum Electronics Conference*, Optica Publishing Group, 2017, CJ 8 4. [Online]. Available:

- https://opg.optica.org/abstract.cfm?URI=CLEO_Europe-2017-CJ_8_4 (cit. on pp. 26, 118).
- [28] S.-f. Gao, Y.-y. Wang, W. Ding, *et al.*, “Hollow-core conjoined-tube negative-curvature fibre with ultralow loss,” *Nature Communications*, vol. 9, no. 1, p. 2828, Jul. 2018. [Online]. Available: <https://doi.org/10.1038/s41467-018-05225-1> (cit. on pp. 26, 73, 77, 118).
- [29] H. Sakr, T. D. Bradley, G. T. Jasion, *et al.*, “Hollow core nanfs with five nested tubes and record low loss at 850, 1060, 1300 and 1625nm,” in *Optical Fiber Communication Conference (OFC) 2021*, Optica Publishing Group, 2021, F3A.4. [Online]. Available: <https://doi.org/10.1364/OFC.2021.F3A.4> (cit. on p. 26).
- [30] G. T. Jasion, H. Sakr, J. R. Hayes, *et al.*, “0.174 db/km hollow core double nested antiresonant nodeless fiber (dnanf),” in *Optical Fiber Communication Conference (OFC) 2022*, Optica Publishing Group, 2022, Th4C.7. [Online]. Available: <https://doi.org/10.1364/OFC.2022.Th4C.7> (cit. on pp. 26, 93).
- [31] Y. Tamura, H. Sakuma, K. Morita, *et al.*, “Lowest-ever 0.1419-dB/km loss optical fiber,” in *Optical Fiber Communication Conference Postdeadline Papers*, Optica Publishing Group, 2017, Th5D.1. [Online]. Available: <https://doi.org/10.1364/OFC.2017.Th5D.1> (cit. on p. 26).
- [32] T. Miya, Y. Terunuma, T. Hosaka, and T. Miyashita, “Ultimate low-loss single-mode fibre at 1.55 μm ,” *Electronics Letters*, vol. 15, pp. 106–108, 4 1979. [Online]. Available: <https://doi.org/10.1049/el:19790077> (cit. on p. 26).
- [33] C. Kao, “Nobel lecture: sand from centuries past: send future voices fast,” *Reviews of Modern Physics - REV MOD PHYS*, vol. 82, pp. 2299–2303, Aug. 2010. [Online]. Available: <https://doi.org/10.1103/RevModPhys.82.2299> (cit. on p. 27).
- [34] S. Shibata, M. Horiguchi, K. Jinguji, S. Mitachi, T. Kanamori, and T. Manabe, “Prediction of loss minima in infra-red optical fibres,” *Electronics Letters*, vol. 17, pp. 775–777, 21 1981. [Online]. Available: <https://doi.org/10.1049/el:19810544> (cit. on p. 27).
- [35] Y. Yue, J. Christiansen, and S. Jensen, “Determination of the fictive temperature for a hyperquenched glass,” *Chemical Physics Letters*, vol. 357, no. 1, pp. 20–24, 2002. [Online]. Available: [https://doi.org/10.1016/S0009-2614\(02\)00434-7](https://doi.org/10.1016/S0009-2614(02)00434-7) (cit. on p. 27).
- [36] Y. Tamura, H. Sakuma, K. Morita, *et al.*, “The first 0.14-dB/km loss optical fiber and its impact on submarine transmission,” *J. Lightwave Technol.*, vol. 36, no. 1,

- pp. 44–49, Jan. 2018. [Online]. Available: <https://opg.optica.org/jlt/abstract.cfm?URI=jlt-36-1-44> (cit. on p. 28).
- [37] B. Bresson, C. Brun, X. Buet, *et al.*, “Anisotropic superattenuation of capillary waves on driven glass interfaces,” *Phys. Rev. Lett.*, vol. 119, p. 235 501, 23 Dec. 2017. [Online]. Available: <https://doi.org/10.1103/PhysRevLett.119.235501> (cit. on pp. 28, 94, 95, 108).
- [38] F. Poletti, “Nested antiresonant nodeless hollow core fiber,” *Opt. Express*, vol. 22, no. 20, pp. 23 807–23 828, Oct. 2014. [Online]. Available: <https://doi.org/10.1364/OE.22.023807> (cit. on pp. 28, 73, 93).
- [39] G. Keiser, *Optical Fiber Communications: Principles and Practice*. Macmillan, 2000 (cit. on p. 29).
- [40] E. A. J. Marcatili and R. A. Schmeltzer, “Hollow metallic and dielectric waveguides for long distance optical transmission and lasers,” *The Bell System Technical Journal*, vol. 43, no. 4, pp. 1783–1809, 1964. [Online]. Available: <https://doi.org/10.1002/j.1538-7305.1964.tb04108.x> (cit. on pp. 29, 50).
- [41] R. Schermer and J. Cole, “Improved bend loss formula verified for optical fiber by simulation and experiment,” *Quantum Electronics, IEEE Journal of*, vol. 43, pp. 899–909, Nov. 2007. [Online]. Available: <https://doi.org/10.1109/JQE.2007.903364> (cit. on p. 30).
- [42] E. Numkam Fokoua, Y. Chen, D. J. Richardson, and F. Poletti, “Microbending effects in hollow-core photonic bandgap fibers,” in *ECOC 2016; 42nd European Conference on Optical Communication*, 2016, pp. 1–3 (cit. on p. 30).
- [43] O. J. H., A. Foued, D. Frédéric, *et al.*, “Hollow-core fibers with reduced surface roughness and ultralow loss in the short-wavelength range,” 1, vol. 14, 2023, p. 1146. [Online]. Available: <https://doi.org/10.1038/s41467-023-36785-6> (cit. on pp. 30, 34, 118, 119).
- [44] F. Melli, L. Rosa, and L. Vincetti, “Analytical formulas for micro-bending and surface scattering loss estimation in tube lattice fibers,” *Journal of Lightwave Technology*, vol. 41, no. 17, pp. 5714–5721, 2023. [Online]. Available: <https://doi.org/10.1109/JLT.2023.3265167> (cit. on pp. 30, 60, 96).
- [45] L. Poladian, N. A. Issa, and T. M. Monro, “Fourier decomposition algorithm for leaky modes of fibres with arbitrary geometry,” *Opt. Express*, vol. 10, no. 10, pp. 449–454, May 2002. [Online]. Available: <https://doi.org/10.1364/OE.10.000449> (cit. on p. 30).
- [46] P. Poggiolini and F. Poletti, “Opportunities and challenges for long-distance transmission in hollow-core fibres,” *J. Lightwave Technol.*, vol. 40, no. 6, pp. 1605–

- 1616, Mar. 2022. [Online]. Available: <https://opg.optica.org/jlt/abstract.cfm?URI=jlt-40-6-1605> (cit. on p. 33).
- [47] C. Goïcoechéa, T. Billotte, M. Chafer, *et al.*, “Fabrication and characterization of iodine photonic microcells for sub-doppler spectroscopy applications,” *Opt. Express*, vol. 31, no. 10, pp. 15 316–15 325, May 2023. [Online]. Available: <https://doi.org/10.1364/OE.484049> (cit. on p. 33).
- [48] M. A. Cooper, J. Wahlen, S. Yerolatsitis, *et al.*, “2.2 kw single-mode narrow-linewidth laser delivery through a hollow-core fiber,” *Optica*, vol. 10, no. 10, pp. 1253–1259, Oct. 2023. [Online]. Available: <https://doi.org/10.1364/OPTICA.495806> (cit. on p. 33).
- [49] J. D. Joannopoulos, S. G. Johnson, J. N. Winn, and R. D. Meade, *Photonic Crystals: Molding the Flow of Light - Second Edition*, REV - Revised, 2. Princeton University Press, 2008. [Online]. Available: <http://www.jstor.org/stable/j.ctvcm4gz9> (visited on 02/17/2023) (cit. on p. 36).
- [50] J. Bures, *Guided Optics: Optical Fibers and All-Fiber Components*, English, ser. Physics Textbook. Wiley-Vch, 2008, p. 368, Supplementary material available free to lecturers. (cit. on p. 36).
- [51] S. G. Johnson and J. D. Joannopoulos, “Block-iterative frequency-domain methods for maxwell’s equations in a planewave basis,” *Opt. Express*, vol. 8, no. 3, pp. 173–190, Jan. 2001. [Online]. Available: <https://doi.org/10.1364/OE.8.000173> (cit. on p. 37).
- [52] T. P. White, B. T. Kuhlmeiy, R. C. McPhedran, *et al.*, “Multipole method for microstructured optical fibers. i. formulation,” *J. Opt. Soc. Am. B*, vol. 19, no. 10, pp. 2322–2330, Oct. 2002. [Online]. Available: <https://doi.org/10.1364/JOSAB.19.002322> (cit. on p. 38).
- [53] B. T. Kuhlmeiy, T. P. White, G. Renversez, *et al.*, “Multipole method for microstructured optical fibers. ii. implementation and results,” *J. Opt. Soc. Am. B*, vol. 19, no. 10, pp. 2331–2340, Oct. 2002. [Online]. Available: <https://doi.org/10.1364/JOSAB.19.002331> (cit. on p. 38).
- [54] Z. Zhu and T. G. Brown, “Full-vectorial finite-difference analysis of microstructured optical fibers,” *Opt. Express*, vol. 10, no. 17, pp. 853–864, Aug. 2002. [Online]. Available: <https://doi.org/10.1364/OE.10.000853> (cit. on pp. 39, 40).
- [55] T. A. Lenahan, “Calculation of modes in an optical fiber using the finite element method and eispack,” *The Bell System Technical Journal*, vol. 62, no. 9, pp. 2663–2694, 1983 (cit. on p. 41).

- [56] A.-K. Tornberg and B. Engquist, “Consistent boundary conditions for the yee scheme,” *Journal of Computational Physics*, vol. 227, no. 14, pp. 6922–6943, 2008. [Online]. Available: <https://doi.org/10.1016/j.jcp.2008.03.045> (cit. on p. 41).
- [57] P. McIsaac, “Symmetry-induced modal characteristics of uniform waveguides - i: summary of results,” *IEEE Transactions on Microwave Theory and Techniques*, vol. 23, no. 5, pp. 421–429, 1975. [Online]. Available: <https://doi.org/10.1109/TMTT.1975.1128584> (cit. on p. 42).
- [58] Sellmeier, “Zur erklärang der abnormen farbenfolge im spectrum einiger substanzen,” *Annalen der Physik*, vol. 219, pp. 272–282, 1871. [Online]. Available: <https://doi.org/10.1002/ANDP.18712190612> (cit. on p. 42).
- [59] J. W. Gooch, “Sellmeier equation,” in *Encyclopedic Dictionary of Polymers*, J. W. Gooch, Ed. New York, NY: Springer New York, 2011, pp. 653–654. [Online]. Available: https://doi.org/10.1007/978-1-4419-6247-8_10447 (cit. on p. 42).
- [60] C.-P. Yu and H.-C. Chang, “Yee-mesh-based finite difference eigenmode solver with pml absorbing boundary conditions for optical waveguides and photonic crystal fibers,” *Opt. Express*, vol. 12, no. 25, pp. 6165–6177, Dec. 2004. [Online]. Available: <https://doi.org/10.1364/OPEX.12.006165> (cit. on p. 43).
- [61] P.-j. Chiang and H.-c. Chang, “A high-accuracy pseudospectral full-vectorial leaky optical waveguide mode solver with carefully implemented upml absorbing boundary conditions,” *Opt. Express*, vol. 19, no. 2, pp. 1594–1608, Jan. 2011. [Online]. Available: <https://doi.org/10.1364/OE.19.001594> (cit. on pp. 43, 161).
- [62] K. Saitoh and M. Koshiba, “Full-vectorial imaginary-distance beam propagation method based on a finite element scheme: application to photonic crystal fibers,” *IEEE Journal of Quantum Electronics*, vol. 38, no. 7, pp. 927–933, 2002. [Online]. Available: <https://doi.org/10.1109/JQE.2002.1017609> (cit. on pp. 43, 44, 161).
- [63] *COMSOL Multiphysics Reference Manual*, COMSOL Multiphysics® v. 5.5, COMSOL AB, Stockholm, Sweden, 2019, pp. 382–396, [Link 1](#), [Link 2](#) (cit. on p. 44).
- [64] A. Oskooi and S. G. Johnson, “Distinguishing correct from incorrect pml proposals and a corrected unsplit pml for anisotropic, dispersive media,” *Journal of Computational Physics*, vol. 230, no. 7, pp. 2369–2377, 2011. [Online]. Available: <https://doi.org/10.1016/j.jcp.2011.01.006> (cit. on p. 44).

- [65] P.-R. Loh, A. F. Oskooi, M. Ibanescu, M. Skorobogatiy, and S. G. Johnson, “Fundamental relation between phase and group velocity, and application to the failure of perfectly matched layers in backward-wave structures,” *Phys. Rev. E*, vol. 79, p. 065 601, 6 Jun. 2009. [Online]. Available: <https://doi.org/10.1103/PhysRevE.79.065601> (cit. on p. 45).
- [66] *Cali*, <https://cali-doc.unilim.fr/materiel-cali2>, Limoges, France, Oct. 2023 (cit. on p. 46).
- [67] *Curta*, <https://redmine.mcia.fr/projects/cluster-curta/wiki>, Bordeaux, France, Oct. 2023 (cit. on p. 46).
- [68] I. A. Sukhoivanov and I. V. Guryev, *Photonic Crystals: Physics and Practical Modeling*. New York, NY: Springer, 2009. [Online]. Available: <https://doi.org/10.1007/978-0-387-89371-7> (cit. on p. 50).
- [69] R. B. Lehoucq, D. C. Sorensen, and C. Yang, “Arpack users’ guide: solution of large-scale eigenvalue problems with implicitly restarted arnoldi methods,” *SIAM*, 1998 (cit. on p. 50).
- [70] *COMSOL Multiphysics Reference Manual*, COMSOL Multiphysics® v. 5.5, COMSOL AB, Stockholm, Sweden, 2019, pp. 269–292, [Link](#) (cit. on p. 52).
- [71] F. Benabid and P. Roberts, “Linear and nonlinear optical properties of hollow core photonic crystal fiber,” *Journal of Modern Optics*, vol. 58, no. 2, pp. 87–124, 2011. [Online]. Available: <https://doi.org/10.1080/09500340.2010.543706> (cit. on p. 54).
- [72] A. W. Snyder and J. D. Love, *Optical Waveguide Theory*. London ; New York: Chapman & Hall, 1983 (cit. on p. 54).
- [73] A. W. Snyder and X.-H. Zheng, “Optical fibers of arbitrary cross sections,” *J. Opt. Soc. Am. A*, vol. 3, no. 5, pp. 600–609, May 1986. [Online]. Available: <https://doi.org/10.1364/JOSAA.3.000600> (cit. on p. 56).
- [74] M. Kharadly and J. Lewis, “Properties of dielectric-tube waveguides,” *Proceedings of the Institution of Electrical Engineers*, vol. 116, no. 2, pp. 214–224, 1969. [Online]. Available: <https://doi.org/10.1049/piee.1969.0045> (cit. on p. 60).
- [75] L. Vincetti and V. Setti, “Extra loss due to fano resonances in inhibited coupling fibers based on a lattice of tubes,” *Opt. Express*, vol. 20, no. 13, pp. 14 350–14 361, Jun. 2012. [Online]. Available: <https://doi.org/10.1364/OE.20.014350> (cit. on p. 60).
- [76] N. Baddour, “Operational and convolution properties of two-dimensional fourier transforms in polar coordinates,” *J. Opt. Soc. Am. A*, vol. 26, no. 8, pp. 1767–1777,

- Aug. 2009. [Online]. Available: <https://doi.org/10.1364/JOSAA.26.001767> (cit. on p. 60).
- [77] D. C. Allan, N. F. Borrelli, M. T. Gallagher, *et al.*, “Surface modes and loss in air-core photonic bandgap fibers,” in *Photonic Crystal Materials and Devices*, A. Adibi, A. Scherer, and S. Y. Lin, Eds., International Society for Optics and Photonics, vol. 5000, SPIE, 2003, pp. 161–174. [Online]. Available: <https://doi.org/10.1117/12.480052> (cit. on pp. 61, 62).
- [78] J. A. West, C. M. Smith, N. F. Borrelli, D. C. Allan, and K. W. Koch, “Surface modes in air-core photonic band-gap fibers,” *Opt. Express*, vol. 12, no. 8, pp. 1485–1496, Apr. 2004. [Online]. Available: <https://doi.org/10.1364/OPEX.12.001485> (cit. on p. 61).
- [79] F. Melli, K. Vasko, L. Rosa, F. Benabid, and L. Vincetti, “Azimuthal Fourier Decomposition for Loss Analysis of Hollow-Core Tube Lattice Fibers Part I: Ideal Fibers,” *TechRxiv*, Aug. 2022. [Online]. Available: <https://doi.org/10.36227/techrxiv.20439645.v1> (cit. on p. 62).
- [80] F. Melli, F. Giovanardi, K. Vasko, L. Rosa, F. Benabid, and L. Vincetti, “Azimuthal Fourier Decomposition for Loss Analysis of Hollow-Core Tube Lattice Fibers Part II: Tube Thickness Variation Effects,” *TechRxiv*, Aug. 2022. [Online]. Available: <https://doi.org/10.36227/techrxiv.20439678.v1> (cit. on p. 62).
- [81] L. Vincetti and V. Setti, “Waveguiding mechanism in tube lattice fibers,” *Opt. Express*, vol. 18, no. 22, pp. 23 133–23 146, Oct. 2010. [Online]. Available: <https://doi.org/10.1364/OE.18.023133> (cit. on p. 66).
- [82] T. D. Bradley, Y. Wang, M. Alharbi, *et al.*, “Optical properties of low loss (70db/km) hypocycloid-core kagome hollow core photonic crystal fiber for rb and cs base-optical applications,” *J. Lightwave Technol.*, vol. 31, no. 16, pp. 3052–3055, Aug. 2013. [Online]. Available: <https://opg.optica.org/jlt/abstract.cfm?URI=jlt-31-16-3052> (cit. on p. 66).
- [83] P. Uebel, M. C. Günendi, M. H. Frosz, *et al.*, “Broadband robustly single-mode hollow-core pcf by resonant filtering of higher-order modes,” *Opt. Lett.*, vol. 41, no. 9, pp. 1961–1964, May 2016. [Online]. Available: <https://doi.org/10.1364/OL.41.001961> (cit. on p. 66).
- [84] S.-f. Gao, Y.-y. Wang, X.-l. Liu, C. Hong, S. Gu, and P. Wang, “Nodeless hollow-core fiber for the visible spectral range,” *Opt. Lett.*, vol. 42, no. 1, pp. 61–64, Jan. 2017. [Online]. Available: <https://doi.org/10.1364/OL.42.000061> (cit. on pp. 66, 77).

- [85] F. BENABID, F. Gérôme, F. ARMANI, and F. OSORIO Jonas DELAHAYE, “Method and device for manufacturing a hollow-core optical fibre,” 2019, FR1912283, WO2021083973A1. [Online]. Available: <https://patents.google.com/patent/WO2021083973A1> (cit. on pp. 67, 96, 108).
- [86] F. Amrani, J. H. Osorio, F. Delahaye, *et al.*, “Design and fabrication of a single-mode and ultra-low loss hollow-core fiber based on kagome-tubular hybrid lattice,” *Conference on Lasers and Electro-Optics*, STu1Q.2, 2021. [Online]. Available: https://doi.org/10.1364/CLEO_SI.2021.STu1Q.2 (cit. on p. 67).
- [87] Y. Hong, X. Lu, S. Gao, *et al.*, “Low loss polarization maintaining anti-resonant hollow core fiber,” in *Optica Advanced Photonics Congress 2022*, Optica Publishing Group, 2022, JTh4A.6. [Online]. Available: <https://doi.org/10.1364/BGPPM.2022.JTh4A.6> (cit. on p. 72).
- [88] M. S. Habib, J. E. Antonio-Lopez, C. Markos, A. Schülzgen, and R. Amezcua-Correa, “Single-mode, low loss hollow-core anti-resonant fiber designs,” *Opt. Express*, vol. 27, no. 4, pp. 3824–3836, Feb. 2019. [Online]. Available: <https://doi.org/10.1364/OE.27.003824> (cit. on p. 73).
- [89] J. W. Nicholson, A. D. Yablon, S. Ramachandran, and S. Ghalmi, “Spatially and spectrally resolved imaging of modal content in large-mode-area fibers,” *Opt. Express*, vol. 16, no. 10, pp. 7233–7243, May 2008. [Online]. Available: <https://doi.org/10.1364/OE.16.007233> (cit. on p. 76).
- [90] B. Debord, A. Amsanpally, M. Chafer, *et al.*, “Ultralow transmission loss in inhibited-coupling guiding hollow fibers,” *Optica*, vol. 4, no. 2, pp. 209–217, Feb. 2017. [Online]. Available: <https://doi.org/10.1364/OPTICA.4.000209> (cit. on p. 77).
- [91] M. Chafer, J. H. Osório, F. Amrani, *et al.*, “1-km hollow-core fiber with loss at the silica rayleigh limit in the green spectral region,” *IEEE Photonics Technology Letters*, vol. 31, no. 9, pp. 685–688, 2019. [Online]. Available: <https://doi.org/10.1109/LPT.2019.2904341> (cit. on pp. 77, 118).
- [92] G. T. Jasion, T. D. Bradley, K. Harrington, *et al.*, “Hollow core nanf with 0.28 db/km attenuation in the c and l bands,” in *Optical Fiber Communication Conference Postdeadline Papers 2020*, Optica Publishing Group, 2020, Th4B.4. [Online]. Available: <https://doi.org/10.1364/OFC.2020.Th4B.4> (cit. on p. 77).
- [93] H. Sakr, Y. Chen, G. Jasion, *et al.*, “Hollow core optical fibres with comparable attenuation to silica fibres between 600 and 1100 nm,” *Nature Communications*, vol. 11, Nov. 2020. [Online]. Available: <https://doi.org/10.1038/s41467-020-19910-7> (cit. on pp. 77, 118).

- [94] F. Amrani, J. H. Osório, F. Delahaye, *et al.*, “Low-loss single-mode hybrid-lattice hollow-core photonic-crystal fibre,” *Light: Science & Applications*, vol. 10, no. 1, p. 7, 2021. [Online]. Available: <https://doi.org/10.1038/s41377-020-00457-7> (cit. on pp. 77, 93).
- [95] T. D. Bradley, J. R. Hayes, Y. Chen, *et al.*, “Record low-loss 1.3db/km data transmitting antiresonant hollow core fibre,” in *2018 European Conference on Optical Communication (ECOC)*, 2018, pp. 1–3. [Online]. Available: <https://doi.org/10.1109/ECOC.2018.8535324> (cit. on p. 77).
- [96] J. M. Fini, J. W. Nicholson, R. S. Windeler, *et al.*, “Low-loss hollow-core fibers with improved single-modedness,” *Opt. Express*, vol. 21, no. 5, pp. 6233–6242, Mar. 2013. [Online]. Available: <https://doi.org/10.1364/OE.21.006233> (cit. on p. 83).
- [97] D. Derks, D. G. A. L. Aarts, D. Bonn, H. N. W. Lekkerkerker, and A. Imhof, “Suppression of thermally excited capillary waves by shear flow,” *Phys. Rev. Lett.*, vol. 97, p. 038 301, 3 Jul. 2006. [Online]. Available: <https://doi.org/10.1103/PhysRevLett.97.038301> (cit. on pp. 89, 96, 107, 113).
- [98] M. Thiébaud, “Quelques aspects de la physique des interfaces cisillées : Hydrodynamique et Fluctuations.” Theses, Université Sciences et Technologies - Bordeaux I, Sep. 2011. [Online]. Available: <https://theses.hal.science/tel-00769006> (cit. on p. 89).
- [99] C. Chindam, N. Nama, M. Ian Lapsley, F. Costanzo, and T. Jun Huang, “Theory and experiment on resonant frequencies of liquid-air interfaces trapped in microfluidic devices,” *Journal of Applied Physics*, vol. 114, no. 19, p. 194 503, Nov. 2013. [Online]. Available: <https://doi.org/10.1063/1.4827425> (cit. on p. 91).
- [100] F. Elie, “Ondes de surface des liquides,” Feb. 2009 (cit. on p. 91).
- [101] M. Rieutord, *Une introduction à la dynamique des fluides: cours avec exercices corrigés*. Masson, 1997 (cit. on p. 91).
- [102] T. Sarlat, A. Lelarge, E. Søndergård, and D. Vandembroucq, “Frozen capillary waves on glass surfaces: an afm study,” *The European Physical Journal B - Condensed Matter and Complex Systems*, vol. 54, no. 1, pp. 121–126, 2006. [Online]. Available: <https://doi.org/10.1140/epjb/e2006-00420-6> (cit. on p. 92).
- [103] J. Jackle and K. Kawasaki, “Intrinsic roughness of glass surfaces,” *Journal of Physics: Condensed Matter*, vol. 7, no. 23, p. 4351, Jun. 1995. [Online]. Available: <https://doi.org/10.1088/0953-8984/7/23/006> (cit. on pp. 92, 107).

- [104] J. M. Elson, J. P. Rahn, and J. M. Bennett, “Relationship of the total integrated scattering from multilayer-coated optics to angle of incidence, polarization, correlation length, and roughness cross-correlation properties,” *Appl. Opt.*, vol. 22, no. 20, pp. 3207–3219, Oct. 1983. [Online]. Available: <https://doi.org/10.1364/AO.22.003207> (cit. on p. 93).
- [105] L. Vincetti, “Empirical formulas for calculating loss in hollow core tube lattice fibers,” *Opt. Express*, vol. 24, no. 10, pp. 10 313–10 325, May 2016. [Online]. Available: <https://doi.org/10.1364/OE.24.010313> (cit. on pp. 93, 115).
- [106] X. Buet, C. Brun, J. Gâteau, *et al.*, “Nondestructive measurement of the roughness of the inner surface of hollow core-photonic bandgap fibers,” *Opt. Lett.*, vol. 41, no. 21, pp. 5086–5089, Nov. 2016. [Online]. Available: <https://doi.org/10.1364/OL.41.005086> (cit. on pp. 94, 95, 113).
- [107] E. N. Fokoua, S. A. Mousavi, G. T. Jasion, D. J. Richardson, and F. Poletti, “Loss in hollow-core optical fibers: mechanisms, scaling rules, and limits,” *Adv. Opt. Photon.*, vol. 15, no. 1, pp. 1–85, Mar. 2023. [Online]. Available: <https://doi.org/10.1364/AOP.470592> (cit. on p. 96).
- [108] F. BENABID, “Method and device for manufacturing an optical fibre,” FR1902656, WO2020187595A1, 2019. [Online]. Available: <https://patents.google.com/patent/WO2020187595A1> (cit. on pp. 97, 119, 120).
- [109] D. Stirzaker, *Stochastic Processes and Models*. Oxford University Press, 2005 (cit. on p. 98).
- [110] K. Vasko, F. Melli, L. Rosa, L. Vincetti, and F. Benabid, “Modal content and confinement loss evolution with surface roughness profile in hollow-core inhibited coupling tube lattice fibers,” *Conference on Lasers and Electro-Optics*, JW3B.40, 2022. [Online]. Available: https://doi.org/10.1364/CLEO_AT.2022.JW3B.40 (cit. on p. 101).
- [111] K. Vasko, L. Vincetti, L. Rosa, and F. Melli, *Roughness Generation*, <https://gitlab.xlim.fr/gppmm/simulations/roughnessgeneration>, Limoges, France, Aug. 2022 (cit. on pp. 103, 168).
- [112] M. Thiébaud and T. Bickel, “Nonequilibrium fluctuations of an interface under shear,” *Phys. Rev. E*, vol. 81, p. 031 602, 3 Mar. 2010. [Online]. Available: <https://doi.org/10.1103/PhysRevE.81.031602> (cit. on p. 108).
- [113] T. H. R. Smith, O. Vasilyev, D. B. Abraham, A. Maciołek, and M. Schmidt, “Interfaces in driven ising models: shear enhances confinement,” *Phys. Rev. Lett.*, vol. 101, p. 067 203, 6 Aug. 2008. [Online]. Available: <https://doi.org/10.1103/PhysRevLett.101.067203> (cit. on p. 108).

- [114] T. H. R. Smith, O. Vasilyev, A. Maciołek, and M. Schmidt, “Laterally driven interfaces in the three-dimensional ising lattice gas,” *Phys. Rev. E*, vol. 82, p. 021 126, 2 Aug. 2010. [Online]. Available: <https://doi.org/10.1103/PhysRevE.82.021126> (cit. on p. 108).
- [115] G. K. Batchelor, *An Introduction to Fluid Dynamics*, ser. Cambridge Mathematical Library. Cambridge University Press, 2000. [Online]. Available: <https://doi.org/10.1017/CB09780511800955> (cit. on p. 108).
- [116] S. C. Xue, R. I. Tanner, G. W. Barton, R. Lwin, M. C. J. Large, and L. Poladian, “Fabrication of microstructured optical fibers-part i: problem formulation and numerical modeling of transient draw process,” *J. Lightwave Technol.*, vol. 23, no. 7, p. 2245, Jul. 2005. [Online]. Available: <https://opg.optica.org/jlt/abstract.cfm?URI=jlt-23-7-2245> (cit. on p. 109).
- [117] Y. Chen and T. A. Birks, “Predicting hole sizes after fibre drawing without knowing the viscosity,” *Opt. Mater. Express*, vol. 3, no. 3, pp. 346–356, Mar. 2013. [Online]. Available: <https://doi.org/10.1364/OME.3.000346> (cit. on p. 109).
- [118] C. Brun, X. Buet, B. Bresson, *et al.*, “Picometer-scale surface roughness measurements inside hollow glass fibres,” *Opt. Express*, vol. 22, no. 24, pp. 29 554–29 567, Dec. 2014. [Online]. Available: <https://doi.org/10.1364/OE.22.029554> (cit. on p. 113).
- [119] F. Yu, M. Cann, A. Brunton, W. Wadsworth, and J. Knight, “Single-mode solarization-free hollow-core fiber for ultraviolet pulse delivery,” *Optics Express*, vol. 26, p. 10 879, Apr. 2018. [Online]. Available: <https://doi.org/10.1364/OE.26.010879> (cit. on p. 118).
- [120] S. Gao, Y. Wang, W. Ding, Y.-f. Hong, and P. Wang, “Conquering the rayleigh scattering limit of silica glass fiber at visible wavelengths with a hollow-core fiber approach,” *Laser & Photonics Reviews*, vol. 14, p. 1 900 241, Dec. 2019. [Online]. Available: <https://doi.org/10.1002/lpor.201900241> (cit. on p. 118).
- [121] F. Hindle, E. Fertein, C. Przygodzki, *et al.*, “Inscription of long-period gratings in pure silica and germano–silicate fiber cores by femtosecond laser irradiation,” *Photonics Technology Letters, IEEE*, vol. 16, pp. 1861–1863, Sep. 2004. [Online]. Available: <https://doi.org/10.1109/LPT.2004.831264> (cit. on p. 119).
- [122] S. Selleri, L. Vincetti, and A. Cucinotta, *Optical and Photonic Components*. Societa Editrice Esculapio, 2015 (cit. on pp. 136, 137).
- [123] H. Haus and W. Huang, “Coupled-mode theory,” *Proceedings of the IEEE*, vol. 79, no. 10, pp. 1505–1518, 1991. [Online]. Available: <https://doi.org/10.1109/5.104225> (cit. on pp. 136, 137).

- [124] E. K. Sharma, J. P. Nath, and N. Dhingra, “Coupled mode theory and coupled mode photonic devices: a review,” *Asian Journal of Physics*, vol. 30, no. 5, pp. 00–00, 2021, [Link](#) (cit. on pp. 136, 137).
- [125] *Wave Optics Module User’s Guide*, COMSOL Multiphysics® v. 5.5, COMSOL AB, Stockholm, Sweden, 2019, pp. 133–141, [Link](#) (cit. on pp. 157, 158).
- [126] L. Yang, L.-L. Xue, Y.-C. Lu, and W.-P. Huang, “New insight into quasi leaky mode approximations for unified coupled-mode analysis,” *Opt. Express*, vol. 18, no. 20, pp. 20 595–20 609, Sep. 2010. [Online]. Available: <https://doi.org/10.1364/OE.18.020595> (cit. on p. 177).

Scientific contributions

Publications in international peer-reviewed journals

- F. Melli, K. Vasko, L. Rosa, F. Benabid, and L. Vincetti, “Azimuthal Fourier Decomposition for Loss Analysis of Hollow-Core Tube Lattice Fibers Part I: Ideal Fibers,” *TechRxiv*, Aug. 2022. [Online]. Available: <https://doi.org/10.36227/techrxiv.20439645.v1>.
- F. Melli, F. Giovanardi, K. Vasko, L. Rosa, F. Benabid, and L. Vincetti, “Azimuthal Fourier Decomposition for Loss Analysis of Hollow-Core Tube Lattice Fibers Part II: Tube Thickness Variation Effects,” *TechRxiv*, Aug. 2022. [Online]. Available: <https://doi.org/10.36227/techrxiv.20439678.v1>.
- J. H. Osório, F. Amrani, F. Delahaye, A. Dhaybi, K. Vasko, F. Melli, F. Giovanardi, D. Vandembroucq, G. Tessier, L. Vincetti, B. Debord, F. Gérôme, and F. Benabid, “Hollow-core fibers with reduced surface roughness and ultralow loss in the short-wavelength range,” *Nature Communications*, vol. 14, no. 1, p. 1146, 2023. [Online]. Available: <https://doi.org/10.1038/s41467-023-36785-6>.

Publications at international peer-reviewed conferences

- K. Vasko, B. Debord, L. Rosa, L. Vincetti, and F. Benabid, “Hybrid inhibited-coupling and photonic bandgap hollow core fiber for telecom wavelength range,” *Conference on Lasers and Electro-Optics US*, JW1A.28, 2021. [Online]. Available: https://doi.org/10.1364/CLEO_AT.2021.JW1A.28.
- F. Delahaye, F. Gérôme, F. Amrani, A. Unterhuber, K. Vasko, B. Debord, M. Andreana, and F. Benabid, “Double-clad hollow-core photonic crystal fiber for nonlinear optical imaging,” *Conference on Lasers and Electro-Optics US*, AF2Q.2, 2021. [Online]. Available: https://doi.org/10.1364/CLEO_AT.2021.AF2Q.2.
- F. Amrani, J. H. Osorio, F. Delahaye, F. Giovanardi, K. Vasko, L. Vincetti, B. Debord, F. Gerome, and F. Benabid, “Design and fabrication of a single-mode and ultra-low loss hollow-core fiber based on kagome-tubular hybrid lattice,” *Conference on Lasers and Electro-Optics US*, STu1Q.2, 2021. [Online]. Available: https://doi.org/10.1364/CLEO_SI.2021.STu1Q.2.
- J. H. Osório, F. Amrani, F. Delahaye, A. Dhaybi, K. Vasko, G. Tessier, F. Giovanardi, L. Vincetti, B. Debord, F. Gérôme, and F. Benabid, “Sub-thermodynamic equilibrium surface roughness in hollowcore fibers for the ultraviolet range,” *The*

- European Optical Society Annual meeting (EOSAM)*, p. 462, Sep. 2021. [Online]. Available: <https://hal.archives-ouvertes.fr/hal-03344737>.
- J. H. Osório, F. Amrani, F. Delahaye, A. Dhaybi, K. Vasko, G. Tessier, F. Giovannardi, L. Vincetti, B. Debord, F. Gérôme, and F. Benabid, “Hollow-core fibers with ultralow loss in the ultraviolet range and sub-thermodynamic equilibrium surface-roughness,” *Conference on Lasers and Electro-Optics US*, SW4K.6, May 2022. [Online]. Available: https://doi.org/10.1364/CLEO_SI.2022.SW4K.6.
 - K. Vasko, F. Melli, L. Rosa, L. Vincetti, and F. Benabid, “Modal content and confinement loss evolution with surface roughness profile in hollow-core inhibited coupling tube lattice fibers,” *Conference on Lasers and Electro-Optics US*, JW3B.40, 2022. [Online]. Available: https://doi.org/10.1364/CLEO_AT.2022.JW3B.40.
 - F. Melli, K. Vasko, L. Rosa, L. Vincetti, and F. Benabid, “Transverse roughness effect on fundamental mode confinement loss and modal content of hollow-core inhibited coupling tube lattice fibers,” in *Optica Advanced Photonics Congress 2022*, Optica Publishing Group, 2022, SoTu1I.3. [Online]. Available: <https://doi.org/10.1364/SOF.2022.SoTu1I.3>.
 - E. Soli, F. Melli, L. Rosa, K. Vasko, F. Benabid, and L. Vincetti, “Analysis of geometrical deformation effects in hollow-core tube-lattice fibers,” *Conference on Lasers and Electro-Optics US*, STh1G.2, 2023. [Online]. Available: https://doi.org/10.1364/CLEO_SI.2023.STh1G.2.
 - A. Dhaybi, J. Osório, K. Vasko, F. Amrani, G. Tessier, B. Debord, F. Gérôme, and F. Benabid, “Picometer-resolution and high dynamic-range profilometer for hollow-core fiber surface roughness characterization,” *Conference on Lasers and Electro-Optics Europe*, pp. 1–1, 2023. [Online]. Available: <https://doi.org/10.1109/CLEO/Europe-EQEC57999.2023.10232489>.

Publications at national conferences without reading committee

- K. Vasko, A. Dhaybi, and F. Benabid, “Simulations of HCPCF with Surface Roughness,” *Journées Fibres Optiques - applications et dernières tendances*, Poster, 23-24 Nov 2022. [Online]. Available: <https://doi.org/10.5281/zenodo.8198691>.

- A. Al Dhaybi, K. Vasko, J. Osorio, F. Amarni, B. Debord, F. Gérôme, and F. Benabid, "Picometer resolution profilometer for hollow-core fiber surface roughness characterization," *Journées Fibres Optiques - applications et dernières tendances*, Poster, 23-24 Nov 2022. [Online]. Available: <https://doi.org/10.5281/zenodo.8375304>.

Outil numérique (1+2D)/3D pour modéliser la diffusion de surface de la lumière d'une fibre creuse à couplage inhibé

Résumé : Ce travail présente le développement d'un outil numérique basé sur la méthode des éléments finis pour étudier et optimiser les performances des fibres creuses à cristal photonique (HCPCF). Divers mécanismes de perte dans ces fibres ont alors pu être analysés. En premier lieu, par une compréhension fine de l'influence des paramètres géométriques sur les pertes et par une approche basée sur une décomposition de Fourier azimutale, plusieurs structures innovantes de fibres creuses ont été proposées permettant d'aller au-delà de l'état de l'art actuel. En particulier, une fibre creuse à maille hybride guidant par couplage inhibé (CI) a été conçue puis fabriquée associant pour la première fois faible perte de confinement et guidage unimodal. Puis, les sources de pertes induites par la rugosité de surface au sein de ces fibres creuses ont été intégrées aux études en développant une approche numérique transverse à 2D et par des équations de tendance. Les calculs ont alors confirmé l'impact d'un nouveau procédé de fabrication par cisaillement mis en place durant l'étape de fabrication permettant de réduire d'un facteur trois l'amplitude du profil de surface des membranes silice. Ce résultat s'est traduit par la démonstration de pertes records des HCPCF-CI aux domaines des courtes longueurs d'onde du visible (< 1 dB/km) et de l'ultraviolet (< 50 dB/km) trouvées en bon accord avec les simulations. En parallèle, un second procédé nommé opto-thermique a débuté permettant pour la première fois d'obtenir un profil de rugosité non stochastique, résultat qui constitue une perspective forte de mes travaux. Enfin, des développements pour étendre ces analyses à l'axe de propagation (simulations 2D+1 puis 3D) ont débuté. En conclusion, l'ensemble de ces travaux a permis de contribuer à réaliser une nouvelle génération de fibres creuses qui à terme pourrait répondre aux défis aussi bien des domaines peu accessibles comme l'ultraviolet que des applications à fort impact sociétal telles que les télécommunications optiques de demain.

Mots clés : Outil numérique, diffusion de surface, couplage inhibé, fibres creuses, modélisation.

Numerical (1+2D)/3D tool to model the surface scattering of light in the inhibited coupling hollow fiber

Abstract: This work presents the development of a numerical tool based on finite element method to study and optimize the performances of photonic crystal hollow-core fibers (HCPCF). Various loss mechanisms in these fibers were analyzed. Firstly, through a detailed understanding of the influence of geometric parameters on losses and by an approach based on an azimuthal Fourier decomposition, several innovative hollow-core fiber designs have been proposed making it possible to go beyond the current state-of-the-art. In particular, a hybrid hollow-core fiber guiding by inhibited coupling (IC) was designed and then manufactured, combining for the first time ultra-low confinement loss and singlemode guidance. Then, the sources of losses induced by surface roughness within these hollow-core fibers were integrated into the studies by developing a transverse 2D numerical approach and scaling formula. The calculations then confirmed the impact of a new shear process implemented during the fabrication, making it possible to reduce the amplitude of the surface profile of the silica membranes by a factor of three. This results in the demonstration of record losses of HCPCF-CI in the short wavelengths of the visible (< 1 dB/km) and the ultraviolet (< 50 dB/km) found in good agreement with simulations. In parallel, a second process called opto-thermal began, making it possible for the first time to obtain a non-stochastic roughness profile, a result which constitutes a strong perspective of my work. Finally, developments to extend these analyzes to the propagation axis (2D+1 and 3D simulations) have begun. To conclude, all of this work has contributed to the realization of a new generation of hollow-core fibers which could ultimately meet the challenges of both the still inaccessible ultraviolet domain and applications with a strong societal impact such as the optical telecommunications of tomorrow.

Keywords: Numerical tool, surface scattering, inhibited coupling, hollow core fibers, modeling.